

The BeamEDM experiment and the measurement of the neutron incoherent scattering length of ^{199}Hg

Inauguraldissertation

der Philosophisch-naturwissenschaftlichen Fakultät
der Universität Bern

vorgelegt von

Estelle Ghislaine Amélie Chanel
von Frankreich

Leiter der Arbeit:

Prof. Dr. Florian Piegsa

Albert Einstein Center for Fundamental Physics
Laboratorium für Hochenergiephysik
Physikalisches Institut



This work is licensed under the Creative Commons
Attribution-NonCommercial-NoDerivatives 4.0 International License.
To view a copy of this license, visit:

<https://creativecommons.org/licenses/by-nc-nd/4.0/>.

The BeamEDM experiment and the measurement of the neutron incoherent scattering length of ^{199}Hg

Inauguraldissertation

der Philosophisch-naturwissenschaftlichen Fakultät

der Universität Bern

vorgelegt von

Estelle Ghislaine Amélie Chanel

von Frankreich

Leiter der Arbeit:

Prof. Dr. Florian Piegsa

Albert Einstein Center for Fundamental Physics

Laboratorium für Hochenergiephysik

Physikalisches Institut

Von der philosophisch-naturwissenschaftlichen Fakultät
angenommen.

Der Dekan:

Bern, 27. October 2021

Prof. Dr. Zoltán Balogh

à Marc Muller et Rodolphe Adam

Acknowledgements

"Étudie bien à l'école pour pouvoir choisir un métier qui te plait et pas te demander pendant 40 ans de ta vie pourquoi tu te lèves le matin", merci maman. Bon même si, je cite "[tu] ne pensais pas que [j']irai aussi loin." Au beau gosse de la famille: Gabi (désolé Rémi), j'ai pu briller grâce à toi et j'espere que tu sera fier. Hein, Tatan c'est la meilleure! Puis elle est pas veille d'abord. Bon, le frère je te mets là aussi pour pas que tu te vexes et pour faire bonne figure, la soeur et le père aussi ;). En vrai je vous aime et vous êtes une partie de ce que je suis. Ma pomme de pin, Brausekpf (tannensapfe), pignouf, papacouillé.... MOUCHE! J'y serai sûrement arrivée sans toi mais ça aurait été vachement moins bien. #femmetetindependante.

Stephy, on doit se parler deux fois par an grand max mais tu as été ma motivation au collège et au lycée. Marc, binôme... tu me manques. On formait un duo de choc et je pense que les années école d'ingé font partie des meilleures. Mon petit Peloux, je referai bien une "petite" rando ;).

Magnus thanks for all the texting and the motivation. It helped a lot. The german group, we had good laughs and laughing is important. If you ever pass by France you are welcome in my house. Jacob... you can be sooooooooooooooooooooo annoying but it is because you are a good friend and you care. I will see you in conferences as you will stay in academia for ever (echo: ever ... ever... ever...) and no we will not go to "La côtelette". Oliver, I can already hear you singing "What can I say but you're welcome". Ivo thanks for being there always. I do not regret my choice of sharing an office with you. I am not good at keeping contact but for you I will. Ciro, thanks for all the talk, coffee, ice-cream ... Alex if you pass by Grenoble again we will definitely go to a nightclub. To the neutron group and the LHEP group in general, I would like to thank you for all the good time.

Vadim, I sincerely want to thank you for the time you have been my supervisor. You helped me find my path and if it was not for you I might never have done a PhD in neutron physics. I won't be able to pass by your office as "regularly" anymore but we will stay in touch.

Florian, I will start by an anecdote: it took me more than two weeks to stop calling you Prof. Piegsa and I think you never actually told me to call you by your first name. This is one evidence of my big lack of confidence when I arrived in

your group but you believed in me and little by little I improved. You were always supportive and you actually listen to what I had to say. This eventually led to long arguments about definitions and mathematical notations... They are moments when I can't express myself so well, and today is one of them but I will try. Jacob joked the other day about me writting in my thesis how a great supervisor you are, and ... he is right: you are an amazing supervisor, not only for the few things I have listed but for everything you do and how much you care. To cite my nephew: "When I am old, I want to be just like you" and I hope I reached you expectation as a first PhD student. ;)

Abstract

BeamEDM is a proof-of-principle apparatus to search for a neutron electric dipole moment using a cold neutron beam with a combined Ramsey and time-of-flight technique. Employing a time-of-flight is essential, as it allows to distinguish the $v \times E$ systematic effect from an electric dipole moment signal. To date, four beamtimes have been performed both at the Paul Scherrer Institute in Switzerland and at the Institute Laue-Langevin in France. The first part of this thesis presents the development of the apparatus and the measurements performed over the different beamtimes.

The nEDM experiment at the Paul Scherrer Institute uses ultra-cold neutrons to measure an electric dipole moment. It requires the use of a mercury co-magnetometer to monitor the magnetic field that the ultra-cold neutrons are probing. Both species can interact with each other via the neutron incoherent scattering length of mercury. This interaction takes the form of a shift in the neutron precession frequency whose sign depends on the mercury atoms' polarization. As the sign of the incoherent scattering length is unknown, the induced shift could be the cause of a systematic effect in the case of a neutron electric dipole measurement. The second part of this thesis details the apparatus, measurement, analysis, and result that has determined the sign of the incoherent scattering length of ^{199}Hg .

Table of contents

List of figures	12
List of tables	17
Part 1 : Neutron beam experiment: BeamEDM	1
1 Cosmological motivation for the neutron electric dipole moment in the particle physics model	3
1.1 Motivation	3
1.2 CP-violation from the EDM	8
1.3 Standard Model and Baryogenesis	9
1.4 Beyond standard model	12
2 Neutron physics	15
2.1 Neutron properties	15
2.2 Forces and Interactions	16
2.3 Measurement principle	21
2.4 Neutron EDM history	26
2.5 The last cold neutron beam experiment	28
3 The BeamEDM experiment	31
3.1 Introduction	31
3.2 Cold neutron beam, and infrastructures	32
3.3 The BeamEDM apparatus	34
3.3.1 Chopper	35
3.3.2 Structure	38
3.3.3 Apertures	39
3.3.4 Radio-frequency spin flipper	39
3.3.5 Vacuum pipes	42
3.3.6 High voltage system	42
3.3.7 Magnetic field	47
3.3.8 Spin analyzer	51

TABLE OF CONTENTS	9
3.3.9 Detector	54
3.3.10 Data acquisition system	56
4 Analysis principle of the phase scan meas...	59
4.1 Determination of the off-resonance value Δ^*	59
4.2 Interpretation of the off-resonance value Δ^*	61
5 Beamtimes	65
5.1 Beamtime 1: PSI September 2017	65
5.1.1 Characterization of the neutron spots in the detector	67
5.1.2 Measurement of the resonance frequency	71
5.1.3 Working range of the apparatus in wavelength	73
5.1.4 Magnetic characterization with a pulsed white beam	77
5.1.5 Magnetic characterization with continuous white beam	79
5.1.6 Summary	82
5.2 Beamtime 2: ILL March 2018	84
5.2.1 Characterization of the wavelength selector	84
5.2.2 Characteristics of the Ramsey apparatus	86
5.2.3 Characterization of the spin flippers	91
5.2.4 Magnetic characterization	93
5.2.5 Summary	97
5.3 Beamtime 3: PSI 2018	99
5.3.1 Characterization of the neutron spots in the detector	101
5.3.2 Measurements with modulated signal	103
5.3.3 $v \times E$ effect measurement with a white beam	109
5.3.4 Investigation on the EDM measurement procedure	111
5.3.5 Summary	114
5.4 Reflectivity measurement: PSI 2018	115
5.5 Beamtime 4: ILL 2020	119
5.5.1 Characterization of the neutron spots in the detector	124
5.5.2 Configuration of the spin flipper signal	126
5.5.3 Working range of the apparatus	127
5.5.4 Magnetic field characterization	129
5.5.5 $v \times E$ measurement	134
5.5.6 Stability measurement for EDM procedure	136
5.6 Summary	138
6 Conclusion	141
6.1 Magnetic Scan	141
6.2 Stability of the neutron phase	143

6.3 $v \times E$ effect	143
6.4 EDM measurement	144
6.5 Outlook	144
Part 2 : Measurement of the neutron incoherent scattering length of Mercury 199	147
7 Theory of the incoherent scattering len...	149
7.1 Scattering length	149
7.2 Incoherent scattering length	151
7.3 Pseudomagnetic Method	152
8 The measurement	155
8.1 Motivation	155
8.2 nEDM Apparatus	156
8.3 Mercury co-magnetometer	158
8.3.1 Advantages of mercury	158
8.3.2 Mercury System	159
8.3.3 Interpretation of the mercury signal	162
8.3.4 Meta file, PMT signal, precession signal	164
8.4 Mercury incoherent scattering length measur...	167
8.5 Data Analysis	169
8.6 Data selection criteria	171
8.7 Results	174
References	177
Appendix A Time evolution operator of the Ramsey...	187
Appendix B Documentation of the coils at PF1b...	191
Appendix C Connection diagram of the leakage current monitor	193
Appendix D Documentation on the spin analyzer motors	195
Appendix E List of the devices used at ILL in 2020	199
E.1 Power supplies for the electric field	199
E.2 Spin flipper system	199
E.3 Vacuum system	200
E.4 Magnetic field	200
E.5 Detector	201

<i>TABLE OF CONTENTS</i>	11
E.6 Magnetic field USB hall probes	201
Appendix F Fluxgate values during the beamtime at ILL in 2018	203
Appendix G Light absorption cross section of mercury	205
Appendix H Unpolarized light level $I(t)$ determined ...	207
Appendix I Metafile data for the density-polariza...	209
I.1 Precession file: $as(t_1)$ and τ	209
I.2 Unpolarized light level values	210
I.3 Light absorption, density, and polarization	211
Appendix Declaration	213
Appendix Curriculum Vitae	214

List of figures

1.1	The anisotropy power spectrum of the microwave background.	6
1.2	Representation of the Sakharov conditions.	7
1.3	Geometric symmetries	8
1.4	Feynman diagram of the neutron EDM from the weak sector.	11
1.5	Feynman diagram of the neutron EDM from the weak sector.	11
2.1	Representation of the effect of gravity on a cold neutron.	17
2.2	Representation of the Bragg scattering and reflectivity diagram . . .	19
2.3	Representation of the neutron by a Bloch sphere in a static field and oscillating field in the rotational frame and in the laboratory frame .	20
2.4	Frequency and amplitude Rabi patterns.	23
2.5	Representation of the neutron spin during a Ramsey technique. . . .	24
2.6	Ramsey pattern.	25
2.7	Neutron EDM limit as a function of the year of publication.	27
2.8	Representation of the apparatus from [DMP ⁺ 77].	29
2.9	Neutron spectrum of the cold neutron beam taken from [DMP ⁺ 77]. .	29
3.1	Picture of the spallation target at PSI and drawing of BOA layout at PSI.	32
3.2	Picture of a wavelength selector from EADS ASTRIUM and Drawing of PF1b layout at ILL.	33
3.3	General sketch of the apparatus with a representation of the neutron spin for each stage.	35
3.4	Picture of the chopper disk used at BOA, PSI in 2018 and representation of a pulse overlap in a time-of-flight measurement. . .	36
3.5	Picture of the chopper used at PF1b in 2020 and schematics of its working principle	36
3.6	Pictures of the aluminum structure	37
3.7	Representation of the end pieces of the aluminum structure and aluminum shielding plates.	38
3.8	Pictures of the different geometries of apertures.	39

3.9 A picture of one of the spin flippers before 2020 and representation of the modulated signal fed into it.	40
3.10 Drawing of the connection between the devices used to control and generate the oscillating field.	41
3.11 Pictures of the vacuum pipes during leak-check, during alignment, and picture of the lifting mechanism.	43
3.12 Pictures of a stack of electrodes	44
3.13 Picture of the different small pieces used to assemble and connect the electrode stacks and picture of the alignment ring of an electrode stack in a vacuum pipe.	45
3.14 Pictures of the feedthroughs used at BOA in 2018 and at PF1b in 2020 and of the connection rods to the electrodes stacks	46
3.15 Representation of the coils.	48
3.16 Picture of the coil connectors and of the fluxgates.	48
3.17 Diagram of the connection between devices for the magnetic stabilization.	49
3.18 Pictures of the structure with magnetic shielding during its characterization in Bern in 2020.	51
3.19 Working principle of the spin analyzer.	52
3.20 Picture of the analyzer used at BOA in 2017	52
3.21 Picture of the analyzer used at BOA in 2017 and the one used for the other beamtimes.	53
3.22 Picture of the end piece of the structure with the spin analyzer, the sliding plate and the detector at BOA in 2018.	55
3.23 Picture of the front, top, and back side of the detector	55
4.1 Representation of the magnetic field components for general calculations and for the $v \times E$ calculation	62
5.1 Picture and schematics of the apparatus for the beamtime at BOA in 2017.	67
5.2 Representation of the effect of the cross-contamination, depolarization, spin flipper efficiency on the spectrum.	69
5.3 TOF and PAD with spots definition at BOA 2017.	70
5.4 Ramsey pattern and phase scan measured at BOA in 2017.	72
5.5 The fit parameters vs neutron wavelength from the measurement of phase scan on resonance measured at BOA in 2017.	75
5.6 Result of the vertical magnetic field scan characterization at BOA in 2017.	77
5.7 Results of the vertical field gradient scans at BOA in 2017.	80

5.8 Results of the longitudinal field, and transversal field scans at BOA in 2017.	81
5.9 Representation of the characterization measurement of the wavelength selector at PF1b in 2018.	85
5.10 Result of the characterization measurement of the wavelength selector at PF1b in 2018.	86
5.11 Picture and schematics of the apparatus for the beamtime at PF1b in 2018.	87
5.12 The different possible configuration of the spin analyzer	89
5.13 Spots definition at ILL 2018 and efficiency of the spin analyzer.	90
5.14 Amplitude and Rabi frequency technique at PF1b in 2018	91
5.15 Ramsey pattern at PF1b in 2018	92
5.16 Neutron phase vs wavelength for several vales of the vertical magnetic fields at PF1b in 2018.	94
5.17 Result of the vertical magnetic field scan at PF1b in 2018.	96
5.18 Comparison of the fit parameters of a phase scan on resonance at PF1b in 2018.	97
5.19 Picture and schematics of the apparatus for the beamtime at BOA in 2018.	100
5.20 TOF and PAD with spots definition at BOA in 2018	102
5.21 Rabi and Ramsey pattern at PSI in 2018 with a continuous white beam.	103
5.22 Fit parameters of a phase scan on resonance at BOA in 2018.	105
5.23 Neutron phase vs. lambda for a phase scan on resonance at BOA in 2018.	107
5.24 Result of the vertical magnetic field scan at BOA in 2018.	108
5.25 Picture and schematic of the $v \times E$ measurement at BOA in 2018.	110
5.26 Result of the $v \times E$ measurement at BOA in 2018.	111
5.27 Reanalysis of the zero field $v \times E$ measurement to test a new measurement and analysis method.	113
5.28 Picture and schematic of the reflectometry measurement at Narziss in 2018.	115
5.29 Result of the $\theta - 2\theta$ measurements for the reflectometry test at Narziss in 2018.	116
5.30 Result of the rocking mode measurements for the reflectometry test at Narziss in 2018.	118
5.31 Reconstructed picture and schematics of the apparatus for the beamtime at PF1b in 2020.	120
5.32 Pictures and schematics of the apparatus at PF1b in 2020 with mumetal.	122

5.33 PAD, TOF and overall spin analyzer efficiency for the beamtime at PF1b in 2020.	125
5.34 Ramsey pattern measured at PF1b in 2020.	126
5.35 Fit parameters of a phase scan on resonance at PF1b in 2020.	128
5.36 Result of the vertical magnetic field scan and vertical magnetic field gradient scan at PF1b in 2020.	130
5.37 Result of the longitudinal and transversal field scans at PF1b in 2020.	132
5.38 Schematic of the fluxgates position at PF1b in 2020 with a proposition of improvement.	134
5.39 Fit parameters of the repeated phase scan and recorded temperature during a stability test at PF1b in 2020.	137
5.40 Asymmetry with a fixed phase measurement and recorded temperature during a stability test at PF1b in 2020.	138
7.1 Schematic of the neutron scattering on a nucleus in the center of mass system	150
8.1 Apparatus for the mercury incoherent scattering length and representation of a Ramsey cycle.	157
8.2 Representation of the hyperfine structure of ^{199}Hg and ^{201}Hg , [Fer13].	159
8.3 Sketch of the mercury co-magnetometer designed for the nEDM experiment.	160
8.4 PMT file signal	165
8.5 Precession file signal	167
8.6 Example of asymmetry A vs. $\Delta\nu$ plot	170
8.7 Representation of the data selection criteria	172
8.8 Result of the incoherent scattering length measurement	174
A.1 Representation of the neutron spin during a Ramsey technique with an inhomogeneous magnetic field.	188
A.2 Mathematica simulation of a phase scan with magnetic inhomogeneities.	190
B.1 Wiring of the vertical coil, also called Y coil in the above documentation.	192
C.1 Diagram of the wiring of the leakage current monitor made by J. Thorne at PF1b, ILL in 2020.	193
F.1 Fluxgate measurement during the magnetic characterization.	204
H.1 PMT signal from run 635 as a function of time zoomed at the beginning of the first cycle.	208

I.1	Data used to estimate the error on the PMT value.	210
I.2	Comparison between the meta file, precession file and PMT file for <i>as</i>	211
I.3	Value of $I(t_0)$ and $I(t_1)$ as function of time for the PMT file and the meta file.	212
I.4	Value of the polarization, absorption ratio, and density from the meta file.	212

List of tables

1.1	C, P and T transformation applied on different quantities.	9
2.1	Neutron characteristics	15
2.2	Neutron energy range	16
2.3	Absorption cross-section, coherent scattering length, and density at room temperature for different materials	18
2.4	Expected sensitivity for the different neutron EDM experiments . . .	27
3.1	Summary of the different beamtimes	32
3.2	Characteristics of BOA and PF1b.	34
3.3	Characteristics of different vacuum gauges.	42
3.4	Characteristics of the two type of fluxgates.	47
4.1	Description of the symbols and notation used for the analysis. . . .	64
5.1	Characteristics of the measurements at BOA in 2017.	66
5.2	Characteristics of the apertures at BOA in 2017.	68
5.3	Spot definition for the beamtime at BOA in 2017	68
5.4	Summarized result of the wavelength selector characterization at PF1b in 2018.	85
5.5	Characteristics of the apertures at PF1b in 2018.	87
5.6	Spot definition at PF1b in 2018	89
5.7	Value of the optimal amplitude of the spin flipper signal for a phase scan measurement at PF1b in 2018.	92
5.8	Characteristics of the apertures at BOA in 2018	99
5.9	Spot definition for the beamtime at BOA in 2018	101
5.10	Parameters of the modulated signal at BOA in 2018.	104
5.11	Parameters of fit for the fast oscillation in the neutron phase at BOA in 2018.	107
5.12	Summarized result of the reflectivity measurements with different samples.	117
5.13	Characteristics of the measurements at ILL in 2020.	119
5.14	Characteristics of the apertures at PF1b in 2020.	121

5.15	Position of the fluxgates at PF1b in 2020.	123
5.16	Spot definition for the beamtime at PF1b in 2020.	124
5.17	Parameters of the modulated signal at PF1b in 2020.	127
5.18	Parameters of the polynomial fit of the neutron phase vs. wavelength and applied transversal magnetic field for the transversal magnetic scan at PF1b in 2020.	133
5.19	Parameters of the polynomial fit of the neutron phase vs. wavelength and applied longitudinal magnetic field for the longitudinal magnetic scan at PF1b in 2020.	134
5.20	Configuration of the field for the different $v \times E$ measurements at PF1b in 2020.	135
5.21	Initial value of the fit parameter of the repeated phase scan stability test at PF1b in 2020.	136
8.1	Excited level number and energy level of the first transition of the mercury isotopes	160
8.2	Isotopic composition of the enriched mercury source and of the natural sample with the thermal neutron absorption cross section $\sigma_{n,a}$ for each of the isotope at room temperature, [Fer13].	161
8.3	Summary of the data taking configuration for the incoherent scattering length measurement	169

Part 1 :

Neutron beam experiment:

BeamEDM

Chapter 1

Cosmological motivation for the neutron electric dipole moment in the particle physics model

This chapter presents the motivation for the present part of this thesis. It starts with the cosmological background starting from the big bang and the baryoasymmetry as a reason of interest for CP violating processes like the neutron Electric Dipole Moment using the following textbook [Per09] and articles [B.14, CDS12]. It is followed by an summary of the CP violation in the standard model of particle physics with a special interest on the neutron EDM and the problem that this model poses with as reference the following articles [CK97, Jar85, PR05, CDVW79]. Finally, an overview of few particle physics models beyond the standard model are presented with their range of the neutron EDM, detailed in [CFRMS19, IRMZ14, SM75, HHX11].

1.1 Motivation

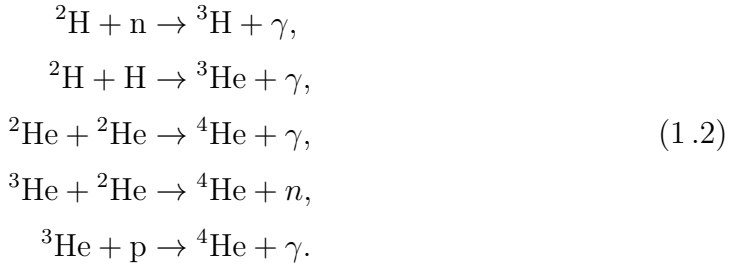
The universe exists, and it is composed of matter. We also know of the existence of antimatter; a particle of antimatter has the same mass as matter but opposite charge and baryonic and/or leptonic number as the equivalent particle of matter. When antimatter interacts with its corresponding matter particle, they annihilate themselves. Thus, there cannot be a universe made of both of them simultaneously in the current laws of physics described by standard model of particle physics. Then, why is there a predominance of matter over antimatter?

Theorists have created models to explain the origin and evolution of our universe. One of them is named the Big Bang theory [P⁺91]. Overall, it describes a succession of events starting from a singularity in space-time around 13.8 billion years ago. By definition of a singularity, space and time cannot be defined at that point. The

singularity evolved into an initial state of the universe, where space and time could be defined. At that moment, all the energy was contained in an infinitesimal volume. The density and temperature were extremely high, and prevented the formation of matter or antimatter. From this state, the universe expanded itself and, by that process, cooled down. During this cool down, baryons (3 quark elements like protons and neutrons) and anti-baryons were created in equal amount. Physics as we know it, i.e. the standard model of particle physics, tells us that matter and antimatter annihilate together one to one. If the matter and antimatter were created in equal amount, none should have survived. However, an asymmetry between matter and antimatter happened about 10^{-32} to 10^{-12} s, leaving an excess of matter. This period is called baryogenesis. The remaining matter started to combine themselves during the so-called nucleosynthesis, i.e. the production of light elements during the early universe. First the combination of neutrons and proton created deuterons:



During a second stage, helium is produced via for example the following reactions:



During a third stage, lithium and beryllium are produced :



The heavier elements could not be produced during the primordial nucleosynthesis but in the star fusion reaction for several reasons explained in chapter 6 of [Per09], including the lack of stable elements for the nuclear numbers 5, 6 or 8. Under gravity the light elements started to form clouds and eventually stars. In the stars, the temperature and density of elements permitted to combine unstable elements like 8Be into heavier elements:



This carbon is in an excited state decays predominantly back into beryllium and helium but there is a small probability (10^{-4}) that this carbon decays by:



From there, heavier elements are created in stars via several reactions, [Per09], leading eventually to the creation of planets. All this resulted from a small excess of matter at the beginning of the universe called baryon asymmetry.

The baryon asymmetry η is defined by $\eta = (N_B - N_{\bar{B}})/(N_B + N_{\bar{B}})$ where N_B and $N_{\bar{B}}$ are the number of respectively baryon and anti-baryon created during the baryogenesis. An estimate of this value with present-day quantities like the number of baryons remaining in our universe N_B^r , is the baryon to photon ratio:

$$\eta = \frac{N_B - N_{\bar{B}}}{N_B + N_{\bar{B}}} = \frac{N_B^r}{N_\gamma + N_B^r} \sim \frac{N_B^r}{N_\gamma}. \quad (1.6)$$

Indeed, the baryons and anti-baryons annihilated with each other into photons and only the excess of matter remained. This can be expressed by $N_B + N_{\bar{B}} = N_\gamma + N_B^r$ where N_γ is the number of photon produced by the annihilation. In addition, the number of remaining baryons is very small compared to the number of photons $N_B^r \ll N_\gamma$.

The photons produced during the annihilation process are still visible today as an anisotropic microwave background [PAA¹⁴, Per09]. The analysis of this microwave background spectrum is one of the predominant approaches to measure the quantity of the remaining baryons. A comprehensive explanation of the cosmological microwave background is available on the website of Prof. Wayne Hu with animated graphs, [CMB]. The microwave background is the radio-waves of the photons of last scattering, i.e. the photon that could finally propagate during the decoupling between matter and radiation. This corresponds to the period when protons and electrons combined themselves into hydrogen atoms. The atoms, unlike the baryon plasma, could not scatter the photons. Hence, the photons could start to travel isotropically without interacting anymore with matter. At that time, their energy was the equivalent temperature of the universe. As the universe was not homogeneous, the density differed at different points in space leading to different temperature of the photons. When the universe expanded, the photons cooled down to a temperature corresponding to a black body of 2.725 K [PW65], however it is not uniform and it is still visible today in the energy spectrum of the CMB as a function of the angular scale as show in Fig. 1.1.¹ The general shape is defined by the overall energy density

¹This is a really simplified version, as a reminder more extensive explanations are available in the textbook [Per09] and in the website [CMB].

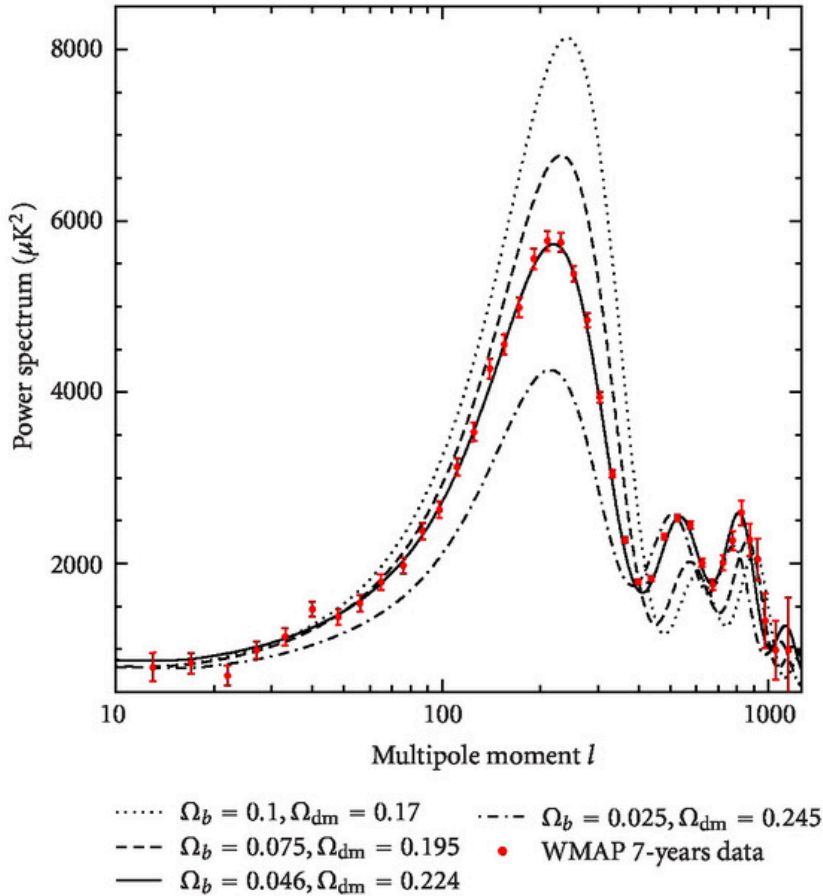


Fig. 1.1: The anisotropy power spectrum of the microwave background from [GD11]. It is the level of temperature fluctuations on patches of various angular scales defined by the multipole moment $l \approx 180 \text{ deg} / \Theta_{CMB}$ where Θ_{CMB} is the angular scale in degree. The different dash lines are the result of calculation with different value of the dark matter density Ω_{dm} and baryon density in the universe Ω_b with the total energy density kept to 1.

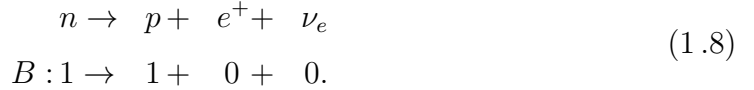
of the universe and the amplitude of the first peak by the density of baryon, used to compute the baryon to photon ratio. [B.14] gives the following result:

$$\eta_{CMB} = (6.176 \pm 0.148) \times 10^{-10}. \quad (1.7)$$

In 1967, Andrei Sakharov presented the three general conditions, represented in Fig. 1.2, for the baryon asymmetry to occur [Sak67].

First, the baryon number conservation must be violated. When conserved, the baryonic number remains the same at all time. This number is $B = \pm 1/3(N_Q - N_{\bar{Q}})$ where N_Q and $N_{\bar{Q}}$ are the number of quark and anti-quark that composed the elements. The sign is positive for matter and negative for antimatter. In the case of baryon $B = 1$, and $B = -1$ for anti-baryons. Over a system, the baryonic number is

the sum over each elements. As an example of conservation is the neutron decay:



On the left, $B = 1$ from the neutron, on the right $B = 1$ from the proton. The positron and electron neutron are leptons therefore with $B = 0$. The baryon number is conserved. The violation of the baryonic number is when this number is not

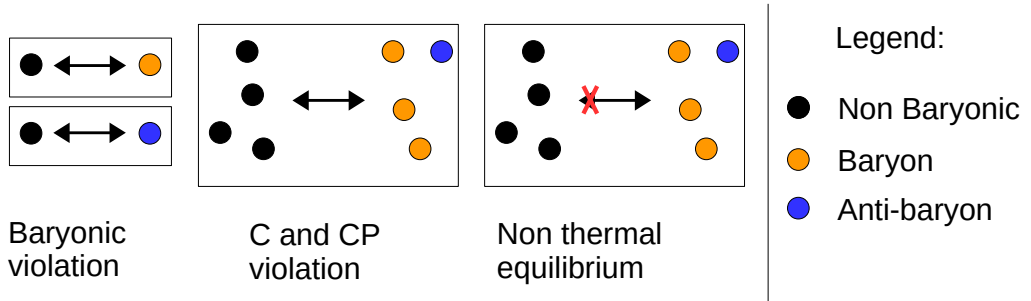
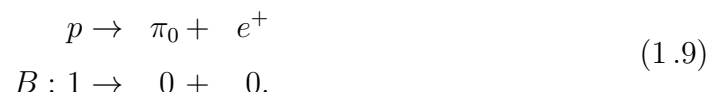


Fig. 1.2: Representation of the Sakharov conditions where the black dots are non baryonic matter, the orange dots the baryons and the blue dots the anti-baryons. The arrows represent the different reactions. The red cross represents a reduction or a prohibition of a reaction.

constant through an interaction. As hypothetical example of such interaction is the proton decay into a neutral pion Π_0 and a positron:



On the left side, $B = 1$ from the proton, on the right side $B = 0$ as the electron is a lepton and the baryon number of the neutral pion is zero.²

Second, the charge (C) and charge-parity conjugation (CP) must be violated. An analogy for the conservation of a symmetry in particle physics is the geometric symmetries: a transformation is applied to the properties of an object, the coordinates of an image in the case of geometric symmetries. If the image does not change with a transformation, it is symmetric. [Fig. 1.3](#) shows an example of geometrical symmetry and asymmetry. In a similar way, in particle physics, a symmetry is said "conserved" when the laws of physics do not change when the transformation associated to this symmetry is applied. A symmetry is "violated" when the laws of physics are not conserved under the associated transformation. We consider three transformations.

²The neutral pion is composed by $\pi_0 = d\bar{d}$ or $\pi_0 = u\bar{u}$.

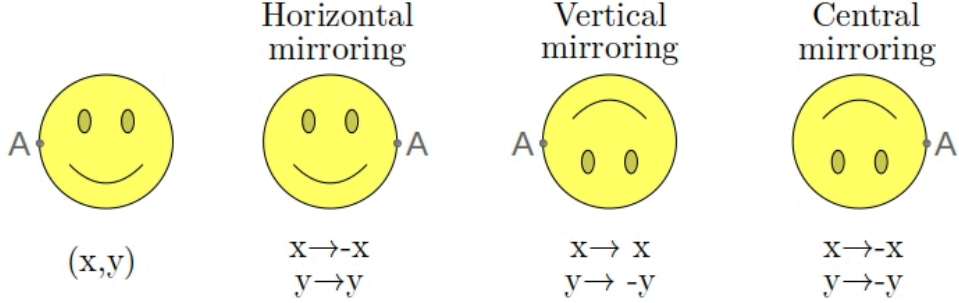


Fig. 1 .3: Representation of an image going through different geometric transformations. The horizontal symmetry is maintained, whereas the vertical and central symmetries are broken. Below each image, the transformation applied on the coordinates is written.

1. The charge conjugation (C) inverts all charges of the particles, $q \rightarrow -q$.
2. The parity transformation (P) inverts the sign of all three spatial coordinates \mathbf{x} . That corresponds to the central mirroring stated above but in a 3D situation $\mathbf{x} \rightarrow -\mathbf{x}$.
3. The time-reversal (T) inverts a process in time, $t \rightarrow -t$.

These transformations can also be combined to test for CP-symmetry, for example. The violation of CP and C in the early universe's mechanism insures that the processes that create matter and anti-matter are not similar, e.g., the reactions on matter prevails from the one on antimatter. Historically, the first measurement of a CP-violation was observed in 1964 [CCFT64], before the publication of the Sakharov conditions.

Finally, a thermal non-equilibrium during an early stage of our universe is required. In thermal equilibrium, a reaction and its counter-reaction happen at the same rate leading to the cancellation of their effect. In order to preserve the existing or created matter, the annihilation rate of matter should be suppressed or slower than the production one.

1 .2 CP-violation from the EDM

The EDM of a neutron, d_n , characterizes the interaction between its spin and the electric field \mathbf{E} . This interaction, in the non-relativist case, can be written as the Hamiltonian \mathcal{H} :

$$\mathcal{H} = -\mu_n \boldsymbol{\sigma} \cdot \mathbf{B} - d_n \boldsymbol{\sigma} \cdot \mathbf{E}, \quad (1.10)$$

where μ_n is the neutron magnetic dipole moment, σ the Pauli spinor, and \mathbf{B} the magnetic field. Their transformation under C, P, and T is summarized in [Table 1.1](#). Under a CP-transformation, [Eq. \(1.10\)](#) becomes

Quantity	Symbol	Charge (C)	Parity (P)	Time (T)
Position	\mathbf{x}	$+\mathbf{x}$	$-\mathbf{x}$	$+\mathbf{x}$
Charge	q	$-q$	$+q$	$+q$
Time	t	$+t$	$+t$	$-t$
"Spin"	σ	$+\sigma$	$+\sigma$	$-\sigma$
Magnetic dipole moment	μ_n	$-\mu_n$	$+\mu_n$	$+\mu_n$
Electric dipole moment	d_n	$-d_n$	$+d_n$	$+d_n$
Electric field	\mathbf{E}	$-\mathbf{E}$	$-\mathbf{E}$	$+\mathbf{E}$
Magnetic Field	\mathbf{B}	$-\mathbf{B}$	$+\mathbf{B}$	$-\mathbf{B}$

Table 1.1: Effects of the charge conjugation, parity transformation and time reversal on different quantities.

$$\begin{aligned} \hat{C} \hat{P} \hat{\mathcal{H}} &= -(-\mu_n) \sigma \cdot (-\mathbf{B}) - (-d_n) \sigma \cdot \mathbf{E} \\ &= -\mu_n \sigma \cdot \mathbf{B} + d_n \sigma \cdot \mathbf{E} \neq \mathcal{H}, \end{aligned} \quad (1.11)$$

corresponding to a violation of CP required for the Sakharov conditions. When applying an additional T transformation on [Eq. \(1.11\)](#), the Hamiltonian becomes

$$\begin{aligned} \hat{C} \hat{P} \hat{T} \hat{\mathcal{H}} &= -\mu_n (-\sigma) \cdot (-\mathbf{B}) + d_n (-\sigma) \cdot \mathbf{E} \\ &= -\mu_n \sigma \cdot \mathbf{B} - d_n \sigma \cdot \mathbf{E} = \mathcal{H} \end{aligned} \quad (1.12)$$

corresponding to a conservation of the initial Hamiltonian under CPT.

1.3 Standard Model and Baryogenesis

In the weak sector of the standard model of particle physics, a CP violation can be found in the Cabibbo–Kobayashi–Maskawa (CKM)[\[KM73\]](#) and Pontecorvo–Maki–Nakagawa–Sakata [\[MNS62\]](#) matrices. These matrices represent respectively the quark and the lepton flavor-changing through the weak interaction. They describe the probability of a decay or transformation of a quark or a lepton i into a quark or a lepton j respectively, denoted by $|V_{ij}|$ for the CKM matrix:

$$\begin{bmatrix} d' \\ s' \\ b' \end{bmatrix} = \begin{bmatrix} V_{ud} & V_{us} & V_{ub} \\ V_{cd} & V_{cs} & V_{cb} \\ V_{td} & V_{ts} & V_{tb} \end{bmatrix} \begin{bmatrix} d \\ s \\ b \end{bmatrix}. \quad (1.13)$$

The left side is the weak interaction doublet partner of the down type quarks (also called flavor eigenstates) and the right side is the mixing matrix with the mass eigenstates of the down type quarks. The CKM matrix can be expressed through a "standard parametrization" [CK84]:

$$\begin{bmatrix} c_{12}c_{13} & s_{12}c_{13} & s_{13}e^{-i\delta_W} \\ -s_{12}c_{23} - c_{12}s_{23}s_{13}e^{i\delta_W} & c_{12}c_{23} - s_{12}s_{23}s_{13}e^{i\delta_W} & s_{23}c_{23} \\ s_{12}s_{23} - c_{12}c_{23}s_{13}e^{i\delta_W} & -c_{12}s_{23} - s_{12}c_{23}s_{13}e^{i\delta_W} & c_{23}c_{13} \end{bmatrix} \quad (1.14)$$

which uses the Euler angles θ_{ij} for $s_{ij} = \sin(\theta_{ij})$ and $c_{ij} = \cos(\theta_{ij})$ and the CP-violating phase δ_W . The Euler angles directly represent the coupling between the quarks; if the angle is zero, the coupling vanishes. The Jarlskog determinant [Jar85] was constructed to give an invariant, i.e. parametrization independent, measure of the size of the CP-violation of the CKM matrix:

$$J = 2M \text{Im}(V_{ud}V_{td}^*V_{tb}V_{ub}^*) = 2c_{12}s_{12}c_{13}^2s_{13}s_{23}c_{23} \sin(\delta) \times M, \quad (1.15)$$

where,

$$M = \frac{(m_u - m_c)(m_u - m_t)(m_c - m_t)(m_d - m_s)(m_d - m_b)(m_s - m_b)}{m_u^3 m_d^3}. \quad (1.16)$$

J is zero for $\delta_W = \{0; \pi\}$, $\theta_{ij} = \{0; \pi/2\}$ and for a quark mass invariance e.g. $m_t = m_c$. This CP-violating factor J is included in several processes involving the quarks eigenstates. One of them is the quark EDM:

$$d_d \simeq e \frac{m_d m_c^2 \alpha_s G_F^2 J}{108\pi^5} f \left(\ln \frac{m_b^2}{m_c^2}, \ln \frac{m_W^2}{m_b^2} \right) \simeq -0.7 \times 10^{-34} e \text{ cm}, \quad (1.17)$$

$$d_u \simeq e \frac{m_u m_s^2 \alpha_s G_F^2 J}{216\pi^5} f \left(\ln \frac{m_b^2}{m_s^2}, \ln \frac{m_c^2}{m_s^2}, \ln \frac{m_b^2}{m_c^2}, \ln \frac{m_W^2}{m_b^2} \right) \simeq -0.15 \times 10^{-34} e \text{ cm}, \quad (1.18)$$

where d_d is the down quark EDM, d_u is the up quark EDM, e is the electron charge, m_W the W boson mass, m_d the down quark mass, m_u the up quark mass, m_c the mass of the charm quark, m_s the mass of the strange quark, m_b the mass of the beauty quark, α_s the strong coupling constant, and f is a polynomial function [CK97]. The quark EDMs contribute to the neutron one but not as the direct sum. The main contribution is the "strong penguin" diagram, represented in Fig. 1.4. It is as a function of the mass of the quarks, the mass of the W boson, and the strong coupling constant [KP95, PR05]. An extensive calculation of diagrams based on heavy baryon chiral perturbation theory can be found in [Sen15]. It gives the overall result:

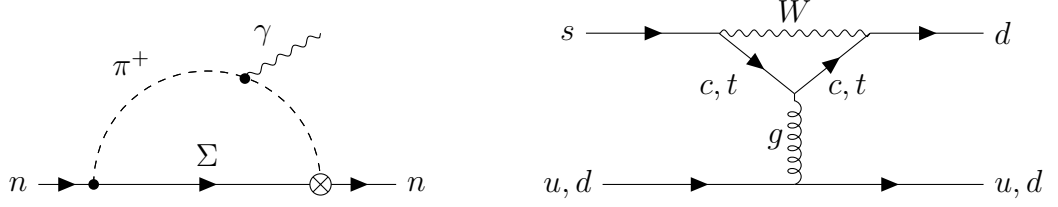


Fig. 1.4: Example of Feynman diagram for the neutron EDM from the weak sector, raising from the strong penguin diagram marked by \otimes on the left diagram and detailed on the right. The other vertexes are CP-conserving.

$$|d_n| = (1 - 6) \times 10^{-32} e \text{ cm.} \quad (1.19)$$

The strong sector of the standard model of particle physics has also a source of CP-violation in the vacuum QCD Lagrangian

$$L_\theta = \frac{\alpha_s}{16\pi} \theta_{QCD} \text{tr}(G^{\mu\nu}, \tilde{G}_{\mu\nu}), \quad (1.20)$$

where $G^{\mu\nu}$ and $\tilde{G}_{\mu\nu}$ are the gluon field and its dual,³ and θ_{QCD} is the CP-violating term, usually called the QCD/vacuum phase or mixing angle [CFRMS19]. This CP-violating constant is directly incorporated to the pion-nucleon coupling constant,

$$\bar{g}_{\pi NN} \approx -\theta_{QCD} (m_\Xi - m_N) \frac{m_u m_d}{F_\pi (m_u + m_d) (2m_s - m_u - m_d)} \approx 0.0038 |\theta|, \quad (1.21)$$

where F_π is the pseudo-vector coupling constant of Ξ -hyperon and the baryon N , m_Ξ and m_N are their respective mass [Mat19][CDVW79]. This coupling contributes to the neutron EDM from the strong sector,

$$d_{n,\theta} \approx e \frac{g_{\pi NN}}{4\pi^2 m_N} \bar{g}_{\pi NN} \ln \left(\frac{m_N}{m_\pi} \right) \approx -(0.9 - 1.2) \times 10^{-16} \theta_{QCD} e \text{ cm}, \quad (1.22)$$

and appears in the CP-violating vertex of the Feynman diagrams [PR05], e.g. Fig. 1.5.

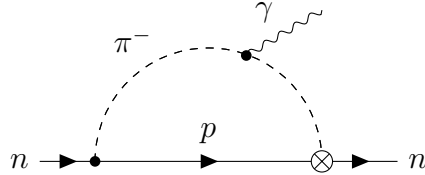


Fig. 1.5: Example of Feynman diagram for the neutron EDM from the strong sector, arising from the $\bar{g}_{\pi NN}$ coupling constant.

³A dual is defined by $\tilde{G}_{\mu\nu} = \epsilon_{\mu\nu\alpha\beta} G^{\mu\nu}$ from Gauge theory.

From the standard model theory, θ is unconstrained and could largely contribute to the CP-violation of the universe, however, it is experimentally restricted to $|\theta| < 10^{-10}$ by the upper limit of the neutron EDM, $|d_n| < 1.8 \times 10^{-26} \text{ e cm}$ (90% C.L.) [AAA²⁰]. This very small value for θ leaves discussion about its naturalness: it is the so-called "strong CP problem".

The CP-violation from the weak and strong sectors together do not contribute enough to the CP-violation requirement for a hot baryogenesis. It is interesting to note that a similar vacuum angle could appear in the weak sector [FPH14][LPT15], thus, contribute to the overall CP-violation from the standard model. Though, even if the calculations are not currently done, the authors of [LPT15] estimated from the limit of the QCD term that the weak vacuum angle would be insufficient for the standard model to explain the whole CP-violation in the case of a hot electroweak baryogenesis.

In conclusion, the SM does not seem to be suitable to explain a hot electroweak baryogenesis, therefore, scientists are looking for extensions to the standard model.

1 .4 Beyond standard model

In this section, a non-exhaustive, short summary of some of the current extensions of the standard model are presented. All these models have a defined range for the EDMs, making EDM measurements excellent probes.

Two-Higgs-doublet model

An extension of the standard model is to consider two Higgs-doublet instead of a single one. If realized in nature, this model would solve the CP-violation requirement of the baryon asymmetry of the universe by adding CP-violating processes [SZ13]. Under specific conditions, it may even explain the formation of dark matter [CZ13].

The model is based on the hypothesis that a CP-violating term exists in the Higgs potential, allowing mixing between the two Higgs. This mixing angle would affect the EDM prediction [IRMZ14]. The current value for the EDMs' upper limit constrains the parameter space for the different types of 2HDM, but they do not exclude it completely [IRMZ14].

This process is a base for supersymmetry models (SUSY).

SUSY

The supersymmetry models are numerous, and it would be dangerous to try to give an exhaustive list of the possible scenari for the EDM. We here try to give an understanding of the global idea of SUSY models. An extended summary is available in [CFRMS19].

In SUSY each particle has its own super-partner. They are called sfermions for the fermions, bosinos for the bosons, and gauginos for gauge bosons. The spin of each super-partner is reduced by 1/2 from the initial particle (fermion S=1/2, sfermion S=0, boson S=1, bosino S=1/2 ...). The supersymmetry is said to be "conserved" if a particle and its super-partner share the same mass and quantum numbers (except for the spin). However, breaking this symmetry would allow the masses to differ, therefore, increases the space parameters for possible CP-violations. The EDMs' limits are excellent probes for these models as they are for the 2HDM ones.

Left-right symmetry

The left-right symmetry models are based on a separate left and right SU(2) space and a symmetry $SU(2)_L \times SU(2)_R \times U(1)_{B-L}$ [SM75]. If the $SU(2)_R$ symmetry is broken above the electroweak scale, ≈ 100 GeV, it means that masses of the left- and right-handed bosons have truly different masses $m_{W_L} \ll m_{W_R}$. Thus, a mixing of the two bosons is possible and a CKM-like matrix is introduced for the W_R .

In that case, the quark EDM is a function of the left/right-handed CP-violating CKM phase and function of the mixing angle of the Ws as well as their mass. In addition, the long-range contribution (equivalent of the penguin diagram in the standard model) is also enhanced by the mixing of the current couplings.

With the discovery of the Higgs mass, some models have evolved, for example, the recently published [AFS20] and [GMS20].

An extra family

If another family of quarks exists, then the CKM matrix would change, and the Jarlskog determinant would change accordingly. Setting their mass between 300 GeV and 600 GeV would lead to normalized Jarlskog determinant of the order of baryon asymmetry and could fulfill the CP-violation condition of a hot electroweak baryogenesis. In that case, the neutron EDM would be of the order of $d_n \sim 10^{-31} e \text{ cm}$ [HHX11]. The current experimental sensitivity does not allow for probing this model.

Chapter 2

Neutron physics

In this chapter, the properties of the neutron are summarized as well as the usual definition of their energy range. In addition, the different interactions that affects a neutron are presented. It is followed by the neutron EDM measurement principle, and a historical summary of neutron EDM experiments.

2.1 Neutron properties

The neutron is a neutral particle of mass m_n . It is a fermion, therefore, has a spin $s=1/2$ and a gyromagnetic ratio γ_n , corresponding to a magnetic moment $\mu_n = \mu_n \sigma = \gamma_n \frac{\hbar}{2} \sigma$. It is also an unstable particle when free. Its mass, lifetime, charge, spin and gyromagnetic ratio are summarized in [Table 2.1](#).

mass (MeV/c ²)	lifetime (s)	charge	spin	γ_n (Hz/μT)
939.6	879.4 ± 0.6	0	1/2	$-2\pi \times 29.1646943$

Table 2.1: *Global neutron characteristics: mass [[Mea08](#)], lifetime [[GZB⁺20](#)], charge [[BGKM88](#)], spin, and gyromagnetic ratio [[Mea08](#)].*

The neutron can be described either as a classical particle or as a wave. Its kinetic energy E_K can be express by the de Broglie wavelength λ :

$$E_K = \frac{m_n v^2}{2} = \frac{h^2}{2m_n \lambda^2}, \quad (2.1)$$

where v is the neutron velocity and h is the Plank constant. Neutrons are usually distinguished by their kinetic energy and their name is related to the equivalent temperature with the Ultra-Cold Neutron (UCN), Very-Cold Neutron (VCN), Cold Neutron (CN), thermal neutron and the epithermal neutrons. The last two ranges have generic names, intermediate neutrons and fast neutrons, see [Table 2.2](#).

Name	E_K	Velocity [m/s]	Wavelength [\AA]
UCN	$\leq 300 \text{ neV}$	≤ 8	≥ 500
VCN	$300 \text{ neV} - 0.12 \text{ meV}$	$7.5 - 152$	$52.2 - 26.1$
CN	$0.12 \text{ meV} - 12 \text{ meV}$	$152 - 1515$	$26.1 - 2.6$
Thermal neutron	$12 \text{ meV} - 100 \text{ meV}$	$1515 - 4374$	$2.6 - 0.9$
Epithermal neutron	$100 \text{ meV} - 1 \text{ eV}$	$4374 - 13\,800$	$0.9 - 0.28$
Intermediate neutron	$1 \text{ eV} - 0.8 \text{ MeV}$		
Fast neutron	$> 0.8 \text{ MeV}$		

Table 2.2: Energy range of the neutron in term of energy, velocity and wavelength.

2.2 Forces and Interactions

Neutrons are subject to all interactions. These interactions and their effect on cold neutrons are presented here. A similar approach for UCN can be found in several textbooks [GRS91, Ste20].

The weak interaction is responsible for the beta decay of the neutron,

$$n \rightarrow p + e^- + \bar{\nu}_e + 781.5 \text{ keV}, \quad (2.2)$$

into a proton (p), an electron (e^-), and an electron anti-neutrino ($\bar{\nu}_e$) with an energy excess of 781.5 keV. The current value published by [GZB⁺20] for the neutron life time, $(876.4 \pm 0.6) \text{ s}$, is an average of the eight best measurements. A global review of the different results is available in [Ste20]. This does not affect cold neutron beam experiments as cold neutrons travel great distances in a short time, but it is a significant consideration for UCN experiments.

The effect of gravity on the neutron's trajectory can be calculated from Newton's second law: the acceleration is equal to the sum of the forces that are applied on an object. Here, the only force considered is gravity, leading to $-g = \dot{v}$ where g is the gravitational acceleration on Earth, v is the neutron velocity, and the dot denotes its time derivative. Using as initial conditions a horizontal velocity $v_y(t = 0) \neq 0$ and a vertical velocity $v_z(t = 0) = 0$, this leads to a conservation of the horizontal velocity $v_y(t) = v_y(0)$ and an increase of the vertical velocity with time $v_z(t) = -gt + 0$. This can be integrated to $h(t) = -\frac{1}{2}gt^2 + h(0)$, where $h(t)$ is the neutron height at a time t . Using $t = y(t)/v_y$ where $y(t)$ is the horizontal position and $y(0) = 0$, one arrives to

$$h(y) - h(0) = -\frac{1}{2}g(y/v_y)^2. \quad (2.3)$$

Neutrons with an horizontal velocity of 1 km/s lose $\sim 5 \mu\text{m}$ of height during the first meter traveled in the horizontal direction, under initial conditions represented in Fig. 2.1A. The calculation has been made for three velocities up to 25 m and is shown in Fig. 2.1B.

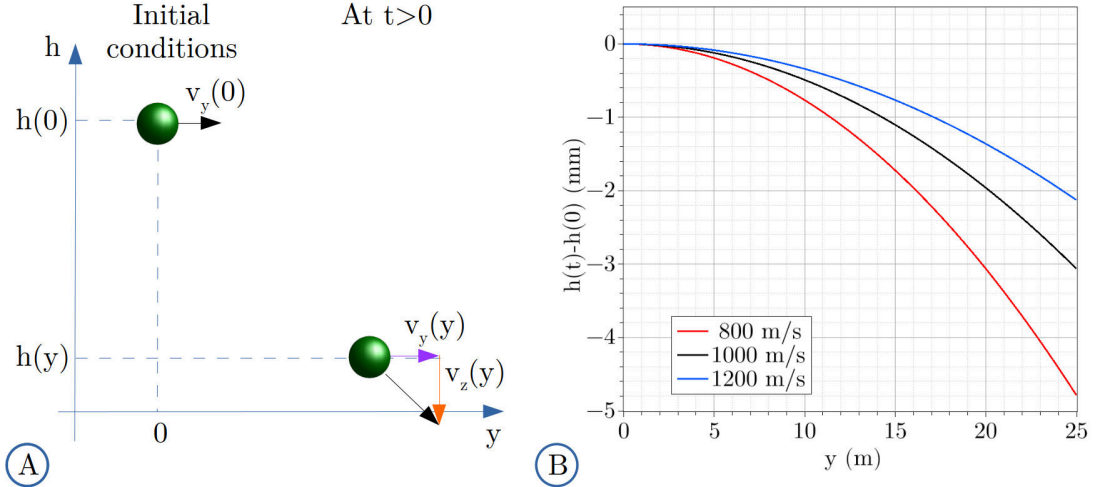


Fig. 2.1: A) Representation of a neutron height vs. horizontal displacement with a horizontal velocity in initial conditions. B) Height difference between the initial state and a later state vs. horizontal displacement for three velocities.

When using a divergent beam, the initial conditions change as $v_z(0) = \pm \tan(\alpha_D)v_y$ where α_D is the initial divergence angle, and Eq. (2.3) becomes

$$h(x) - h(0) = -\frac{1}{2}g(y/v_y)^2 \pm \tan(\alpha_D)y. \quad (2.4)$$

The divergence is usually the dominating effect.

The strong interaction is responsible for the absorption and the scattering of the neutron. In the case of this section, the Fermi potential V_F formalism [FM47] is used to characterize the neutron scattering property of a material. One can define the neutron critical incident angle, θ_c , i.e. the angle between the neutron trajectory and the material surface, until which a neutron of energy E would undergo a total reflection,

$$\sin(\theta_c) = \left(\frac{V_F}{E}\right)^{1/2}, \quad (2.5)$$

where the Fermi potential of the material, V_F , is defined by

$$V_F = \frac{\hbar^2}{2\pi m_n} \rho b, \quad (2.6)$$

with ρ the nucleon number density and b the scattering length. Table 2.3 provides the scattering length, typical density at room temperature, and absorption cross-section

of a few elements that can be used for neutron guides, spin analyzer, or chopper systems.

Element	σ_a (b)	b (fm)	ρ (g/cm ³)
Fe	2.56	9.45	7.9
Si	0.171	4.1491	2.3
Ni	4.49	10.3	8.9
Co	37.18	2.49	8.9
Ti	6.09	-3.438	4.5
Al	0.231	3.449	2.7
¹⁰ B	3835	-4.7	2.3
Ga	49700		7.9

Table 2.3: *Absorption cross-section, coherent scattering length, and density at room temperature for different materials. The absorption cross-sections and scattering lengths are taken from [Sea92].*

The effective critical angle until which the neutrons of a given wavelength are reflected can be increased by using the so called "Bragg diffraction" [BB13]. A full description of this effect can be found in the book [Siv11]. To understand the principle one has to consider the neutron as a wave when interacting with a multilayer structure. When a neutron wave is reflected by two planes of the material as represented in Fig. 2.2A, there is a path difference between the two waves (represented by a green line) which is dependent on the spacing of the two layers d and the incident angle θ . These two waves interfere constructively when their wavelength is a multiple of the path difference:

$$k\lambda = 2d \sin(\theta), \quad (2.7)$$

where k is the diffraction order, i.e. an integer. This means that the neutron is reflected if Eq. (2.7) is fulfilled. Assuming $k = 1$, if d is fixed, a neutron with a given wavelength would be reflected by that process for a unique incident angle. On the contrary, if the multiple layers of the material are spaced differently, e.g. $d_1 > d_2 > d_3$, a neutron could be reflected for different incident angles as presented in Fig. 2.2B. By choosing the correct range of spacing for the layers, the peaks can overlap and extend continuously the reflection to higher angles. The layer are usually made of a material with a high Fermi potential, e.g. Ni, spaced by layer of low Fermi potential component, e.g. Co. The performance of these so-called super-mirrors is usually express by their m -value, defined by:

$$m = \frac{\sin(\theta_c)}{\sin(\theta_{c,Ni})}, \quad (2.8)$$

where θ_c and $\theta_{c,Ni}$ are the critical angles of the mirror and a single layer of natural nickel, respectively, for the same neutron wavelength.

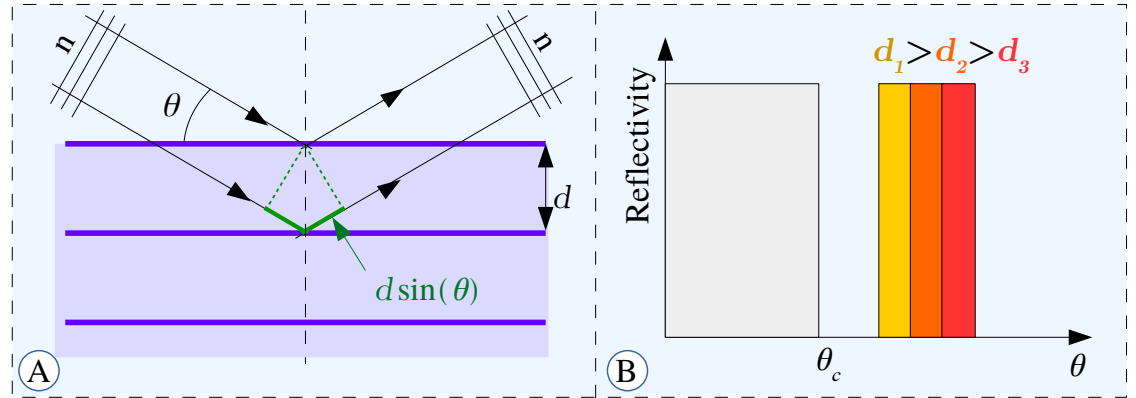


Fig. 2.2: A) Representation of the Bragg scattering of a neutron wave (continuous black lines) on a multilayer structure where the high Fermi potential layers are represented by purple lines. B) Diagram of the reflectivity of a material vs the angle at which the neutrons scatter on it, for a fixed energy of the neutrons. The light gray is the scattering coming from the Fermi potential of the material, the colored boxes are the peaks from the Bragg scattering for different gap thickness.

The electromagnetic interaction should also be considered even though the neutron is a neutral particle - measurements have been able to determine that $q_n = (-0.4 \pm 1.1) \times 10^{-21} e$ [BGKM88]. Indeed, the neutron is a fermion (spin 1/2), thus, it has a finite magnetic dipole moment, μ_n , of magnitude $\mu_n = -0.966 \times 10^{-26} \text{ A m}^2 = (-1.91304184 \pm 8.8 \times 10^{-7})\mu_N$, which is anti-parallel to the spin and where μ_N is the nuclear magneton [GRM⁺79].

The potential energy of a neutron in a static magnetic field \mathbf{B} is given by

$$U_m = -\mu_n \cdot \mathbf{B} = \pm 60.3 \text{ neV} \times \frac{B}{1 \text{ T}}, \quad (2.9)$$

where the positive and negative signs are for a parallel and anti-parallel configurations, respectively, between the spin and the magnetic field. This can be used to separate one spin state from the other, for example combined with an appropriate Fermi potential material.

The force experienced by neutrons in a generic magnetic field is relative to the gradient,

$$F = -\nabla(\mu_n \cdot \mathbf{B}) = \pm |\mu_n| \nabla B. \quad (2.10)$$

Neutrons with a spin parallel or anti-parallel to the local magnetic field are repelled or attracted by high fields; they are called low or high field seekers respectively. Usually, this is only used for UCN.

The torque, \mathbf{M} , of a magnetic field acting on the neutron spin follows

$$\mathbf{M} = \frac{1}{\gamma_n} \frac{d\mu_n}{dt} = \mu_n \times \mathbf{B}. \quad (2.11)$$

Solving this equation for a static magnetic field and an initial superposition state of the spin, one can classically represent the neutron spin precessing around the magnetic field at a frequency,

$$\omega_n = -\gamma_n B, \quad (2.12)$$

called Larmor frequency. Solving Eq. (2.11) for a slowly varying field ($B^{-1}d(B)/dt \ll \omega_n$), one finds that the neutron spin "follows" the magnetic field adiabatically.

To understand the effect of a circularly oscillatory field, it is easier to place the observer in the rotating frame of the system defined by $\boldsymbol{\Omega} = -\gamma_n \mathbf{B}$. For a static field, Eq. (2.11) becomes

$$\frac{d\mu_n}{dt} = \gamma_n \mu_n \times \left(\mathbf{B} + \frac{\boldsymbol{\Omega}}{\gamma_n} \right) \quad (2.13)$$

in a rotating frame and $d\mu_n/dt = 0$. The evolution of a neutron spin is represented in Fig. 2.3 for a static field in the laboratory frame and in the rotating frame. One can apply a circularly oscillating field of frequency ω_n . This field would be static in the rotating frame and the neutron spin would precess around this seemingly static field in the rotating frame as represented in Fig. 2.3.

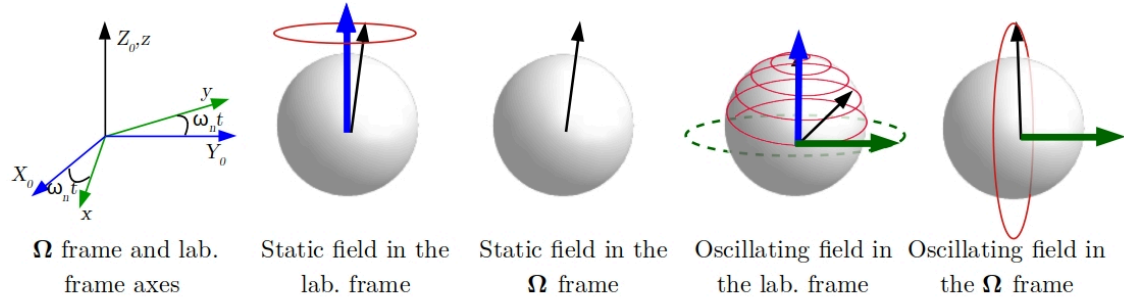


Fig. 2.3: Representation of the neutron by a Bloch sphere with the static magnetic field in blue, the oscillating magnetic field in green in the rotational frame and in the laboratory frame whose axes are represented in green and in blue respectively, on the very left. The neutron spin is represented by a black arrow and its path is represented by a red line.

When considering an electric field \mathbf{E} , all the equations can be modified by replacing the magnetic field and magnetic dipole moment by the electric field and electric dipole moment. In an electric and magnetic field the potential energy becomes

$$U = -\mu_n \cdot \mathbf{B} - \mathbf{d}_n \cdot \mathbf{E}, \quad (2.14)$$

the force becomes

$$F = -\nabla(\boldsymbol{\mu}_n \cdot \mathbf{B}) - \nabla(\mathbf{d}_n \cdot \mathbf{E}), \quad (2.15)$$

and the Larmor frequency becomes

$$\omega_n = -\gamma_n B - \frac{2d_n}{\hbar} E, \quad (2.16)$$

with $\mathbf{d}_n = d_n \boldsymbol{\sigma}$.

In addition, it is known from electromagnetism that a particle with a velocity v in an electric field E sees a pseudo-magnetic field given by:

$$\mathbf{B}_{v \times \mathbf{E}} = -\frac{\mathbf{v} \times \mathbf{E}}{c^2}, \quad (2.17)$$

This pseudo magnetic field adds itself to the "external" magnetic field, changing its magnitude and potentially its direction. This is called the $v \times E$ effect and it was one of the limitations of the neutron EDM experiments as described in [Section 2.5](#).

2.3 Measurement principle

As a non-zero neutron EDM corresponds to an additional term in the Larmor frequency [Eq. \(2.16\)](#), one can measure this quantity as a function of the electric field to search for an EDM. There are two main techniques to find the Larmor frequency of neutrons.

The Rabi technique was developed in 1938 to measure the magnetic moment of nuclei [\[RZMK38\]](#). With the exclusion of the polarization of the beam and the spin state detection, the measurement consists of performing one spin flip in a static magnetic field, \mathbf{B}_0 , by applying a circularly oscillating magnetic field, \mathbf{B}_1 , orthogonal to the static field. The frequency, ω_{RF} , and amplitude of this rotational field are scanned to find the optimal parameter for which a π spin flip is obtained.

It can be intuitively understood by the following classical description. If the rotational frequency of the magnetic field does not match the precession frequency of the neutron, this rotational field would not appear static in the rest frame of the neutron spin defined by [Eq. \(2.13\)](#). On the contrary, when they match, the neutron spin would see the seemingly static orthogonal field as represented in [Fig. 2.3](#).

In a more mathematical description [\[RZMK38\]](#), the probability that the neutron spin is flipped to the opposite spin state follows

$$P_{Rabi} = \frac{\omega_1^2}{\Delta^2 + \omega_1^2} \sin^2 \left(\frac{\tau \sqrt{\Delta^2 + \omega_1^2}}{2} \right), \quad (2.18)$$

where $\Delta = \omega_{RF} - \omega_n$ defines the off-resonance value between the rotational frequency ω_{RF} of oscillating magnetic field and the Larmor frequency, the amplitude of the oscillating magnetic field B_1 is expressed as a frequency $\omega_1 = -\gamma_n B_1$, and τ is the interaction time between the neutron spin and \mathbf{B}_1 . If $\Delta \neq 0$, a perfect π flip is impossible, the maximal probability is

$$P_{max} = \frac{\omega_1^2}{\Delta^2 + \omega_1^2} \quad (2.19)$$

for the following condition

$$\tau^2(\Delta^2 + \omega_1^2) \equiv \pi^2. \quad (2.20)$$

The larger ω_1 is compared to Δ the higher is the local maximum in the spin flip probability P_{Rabi} . With the assumption $\Delta \ll \omega_1$, one can expand Eq. (2.18)

$$P_{Rabi} = P_{max} \sin^2 \left(\frac{\tau \omega_1}{2} + \frac{\tau \Delta^2}{4 \omega_1} + O \left(\frac{\Delta^4}{\omega_1^3} \right) \right). \quad (2.21)$$

And for $\Delta = 0$, i.e. $\omega_{RF} = \omega_n$, we retrieve that the flipping process is optimal

$$P_{Rabi} = P_{max} \sin^2 \left(\frac{\tau \omega_1}{2} \right), \quad (2.22)$$

with $P_{max} = 1$. In that configuration, the requirement of a " π " spin flip, $P_{Rabi} = 1$, corresponds to

$$\tau \omega_1 \equiv \pi. \quad (2.23)$$

In practice, for neutron EDM experiments, one computes from the measured (or set) value of the static magnetic field, the equivalent neutron Larmor frequency $\omega_n = -\gamma_n B$, in order to have an initial value of the frequency, ω_{RF} , of the oscillating magnetic field, \mathbf{B}_1 . Then, the amplitude ω_1 is scanned to find the value with maximal spin flip probability at the approximated frequency, therefore, the maximal visibility of the signal. Finally, the frequency, ω_{RF} , is scanned to find the actual Larmor frequency. An example of a Rabi pattern is given in Fig. 2.4 for an amplitude scan and a frequency scan using Eq. (2.18). For the calculation of the frequency scans, two flipping pulse duration $\tau = 0.25$ ms and $\tau = 0.5$ ms to show the broadening of the linewidth for higher interaction time, Eq. (2.20). These duration were chosen to corresponds to the time that a neutron of 2.5 Å and 5 Å get flipped in the presented experiment in Chapter 3 . For the calculations of the amplitude scans, the flipping pulse duration was fixed to $\tau = 5$ ms. In the off resonance case, $\Delta = 100$ Hz, the local maximum increases with ω_1 as described in Eq. (2.19).

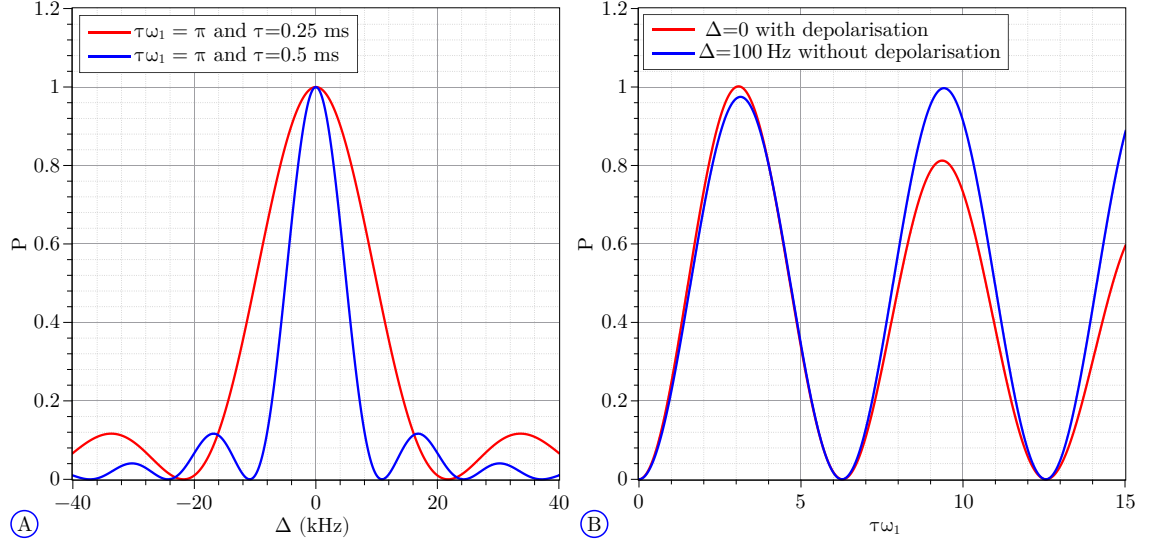


Fig. 2.4: A) Spin flip probability as a function of the off-resonance value Δ for the optimal amplitude-interaction time, $\tau\omega_1 = \pi$, with $\tau = 0.25$ ms in red and $\tau = 0.5$ ms in blue. B) Spin flip probability as a function of $\tau\omega_1$ for an off-resonance value, $\Delta = 100$ Hz, in blue and on resonance in red. For the off-resonance case, the calculation was done by fixing $\tau = 5$ ms and changing ω_1 . The red curve has an exponential depolarization as a function of $\tau\omega_1$ with decay constant of 30. These values for τ and the decay constant were chosen to show the modulation effect of $\omega_1/(\Delta + \omega_1)$ and on the amplitude Rabi pattern respectively.

The Ramsey technique of oscillatory fields was developed in 1950, in the molecular beam framework [Ram50]. With the exclusion of the polarization of the beam and the spin state detection, this technique can be separated into three stages represented in the neutron frame work in Fig. 2.5.

1. The first stage is a spin flip. A circularly oscillating magnetic field at frequency, ω_{RF} is applied with an amplitude, ω_1 , and a duration τ such that $\tau\omega_1 = \pi/2$ in order to perform a $\pi/2$ flip when on resonance i.e. $\omega_{RF} = -\gamma_n B$.
2. The second stage is a free precession. The neutron spin processes freely in a static magnetic field, i.e. without oscillating field.
3. The third and last stage is again a spin flip. A second oscillating magnetic field, with the same frequency ω_{RF} and phase coherent with the first one is applied with the same product of amplitude and interaction time, $\tau\omega_1 = \pi/2$. If the phase between the two oscillating fields is zero, $\theta_{RF} = 0$ and the system is on resonance $\omega_{RF} = -\gamma_n B$ a second $\pi/2$ flip is performed leading to a probability of 1 to be in the opposite spin state.

The total spin flipping probability is extended from [Pie09] to a general case where the magnetic field is not homogeneous over the system in Appendix A. In the special case where the field is homogeneous, the probability of a spin flip follows

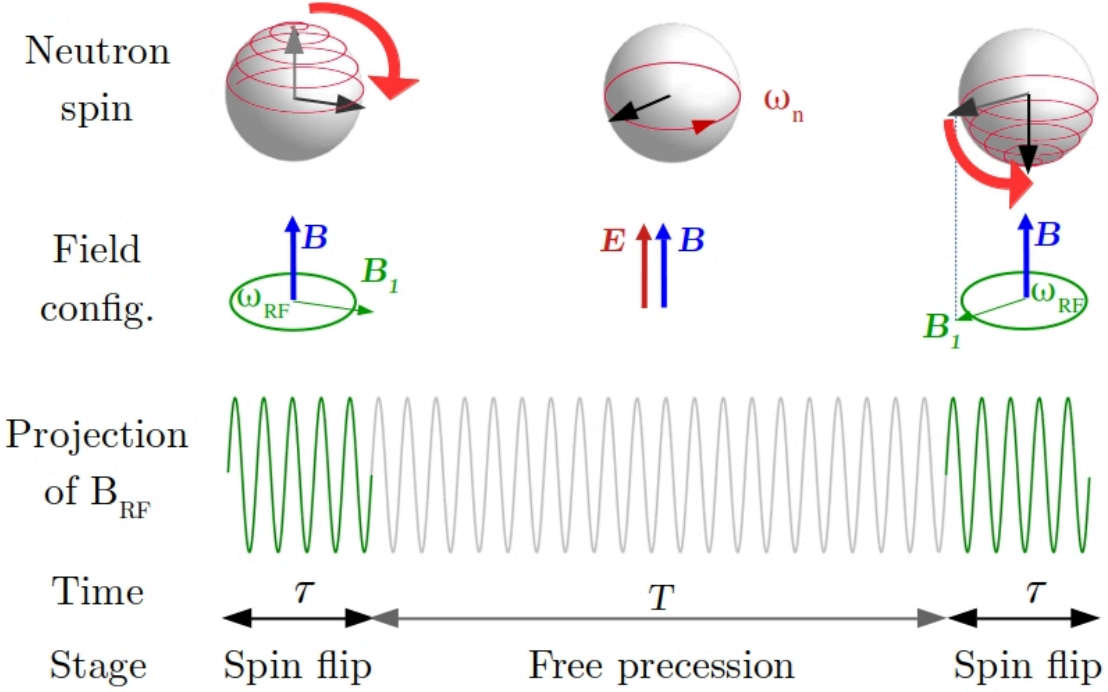


Fig. 2.5: Representation of the neutron spin as a function of the fields configuration for the different stages of a Ramsey technique on resonance. As additional information, the projection of the rotational fields vs. time is display to show the coherence between the two fields: the green lines represent rotational field during the spin flip, the gray line is the continuation of the first green one during the free precession time to show the phase coherence with the second green line.

$$P = \left| \begin{pmatrix} 0 \\ 1 \end{pmatrix} \cdot U_3 \cdot U_2 \cdot U_1 \cdot \begin{pmatrix} 1 \\ 0 \end{pmatrix} \right|^2, \quad (2.24)$$

where U_1 , U_2 , and U_3 are the propagation matrix for the stages 1, 2, and 3,

$$U_1(\tau) = \begin{pmatrix} \cos(\frac{\Omega\tau}{2}) + i\frac{\Delta}{\Omega}\sin(\frac{\Omega\tau}{2}) & -i\frac{\omega_1}{\Omega}\sin(\frac{\Omega\tau}{2}) \\ -i\frac{\omega_1}{\Omega}\sin(\frac{\Omega\tau}{2}) & \cos(\frac{\Omega\tau}{2}) - i\frac{\Delta}{\Omega}\sin(\frac{\Omega\tau}{2}) \end{pmatrix}, \quad (2.25)$$

$$U_2(T) = \begin{pmatrix} e^{\frac{i}{2}(T\Delta)} & 0 \\ 0 & e^{-\frac{i}{2}(T\Delta)} \end{pmatrix}, \quad (2.26)$$

$$U_3(\tau) = \begin{pmatrix} \cos(\frac{\Omega\tau}{2}) + i\frac{\Delta}{\Omega}\sin(\frac{\Omega\tau}{2}) & -i\frac{\omega_1}{\Omega}e^{-i\theta_{RF}}\sin(\frac{\Omega\tau}{2}) \\ -i\frac{\omega_1}{\Omega}e^{-i\theta_{RF}}\sin(\frac{\Omega\tau}{2}) & \cos(\frac{\Omega\tau}{2}) - i\frac{\Delta}{\Omega}\sin(\frac{\Omega\tau}{2}) \end{pmatrix}, \quad (2.27)$$

where $\Omega = \sqrt{\Delta^2 + \omega_1^2}$ with $\Delta = \omega_{RF} - \omega_n$, and T is the interaction time in the magnetic and electric fields. When expanded, Eq. (2.24) becomes

$$P = \frac{\omega_1^2}{\Omega^4} \left[\Delta(\cos(\tau\Omega) - 1) \sin\left(\frac{\Delta T + \theta_{RF}}{2}\right) + \Omega \cos\left(\frac{\Delta T + \theta_{RF}}{2}\right) \sin(\tau\Omega) \right]^2. \quad (2.28)$$

This corresponds to Eq.B.11 in [Pie09]. The probability P for $\tau = 0.5 \text{ ms}$, $T = 5.25 \text{ ms}$, $\omega_1 = \pi/(2\tau)$, and $\theta_{RF} = 0$ as a function of Δ is given in Fig. 2.6. This value corresponds to a neutron passing through the apparatus presented in Chapter 3 with a wavelength of 5 \AA . The shape of the envelop is defined in first order by τ and the number of oscillations by T .

If we consider now an electric field and a neutron EDM, the neutron frequency follows Eq. (2.16). The off-resonance value in the free precession region includes an additional term $\Delta^* = \omega_{RF} - (-\gamma_n B - \frac{2d_n}{\hbar} E)$ also leading to an additional term in Eq. (2.28):

$$P = \frac{\omega_1^2}{\Omega^4} \left[\Delta(\cos(\tau\Omega) - 1) \sin\left(\frac{T\Delta^* + \theta_{RF}}{2}\right) + \Omega \cos\left(\frac{T\Delta^* + \theta_{RF}}{2}\right) \sin(\tau\Omega) \right]^2, \quad (2.29)$$

derived in appendix A. In first approximation, the presence of a non-zero EDM would shift the pattern horizontally as represented in Fig. 2.6B. Taking the derivative according to Δ we know that one of the extrema is for $T\Delta^* = 0$ if $\theta_{RF} = 0$

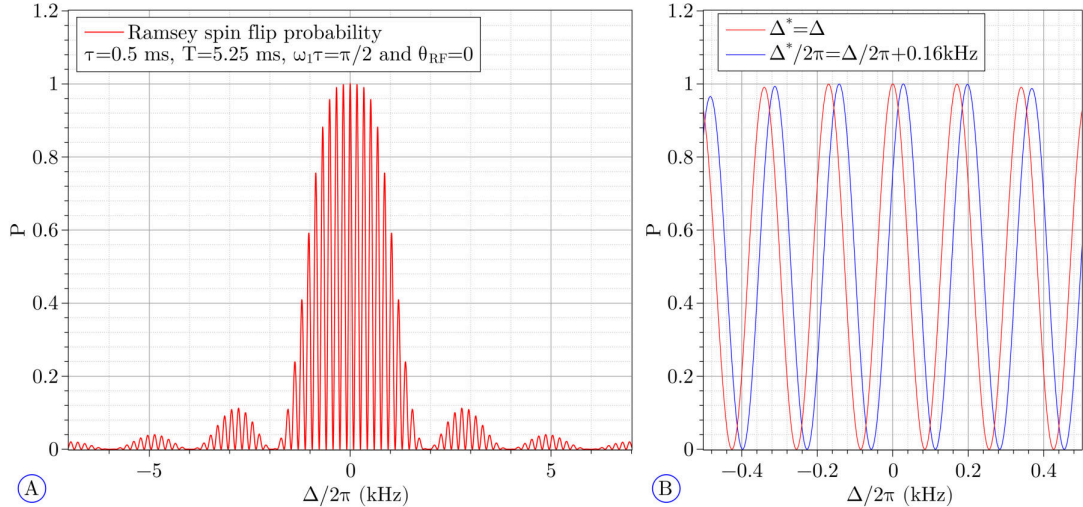


Fig. 2.6: A) Probability of a full spin flip from Eq. (2.28) as a function of $\Delta/2\pi$ for a Ramsey technique with $\tau = 0.5 \text{ ms}$, $T = 5.25 \text{ ms}$, $\omega_1\tau = \pi/2$, and $\theta_{RF} = 0$. B) Probability of a full spin flip from Eq. (2.29) as a function of $\Delta/2\pi$ with $\Delta^* = \Delta$ and $\Delta^*/2\pi = \Delta/2\pi + 0.16 \text{ kHz}$ for a Ramsey technique with $\tau = 0.5 \text{ ms}$, $T = 5.25 \text{ ms}$, $\omega_1\tau = \pi/2$, and $\theta_{RF} = 0$.

In practice, a Rabi technique is first performed to determine $\tau\omega_1 = \pi/2$ and a first estimate of the resonance frequency $\omega_{RF} = -\gamma_n B$. Then, the Ramsey technique

is performed by scanning ω_{RF} which changes accordingly the off-resonance value Δ .

A phase scan is a modified Ramsey technique that scans the phase between the two oscillating field, θ_{RF} , rather than the frequency. It has the advantage to always be in the case $\omega_{RF} = -\gamma_n B$, i.e. $\Delta = 0$ in [Eq. \(2.29\)](#). This simplifies greatly this equation into

$$P = \cos^2 \left(\frac{\theta_{RF} + \Delta^* T}{2} \right) \sin^2(\omega_1 \tau), \quad (2.30)$$

as a reminder $\Delta^* = \omega_{RF} - \omega_n$ is the off-resonance value for the free precession region only. It includes all the effects that can affect the neutron precession during the free precession period. It can be interpreted as the frequency shift between the neutron precession and the oscillating field during the free precession period. In the case of a phase scan, a full spin flip over the entire setup is maximized for $\theta_{RF} = -\Delta^* T$.

2 .4 Neutron EDM history

The search for the neutron EDM started in 1950 [[PR50](#)]. The first result was not the product of one measurement dedicated to the neutron [EDM](#) but the (re-)analysis of data from different scattering measurements to get an indication about the neutron [EDM](#). It was then followed by a great enthusiasm in the late 1960s after the discovery of the CP violation in the neutral kaon decays [[CCFT64](#)] and many experiments using cold neutron beam improved the neutron [EDM](#) limit. In the late 1970s, the development of UCN sources offered a new technology for neutron [EDM](#) experiments and from the early 1980s all beam experiments were replaced by UCN experiments. Indeed, UCN have an energy, $E < 300 \text{ neV}$, smaller than the Fermi potential of most materials. Due to this property, UCN can be stored in material containers which allows to perform measurements on a longer time scale, effectively improving the sensitivity $\sigma(d_n)$ of an [EDM](#) measurement using the Ramsey technique, [[SW16](#)], given by:

$$\sigma(d_n) \propto \frac{1}{\sqrt{N \alpha_V E T}}, \quad (2.31)$$

where N is the number of neutrons analyzed, T is the interaction time, E is the magnitude of the electric field, and α_V the visibility of the signal. [Fig. 2.7](#) shows the evolution of the neutron [EDM](#) limit as a function of year of publication from [[SPR57](#), [SN67](#), [MDBR67](#), [DBMR68](#), [BMDR69](#), [DMR73](#), [DMP⁺77](#), [ABB⁺80](#), [ABB⁺81](#), [PSG⁺84](#), [SCP⁺90](#), [ABB⁺92](#), [ABB⁺96](#), [HBG⁺99](#), [BDG⁺06](#), [PAA⁺15](#), [SKP⁺15](#), [AAA⁺20](#)].

The current limit $|d_n| < 1.8 \times 10^{-26} e \cdot \text{cm}$ (90 % CL) is set by the nEDM collaboration based at the [Paul Scherrer Institute \(PSI\)](#) [[AAA⁺20](#)]. This collaboration

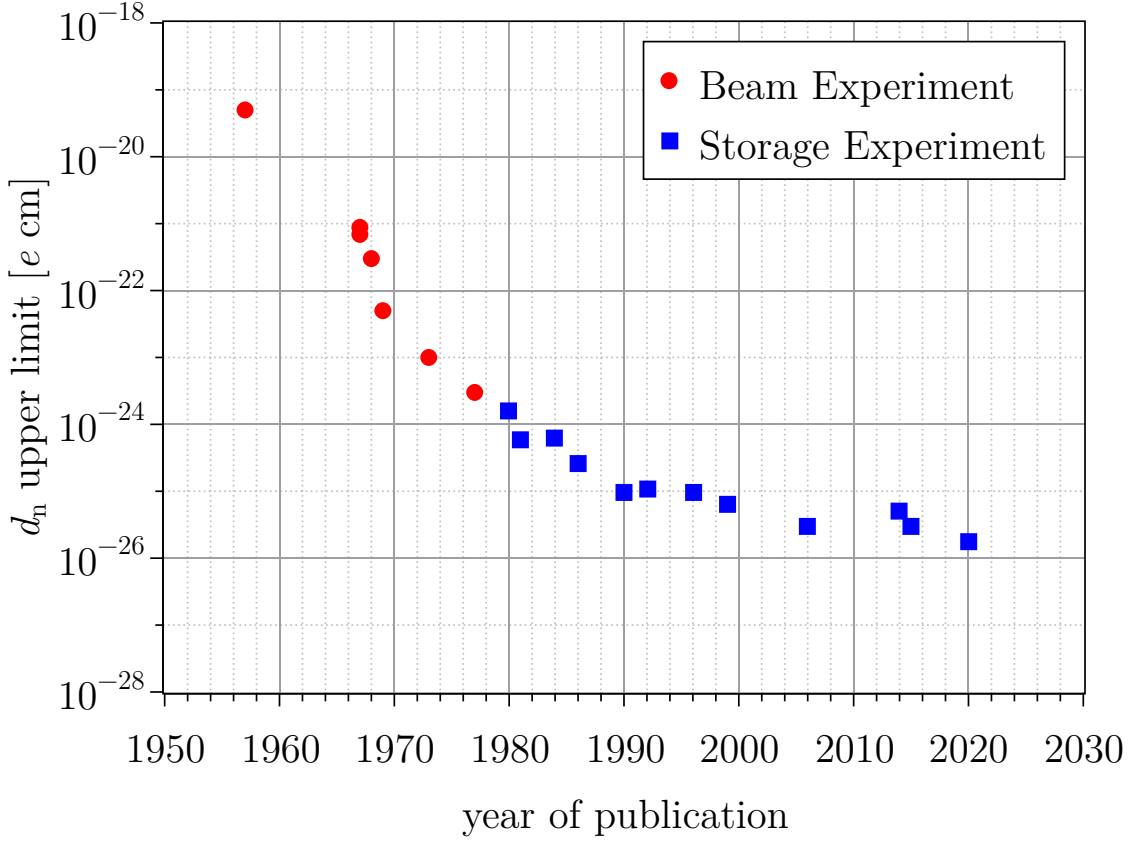


Fig. 2.7: Neutron EDM limit as a function of the year of publication. The red dots represent the cold neutron beam experiment and the blue squares the UCN storage experiments.

is already planning an upgrade, called n2EDM, in order to push even further the measurement with a planned sensitivity of $10^{-27} e \cdot \text{cm}$ for four years of measurement. To do so, the apparatus will have a double chamber, and will measure with an increased electric field and increased neutron statistics. Other UCN experiments are also planning to improve upon the limit in the next decade. Table 2.4 summarizes the expected sensitivity for the different experiments.

In addition, few exotic experiments have been developed. [AAA¹⁹] has developed a completely new measurement idea using the interaction of the UCN with ${}^3\text{He}$, [FJK⁰⁹] proposes to use the interaction of the UCN with crystals, and [EZR¹⁹] goes back to the origins with a cold neutron beam experiment but in combination with a time-of-flight technique to overcome some historical limitations. Its development, technique, results, and future are discussed in this thesis.

2.5 The last cold neutron beam experiment

The last EDM experiment that used a beam of cold neutrons [DMP⁷⁷] operated with the apparatus represented in Fig. 2.8. The apparatus was an improved version

Experiment	sensitivity ($e \cdot \text{cm}/\sqrt{\text{day}}$)	ref
TUCAN	10^{-26}	[Tak21]
n2EDM	2.6×10^{-26}	[ABB ⁺ 21]
PanEDM	7.9×10^{-27}	[Fil21] and [DBC ⁺ 19]
LANL EDM	3×10^{-26}	[Chu21]
BeamEDM	5×10^{-26}	[EZR ⁺ 19]
SNS EDM	$2 \rightarrow 3 \times 10^{-27}$	[AAA ⁺ 19]
DEDM	2×10^{-25}	[FJK ⁺ 09]

Table 2.4: *Expected sensitivity per day for the different neutron EDM experiments. The four first experiments are the continuation of the previous storage experiments, BeamEDM is the continuation of the beam experiments, and SNS EDM and DEDM are based on new concepts.*

of the one described in [BMDR69] for the previous experiment. It was installed at the **Institute Laue-Langevin (ILL)**, in France, on a cold beamline whose spectrum is displayed in Fig. 2.9. It was composed of:

- a polarizer, based on the selection of one spin state with a Co-Fe mirror in a high magnetic field,
- two spin flippers at the beginning and at the end of the free precession region,
- a passive magnetic shield made out of two layers of 2.54 mm thick Moly Permalloy,
- a homogeneous magnetic field of 1.7 mT, generated by permanent magnets, covers the spin flippers and the free precession region,
- a set of 1.8 m long electrodes, vacuum chamber, which can hold 100 kV with a gap of 1 cm,
- a spin analyzer working on the same principle as the polarizer,
- and a high flux detector capable of counting 5×10^6 n/s over the detector area of 10 cm^2 .

This was placed on a turn-table in order to rotate the apparatus by 180° every other day. With such a procedure, the angle between the neutron velocity and the electric field was inverted leading to an inversion of the $v \times E$ systematic effect. From measurements in the two orientations, the strength of the $v \times E$ effect could be determined and compensated for. Dress et. al measured $d_n = (0.4 \pm 1.1) \times 10^{-24} e \cdot \text{cm}$ but "arbitrarily increased" (sic. [DMP⁺77]) the experimental error to $1.5 \times 10^{-24} e \cdot \text{cm}$ because of instability in some of their systematic effects. They published an upper limit of $|d_n| < 3 \times 10^{-24} e \cdot \text{cm}$ (90 % CL).

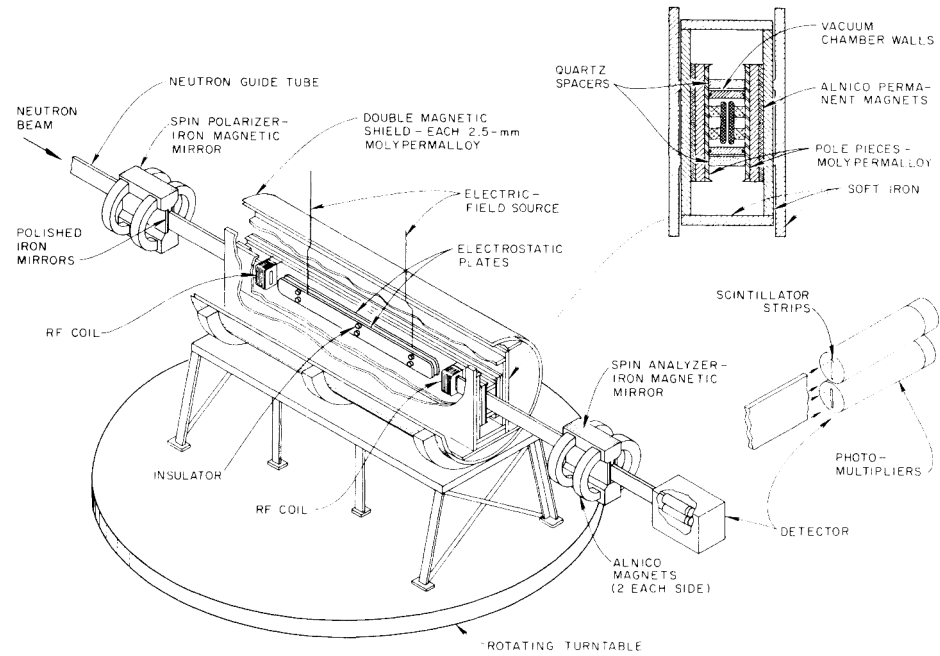


Fig. 2.8: Representation of the apparatus from [DMP⁺77] with the major components. The two inserts on the right show a radial cross section of the apparatus through the middle and the inside of the detector. They indicate material information that are not present in the central drawing.

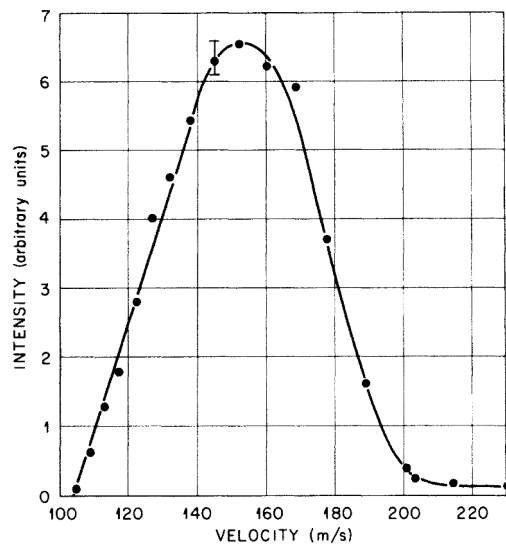


Fig. 2.9: Neutron spectrum of the cold neutron beam taken from [DMP⁺77].

Chapter 3

The BeamEDM experiment

BeamEDM is an experiment in a proof-of-principle stage that ultimately aims to measure a neutron EDM with a sensitivity that would be complementary and competitive with future UCN experiments. It uses the cold neutron beam experiment concept and combines it with a time-of-flight measurement to distinguish between the $v \times E$ signal from an EDM signal. This chapter starts with a short introduction about the project and the different facilities where the apparatus has been installed. Then, it details the different components of the apparatus, hardware, and software with the main changes that occurred over the last four years thanks to a group effort.

3.1 Introduction

In 2013, the first article [Pie13] was published on the BeamEDM project where the concept, the potential systematic effects, and ultimate sensitivity goal is defined. BeamEDM is a neutron EDM experiment using a pulsed cold neutron beam.

The idea of a beam experiment is not new. The first neutron EDM experiments were using cold beams, however, they were limited by systematic effects like the relativistic $v \times E$ effect. BeamEDM, with its time-of-flight technique, distinguishes a first-order $v \times E$ signal from an EDM without the need for a relative measurement unlike the last cold neutron beam experiment [DMP⁷⁷].

Currently, BeamEDM is in a proof-of-principle stage that aims to characterize the systematic effects and give a first estimate of the sensitivity of the full scale experiment. Its current goal is not to be competitive with current experiments but to demonstrate that this novel technique could be used to measure an EDM. So far, four beamtimes with the Ramsey apparatus have been performed either in France, at the Institute Laue-Langevin (ILL) at PF1b, or in Switzerland, at the Paul Scherrer Institute (PSI) at BOA. These beamtimes are summarized in [Table 3.1](#). A description of the beamlines and the apparatus are presented hereafter.

Beamtime	1	2	3	4
Year	2017	2018	2018	2020
Starting date	28/08	07/03	21/09	06/08
Ending date	17/09	27/03	24/10	15/09
Duration	21 days	21 days	34 days	41 days
Beamline	BOA	PF1b	BOA	PF1b

Table 3 .1: Summary of the different beamtimes with the year, their staring and ending dates, their duration and the beamline where they were installed.

3 .2 Cold neutron beam, and infrastructures

Currently, the two of the high-intensity cold neutron sources in Europe are the Paul Scherrer Institute in Switzerland and the Institute Laue-Langevin in France.

The Paul Scherrer Institut (PSI) has a spallation source that produces neutrons: A high-intensity proton beam hits a tungsten/lead target (Fig. 3 .1) and produces a "cloud" of fast neutrons. These neutrons are moderated in liquid deuterium at 25 K [PSI], and guided to the different beamlines, including the "Beamline for neutron Optics and other Approaches" (BOA) [BOA].¹

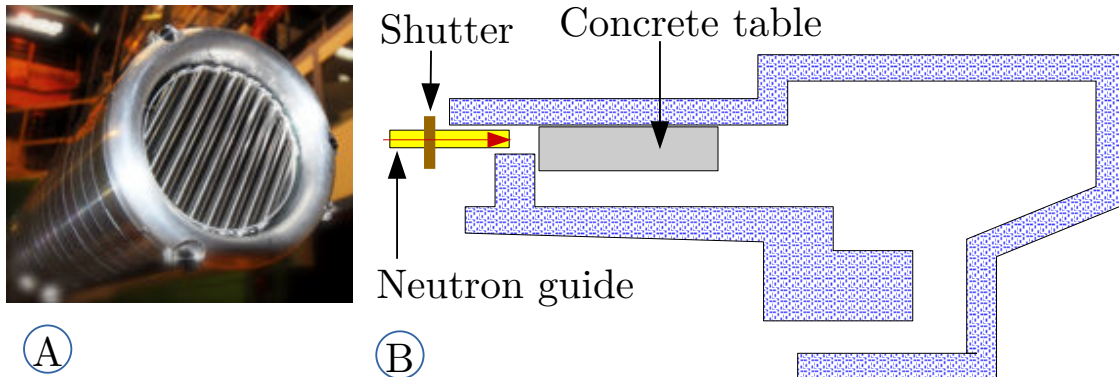


Fig. 3 .1: A) Pictures of the spallation target at PSI [Tar]. B) Drawing of BOA layout with the instrument shutter, the neutron guide in yellow and the concrete table in the experiment area.

BOA is the beamline where the BeamEDM experiment was set up for the first beamtime in 2017 and the third in 2018, see Table 3 .1. It is composed of a 2.7 m guiding tube from the cold source to a polarizer, based on a combination of $m=2$ and $m=3.3$ super-mirrors in a high magnetic field of 30 mT, generated by permanent magnets [MPL⁺¹⁴]. It has a polarization of about 96.6 % for a cold neutron beam with a peak in the de Boglie wavelength distribution at 3.5 Å and a flux of the order of $1 \times 10^8 \text{ n cm}^{-2}\text{s}^{-1}$, [HvE⁺¹²]. These characteristics are summarized in Table 3 .2.

¹A different name is found in [MPL⁺¹⁴]: "Beamline for neutron Optics and other Application"

The experimental area is a closed room of 8.5 m length made of concrete blocks for radiation shielding. This room contains a 3 m long concrete table at the upstream end of the beamline to set additional instrumentation available for the users. In the case of BeamEDM, the following items were used:

- a set of boron-aluminum disks with different sizes for the opening slit that defines the geometry of the neutron beam,
- an alignment laser,
- an adiabatic spin-flipper,
- three movable-tables that can be translated and rotated with motors,
- a chopper system, based on a turning disk.

The Institute Laue-Langevin (ILL) produces neutrons via a heavy-water nuclear power plant dedicated to research. It has a specific fuel element shape to maximize the production of neutrons and the delivery to the different neutron guides. Liquid deuterium sources cool regions of the reactor near the cold neutron guides, to moderate the neutrons to lower energy and transport them to their beamlines.

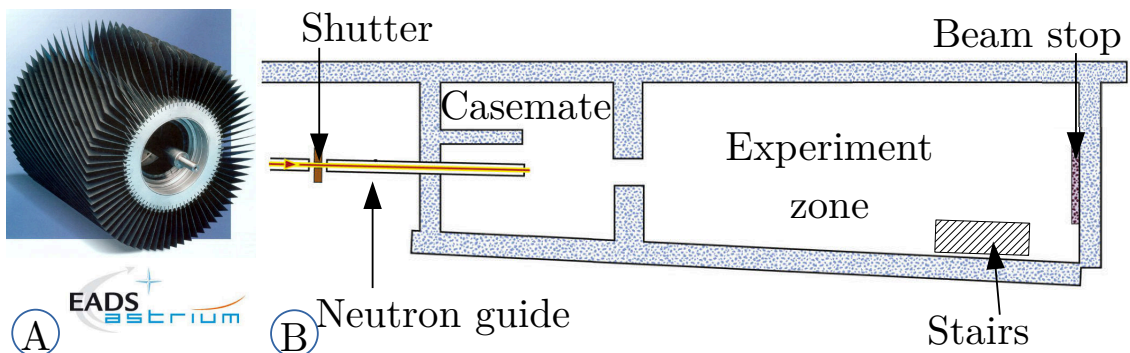


Fig. 3.2: A) Picture of a wavelength selector from EADS ASTRIUM. B) Drawing of PF1b layout with the instrument shutter, the neutron guide in yellow, the casemate and the experiment zone, adapted from [PF1].

One beamline is the "Polarised cold neutron beam facility" (PF1b) [PF1], where BeamEDM was set up for the second beamtime in 2018 and the last one in 2020, see Table 3.1. It has one of the most intense cold neutron beams in the world. Its characteristics are compared to BOA in Table 3.2.

The experimental area is a pit, open on the top, which allows the user to set up the apparatus more easily, but adds constraints with respect to radio-protection as the control room is adjacent to it. A shielded room, the casemate, placed upstream of the experimental area, allows to install any devices that would generate too much radiation in the experimental area.

The instrument can provide a polarizer, a wavelength selector, and an adiabatic spin flipper in the casemate. The wavelength selector consists of a set of bent absorbing blades that are radially assembled. The selector rotates around its central axis, allowing the neutrons with a velocity matching the movement of the blades to be transmitted. The others are absorbed by the blades when colliding with them. A drawing of the beamline and a picture of a wavelength selector are shown in [Fig. 3.2](#).

Beamline	λ_{peak} (Å)	Flux (cm $^{-2}$ s $^{-1}$)	Polarization	XS (cm 2)	Exp. length (m)
BOA	3.5	$\approx 10^8$	96.6 %	4×15	8.5
PF1b	4.5	$\approx 5 \times 10^9$	99.7 %	6×8	≈ 10

Table 3.2: Characteristics of BOA and PF1b extracted from [[MPL⁺14](#), [HvE⁺12](#)] and [[KNPS05](#), [ADH⁺06](#)]. The stated wavelength is the peak value, the flux is for a polarized beam with the degree of polarization, the cross section (XS) of the beam at the exits of the beamline is displayed as width \times height. The available length is an estimate of the floor length of the experimental area. In the case of BOA, a concrete table takes about 3 m of the floor space.

3.3 The BeamEDM apparatus

The BeamEDM apparatus is composed of several key elements for a time-of-flight and Ramsey technique:

- A polarizer is already included in or provided by the beamlines. It produces a polarized neutron beam.
- An adiabatic fast passage (AFP) spin flipper is provided by the beamline. It is usually installed between the polarizer and the chopper. It works on a combination of gradient field and RF field [[GOR97](#), [LDD20](#)] which flips the neutron spin from one spin state to the other for a large spectrum i.e. in an adiabatic way.
- A chopper creates neutron pulses from the continuous beam with a typical pulse length of 1 ms and a typical frequency between 20 Hz and 50 Hz.
- Several sets of apertures define the beam(s) according to the geometry of their opening. They can separate the initial beam into two, called top and bottom beams, set their width and height as well as their divergence.
- Two spin flippers perform the $\pi/2$ flip of the neutron spin for the Ramsey technique

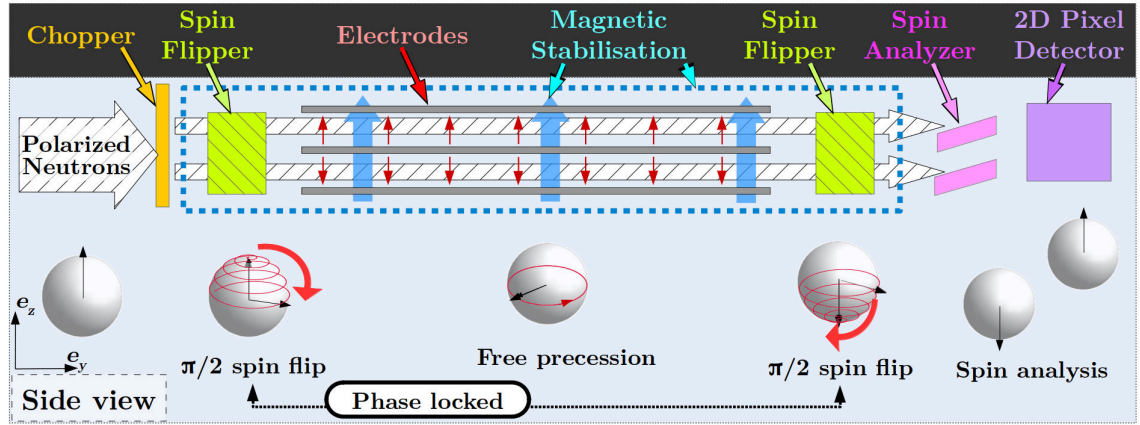


Fig. 3.3: Sketch of the apparatus with the polarized neutron beam (black and white arrows), the chopper (yellow thin rectangle), the spin flippers (slashed green boxes), the electrodes (long thin gray rectangles) that generate the electric field (thin red arrow), the magnetic field (blue arrows) and the region where it is stabilized (dashed blue line), the spin analyzer (parallel pink parallelograms), and the detector (purple square). Below is a representation of the neutron spin and the different steps with an emphasis on the phase lock of the two spin flip coils.

- Eventually, sets of electrodes generate opposite electric fields for the top and bottom beam.
- Coils that set and stabilize the magnetic field with the use of three-dimensional fluxgates. Eventually, mumetal and aluminum plates are used as magnetic and RF shielding.
- A spin analyzer made of Fe-Si super-mirrors in a strong magnetic field, separates spatially the neutrons according to their spin state.
- A neutron detector with a spatial and temporal resolution detects the neutrons.

The full setup is sketched in [Fig. 3.3](#) with the exception of the polarizer and adiabatic spin flipper. The components are explained in the following sections.

3.3.1 Chopper

The chopper system has changed for each beamtime. In the beginning, the BeamEDM experiment did not have its own chopper but used the single slit rotating disk one available at BOA in 2017. For the third beamtime, at BOA in 2018, a double-slit chopper disk was designed and constructed. A picture of this disk is shown in [Fig. 3.4](#).

The disk is made of 5 mm thick absorbing material (Al and $\sim 30\% {}^{10}\text{B}$), so that the neutrons can only pass through the slits. The slits themselves have an angular

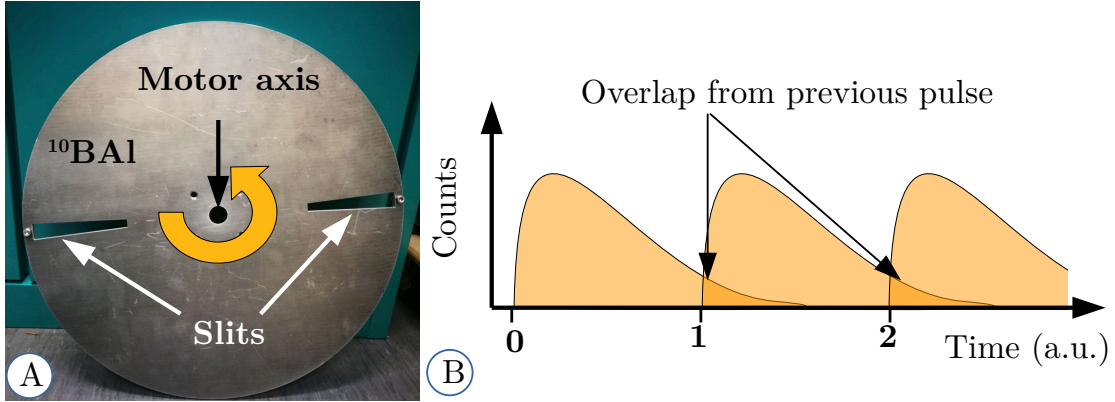


Fig. 3.4: A) Picture of the chopper disk designed for the beamtime at BOA in 2018. B) Scheme of the neutron spectrum for each chopper pulse. The darker areas represents the frame overlap from one neutron pulse to the next. The slowest neutrons of one pulse arrive at the detector position at the same time as the fastest neutron of the next pulse.

opening of 5° wide leading to a duty cycle of $2 \times 14\%$. Because of the two slits, the frequency of the pulse is the double of the rotation frequency.

The rotational frequency of the chopper is usually chosen from mechanical constraints but also in combination with the distance to the detector in order to reduce the overlap between pulses represented in Fig. 3.4B . The higher the frequency, the closer are the pulses in time and the more overlap is caused.

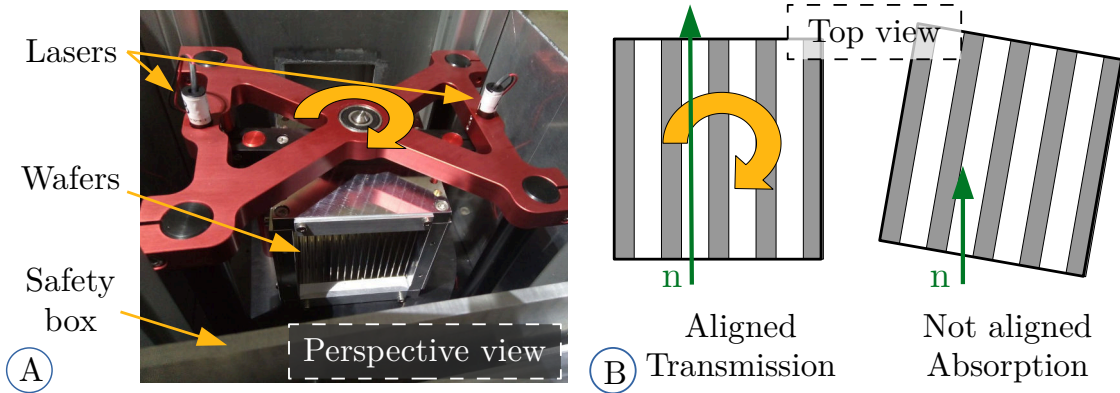


Fig. 3.5: A) Picture of the chopper used at PF1b in 2020. B) Schematics of the working principle view from the top, the wafers represented by the gray stripes are the absorbing material (wafers themselves), and in white is the air gap in-between.

For the last beamtime, at PF1b in 2020, a new chopper was designed [CAZ⁺]. It is based on the Fermi chopper principle [FMM47], i.e. with a rotational axis perpendicular to the neutron beam. It consists of several plates of absorbing material (Si wafers with GdTi coating) separated by air, see Fig. 3.5. With this geometry, the neutron beam is cut according to its angle with respect to the wafers, as represented in Fig. 3.5B, which allows for a larger beam. The open and close positions are

Fig. 3.6: Pictures of A) one single cube at PF1b in 2020 B) the laser cut plates, used to build and align the cubes, C) the entire structure in the laboratory in Bern in 2021.



recorded with the help of lasers and photo-diodes also visible on [Fig. 3.5A](#). In addition, the chopper is placed in an aluminum box for safety reasons and a canister below contains the electronics for device communication.

In both cases (disk or wafers), an electronic pulse is sent to the other components of the experiment when the chopper is in open position. This gives the starting point for the time-of-flight information.

3.3.2 Structure

The structure of BeamEDM is entirely modular to facilitate transport and expansion. It consists of several cubes of $1 \times 1 \times 1 \text{ m}^3$ made of non-magnetic materials like aluminum profiles [[Ite](#)], shown in [Fig. 3.6A](#). They were designed and built in the laboratory at the University of Bern to support the coils, vacuum pipes, spin flippers etc.

The alignment of the cubes is important as they are the foundation of the experiment. It is done during the construction of each cube with two laser-cut plates, shown in [Fig. 3.6B](#). A finer alignment is performed manually when several cubes are assembled together as in [Fig. 3.6C](#).

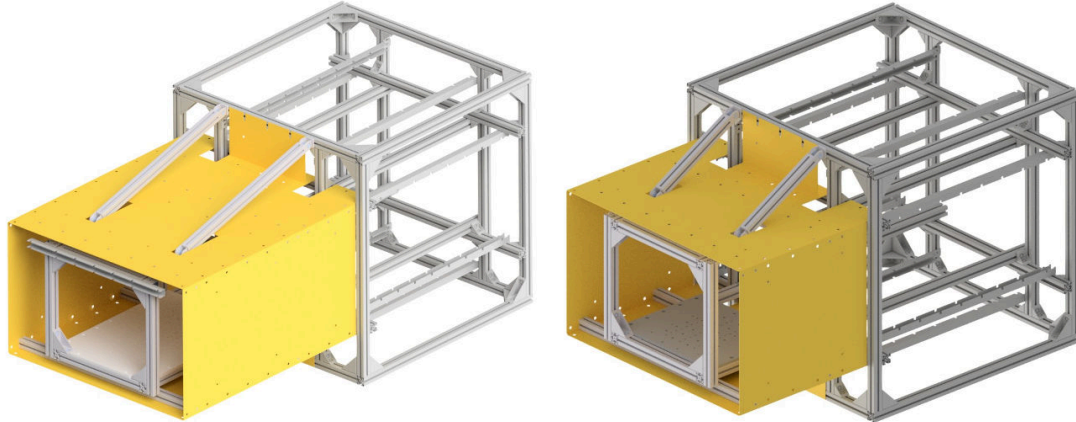


Fig. 3.7: Representation of the end pieces attached to a cube, taken from [[Got21](#)]. The yellow plates represent the aluminum shielding as present at PF1b in 2020. The longest cuboid is set on the downstream end of the apparatus and holds the spin analyzer and the detector. The smallest cuboid is installed on the upstream end of the structure.

In addition to these cubes, two smaller cuboids are placed at the beginning and at the end of the apparatus. A representation of the two cuboid pieces is shown in [Fig. 3.7](#).

3.3.3 Apertures

The apertures are composed of an aluminum structure and neutron absorbing plates, made of ^{10}B and aluminum called "BorAl". There exist several types of apertures, shown in [Fig. 3.8](#).

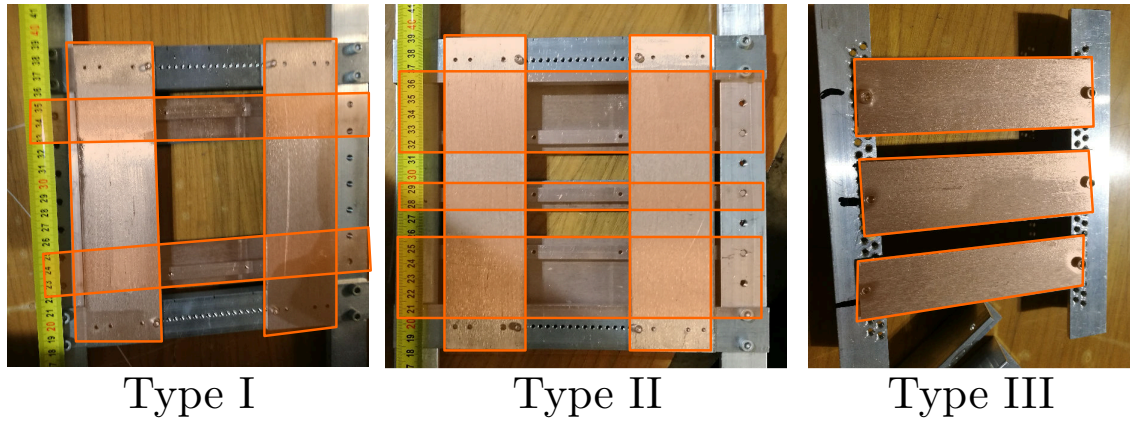


Fig. 3.8: Pictures of the different types of apertures taken after the dismounting of the apparatus PF1b in 2020. The absorbent components are marked by transparent orange areas.

- Type I, used for radiation reduction. Early in the beamline, it defines the shape of the full beam before the apparatus to decrease the radiation and neutron background levels in the experimental area.
- Type II, used for beam definition. These apertures define the beam(s) in several ways, they cut the beam into two smaller ones, the top beam and bottom beam, and set their width, height, and divergence.
- Type III, used for noise reduction in the detector. On the upstream side of the analyzer, it absorbs the neutrons that would otherwise fly directly to the detector without being analyzed by the super mirrors, i.e. the neutrons that fly in-between the mirrors.

3.3.4 Radio-frequency spin flipper

In [Chapter 2](#), it has been explained that the neutron spin can be flipped by applying a circularly rotating magnetic field. This can also be done with a linearly oscillating magnetic field as it can be interpreted as the sum of two circularly oscillating magnetic fields of the same frequency and amplitude, but one going clockwise the other counter-clockwise [[BS40](#)]. These linear fields are generated by a sinusoidal signal sent to a coil, called "spin flipper" whose axis is longitudinal to the beam ([Fig. 3.9A](#)).

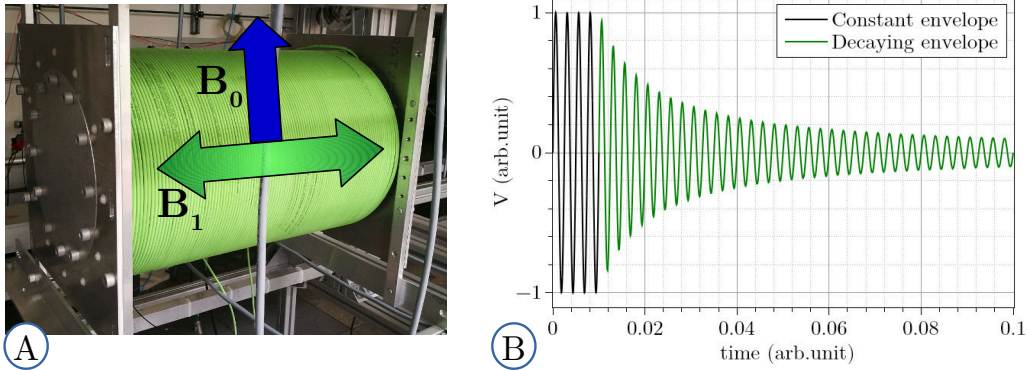


Fig. 3.9: A) A picture of one of the spin flippers before 2020, the blue arrow represents the static magnetic field in vertical direction. The green double arrow represents the linearly oscillating magnetic field. B) A representation of the modulated signal fed into the spin flippers when run in a time-of-flight mode.

The spin flippers are 25 cm in diameter so that they do not cut the beam and $\ell_{SF} = 40$ cm in length. This length was chosen for two reasons. Firstly, the fastest neutrons that we analyze should see a full oscillation of the field, $\tau > 2\pi/\omega_{RF}$ where ω_{RF} is the frequency of sinusoidal signal and τ is the spin flip duration, in the case of this experiment, the neutron time-of-flight over the spin flipper length. If we define as λ_c the critical wavelength of a neutron that see exactly one oscillation of the magnetic field, λ_c follows:

$$\frac{1}{\lambda_c} = \frac{m_n \ell_{SF} \omega_{RF}}{\hbar}. \quad (3.1)$$

This argument is linked to the choice of the magnitude B of the static magnetic field as $\omega_{RF} = -\gamma_n B$ when the spin flippers are on resonance. Secondly, the required amplitude to flip the neutrons should be achievable (from an approximate wavelength range of 2 Å to 20 Å). Indeed from Eq. (2.22) and/or Eq. (2.30), we know that the neutron spin flip is optimized according to $\tau \omega_1 = \pi/2$ where $\omega_1 = -\gamma_n B_1$ is the amplitude of the oscillatory field expressed in frequency and $\tau = \lambda m_n \ell_{SF} / \hbar$ is the flipping pulse duration.

As τ is a function of the wavelength, a simple sinusoidal signal would not flip equally the neutrons with different energy. This problem is solved by modulating the envelope of the sinusoidal signal by a factor $1/\tau = 1/(t \times \ell_{SF}/d_{CD})$, where t is the time-of-flight information and d_{CD} the total length between the chopper and the detector. As this formula is divergent at $t = 0$, the modulated signal S starts with a constant envelope until a predefined time t_0 , then it follows

$$S = S_0 \sin(\omega_{RF} t + \theta_i) \times \left(\frac{t_0 - t_1}{t - t_1} \right)^p, \quad (3.2)$$

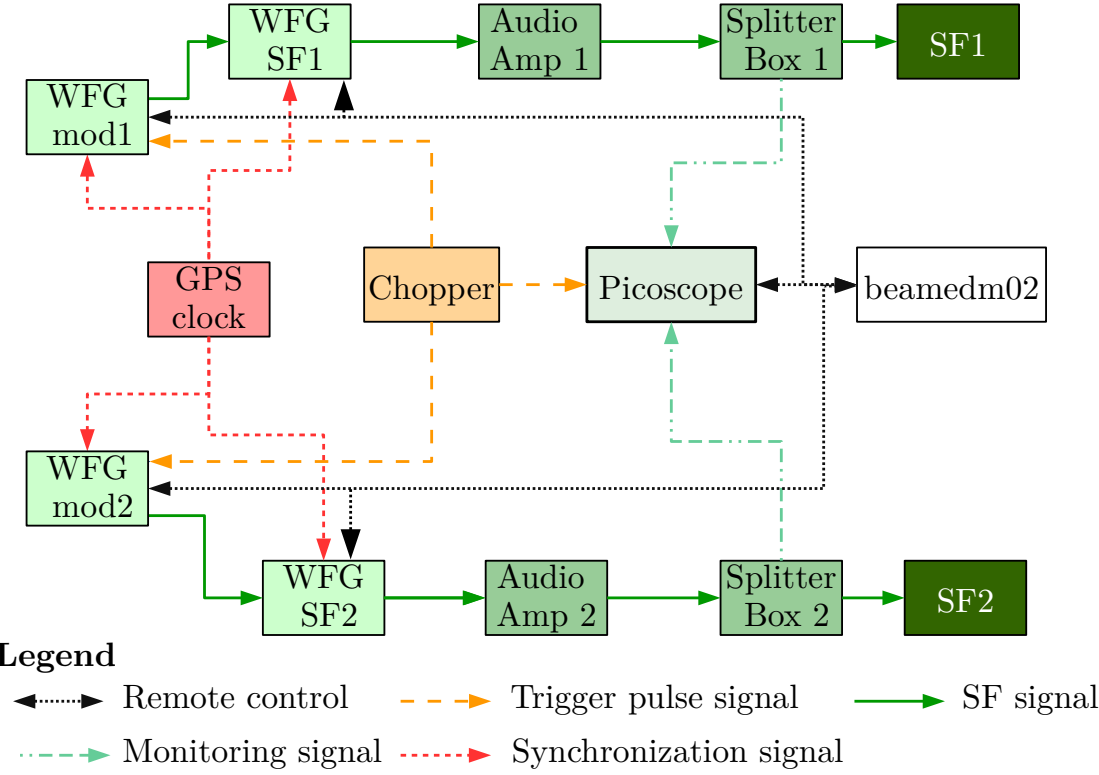


Fig. 3.10: Drawing of the connection between the devices used to control and generate the oscillating field at ILL in 2020.

where S_0 is the amplitude of the signal, ω_{RF} its frequency, θ_i with $i \in \{1; 2\}$ is the phase from the chopper pulse for the first or second spin flipper and $p \approx 1$ is a corrective factor. An example of the full signal as a function of time for one chopper pulse is displayed in Fig. 3.9B. This modulation has been set up for the first time at BOA in 2018 and is documented in [Sta19].

The electronic system that generated the modulated signal during the beamtime at PF1b, ILL, in 2020 is presented hereafter. The first waveform generators, labeled "WFG mod1" and "WFG mod2", generated the envelop of the modulated signal. The waveform generators, labeled "WFG SF1" and "WFG SF2", fill this envelop with a sinusoidal function to create the complete signal presented in Eq. (3.2). The modulated signal was then sent to two audio amplifier, ("Audio Amp"), after which each signal was separated into two by the "splitter box" which also contains a high power 200Ω resistor to achieve a close to frequency independent signal strength for the main signal. One part of the signal was sent to the spin flippers and an other with a reduced amplitude was sent to the picoscope for monitoring. For each neutron pulse, the chopper was sending a trigger to the picoscope, WFG mod1, and WFG mod2 in order to repeat the modulation pattern at that precise time, i.e. synchronized with the neutron pulses. The second waveform generator with the channels "WFG SF1" and "WFG SF2" was not synchronized with the chopper

pulse on purpose in order to avoid systematic effect presented in [Chapter 5](#) . All waveform generators were synchronized by a GPS clock which allowed to have a phase coherence between the two sinusoidal signals. A diagram of the connections between the devices is displayed in [Fig. 3.10](#). The waveform generators and the picoscope were controlled remotely by the computer named "beamedm02". For the complete product name of these devices refer to appendix [E](#)

For the last beamtime, i.e. at PF1b in 2020, the spin flippers were redesigned to be under vacuum in order to decrease the neutron losses and radiation from scattering in air, but their dimensions did not change.

3 .3.5 Vacuum pipes

The vacuum pipes, displayed in [Fig. 3.11A](#), are essential for the HV operation, but also to reduce the radiation due to neutron scattering in air and the neutron losses. The pipe is composed of two end caps and 1 m long sections to be as modular as the structure and have an inside diameter of ≈ 30 cm, which leaves some space for the holding structure of the electrodes. In addition, the feet of the vacuum pipes have alignment screws to lift or lower the full chamber [Fig. 3.11B&C](#).

To monitor the vacuum in the vacuum pipes several pressure gauges from Pfeiffer have been used in combination with a Maxigauge measurement and control unit, D-35614A. The vacuum gauges characteristics are summarized in [Table 3.3](#).

Name	TPR 280	PCR 280	PKR 361
Range (mbar)	$5 \times 10^{-4} - 1 \times 10^3$	$5 \times 10^{-5} - 1.5 \times 10^3$	$1 \times 10^{-9} - 1 \times 10^3$
Precision	15%	15%	30%
Max pressure (bar)	10	5	10
Datasheet	[Pfec]	[Pfea]	[Pfeb]

Table 3.3: Characteristics of different vacuum gauges with their respective measuring range, their overall precision, the maximum pressure they can withhold and the reference to their datasheet.

The pipes have been leak-tested in February 2020 up to 10^{-9} mbar/l/s with a helium leak-detector, see [Fig. 3.11A](#).

3 .3.6 High voltage system

The high voltage system is composed of: the electrodes, their holding structure, the feedthrough, and the leakage current monitor. They were used for the first time at BOA, PSI in 2018 with the exception of the leakage current monitor used only for the last beamtime, PF1b 2020.

Fig. 3.11: A) Picture of the leak checking measurement of one vacuum pipe with the two end caps (Bern, 2020), B) Picture of the vacuum pipe with one high voltage stack inside during alignment with a laser at PF1b in 2020. The white Teflon piece around the electrodes is used to see the laser light for a rough alignment and to protect the electrodes during the mounting and transport of the stack. C) Picture of one foot of the vacuum pipes with, on each side, two screws and one brass pin. One of the screws allows to lift the foot higher, the other one pulls it lower. The pin is for alignment. From this screws, one can align the full vacuum chamber in height.



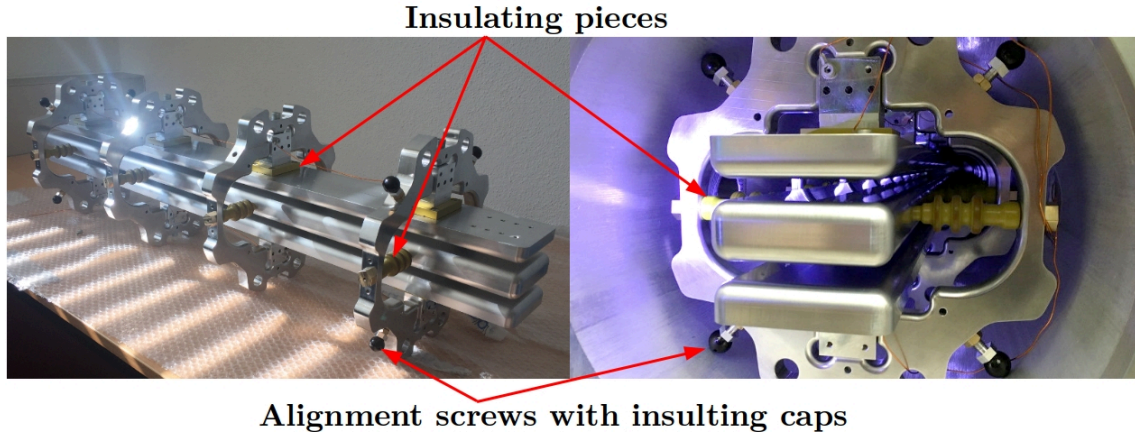


Fig. 3.12: Pictures of a stack of electrodes on their holding structure with a distance between electrodes of 1 cm. The left picture was taken in the laboratory at the University of Bern, the right one was taken at BOA in 2018.

The electrodes

There are two geometries for the electrodes depending if they are at high voltage or at the ground. The high voltage electrodes have a thickness of 3 cm and every edge has a radius of 1 cm to avoid high electric field regions from sharp edges. The ground electrodes are 2 cm thick and their edges have a radius of 1 cm except on the (backside) edges that do not see a high electric field. Both electrode types are 9 cm wide. For a better representation, two pictures of a set of electrodes on their holding structure are displayed in [Fig. 3.12](#).

The geometry of the electrodes did not change with time, however, several electrode stacks were produced with different surface quality:

- only machined,
- machined and hand polished,
- diamond milled.

The first electrodes that were only machined had a rough surface. They were directly sent to a mechanical polishing company to improve their surface quality and get the smoothest surface possible to avoid high electric field region from microscopic sharp points. It also has the advantage of improved neutron reflectivity as a measurement has shown, see [Section 5.4](#). Later, other sets of electrodes were diamond milled to have a smoother surface for further improvement of the experiment. So far, only the mechanically polished electrodes have been used in beamtimes.

The holding structure

One stack of electrodes (two ground and one high voltage) are assembled with four rings, see [Fig. 3.12](#). The high voltage electrode is placed in the middle of the rings



Fig. 3.13: A) Pictures of 1) Teflon heads for the alignment screws (2020), 1') alignment screws (2018), 2) insulator to hold the high voltage electrode 3) aluminum blocks to fix the ground electrodes to the rings that hold them with a Teflon piece to insulate them from it, 4) copper wires to connect the ground electrodes, 5) Teflon support to mount the electrode stack, 6) pins to connect the high voltage electrodes. B) Alignment ring with 4 pins to align the electrodes stacks with respects to the vacuum pipes. The pins matches the four holes in the rings that hold the electrodes.

and is held with castellated insulating pieces made of Torlon. The rings also hold the ground electrodes with blocks of aluminum and Teflon plates that can insulate the ground electrode from the rings if so desired. Individual components are displayed in Fig. 3.13A.

In order to align the electrodes with the beam and the apertures, alignment rings and pins, shown in Fig. 3.13B, are used. The alignment rings are fixed to the vacuum pipes so that their pins have a fixed place with respects to the pipe. When the holes in the rings of the electrodes stacks matches the pins of the alignment rings, the electrodes are centered in the pipe. In practice the stack is placed in the vacuum pipe first and then the alignment rings are inserted and by that they align the stack. Once the stack is aligned, the alignment screws fix its position relative to the pipe. These screws are equipped with spherical insulating heads to facilitate the insertion of the stack in the vacuum pipes without scratching them and to insulate the rings to the vacuum pipe. A finer alignment in height is done with the help of a laser for both the electrodes and the vacuum pipes as shown in Fig. 3.11B.

To connect the electrode stacks, copper wires are attachment on the backside of the ground electrodes and copper pins are set in the central high voltage electrodes.

The feedthrough

The high voltage is generated from a commercial power supply: the FUG HCB40-200000. The documentation for this device was not found; the closest one is [ele]. It can generate voltage up to ± 200 kV with a maximum current of ± 20 μ A in one of



Fig. 3.14: A) Picture of the small size standard ceramic feedthrough. B) Picture of the large custom feedthrough, designed and produced in Bern for operation at ± 200 kV. C) Examples of rods for the connection to the electrodes.

his two modes. This mode is the only one used during beamtime and tests. All the functionality can be controlled remotely including the change in polarity. It has a port for a 160 kV R24 cable whose other end is connected to the feedthrough.

During the first use of the high voltage system (BOA 2018), a small size, commercial feedthrough was used, [Fig. 3.14A](#). It was connected to the high voltage electrode via a rod of about 2 cm diameter, ending with a banana plug.

For our last beamtime, at PF1b, ILL in 2020, a non-magnetic, larger custom feedthrough was designed, build, and tested in the laboratory at Bern University, [Fig. 3.14B](#). It can hold a voltage up to ± 200 kV which is the limit of the high voltage power supply.² However, the R24 cable is magnetic due to a stainless steel component, thus, the feedthrough was placed further away from the electrodes than before. For practical reasons and to reduce the mechanical stress from misalignment, the connection to the electrodes was done with two rods instead of one, an example of such rods are shown in [Fig. 3.14C](#).

²In that case, the closest ground potential was the walls of the vacuum tank at a distance of about 20 cm, [Fig. 3.14B](#)

Leakage Current monitor

The leakage current monitor can measure independently the current that leaks from the high voltage to a ground electrode and/or the rings that hold them. This is important as any current would generate a magnetic field and possibly contribute to a systematic effect. The present design is a two channel device that converts a current in a range of $\pm 10 \text{ nA}$ into a voltage of $\pm 10 \text{ V}$ and samples it with a 16 bit resolution and sends it to the computer for recording. The signal sent to the computer is optically isolated from the initial signal in order to protect the electronics (e.g. the computer) from residual discharges, see Appendix C. This leakage current monitor was used for the first time at PF1b, ILL, in 2020.

3.3.7 Magnetic field

The magnetic field system is composed of main and stabilization coils, magnetic shielding, and magnetic sensors. The study of these elements is documented in [Got21][Gsp21], the main topic of the theses being the magnetic shielding.

Magnetic sensors

To monitor the magnetic field, the BeamEDM experiment uses fluxgates. The number increased with time for initial 5 FLC3-70 fluxgates to a total of 8 FLC3-70 fluxgates and 8 SENSYS-250 fluxgates. For the beamtime in 2020, the eight SENSYS-250 fluxgates were used to monitor the field of $220 \mu\text{T}$, see Fig. 3.15. In addition, the SENSYS-250 have a better accuracy and are less sensitive to thermal drifts. The two types of fluxgates, shown Fig. 3.16B, have different properties summarized in Table 3.4.

FG name	reference	Range	Rel. error	conv.factor	Drift
FLC3-70	Stefan Mayer-FLC3-70	$\pm 200 \mu\text{T}$	$\pm 1\%$	$35 \mu\text{T}/\text{V}$	$< 2 \text{nT}/\text{K}$
SENSYS-250	SENSYS-FGM3D/250	$\pm 250 \mu\text{T}$	$\pm 0.1\%$	$25 \mu\text{T}/\text{V}$	$< 0.3 \text{nT}/\text{K}$

Table 3.4: Characteristics of the two type of fluxgates [IGC] [SEN]. with their product name, the measurement range, the relative error on the measurement, the conversion factor from volt to microtesla, and thermal drift.

Main and stabilization coils

To perform a Rabi or Ramsey technique, the BeamEDM experiment requires a static, in our case vertical, magnetic field. This field is of the order of hundreds of microtesla so the Larmor frequency matches the length of the spin flippers as defined in Eq. (3.1). The field is produced by several rectangular Helmholtz-like coils, installed on the aluminum structure. Their global geometry is shown in Fig. 3.15.

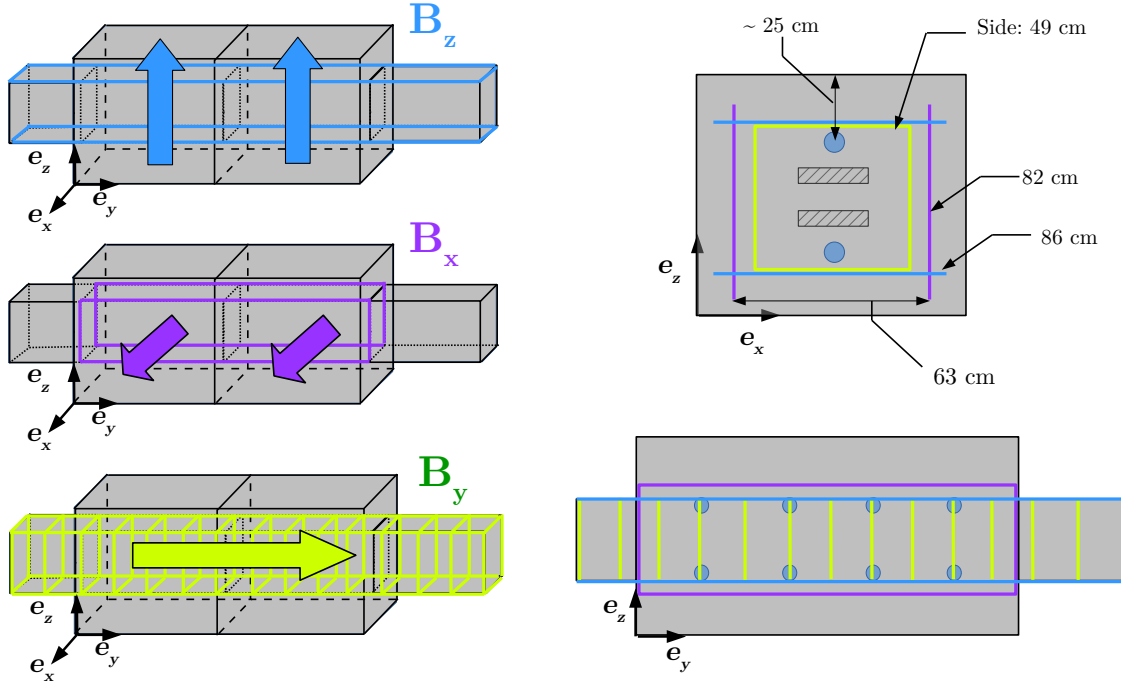


Fig. 3.15: Representation of the coils winding for the vertical, longitudinal, and transversal field by blue, green, and purple lines respectively. The black lines represents the structure composed of only two cubes and the two end pieces for simplicity. The position of the fluxgates as they were at the last beamtime, at PF1b, ILL 2020 is also represented by blue dots.

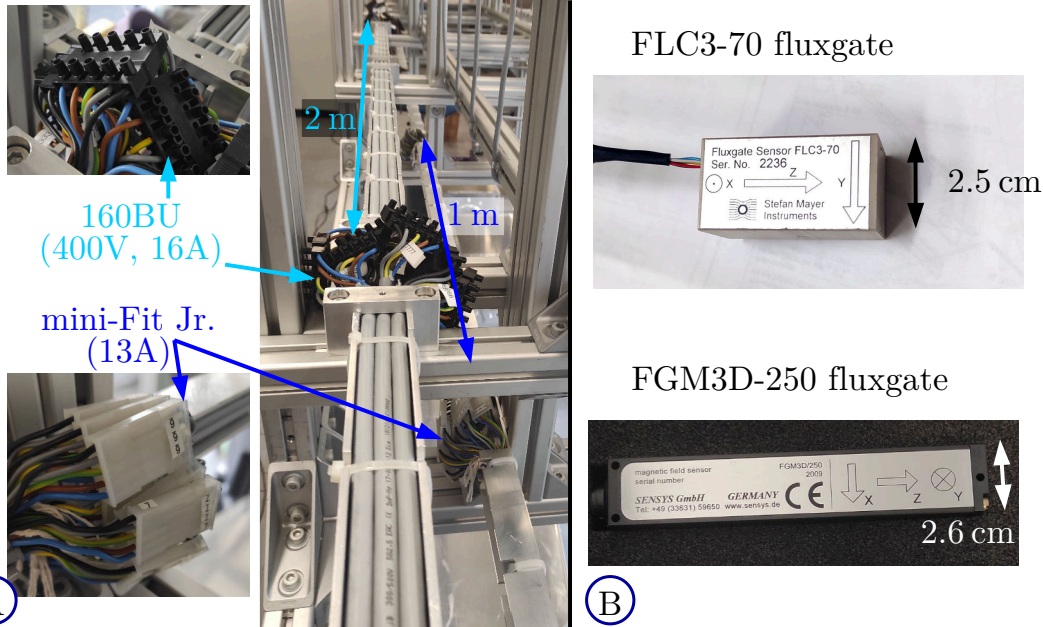


Fig. 3.16: A) Picture of the 160BU and mini-Fit Jr. connectors. B) Picture of the FLC3-70 and FGM3D-250 fluxgates taken in the laboratory in Bern. Their characteristics are summarized in Table 3.4.

In the beginning, the coils were composed of several one-meter-long segments. They were mounted permanently on the structure and connected together by the 39-01-4050 connector of the mini-Fit Jr. series [Far] shown in Fig. 3.16A. The longitudinal and transversal coils do not require high currents as in the normal mode of the experiment, they should only compensate for static longitudinal and transversal magnetic field background. The wires of the coils are separated in two: the main coil that sets a field within a user defined tolerance and a stabilization coil that correct the field from small drift. For the last beamtime at PF1b, ILL in 2020, the longitudinal and transversal coils were independently powered by two KEYSIGHT E3634A DC power supplies each. One for the stabilization coil, the other for the main coil.

The vertical coil on the other hand generates a field of hundreds of microtesla. The coil was redesigned for the last beamtime, PF1b 2020. The connectors were changed from the mini-Fit Jr. ones to 160BU ones [Met], shown in Fig. 3.16, in order to have a better contact therefore a lower resistance. In addition, each segment was designed on a two-meter scale in order to reduce the resistance of the whole coil, see Appendix B. Due to the size of each segment, the coil segments have to be removed when disassembling the apparatus which is not the case for the transversal and longitudinal coils. As a comparison, the magnetic field was set around $130 \mu\text{T}$ before the change of coils and $220 \mu\text{T}$ after. To achieve this field, the main coil was powered by two FUG NTN 1400.

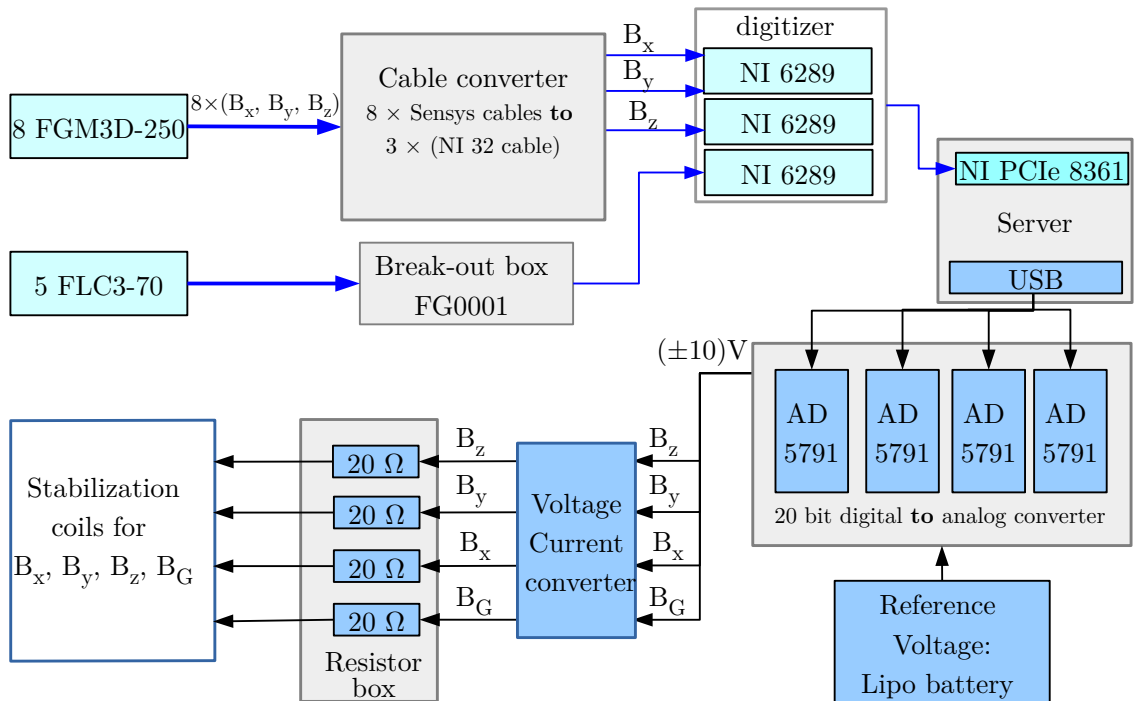


Fig. 3.17: Diagram of the connection between devices for the magnetic stabilization.

In addition, four additional coils were used for the stabilization of the vertical, transversal, longitudinal field and vertical field gradient. Their geometry is the same as the main coils of the same direction. The details are presented in appendix B. The stabilization works hand in hand with the fluxgates. The internal fluxgates send the magnetic field information to a digitizer (three NI6289 - [ins]) that send the measured values of the x, y and z components of the magnetic field from all fluxgates to a dedicated National Instrument card (NI PCIe 8361- [PCI]) installed on the server named "beamedm04". The server then computes the value to send to each of the four 20 bit voltage digital to analog converter - AD5791, [AD5]. The analogue voltages are then converted into currents and sent to stabilization coils with a load of 20Ω for each of them. An schematic diagram is displayed in Fig. 3.17. The connection for the external fluxgates is also displayed in the same figure. The break-out box FG0001 was designed in the laboratory in Bern and makes the conversion from the fluxgates' cable to the National Instrument one.

Magnetic shielding

Mu-metal is a composite alloy with about 77 – 80 % nickel, 16 % iron, and small amounts of various other elements [Mag]. It has a high relative magnetic permeability ($\mu = 50\,000\text{--}500\,000$), thus, it is an efficient shield for static or low-frequency magnetic fields.

In 2020, each cube was covered by 2 layers of 1.6 mm thick mu-metal to shield from low frequency and static magnetic fields. Each layer is separated from the other one by 19 mm with an insulating material. The plates are squares with each side being 1 m long to match the cubes size with holes for the feet of the structure. The two layers are connected to the layers of the other plates with L-shape corner pieces on the outside and inside of the plate, visible in Fig. 3.18. The mu-metal plates, with the geometry shown in Fig. 3.18, have been characterized by [Gsp21] and [Got21] in the laboratory in Bern at the beginning of 2020. It resulted in a shielding factor of about 200 for vertical static magnetic background.

Due to time constraints, the end pieces of the structure were not shielded with mumetal for the last beamtime, at PF1b in 2020. In order to avoid picking up high frequency magnetic field in the coils, the end pieces were shielded with aluminum plates as represented in Fig. 3.7. In addition, two high current resistors of 100Ω were added in the loop of the main vertical coil. These resistances decrease any AC current that would be picked up.

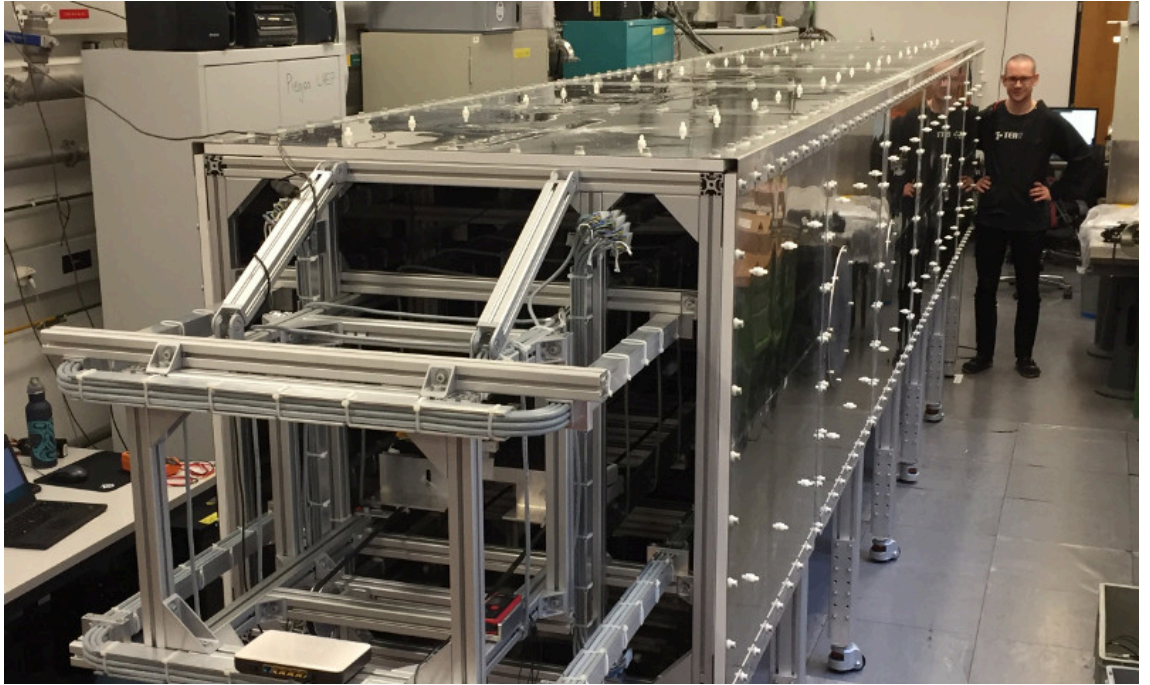


Fig. 3 .18: Pictures of the structure with magnetic shielding during its characterization in Bern in 2020.

3.3.8 Spin analyzer

The working principle of the spin analyzer is based on the Bragg diffraction on a set of ferromagnetic super-mirrors in a strong magnetic field, explained in [Chapter 2](#). The magnetic field aligns the spin of the unpaired electrons from Fe in the mirror leading to an enhancing of the local magnetic field. This strong magnetic field creates an energy shift according to the neutron spin state, [Eq. \(2.9\)](#), e.g. the neutrons with a spin "up" will have a higher potential energy than the one with a spin "down", as represented in [Fig. 3.19](#). This difference in energy is then used to separate the two spin states: if the equivalent Fermi potential of the mirror at the given angle is in-between the two energy states of the neutrons, one state will be reflected and the other will be transmitted. As these states corresponds to the spin states, the neutrons are then separated in space according to their probability to be in a certain state, as shown in [Fig. 3.19B](#).

For the first beam time, at BOA in 2017, only one super mirror, borrowed from SwissNeutronics [[Swi](#)], was used to reflect the neutrons horizontally. The mirror was a glass mirror sputtered with FeSi, visible in [Fig. 3.20](#). The characteristics of this mirror are not available, but its m-value is expected to be low.

A new analyzer has been designed for the beamtime at PF1b, in 2018. It is based on the same concept as the previous one, but it has two sets of $m=5$ Fe/Si super-mirrors, one for each beam ([Fig. 3.21A](#)). The mirrors are oriented to reflect vertically one spin state, as shown in [Fig. 3.21B](#). In addition, the permanent magnets

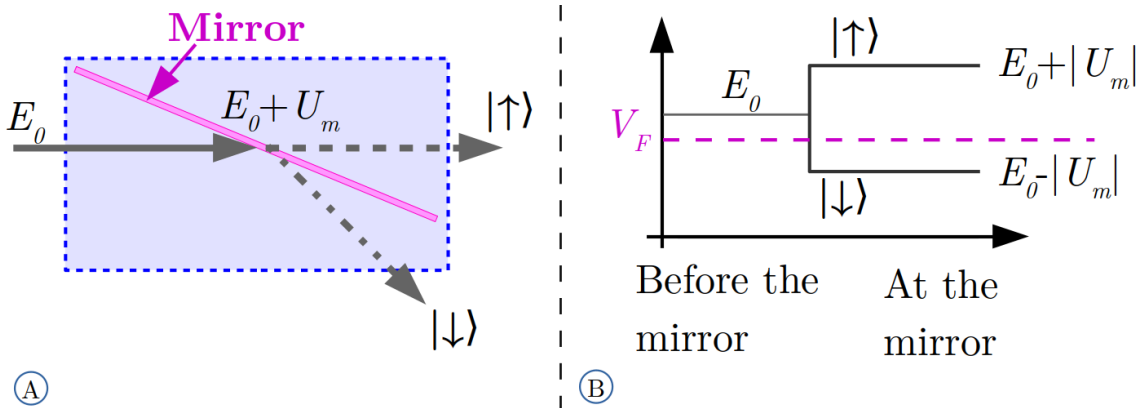


Fig. 3.19: A) Representation of the spin analyzer working principle with in gray arrows the neutron beams and in pink rectangle the spin analyzer mirror in a strong magnetic field represented by the blue region. The energy of the neutron is defined as E_0 outside the spin analyzer magnetic field and $E_0 + U_m$ inside where U_m is the potential energy defined in Eq. (2.9). The two spin states are labeled as $|\uparrow\rangle$ and $|\downarrow\rangle$. B) Energy diagram of the neutrons as a function of their spin state before the mirror and at the mirror i.e. inside the strong magnetic field. V_F represents the equivalent Fermi potential of the material that defines if a neutron is reflected or transmitted at a angle according to Eq. (2.7).

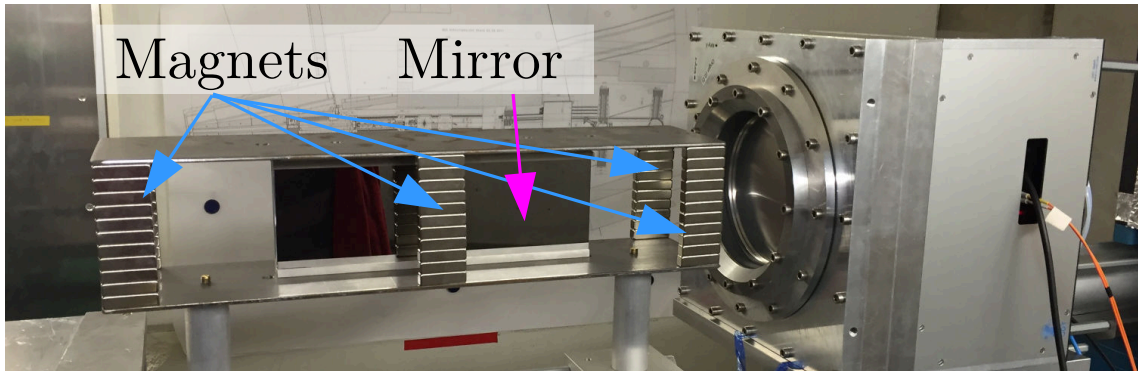


Fig. 3.20: Pictures of the analyzer and the detector at BOA in 2017.

that generate the magnetic field are included in the spin analyzer casing, at the top and bottom of the mirrors. Each set of mirrors can be inclined with respect to the neutron beam independently and remotely by motors fixed on the lateral side on the spin analyzer casing, Fig. 3.21C. A documentation on the motor system is available in appendix D.

The incidence angle between the mirror and the beam is optimized during beamtime so that a broad range of the neutron spectrum around 4 \AA can be analyzed. This is done by measuring the integrated count in the reflected and transmitted beam when the adiabatic spin flipper is active and inactive, i.e. for each spin state. In addition, the mirrors should cover all of the beam, otherwise some neutrons are not analyzed. In 2020, at PF1b, a set of apertures has been added to the upstream side

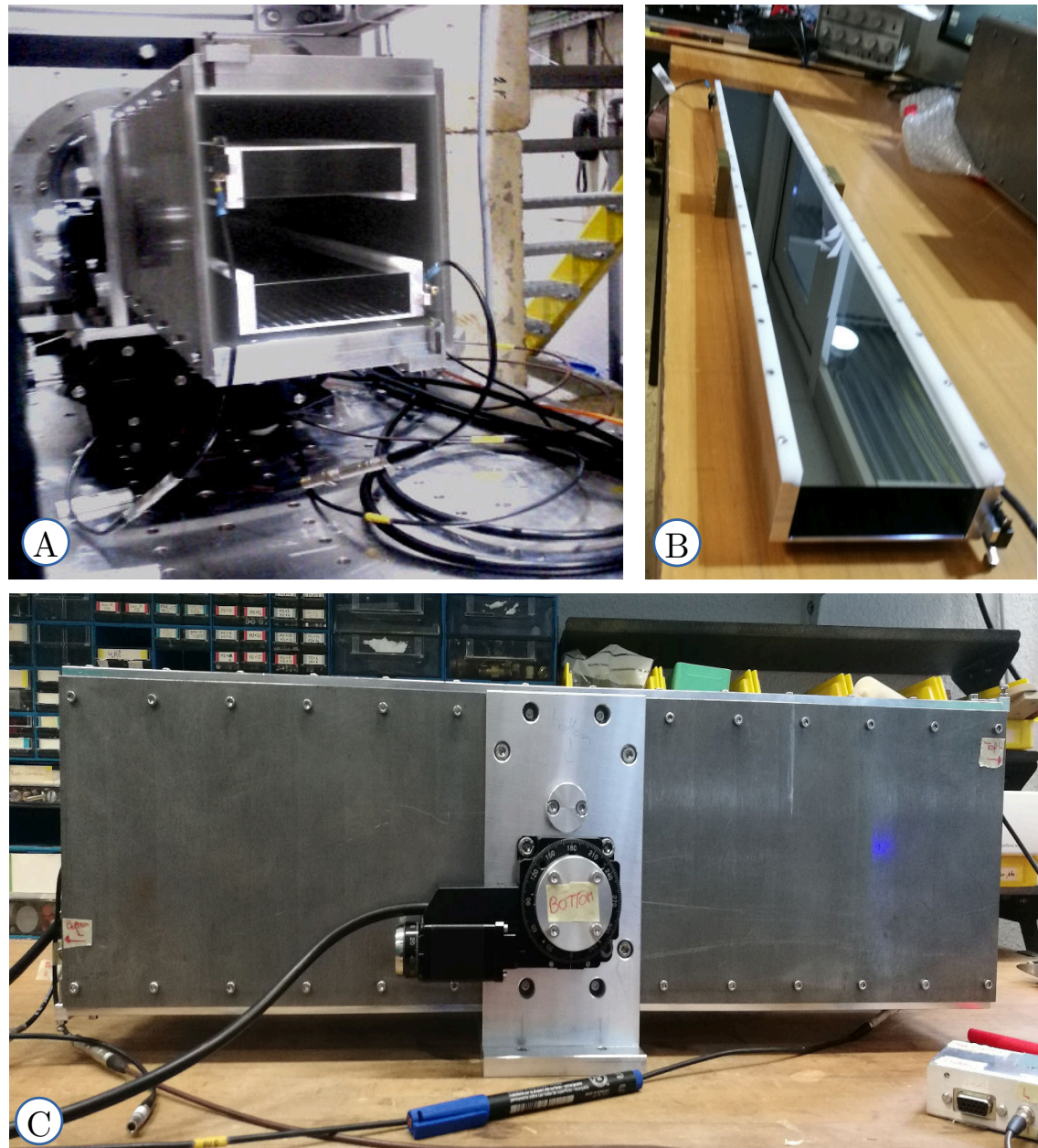


Fig. 3.21: A) Pictures of the analyzer from the upstream side at PF1b in 2018. B) Pictures of super mirror wafers in their holding structure at PF1b in 2020. The mirrors are clamped to the metallic structure by Teflon pieces (white). C) Pictures of the analyzer from the lateral side at Bern University in 2020,

of the analyzer, as displayed in Fig. 3.8c, in order to avoid any additional background from the direct beam when the mirrors do not cover the full beam cross-section.

3.3.9 Detector

The neutron detector is a commercial type detector with a custom design for the BeamEDM experiment, CASCADE-E, made by the CDT company [CDT]. It is composed of ^{10}B coated, Gas Electron Multiplier-GEM foils at high voltage placed inside an ArCO_2 buffer gas, and a readout structure. The absorption reaction of a neutron on ^{10}B ,



creates α particles that ionizes the gas and leads to an electron cascade amplified by the GEM foils in the ArCO_2 buffer gas. The readout structure is separated into 16×16 pixels of area $6.5 \times 6.5 \text{ mm}^2$ each to determine the position of the initial neutron. Its minimum time-of-flight bin size is $0.1 \mu\text{s}$ but the one used in beamtime is usually $10 \mu\text{s}$.

Pictures of the front, top, and back side of the detector are shown in Fig. 3.23. On the front side, a thin aluminum disk ($\approx 0.5 \text{ mm}$) defines the measurement window. The top side presents the device communication ports. The "Lemo" ports are for analogue signals and are not used during beamtime. The port label "Trigger" receives the pulse generated by the chopper when rotating to inform the upcoming of a neutron pulse. It is used for the time-of-flight mode of the detector. And the ports labeled "Data" or "SiS Opto" is the port that goes to an optodecoupler and the computer for data-recording and remote control. On the back side, a gas inlet and outlet with a valve maintains the flushing of the buffer gas. There is also the HV socket to power the GEM foils and the electronics socket to power the electronics.

The detector can be run in two modes:

1. The PAD mode creates a 2D image of the neutron counts in the detector integrated over time, see Fig. 5.3. There is no time information and therefore the detector does not need a trigger to measure. For this mode, the main parameter is the measurement time, i.e. the time period for which the detector accumulates the neutron counts for each pixel.
2. The time-of-flight (TOF) mode creates a time-of-flight spectrum for each pixel. The time-of-flight information is defined by each chopper pulse and the spectrum is built up by folding the neutron counts over the period of a chopper cycle. In other words, for each chopper pulse, the pulse's neutron spectrum is accumulated onto the previous one. For this mode, the main parameters are the time-of-flight bin size, the maximum size of the time-of-flight spectrum,

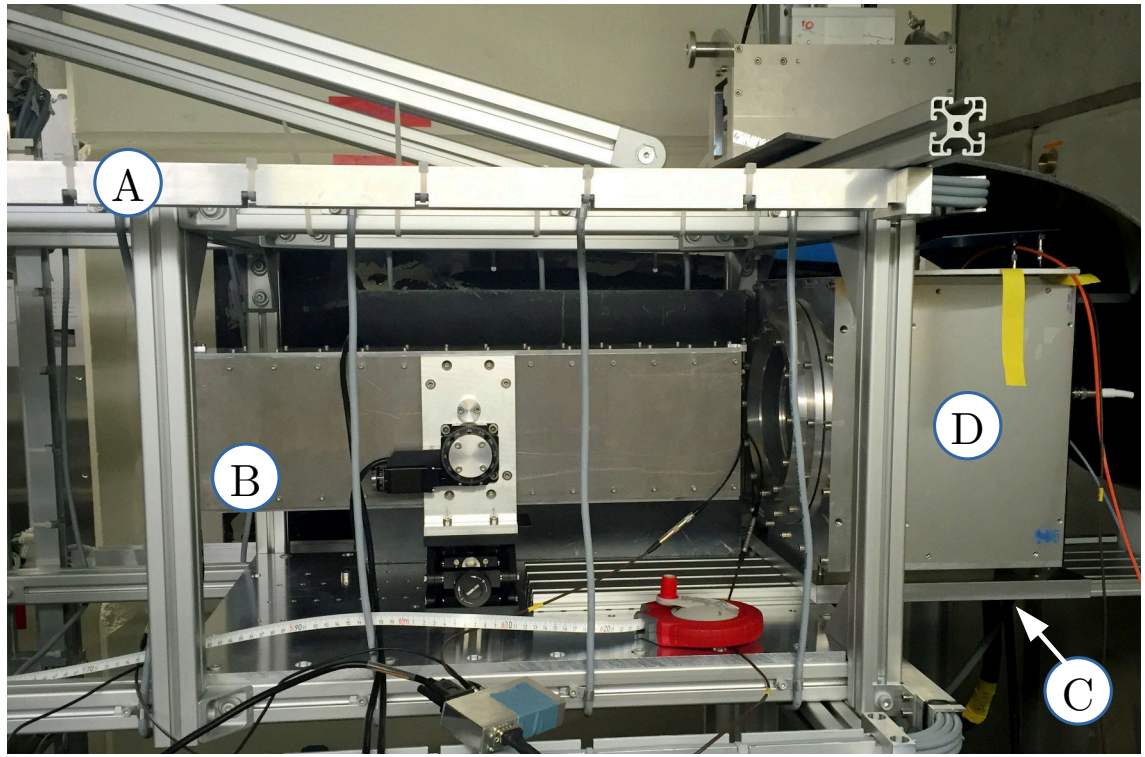


Fig. 3.22: Picture of A) the last cuboid with B) the spin analyzer inside and C) the sliding plate that holds D) the detector (2018 BOA).

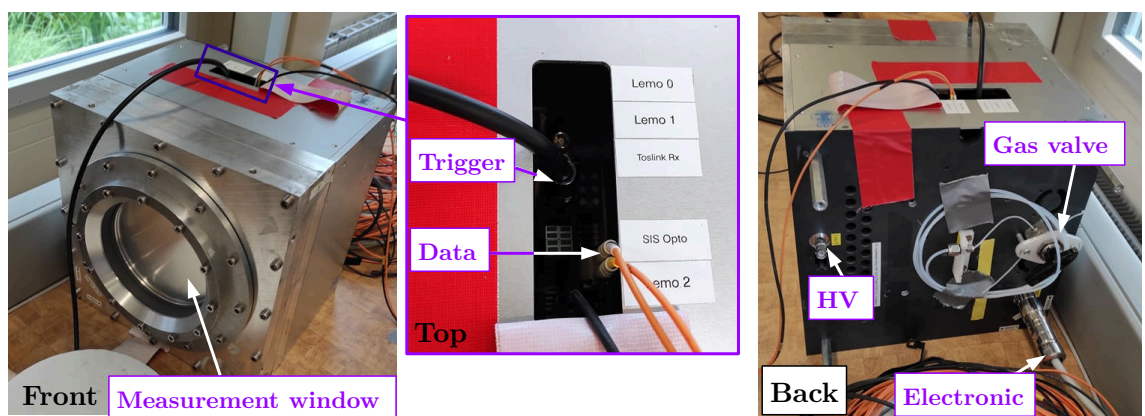


Fig. 3.23: Picture of the front, top, and back side of the detector with label of the measurement window, the trigger input cable, the two optical fiber cables that receive and send information from the computer to the detector, the HV power supply socket, the electronics power supply socket, and the valve for the buffer gas.

and the number of chopper pulses (called sweeps) used to create the spectrum before the measurement stops. There is also the option to define the end of the measurement by an electronic pulse sent to the detector, in that case, the number of sweeps is not defined.

Since the beamtime at PF1b in 2018, a sliding plate fixed on one end of the structure defines the position of the detector with respect to the analyzer, see [Fig. 3.22](#). It is chosen such that the transmitted and reflected beams are well separated in space but still inside the detector's pixel array when they reach it.

3 .3.10 Data acquisition system

The data acquisition (DAQ) system changed between 2018 and 2020 because of the limitations of the initial one. Both are presented hereafter.

The first edition, used at BOA and PF1b from 2017 to 2018, is based on several Labview programs and a dedicated software for the Cascade detector. It generates several ASCII output files:

- "****.txt" : setting file for the Cascade software. It records the configuration for the Cascade software, including a timestamp and the structure of the measurement file. The name of the output file can be changed in the software.
- "****.tof" / "****.pad" : measurement file for the Cascade software. It records the neutron counts in the pixels for each time-of-flight bin. Its structure is defined in the setting file according to the measurement type (PAD/TOF). The name of the output file is the same as the setting file, the extension changes to ".tof" or ".pad" according to the measurement type.
- "LogFile-****.dat" : slow control data log from the Labview program. It contains the value of the fluxgates, the frequency, amplitude, and phase of the spin flippers' signal, and the computer time, recorded with a 1 Hz frequency. This file is appended on until the name is changed. Thus, it was not linked to the measurements.
- "Ramsey-****.dat" : scan file from the Labview program. It records the time at the beginning of a measurement, and the average over the measurement of each piece of information from the slow control data file. The version of 2018 also records the information from the monitor detector at BOA, PSI. The first part of the output file name can be changed in the software. This file is created only when an automatic scan over a parameter was performed, e.g. the phase between the spin flippers during a phase scan.

- "*****.dat" : high voltage data from the Labview program. It records the information from the high voltage power supply. This was only developed for the beamtime at BOA in 2018. The name was completely defined by the user with the exception of the extension.

However, this system was not optimal because of several reasons: bugs in the Cascade software that causes shutdowns of the program, different time stamps for the softwares, ASCII files etc. The Labview programs and the detector software were installed on different computers. Because of unresolved bugs in the Cascade software, the computer running this software could not be linked to the internet and thus was not synchronized with the Labview computer. The resulting time difference between the files could be solved externally by comparing the timestamps in the Labview scan file and the Cascade setting file when such files existed.³

For the beamtime at PF1b in 2020, the DAQ system was completely redesigned using the MIDAS framework [MID]. It is a modular DAQ system divided in front ends (FE):

- The mtsc FE controls and monitors the electric field power supply, the detector high voltage power supply, the magnetic field power supplies, the vacuum gauges, the chopper, the leakage current monitor, and the thermocouples.
- The detector FE controls the settings of the detector. It allows to define all the parameters of the detector for a measurement.
- The spin flipper FE controls and monitors the waveform generators that send the signal to the audio amplifier and spin flippers. This includes the sinusoidal function but also its envelope. The front end monitors the signal via the picoscope and records the measured phase of the spin flippers.
- The magnetic field FE includes the reading of the fluxgates and stabilization of the magnetic field in association with the mtsc FE.
- The online display plots the 2D image of the neutron counts in the detector or the time-of-flight measurement. This was not heavily used, instead, most of the analysis done during beamtime was performed on the output files themselves.
- The online analyzer records the settings and data of the measurement in a ROOT file. It is not working on the MIDAS framework, but on an extension of the data processing, ROOTANA [RTA]. This analyzer also checks the

³Some of the scans were done manually at BOA in 2017, therefore, the time information is lost and the slow control data files could not be used for the data analysis.

conformity of the data during each measurement, for example, if the detector is not counting any neutrons, an alarm is triggered.

This DAQ system is run over four computers. "beamedm01" runs the midas framework, "beamedm02" runs the spin flipper system, "beamedm03" runs the slow control and chopper system, and "beamedm04" runs the magnetic field stabilization and the online analyzer. All these computers are synchronized and communicate with each other with the master computer being "beamedm01".

Chapter 4

Analysis principle of the phase scan measurements

This chapter develops the analysis procedure used on the data collected during beamtimes, see [Chapter 3](#), from the spin flip probability of a phase scan defined in [Section 2.3](#). Two concrete examples are detailed, one based on a magnetic field effect, the second one on the $v \times E$ effect.

As a note for the reader that is already familiar with Ramsey measurement and analysis outside this thesis, the notations used do not follow the usual convention. As most of the measurements are phase scans, the frequency of the sinusoidal signal sent to the spin flipper ω_{RF} is rarely scanned. At the beginning of each beamtime, a Ramsey measurement is performed to fix the value of this frequency so that it matches the neutron precession frequency in a reference magnetic field B_0 such that $\omega_{RF} = \omega_0 = -\gamma_n B_0$. We define $\Delta = \omega_{RF} + \gamma B$ as the off-resonance value at the spin flipper positions, and by $\Delta^* = \omega_{RF} + \gamma(B + B_{v \times E} + B_{EDM})$ the off-resonance value inside the free precession region. The difference is important as for a phase scan it is assumed that $\Delta = 0$. On the contrary, Δ^* is the signal that we want to measure. All the symbols are summarized in [Table 4.1](#).

4.1 Determination of the off-resonance value Δ^*

From section, [Eq. \(2.30\)](#) gives the probability P of a π spin flip for a phase scan measurement. An equivalent of this probability is the number of neutrons in the flipped spin state,

$$\begin{aligned} N\downarrow &= N \times P = N \sin^2(\omega_1 \tau) \cos^2 \left(\frac{\theta_{RF} + T\Delta^*}{2} \right) \\ &= \frac{N \sin^2(\omega_1 \tau)}{2} [1 + \cos(\theta_{RF} + \Delta^* T)], \end{aligned} \tag{4.1}$$

where N is the total number of neutrons, θ_{RF} is the phase between the two oscillating fields, Δ^* is the off-resonance value inside the free precession region, and T is the interaction time. One can write a similar equation for the number of neutron with the spin up,

$$\begin{aligned} N_{\uparrow} &= N \times (1 - P) = N \left[1 - \sin^2(\omega_1 \tau) \cos^2 \left(\frac{\theta_{RF} + \Delta^* T}{2} \right) \right] \\ &= N \left(1 - \frac{\sin^2(\omega_1 \tau)}{2} [1 + \cos(\theta_{RF} + \Delta^* T)] \right), \end{aligned} \quad (4.2)$$

To be independent of the fluctuation of the total number of neutrons, one can look at the asymmetry, defined by

$$A = \frac{N_{\downarrow} - N_{\uparrow}}{N_{\uparrow} + N_{\downarrow}} = \cos(\theta_{RF} + \Delta^* T). \quad (4.3)$$

The statistical error on the asymmetry is then linked to N_{\downarrow} and N_{\uparrow} ,

$$\sigma(A) = \sqrt{\frac{4N_{\downarrow}N_{\uparrow}}{(N_{\uparrow} + N_{\downarrow})^3}}. \quad (4.4)$$

The asymmetry data A vs. θ_{RF} , can then be fitted by a usual cosine function,

$$A = A_0 \cos(\theta_{RF} + \varphi) + A_1, \quad (4.5)$$

where A_0 , A_1 , and φ are free parameters of the fit. In the case were the neutrons are not counted with the same efficiency for N_{\downarrow} and N_{\uparrow} , the formalism of Eq. (4.5) can be extended with an additional parameter, A_2 the distortion factor, in the fit function:

$$A = \frac{A_0 \cos(\theta_{RF} + \varphi) + A_1}{1 + A_2 \cos(\theta_{RF} + \varphi)}. \quad (4.6)$$

The parameters of the fit yield the following information:

- A_0 , the amplitude of the cosine. Its value is one in ideal condition, and differs from one if:
 - the amplitude of the flipping pulses do not match their duration $\omega_1 \tau \neq \pi/2$,
 - the off-resonance value at the spin flippers position is not zero: $\Delta \neq 0$, see Eq. (2.29) and/or appendix A,
 - the beam is not fully polarized, see derivation in appendix B in [Pie09],
 - the neutron background is not negligible. Indeed, if there is a constant additional term in Eqs. (4.1) and (4.2), $N_{\downarrow} - N_{\uparrow}$ could never be equal to $N_{\downarrow} + N_{\uparrow}$.

- A_1 , the offset of the cosine, represents the number of neutrons that cannot be flipped properly or analyzed properly. Its value is zero in ideal condition. It differs from zero if the background is higher in one spin state than the other.
- A_2 , the distortion factor, represents the difference between the maximum of N_\downarrow and N_\uparrow . Its ideal value is zero.
- φ , the phase of the cosine from Eq. (4.5) can be identified to $T\Delta^*$ from Eq. (4.3). It will be referred as the neutron phase.

4.2 Interpretation of the off-resonance value Δ^*

The off-resonance value can be caused by an interaction of a non-zero EDM with an electric field, the magnetic dipole moment with a magnetic or pseudo-magnetic field, e.g. Eq. (2.17), or a combination of the two effects Eq. (2.16).

For a non zero electric dipole moment in an electric field of magnitude E and a magnetic field of magnitude $B_0 + \delta B_0$, the neutron phase follows:

$$\varphi = \Delta^* T = \omega_0 T + \left(\gamma_n B - \frac{2d_n}{\hbar} E \right) T = \gamma_n \delta B_0 T - \frac{2d_n}{\hbar} ET. \quad (4.7)$$

With the BeamEDM apparatus, the neutrons from the top and bottom beams see an opposite electric field but the same magnetic field, if we consider no gradient. The neutron phase from the top and bottom beams follow:

$$\begin{aligned} \varphi_t &= \Delta^* T = \gamma_n \delta B_0 T - \frac{2d_n}{\hbar} ET, \\ \varphi_b &= \Delta^* T = \gamma_n \delta B_0 T + \frac{2d_n}{\hbar} ET. \end{aligned} \quad (4.8)$$

Computing the sum and difference of the neutron phase yields:

$$\begin{aligned} \Phi_+ &= \varphi_t + \varphi_b = 2\gamma_n \delta B_0 T, \\ \Phi_- &= \varphi_t - \varphi_b = -\frac{4d_n}{\hbar} ET. \end{aligned} \quad (4.9)$$

When considering an additional gradient field $\pm B_g/2$ at the top and bottom beam, Φ_+ is unchanged but Φ_- becomes:

$$\Phi_- = \gamma_n B_g T - \frac{4d_n}{\hbar} ET. \quad (4.10)$$

To distinguish a gradient field from an electric dipole moment, the electric field is reversed regularly. A drift of the gradient field correlated with the electric field

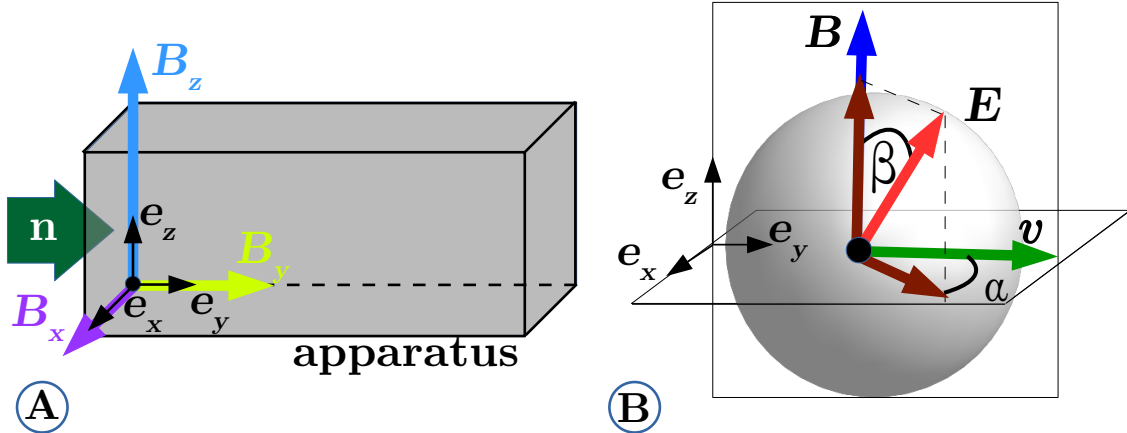


Fig. 4.1: A) Representation of the magnetic field components where the reference is the apparatus. The direction for the longitudinal axis is defined along the neutron beam and the vertical axis defined in opposite direction with respects to gravity. B) Representation of the field configuration on a Bloch sphere for the $v \times E$ calculation, where the blue arrow is the magnetic field, the red arrow is the electric field which makes an angle β with the magnetic field and an angle α with the neutron velocity represented by a green arrow.

reversal could not be resolved from an EDM signal. This is one of the systematic effects of BeamEDM.

For a magnetic offset in the precession region, the neutron phase follows

$$\varphi = \Delta^* T = \omega_0 T + \gamma_n B T = \omega_0 T \pm \gamma_n T \sqrt{B_z^2 + B_y^2 + B_x^2} \quad (4.11)$$

where the \pm sign is the sign of the magnetic field magnitude, B is the magnitude of the magnetic field, B_z is vertical component, B_x transversal component, and B_y is the longitudinal component as presented in Fig. 4.1A. With the assumption that the transversal and longitudinal components are small compared to the vertical component, $B_z \gg B_y + B_x$, one can perform a Taylor expansion of Eq. (4.11) into:

$$\varphi = \Delta^* T = \omega_0 T + \gamma_n T \left[B_z + \frac{B_x^2 + B_y^2}{2B_z} + O\left(\frac{(B_x^2 + B_y^2)^2}{B_z^3}\right) \right], \quad (4.12)$$

which is linear with B_z when $B_x = B_y = 0$ and quadratic in B_x and B_y in first order.

For the $v \times E$ effect, we assume that the magnetic field is along the vertical axis only, the neutron velocity along the longitudinal axis, i.e. perpendicular to the magnetic field and the electric field has non-zero components along all axis as presented in Fig. 4.1B. One can define the angle that the electric and magnetic field form by β and the angle between the projection of the electric field on the horizontal

plane by α . With these notations, the vertical component of the pseudo-magnetic field is given by

$$B_{v \times E, z} = \mathbf{B}_{v \times E} \cdot \mathbf{e}_z = \frac{E \sin(\beta) v \sin(\alpha)}{c^2}, \quad (4.13)$$

and the transversal component is given by

$$B_{v \times E, x} = \mathbf{B}_{v \times E} \cdot \mathbf{e}_x = -\frac{E \cos(\beta) v}{c^2}. \quad (4.14)$$

There is no longitudinal component as it is the direction of the neutron beam. With these contributions, the phase becomes

$$\varphi = \omega_{RF} T \pm \gamma_n T \sqrt{(B + B_{v \times E, z})^2 + (B_{v \times E, x})^2}, \quad (4.15)$$

where the sign is the sign of B . Assuming $B + B_{v \times E, z} \gg B_{v \times E, x}$, and $\omega_{RF} + \gamma_n B = 0$, one can Taylor expand this equation into:

$$\begin{aligned} \varphi &= \omega_{RF} T + \gamma_n T (B + B_{v \times E, z}) \left[1 + \frac{1}{2} \left(\frac{B_{v \times E, x}}{B + B_{v \times E, z}} \right)^2 + O \left(\frac{B_{v \times E, x}}{B + B_{v \times E, z}} \right)^4 \right] \\ &= \gamma_n T B_{v \times E, z} + \gamma_n T \frac{B_{v \times E, x}^2}{2B + 2B_{v \times E, z}} + O \left(\frac{B_{v \times E, x}^4}{(B + B_{v \times E, z})^3} \right) \\ &\approx \gamma_n \frac{E \sin(\beta) \ell \sin(\alpha)}{c^2}, \end{aligned} \quad (4.16)$$

where $\ell = v \times T$ is the length corresponding T , for a velocity, v . The $v \times E$ effect was the limiting factor for the early cold neutron beam experiments as it is linear with electric field in first order, i.e., could mimic an EDM. However, unlike the EDM, its phase contribution is independent of the interaction time in first order.

By doing a time of flight measurement, the BeamEDM experiment can distinguish an EDM signal from a first order $v \times E$ effect. The second order effect is independent of the sign of the electric field. It is not a systematic effect for an EDM measurement as the BeamEDM experiment uses two beams with opposite electric field. Looking at the difference of the two beams suppress this second order $v \times E$ effect if the two electric field have the same magnitude and the effect of an inhomogeneous magnetic field. This phase difference Φ_- is sensitive to magnetic field gradient effect.

Symbol	Description
B_0	The reference or resonance field.
B	The norm of the magnetic field which does not include pseudo-magnetic effects.
δB	The deviation from the resonance field.
δB_0	The deviation from the resonance field common to the top and bottom beam.
B_g	The vertical field gradient over the distance of the two beams
B_G	The vertical field gradient measured by fluxgates over their vertical separation
$B_{v \times E}$	The pseudo magnetic field raising from the $v \times E$ effect.
B_{EDM}	The effect of the electric dipole moment on the neutron spin written as a magnetic field.
ω_0	The Larmor frequency corresponding to the reference field. For phase scan measurements, $\omega_{RF} = \omega_0$.
ω_{RF}	The frequency of the sinusoidal function sent to the spin flippers.
Δ	The off-resonance value at the spin flipper positions. It follows $\Delta = \omega_{RF} - \gamma B$ and it is usually assumed to be zero.
Δ^*	The off-resonance value inside the free precession region. It follows $\Delta = \omega_{RF} - \omega_n = \omega_{RF} - \gamma(B + B_{v \times E} + B_{EDM})$. It is the signal we want to measure.
ω_n	The neutron precession frequency. It includes the effect from the pseudo-magnetic fields.
N	Total number of neutrons.
N_\uparrow	Number of neutrons in the "up" state.
N_\downarrow	Number of neutrons in the "down" state.
A	The asymmetry defined in Eq. (4.3) .
θ_{RF}	The phase between the two oscillating fields.
ω_1	The amplitude of the linearly oscillating field.
τ	The duration of the spin flip.
T	The interaction time.
A_0	The amplitude of the fit functions defined in Eq. (4.5) and Eq. (4.6) .
A_1	The offset of the fit functions defined in Eq. (4.5) and Eq. (4.6) .
A_2	The distortion parameter of the fit function defined in Eq. (4.6) .
φ	The phase of the fit functions defined in Eq. (4.5) and Eq. (4.6) .
φ_t	The neutron phase of the top beam
φ_b	The neutron phase of the bottom beam
Φ_+	The sum of the neutron phase of the top and bottom beams: $\Phi_+ = \varphi_t + \varphi_b$
Φ_-	The difference of the neutron phase between the top and bottom beams: $\Phi_- = \varphi_t - \varphi_b$.
e_x	The vector that defines the x-direction also called transversal direction according the apparatus.
e_y	The vector that defines the y-direction also called longitudinal direction according the apparatus.
e_z	The vector that defines the z-direction also called vertical direction according the apparatus.
β	The angle between the electric and magnetic field.
α	The angle between the projection of the electric field in the xy-plane and the neutron beam direction.

Table 4.1: Description of the symbols and notation used for the analysis.

Chapter 5

Beamtimes

This chapter describes the four beamtimes with the Ramsey apparatus described in [Chapter 3](#) and the data analysis of the measurements, focusing on the magnetic field characterization with neutrons. The first beamtime was a proof-of-principle that a Ramsey technique and phase scan could be performed with the apparatus and that its result was reproducing the magnetic field condition of the experiment. The second beamtime made use of the monochromatic beam available at the Institute Laue-Langevin to start the investigation of a wavelength-dependent signal to improve the flipping process of a Ramsey technique or phase scan. The third beamtime continued this work with a pulsed white beam at the Paul Scherrer Institute and started the premise of the $v \times E$ characterization of the apparatus. The fourth and last beamtime concluded the investigation on the flipping process and continued the characterization of the $v \times E$. The first EDM measurement was performed during this beamtime using two measurement procedures to demonstrate the sensitivity of the apparatus and its potential improvement. A summary of these four beamtimes is recorded in [Table 3.1](#). Additionally, an auxiliary measurement was performed at the Narziss beamline at the Paul Scherrer Institute to characterize the reflectivity of the electrodes.

5.1 Beamtime 1: PSI September 2017

A beamtime with the BeamEDM Ramsey apparatus was performed at BOA, PSI in 2017 from 28/08 to 17/09. As it was the first one, the goals were:

- to perform a Ramsey technique and define the resonance frequency of the apparatus for a reference magnetic field B_0 ,
- to test the linear time-of-flight behavior with a phase scan,

- the characterization of the magnetic field sensed by the neutrons and its discrepancy from the set field. [Table 5.1](#) summarizes the characteristics of the measurements performed for this characterization.

Field	B_z	B_G	B_y	B_x
Ref. value (μT)	-125	-5.5	0	0
Number of configuration	3	7	8	8
Beam type	pulsed	continuous	continuous	continuous
Graphs	Fig. 5.6	Fig. 5.7	Fig. 5.8	Fig. 5.8

Table 5 .1: *Characteristics of the measurement performed at BOA in 2017 for the characterization of the field sensed by the neutrons. It records, the fields that are scanned, the reference value for this field, how many values are scanned (num. configuration), type of beam (if the measurement was performed with a pulsed white beam or a continuous white beam, and the reference to the graphs where the results are displayed.*

A picture of the apparatus is shown in [Fig. 5.1](#). The beams were defined in shape and divergence by four apertures whose characteristics are summarized in [Table 5.2](#). The apertures A3 and A4 were cutting the beam into two smaller ones, called top and bottom beams, in order to do relative measurements. The time-of-flight measurement was performed by a single-slit chopper-disk with a rotational frequency of 10 Hz, placed at a distance $d_{CD} = 6.04\text{ m}$ to the detector for the measurement in [Section 5.1.4](#). All other measurements have been done with a continuous white beam. The upstream spin flipper (SF1) was placed in the middle of the first of the four cubes of the structure. The distance from the chopper to the center of SF1 is $d_{CSF} = 1.24\text{ m}$. The downstream spin flipper (SF2) was placed in the center of the last cube of the structure, i.e. at a 3 m distance center to center from SF1, $d_{SF} = 3\text{ m}$. The signal sent to the spin flippers was a sinusoidal signal to set the linearly oscillating magnetic field in the direction longitudinal to the beam. FLC3-70 fluxgates were placed on the top and the bottom of each spin flipper, monitored the vertical field difference $B_G = -5.5\text{ }\mu\text{T}$ over a vertical separation of the fluxgates $d_{FG} \approx 49\text{ cm}$. The gradient could not be stabilized at zero because of a saturation of the power-supply for the gradient coil. An additional fluxgate, aligned with fluxgates on the top of the spin flippers, was mounted in the middle of the structure. It was used to stabilize the magnetic field at $B_z = -80\text{ }\mu\text{T}$ for the vertical component and $B_x = B_y = 0\text{ }\mu\text{T}$ for the longitudinal and transversal components. All fluxgates were centered in the traversal axis with respect to the cubes, and they were placed at a distance of 0.76 m, 1.90 m and 4.18 m from A3. The vacuum pipe was placed in between the spin flippers in order to decrease the neutron scattering in air. It was approximately 2.4 m long and did not contain any electrodes yet. Therefore, there was no electric field

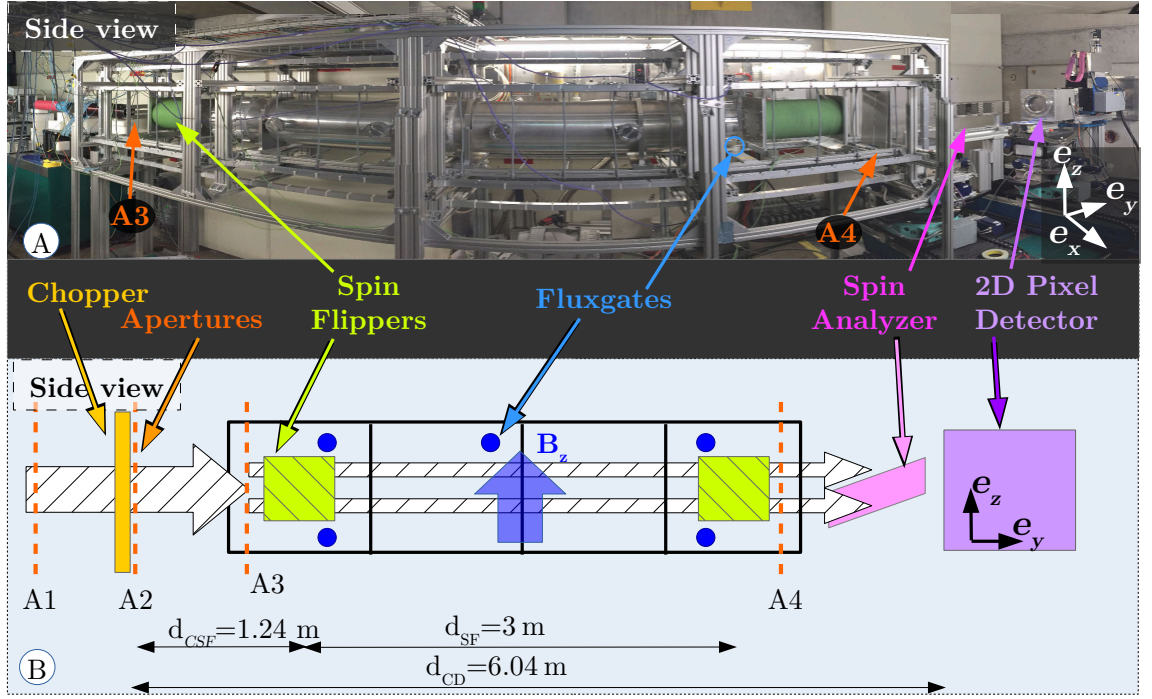


Fig. 5.1: A) Picture of the BeamEDM apparatus at BOA in 2017 with indications for the apertures A3, A4 and one visible fluxgate. B) Sketch of the apparatus with the $(1 \times 1 \times 1) \text{ m}^3$ cubes of the structure (black rectangles), the different apertures (orange dashed lines), the fluxgates (full blue circle), the vertical field (thick blue arrow), the chopper (yellow box), the spin flippers (slashed green boxes), the analyzer (pink parallelogram) and the detector (purple cube). The beams go from left to right and are represented by white and black arrows.

in the free precession region defined by the spin flippers. Downstream of the spin flippers, the spin analyzer was a single mirror from SwissNeutronics in a magnetic field produced by permanent magnets. It reflected horizontally the neutrons into the detector, see Fig. 5.3A.

5.1.1 Characterization of the neutron spots in the detector

A time-of-flight measurement was performed with the adiabatic spin flipper (AFP) off and on -without any additional spin flips from SF1 or SF2. The AFP changes the polarization of the neutron beam in an upstream location from the apparatus. This is done to define the contours of the beam spots and measure their spectrum. We can define for this beamtime that AFP=on leads to reflection of the beam. Inversely, AFP=off leads to a transmission of the beam by the spin analyzer mirror. This is represented by the ideal case in Fig. 5.2.

First, the spots for the different spin states of each beam are defined by a rectangular shape shown in Fig. 5.3A&B and summarized in Table 5.3. It is interesting to note that the background level in the reflected spots in Fig. 5.3A

Label	A1	A2	A3	A4
Type	I	I	II	II
Opening width (mm)	5	5	≈ 70	3-4
Opening height (mm)	80	60	2×15	2×15
Separation height (mm)			15	15
Distance to chopper (m)	-2.14	0.27	0.76	4.48

Table 5 .2: Characteristics of the apertures at BOA in 2017 defined by their type, see [Section 3 .3 .3](#), their opening width and height, the height of the absorbing plates that cuts the beam in two, and their distance to the chopper.

Spot	Top Trans.	Top Refl.	Bottom Trans.	Bottom Refl.
Bottom left corner	(8;10)	(12;10)	(8;3)	(12;3)
Top right corner	(9;13)	(13;13)	(9;6)	(13;6)

Table 5 .3: Definition of transmitted (Trans.) and reflected (Refl.) spots for the top and bottom beams. The squares are defined by the coordinate of their bottom-left and top-right corners in units of pixels.

and in the transmitted spot in [Fig. 5 .3B](#) is not negligible. This can be due to the polarization of the beam, the AFP efficiency, the efficiency of the spin analyzer at high and low wavelengths, and potentially the cross contamination between the spots. The effects are presented in [Fig. 5 .2](#) and detailed hereafter. To explain these causes, one needs to distinguish between the reflected or transmitted beams and their respective spots. The beams are composed of the neutrons that underwent reflection or transmission on the spin analyzer mirror. They are represented by the gray spots on the detector pixels in [Fig. 5 .2](#). The spots are the neutrons that are counted in a defined region of the detector. They are represented by blue rectangles in [Fig. 5 .2](#).

The cross contamination is defined by the overlay of the two beams inside the definition of a spot. The example presented in [Fig. 5 .2](#) corresponds to a contamination of the transmitted spot by the reflected beam. In that case, when all the neutrons undergo a reflection, some of them are still counted in the transmitted beam, thus it is visible in the neutron spectrum of the spots. When all the neutrons are transmitted, the spectrum is identical to the ideal case as there is no contamination of the reflected spot by the transmitted beam. To reduce the cross contamination, there is always at least one pixel row and column that separates the contour of the spots. The counts in [Fig. 5 .3C](#) could be interpreted as a cross-contamination of less than 10 %, but this can also be due to other effects like the AFP efficiency, explained hereafter.

The depolarization of the beam corresponds to the case where part of the beam has the same probability of being reflected or transmitted. Thus half of these

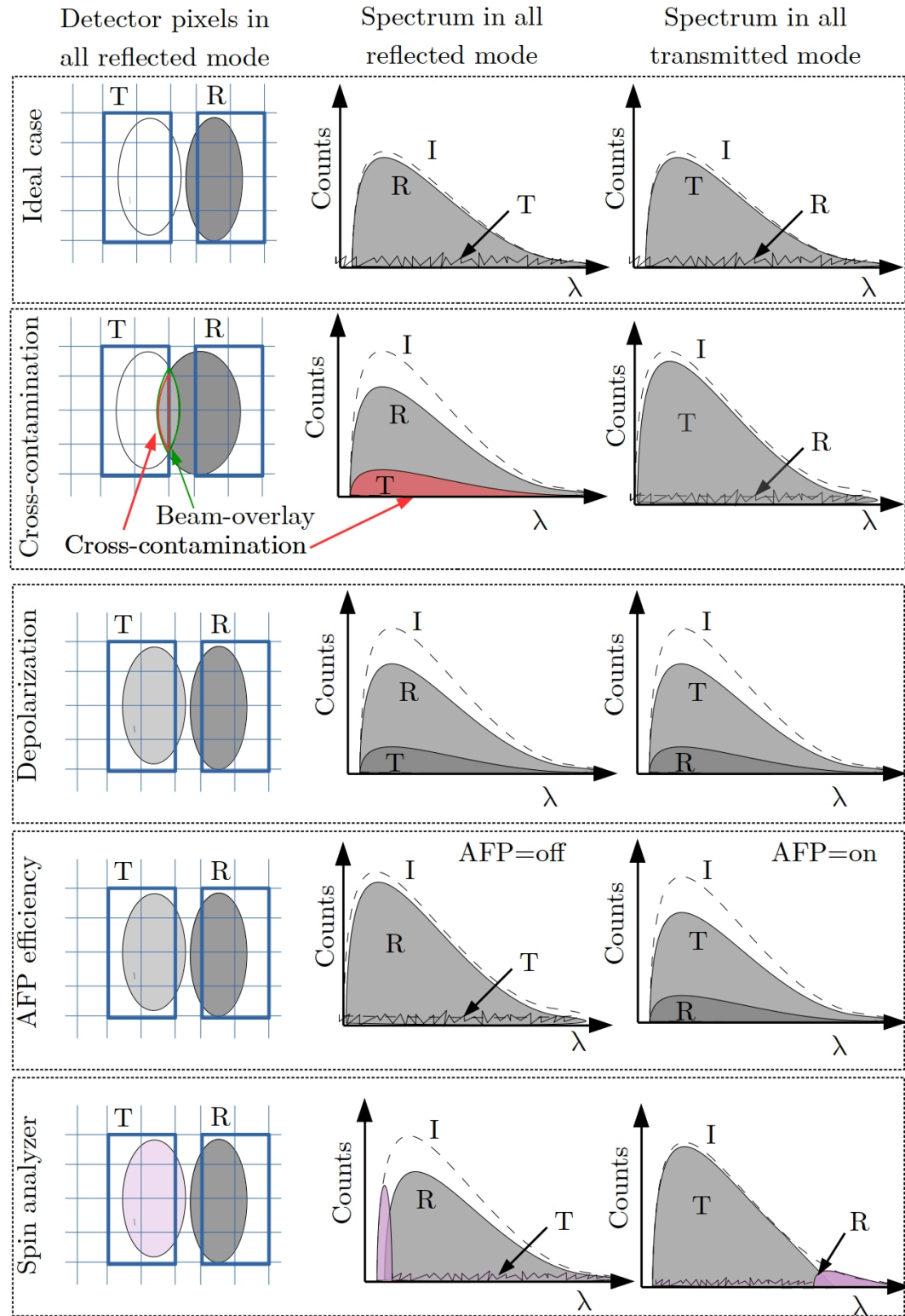


Fig. 5.2: Representation of the effect of the cross-contamination, depolarization, spin flipper efficiency on the spectrum. The "I" stands for incident beam, it represents the spectrum over the entire detector. The "R" stands for reflected and "T" for transmitted. The associated spectra are defined by the definition of the respective spots from the detector pixels.

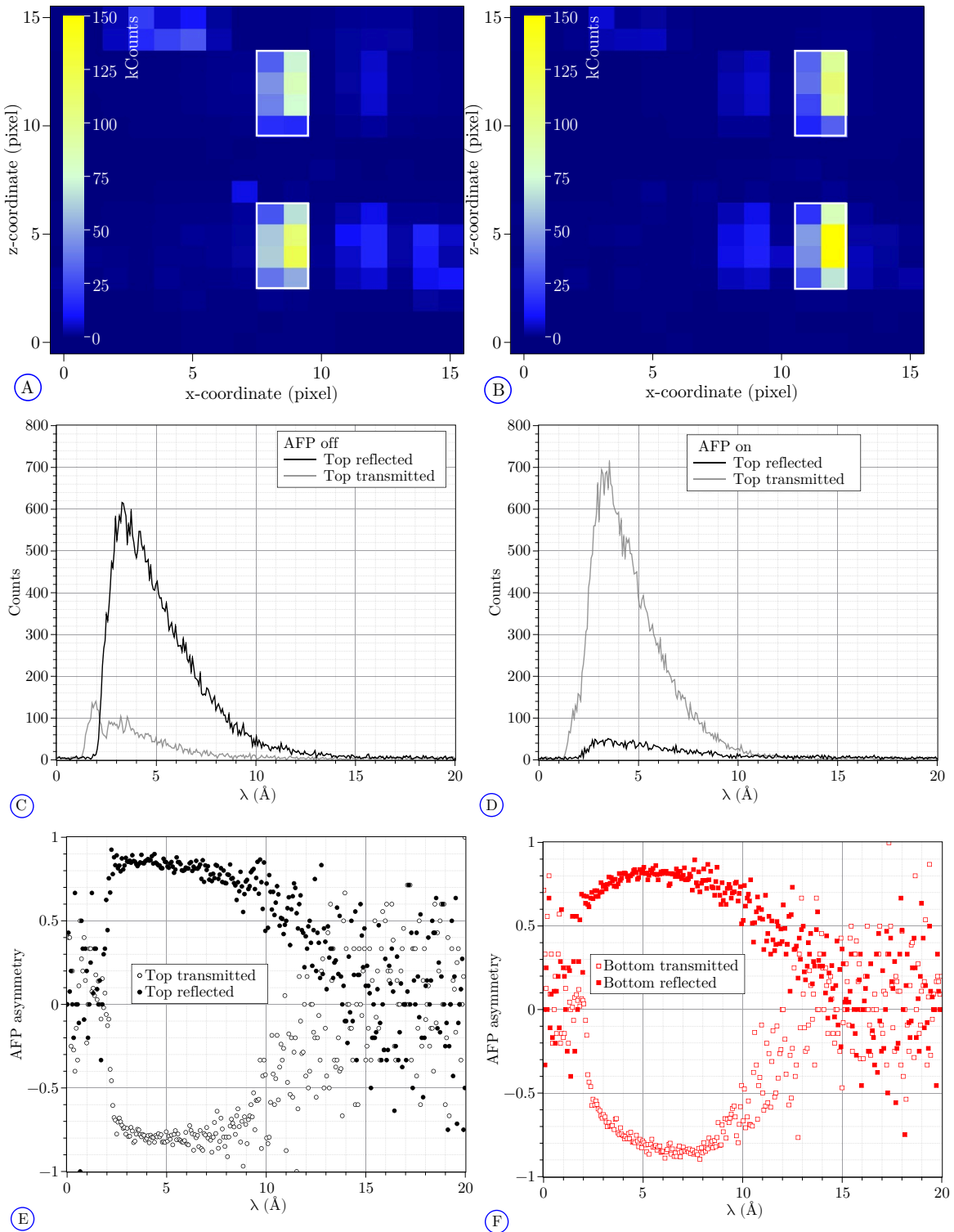


Fig. 5.3: A and B) Neutron counts in the detector pixels integrated over all wavelengths with the adiabatic spin flipper off and on respectively. C and D) Number of count integrated over the top-reflected and top-transmitted spots versus the neutron wavelength for the adiabatic spin flipper (AFP) off and on respectively. E and F) AFP asymmetry for all spots versus the neutron wavelength for the top and bottom beams respectively.

neutrons will be transmitted by the mirror and the other half will be reflected. This is independent of the initial polarization state. The counts in [Fig. 5.3C](#) could be interpreted as a minimum polarization of the beam of about 90 % however the loss in polarization cannot be distinguished from the other effects.

The AFP efficiency corresponds to the number of neutrons whose spin is not flipped when the AFP is on. As we defined that AFP=on corresponds to a reflection mode, the neutrons whose spin is not flipped are counted in the transmitted spot. When the AFP=off, its efficiency does not play a role and the spectrum corresponds to one of the ideal case. From the spectra, it is impossible to distinguish a cross contamination from the AFP efficiency in [Fig. 5.2](#), however, AFP usually have an efficiency better than 99 %.

The efficiency of the spin analyzer is dependent on the wavelength. At low wavelengths, the energy of the neutrons is higher than the equivalent Fermi potential of the mirror at a given angle for all spin states, see [Fig. 3.19](#), thus, the neutrons are always transmitted. Inversely, at high wavelengths, the energy of the neutrons is lower than the equivalent Fermi potential for all spin states, thus, the neutrons are always reflected. This is visible in [Fig. 5.3C](#) at $\lambda < 1.8 \text{ \AA}$ where the number of counts in the transmitted spot is the same regardless of the polarization and the reflected spot has a zero count. The effect of the spin analyzer efficiency at high wavelengths is not visible due to low contrast.

For simplification all these effects are grouped under the name of "overall spin analyzer" efficiency which represents the efficiency of the apparatus to determine the spin state of the neutrons. For a quantitative analysis, the so called "AFP asymmetry" is calculated by:

$$A_{\text{AFP}} = \frac{N_0 - N_1}{N_0 + N_1} \quad (5.1)$$

for each spot where N_0 is the number of counts in the spot when the adiabatic spin flipper is off and N_1 when the adiabatic spin flipper is on. The result of these calculations is shown in [Fig. 5.3D](#) as a function of the wavelength and one can approximate the working range for the overall spin analyzer by the range where $|A_{\text{AFP}}| > 0.6$, i.e. $\lambda \in [2.2; 10] \text{ \AA}$.

In addition, in [Fig. 5.3A&B](#), a few pixels outside the spots have a non-negligible number of count. One could find several reasons for this effect but as it was the first use of the detector, this was not noticed during beamtime and these pixels were not investigated further.

5.1.2 Measurement of the resonance frequency

Performing a Rabi frequency scan with each of the spin flippers with a white continuous beam, the resonance frequencies could be measured to be $\approx 4.4 \text{ kHz}$ and

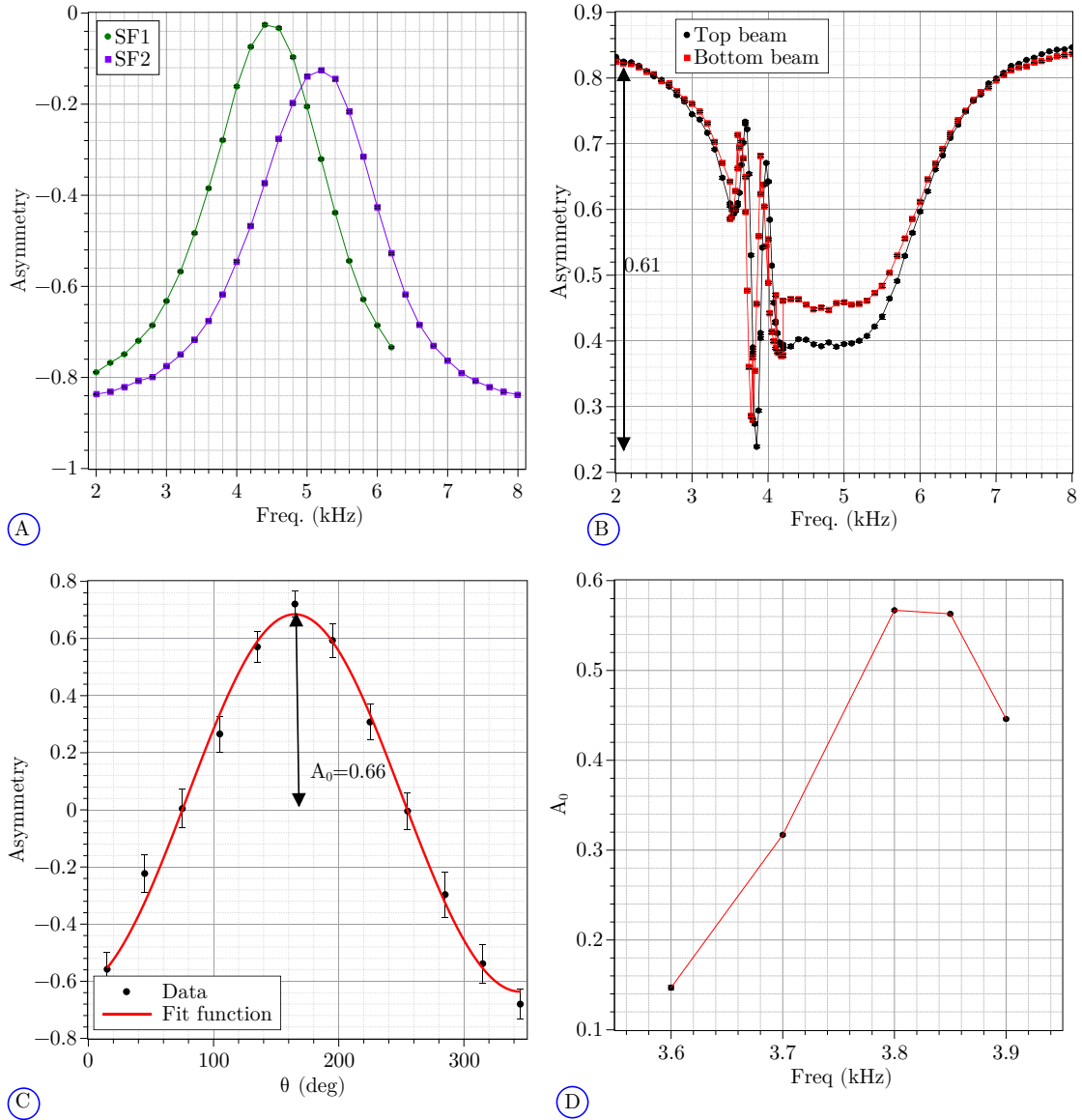


Fig. 5.4: A) Asymmetry vs. set frequency of the spin flipper for a Rabi technique with a continuous white beam analyzed for the top beam. B) Asymmetry vs. set frequency of the spin flippers for a Ramsey technique with a continuous white beam. C) Asymmetry vs. phase between the spin flippers for a phase scan technique on resonance $f_0 = 3.85$ kHz with a pulsed white beam, see Section 5.1.3, analyzed for $\lambda = 4.6\text{\AA}$. This is fitted by Eq. (4.6). D) Amplitude of the cosine fit for the phase scan measurement performed at different frequencies with a continuous white beam. The data are from the top beam.

≈ 5.2 kHz for the SF1 and SF2 respectively, see Fig. 5.4A. The difference between the two frequencies is due to the inhomogeneity of the magnetic field: $B_z = -134$ μ T and $B_z = -150$ μ T at the SF1 and SF2, and only $B_z = -80$ μ T at the position of the middle fluxgates.¹

A Ramsey scan, displayed in Fig. 5.4B, was performed with continuous beam to determine the optimal frequency of the apparatus. The frequency was scanned from 2000 Hz to 8000 Hz in steps of 100 Hz. The value of the asymmetry, Eq. (4.3), at low and high frequencies differs from the expected value of 1 due to the overall spin analyzer efficiency.

The "peak-to-peak" amplitude of the pattern is 0.61, instead of 2 in the ideal case, due to two reasons.

Firstly, the measurement was performed with a continuous white beam and as the amplitude of the spin flipper signal and the spin analyzer are not optimized for all velocities the amplitude decreases. The overall spin analyzer efficiency is already discussed previously and the wavelength dependency is displayed in Fig. 5.3D. The flipping process is developed in Section 2.3. In comparison, analyzing a phase scan performed with a pulsed white beam gives a peak-to-peak amplitude of 1.32 for $\lambda = 4.6$ \AA , shown in Fig. 5.4C.

Secondly the inhomogeneity of the magnetic field at the spin flippers positions makes it impossible to work with the resonance frequency of both spin flippers, hence, the flipping process is not optimized. The interference pattern around 3.8 kHz defines the resonance frequency of the apparatus. It is interesting to note that the resonance of the apparatus is not in between the resonance frequency of the individual spin flippers. The reason for this is unknown.

In addition, to confirm the value of the resonance frequency of the apparatus, several phase scans were performed at different frequencies between 3.60 kHz and 4.00 kHz with a continuous white beam. The size of the frequency steps was adapted during the measurement from 100 Hz to 50 Hz. The measurement confirmed the previously stated value of $f_0 = (3.85 \pm 0.03)$ kHz where the error is estimated from the lowest step size.

5.1.3 Working range of the apparatus in wavelength

To define the working range of the Ramsey apparatus, we analyze a phase scan performed with a pulsed white beam, ideally on resonance. This is an a posteriori determination and a different method was used during beamtime [Sta19]. The data analysis principle is described in Chapter 4: the asymmetry is computed with Eq. (4.3) from the previously defined spots as a function of the phase between the

¹The value reported at SF1 and SF2 are the average of the top and bottom fluxgates value.

two spin flippers for each time bin. This is then fitted with a cosine of amplitude A_0 , offset A_1 , distortion parameter A_2 , and phase φ , defined by [Eq. \(4.6\)](#). An example of a cosine fit is shown in [Fig. 5.4C](#). The determination of the working range is done by the interpretation of the evolution of the fit parameters (except A_2 which is a corrective factor) over the neutron spectrum, shown in [Fig. 5.5](#) for the top beam.

- From 0 to 1.1 Å: the signal is mostly coming from neutron background $A_0 = A_1 = 0$. The statistics is low which is why the χ^2/NDF is close to 0 and the error on the parameters is high.
- From 1.1 to 1.6 Å: A_1 follows the spectrum curve as the ratio signal over noise increases. Indeed, at low wavelength the spin analyzer cannot distinguish the spin states and all the neutrons are transmitted, therefore, $A_1 \rightarrow 1$ and $A_0 = 0$.
- From 1.6 to 2.3 Å: the spin analyzer is working at a better efficiency. It is visible in the decrease of A_1 .² This is combined with an increase of the spin flip efficiency from around 2 Å, visible in the increase of A_0 .
- From 2.3 to 7.25 Å: This is the working range of the Ramsey apparatus, it is defined by the end of the peak at 2.3 Å and inflection point at 7 Å in A_1 . It is extended to 7.25 Å where $A_1 = 0$. In this range, the visibility of the signal (i.e. A_0) is in an acceptable range, $A_0 > 0.3$, with a maximum of 0.7 at 4 Å which, therefore, corresponds to the optimal wavelength for the fixed amplitude i.e. following $\omega_1\tau = \pi/2$. The offset A_1 has a linear behavior in first approximation with $A_1 = 0$ at 4 Å, confirming the idea of a maximal spin flip probability at that wavelength. In this region the χ^2/NDF of the cosine fit is centered around one.
- From 7.25 to the end, the spin flipper efficiency decreases, $A_1 \rightarrow -1$ and $A_0 \rightarrow 0$, and the statistics diminishes.

From [Eq. \(4.11\)](#), one can estimate the behavior of the neutron phase for the top and bottom beams as a function of the different parameters of influence:

$$\begin{aligned}\varphi_t(\delta B_0, B_g, T) &= \omega_{RF} + \gamma_n B T = \gamma_n (B_g/2 + \delta B_0) T, \\ \varphi_b(\delta B_0, B_g, T) &= \omega_{RF} + \gamma_n B T = \gamma_n (-B_g/2 + \delta B_0) T,\end{aligned}\tag{5.2}$$

using the notation described in [Table 4.1](#), where T is the interaction time, B is the magnitude of the magnetic field such that $B = B_0 + \delta B_0 \pm B_g/2$ where the sign is positive for the top beam and negative for the bottom beam. δB_0 is the deviation

²As a reminder, the value of A_1 for a fully polarized beam without spin flip is ± 1 for an ideal spin analyzer. The sign depends of the polarization of the neutron, and the definition of the asymmetry formula.

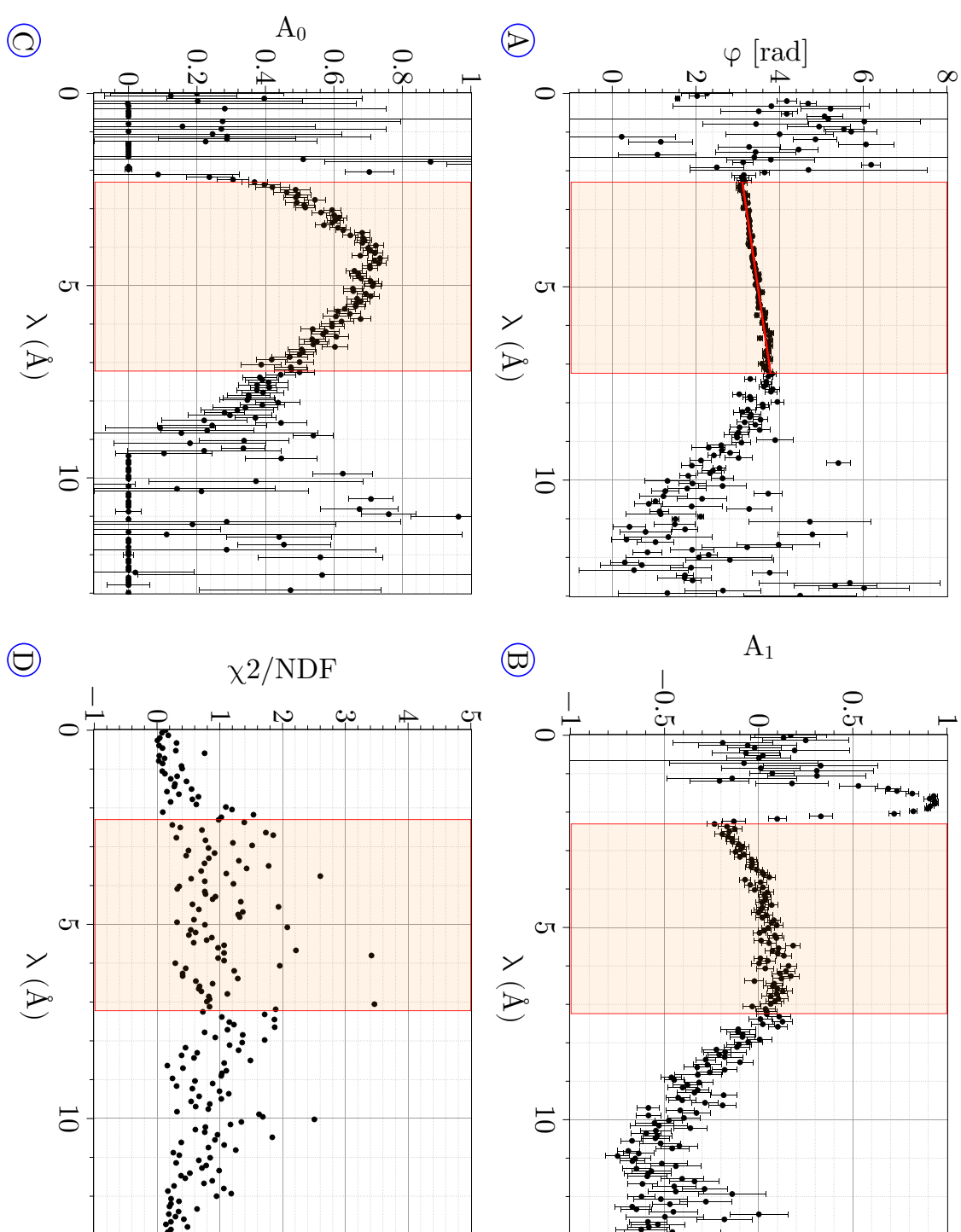


Fig. 5.5: The fit parameters φ , the offset A_1 , the amplitude A_0 and the reduced χ^2 versus the neutron wavelength λ for the top beam with $B_z = -80 \mu\text{T}$ and $B_G = -5.5 \mu\text{T}$. The region of interest is depicted by an orange box.

from the resonance field common to the top and bottom beams and B_g is the vertical field gradient over the distance of the top and bottom beams. It follows:

$$\begin{aligned}\Phi_-(B_g, T) &= \varphi_t - \varphi_b = \gamma_n B_g T, \\ \Phi_+(\delta B_0, T) &= \varphi_t + \varphi_b = 2\gamma_n \delta B_0 T.\end{aligned}\quad (5.3)$$

Thus, the phase difference Φ_- gives information about the magnetic field gradient, while, Φ_+ contains information about δB_0 .

The result of the analysis of Φ_+ and Φ_- as a function of the wavelength is displayed in [Fig. 5.6](#). A linear fit of Φ_+ on the previously defined working range gives:

$$\frac{\partial \Phi_+}{\partial \lambda} = (11 \pm 7) \text{ mrad/Å} \quad (5.4)$$

with $\chi^2/NDF = 1.15$ for 72 degrees of freedom (NDF). This corresponds to an off-resonance field common to the top and bottom beams $\delta B_0 = (0.04 \pm 0.03) \mu\text{T}$. A second linear fit of Φ_- gives:

$$\frac{\partial \Phi_-}{\partial \lambda} = (261 \pm 7) \text{ mrad/Å} \quad (5.5)$$

with $\chi^2/NDF = 1.07$ for 72 degree of freedom (NDF). This corresponds to a difference of magnetic field between the top and bottom beams of $B_g = (-1.90 \pm 0.05) \mu\text{T}$.

The measurement was performed with a field gradient of $B_G = -5.5 \mu\text{T}$, stabilized from the difference in the magnetic field recorded by the fluxgates above and below the spin flippers, over a distance of $d_{FG} = (49 \pm 1) \text{ cm}$. In reality the fluxgate at the position of SF1 recorded a gradient of $-9.4 \mu\text{T}$ where the fluxgates at the position of SF2 a gradient of $-1.6 \mu\text{T}$. Assuming that the field has a linear behavior as function of the vertical position, one can expect a gradient field of about $B_g = d_{bt}/d_{FG} B_G = (-0.44 \pm 0.45) \mu\text{T}$, where the $d_{bt} = 3 \text{ cm}$ corresponds to the distance center-to-center between the top and bottom beams and d_{FG} is the vertical separation of the fluxgates and the error is estimated from the deviation of the two values recorded by the fluxgates. The measured value is more than three sigma away from the expectation which is probably due to the underestimation of the error on B_g . This does not take in account the possibility of a higher magnetic field gradient in between SF1 and SF2 that at their respective position. A dedicated measurement with a continuous white beam was performed to characterize the gradient field, see [Section 5.1.5](#).

5.1.4 Magnetic characterization with a pulsed white beam

To see the difference between the field probed by the neutron and the set field, the vertical component of the magnetic field was scanned from $B_z = -82 \mu\text{T}$ to

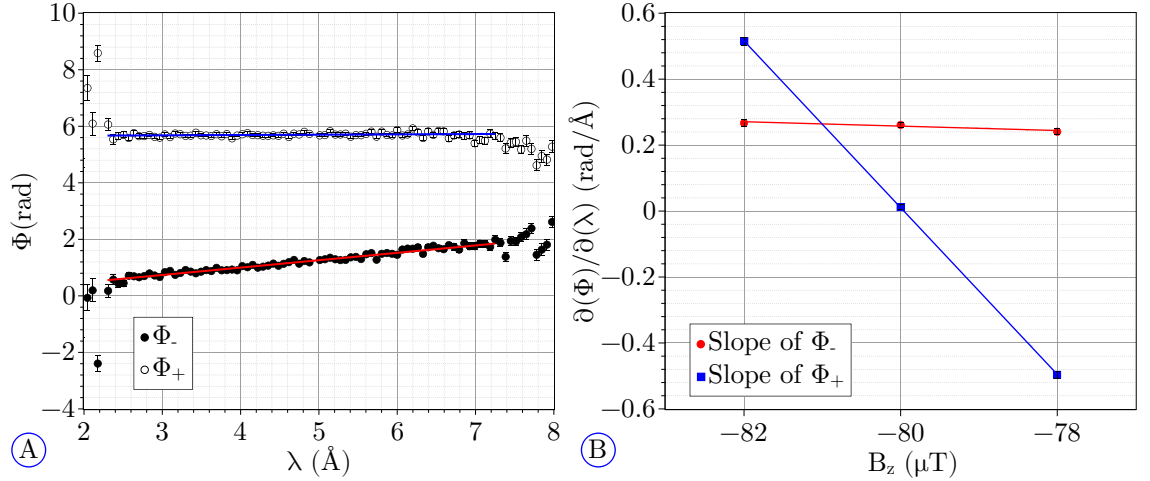


Fig. 5.6: A) Sum (open circle) and difference (full black circle) of the phase from the top and bottom beam over the neutron wavelength for $B_z = -80 \mu\text{T}$ and $B_G = -5.5 \mu\text{T}$ in the region of interest. B) Derivative of the sum (red circle) and difference (blue square) of the phase from the top and bottom beam over the neutron wavelength vs. the set magnetic field.

$B_z = -78 \mu\text{T}$ in steps of $2 \mu\text{T}$. The change in magnetic field was done manually by ramping up or down the current in the vertical coil until it achieved the desired field. Only then the stabilization was turned on. For each magnetic field configuration, a phase scan was performed. The slope of the neutron phase sum Φ_+ (and difference Φ_-) over the wavelength has been calculated with a linear fit and the results are shown in Fig. 5.6B as a function of the set magnetic field.

Using Eq. (5.3) and replacing the interaction time by the equivalent wavelength,

$$T = \frac{d_{SF}}{v} = \frac{\lambda m_n}{h} d_{SF}, \quad (5.6)$$

with $d_{SF} = 3000 \pm 1 \text{ mm}$ the distance between the spin flippers (center to center), m_n the neutron mass, and v the neutron velocity.³ One expects a linear increase of the slope of the neutron phase sum over wavelength with δB_0 , following:

$$\left. \frac{\partial^2(\Phi_+)}{\partial \lambda \partial(\delta B_0)} \right|_e = 2\gamma_n \frac{m_n d_{SF}}{h} = (-277.9 \pm 0.1) \text{ mrad}\text{\AA}^{-1}\mu\text{T}^{-1}, \quad (5.7)$$

where the error is coming from the error on d_{SF} . To estimate the accuracy on the variation of the set field, the deviation of the value of each fluxgate from the set field is corrected by the static background.⁴ The standard error of these calculations yields an error of $0.2 \mu\text{T}$ for a deviation of $2 \mu\text{T}$. From a linear fit on the measurement

³The error on d_{SF} was defined at 1 mm from the graduation of the measuring tape.

⁴The considered static background is the field in homogeneity for the reference measure, see Table 5.1.

presented in [Fig. 5.6B](#), we obtain:

$$\left. \frac{\partial^2(\Phi_+)}{\partial \lambda \partial B_z} \right|_m = (-253 \pm 3 \pm 25) \text{ mrad}\text{\AA}^{-1}\mu\text{T}^{-1}, \quad (5.8)$$

where the error of $\pm 3 \text{ mrad}\text{\AA}^{-1}\mu\text{T}^{-1}$ is the statistical error and yields a $\chi^2/NDF = 0.58/1$ for the fit. The error of $\pm 25 \text{ mrad}\text{\AA}^{-1}\mu\text{T}^{-1}$ corresponds to an error of $0.2 \mu\text{T}$.

Two alternative interpretation of this result can be done. Instead of considering an error of $0.2 \mu\text{T}$ on the magnetic field steps from the different value of the fluxgates, one could compute from the [Eq. \(5.8\)](#) the variation of magnetic field that the neutrons probes. This is possible because the χ^2/NDF of the linear fit with the statistical error only is acceptable according to the theoretical χ^2 distribution. Using [Eqs. \(5.7\)](#) and [\(5.8\)](#), one can estimate that the neutrons probed a variation of the magnetic field of $(2.20 \pm 0.02) \mu\text{T}$ when considering an interaction length of $d_{SF} = 3000 \pm 1 \text{ mm}$.

An equivalent calculation could be done to determine the interaction length when assuming that the variation of the magnetic field is $2 \mu\text{T}$. It would lead to an decrease of $(29.5 \pm 3) \text{ cm}$ of the interaction length. This corresponds to the length of the region in between the spin flippers plus an addition 10.5 cm from the length of the spin flippers where each spin flipper is 40 cm long. This new definition of the interaction length would include about 13% of the spin flippers length. In comparison, [\[AAA⁺20\]](#) includes 2.5 s of the total flipping pulse duration 4 s which represents 62% of the flipping pulses. The reduction of the interaction length is therefore considered unrealistic.

The same analysis can be done with the Φ_- in order to see the evolution of the gradient from the set field. From the measurement, we obtain

$$\left. \frac{\partial^2(\Phi_-)}{\partial \lambda \partial B_z} \right|_m = (-6.7 \pm 3.5) \text{ mrad}\text{\AA}^{-1}\mu\text{T}^{-1}, \quad (5.9)$$

with $\chi^2/NDF = 0.55/1$ which leads to

$$2 \frac{\partial B_g}{\partial B_z} = \frac{\partial^2(\Phi_-)}{\partial \lambda \partial B_z} / \frac{\partial^2(\Phi_+)}{\partial \lambda \partial B_z} = (3 \pm 1)\%. \quad (5.10)$$

In other words, increasing the vertical component of the magnetic field by $1 \mu\text{T}$ also increases the vertical field gradient by around 30 nT . This characterization is important as a gradient field could mimic an EDM if correlated to the electric field reversal. For example, a 30 nT shift in the gradient corresponds to an EDM of $|d_n| = 4 \times 10^{-23} e \text{ cm}$ for an electric field of 100 kV/cm on a 2 m long section, using [Eq. \(4.10\)](#).

5.1.5 Magnetic characterization with continuous white beam

In addition to scanning the vertical magnetic field B_z ; the gradient B_G , the transversal B_x , and the longitudinal B_y fields have been scanned too. However, to increase statistics, the measurements were performed with a continuous beam.

To characterize the setup with the vertical field gradient, the gradient B_G set over the vertical separation of the fluxgates was scanned from $B_G = -8.5 \mu\text{T}$ to $B_G = -2.5 \mu\text{T}$ in steps of $1 \mu\text{T}$ and a phase scan was performed at each field value. Because of the continuous beam, the neutron phase cannot be computed as a function of the wavelength. Instead, the analysis is performed only as a function of the applied field gradient, and Eq. (5.2) becomes:

$$\begin{aligned}\varphi_t(\delta B_0, B_g) &= (\omega_{RF} - \gamma_n B) \bar{T} = \gamma_n (B_g/2 + \delta B_0) \bar{T}, \\ \varphi_b(\delta B_0, B_g) &= (\omega_{RF} - \gamma_n B) \bar{T} = \gamma_n (-B_g/2 + \delta B_0) \bar{T},\end{aligned}\quad (5.11)$$

where \bar{T} is the averaged interaction time for the beam spectrum without the chopper, i.e. an unknown constant, assumed to be identical for the top and bottom beam. Assuming that $\delta B_0 = 0$, one expects a positive slope for the top beam and a negative one for the bottom beam of same amplitude. In Fig. 5.7A, the phase of the top and bottom beams have both a negative slope i.e. they are both in the positive field region of the field gradient. In other words, the gradient contributes to δB_0 . This is also visible in Φ_+ in Fig. 5.7B.

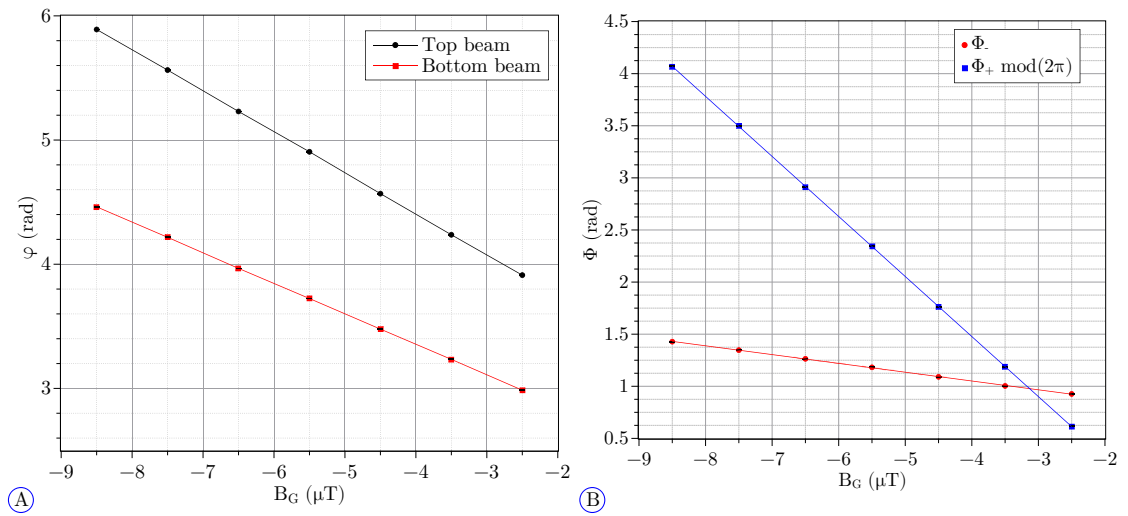


Fig. 5.7: A) Neutron phase for the top and bottom beam as a function of the set magnetic field gradient. B) Phase sum of the top and bottom beam as a function of the set magnetic field gradient.

For a quantitative result, the effective wavelength $\bar{\lambda} = (5 \pm 1) \text{\AA}$ was estimated from a mean of the wavelengths with as weight the AFP asymmetry from Fig. 5

.3E, convoluted with the neutron spectrum. This weight takes into account the contribution of each wavelength to the visibility of the phase scan signal. The error is an educated guess. Replacing $\bar{\lambda}$ in Eq. (5.3), one can approximate:

$$\left. \frac{\partial \Phi_-}{\partial B_g} \right|_e \approx \gamma_n \frac{m_n d_{SF}}{h} \bar{\lambda} = (0.7 \pm 0.1) \text{ rad } \mu\text{T}^{-1}, \quad (5.12)$$

From the linear fit in Fig. 5.7, one gets:

$$\begin{aligned} \left. \frac{\partial \Phi_-}{\partial B_G} \right|_m &= (-84.45 \pm 0.09 \pm 3) \text{ mrad } \mu\text{T}^{-1}, \\ \text{and} \\ \left. \frac{\partial \Phi_-}{\partial B_g} \right|_m &= \left. \frac{\partial \Phi_-}{\partial B_G} \right|_m \times \frac{d_{FG}}{d_{bt}} = (-1035 \pm 1 \pm 41) \text{ mrad } \mu\text{T}^{-1}, \end{aligned} \quad (5.13)$$

where the error of $0.09 \text{ mrad } \mu\text{T}^{-1}$ (and $1 \text{ mrad } \mu\text{T}^{-1}$) is from statistics with a $\chi^2/NDF = 0.61$ for the fit and the error of $3 \text{ mrad } \mu\text{T}^{-1}$ (and $41 \text{ mrad } \mu\text{T}^{-1}$) are an estimate of the error on the variation of the magnetic field gradient and may be under estimated. The expected and measured values are of the same order of magnitude but are more than three sigma away from each other. This is probably due to a wrong estimate of B_g over the full length of the apparatus. An investigation on the magnetic field background should be performed to confirm this.

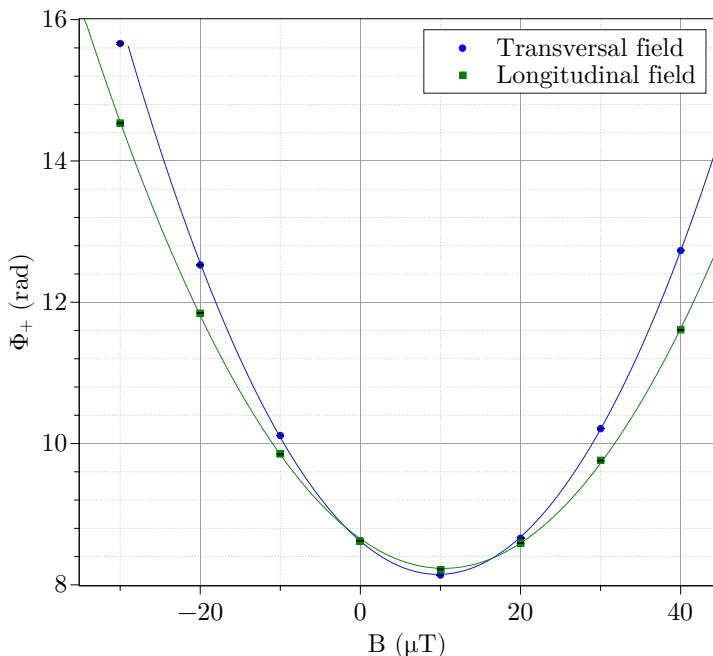


Fig. 5.8: Phase sum of the top and bottom beam as a function of the longitudinal and traversal field.

For both measurements with the variation of the traversal B_x and longitudinal B_y fields, the field was scanned from $-30 \mu\text{T}$ to $+40 \mu\text{T}$ in steps of $10 \mu\text{T}$ and for each value a phase scanned was performed. Because of the continuous beam, the neutron phase cannot be computed as a function of the wavelength. Instead, the analysis is performed only as a function of the applied field, and the neutron phase for each beam can be estimated from Eq. (4.11) by:

$$\begin{aligned}\varphi_t(B_x, B_y, B_0, B_g, \delta B_0) &= \omega_{RF} \bar{T} + \gamma_n \bar{T} \sqrt{B_x^2 + B_y^2 + (\delta B_0 + B_g/2 + B_0)^2}, \\ \varphi_b(B_x, B_y, B_0, B_g, \delta B_0) &= \omega_{RF} \bar{T} + \gamma_n \bar{T} \sqrt{B_x^2 + B_y^2 + (\delta B_0 - B_g/2 + B_0)^2}.\end{aligned}\quad (5.14)$$

Here again, the vertical component of the magnetic field is separated into B_0 the reference field from which $\omega_{RF} = \omega_0 = -\gamma_n B_0$ was set, the vertical field gradient sensed by the top or bottom beams B_g , and the off-resonance field common to both beams δB_0 . Assuming $\delta B_0 \pm B_g \ll B_0$ and $B_x^2 + B_y^2 \ll B_0^2$, one can expect:

$$\begin{aligned}\Phi_+(B_x, B_y, B_0, B_g)|_e &= 2\gamma_n \bar{T} \sqrt{B_x^2 + B_y^2 + B_z^2} + 2\omega_{RF} \bar{T}, \\ &\approx \gamma_n \frac{m_n d_{SF} \bar{\lambda}}{h} \left(2\delta B_0 + \frac{B_x^2 + B_y^2}{B_0} \right),\end{aligned}\quad (5.15)$$

with $\gamma_n m_n d_{SF} \bar{\lambda} / (B_0 h) = (5.7 \pm 1.1 \pm 0.9) \text{ mrad } \mu\text{T}^{-1}$, using as $B_0 = [-(134 + 150 + 80)/3 \pm 70/3] \mu\text{T}$ the average of the value recorded by the fluxgates. The error of $0.9 \text{ mrad } \mu\text{T}^{-1}$ is from the error on B_0 and the error of $1.1 \text{ mrad } \mu\text{T}^{-1}$, is from the uncertainty on $\bar{\lambda}$.

The data presented in Fig. 5.8 have an additional fixed error of $0.02 \mu\text{T}$ estimated from the stability of the fluxgates reading. It contributes to the polynomial fit of the data with the variation of the transversal field in Fig. 5.8 which gives:

$$\Phi_+(B_x)|_m = 4.99(2) \times 10^{-3} [\text{rad}/\mu\text{T}] (B_x - 9.71(4) [\mu\text{T}])^2 + 8.15(1) [\text{rad}] \quad (5.16)$$

with a $\chi^2/NDF = 1.1$. The value at $-40 \mu\text{T}$ was excluded due to a saturation of the gradient coil power supply. From the values of the fit, one can estimate the fixed offset of $(9.71 \pm 0.04) \mu\text{T}$ of the set transversal field from zero. The quadratic factor of $(4.99 \pm 0.02) \text{ mrad}/\mu\text{T}$ is in agreement with the theoretically expected value of $(5.7 \pm 1.1 \pm 0.9) \text{ mrad } \mu\text{T}^{-1}$. As we are working with a white beam, the offset of $(8.15 \pm 0.01) \text{ rad}$ cannot be interpreted as we see from Fig. 5.6 that a general offset could appear even with a pulsed beam.

The same could be done on the data with the variation of the longitudinal field with the same fixed error on B_y . The polynomial fit in Fig. 5.8 gives:

$$\Phi_+(B_y) = 3.91(3) \times 10^{-3} [\text{rad}/\mu\text{T}] (B_y - 10.41(7) [\mu\text{T}])^2 + 8.22(2) [\text{rad}] \quad (5.17)$$

with a $\chi^2/NDF = 2.2$. The same comment as for the data with the transversal field variation apply here. It is interesting to note that the data with transversal and longitudinal field variations do not have the same quadratic factor. It can be due to a difference in the magnetic field background or to a different accuracy when setting the transversal or longitudinal fields as two coils have a different geometry.⁵

5 .1.6 Summary

During this beamtime, the objectives were met. The first Ramsey technique with the BeamEDM apparatus was performed. It resulted in the determination of the resonance frequency of the apparatus, even though it was with a continuous beam and the magnetic field was not homogeneous. The working range of the apparatus in wavelength was defined from a phase scan close to resonance with a pulsed white beam. This measurement confirmed that the neutron phase has a linear behavior as a function of the neutron wavelength as shown in Fig. 5 .5. Then, two additional phase scans were performed with a pulsed white beam with an offset in the vertical magnetic field of $\pm 2 \mu\text{T}$. This offset from the resonance field could be re-calculated from the neutron phase shown in Fig. 5 .6. A similar characterization of the apparatus with longitudinal field, transversal field and vertical field gradient was performed but with a continuous white beam, requiring the computation of an effective wavelength. This was done by weighting the spectrum with the AFP asymmetry in Fig. 5 .3E to take into account only the neutrons that could be analyzed by the spin analyzer. For the measurement with the variation of the magnetic field gradient in Fig. 5 .7, the top and bottom beams are sensing an additional field of same sign Fig. 5 .7. This can be interpreted as the center of the gradient field being above the top beam. This hypothesis would also explain the additional (non gradient) vertical field observed in Fig. 5 .7B. In addition, the gradient that the neutrons probe differs from the set field by a factor 1.5. This discrepancy could be due to the background field. Indeed the fluxgates at the position of SF1 and SF2 measure a field gradient of $-9.4 \mu\text{T}$ and $-1.4 \mu\text{T}$, respectively, over their vertical separation. In the future, the effect of the gradient should be investigated in a more homogeneous field and the field background should be mapped. For the measurement with the variation of the longitudinal and transversal field in Fig. 5 .8, the data from the neutron phase show the expected quadratic behavior when considering a fixed offset of $(-9.71 \pm 0.04) \mu\text{T}$ for the transversal field and $(-10.41 \pm 0.07) \mu\text{T}$ for the longitudinal field which could be due to the magnetic background. The significant difference between the value for the longitudinal and transversal field can be due to a different accuracy when setting the transversal or longitudinal fields as two coils have a different geometry.

⁵For example, changing the transversal magnetic field value by $10 \mu\text{T}$ changes the longitudinal field recorded by the fluxgates at the position of SF1 by $0.15 \mu\text{T}$.

To investigate this further, additional fluxgates and a more homogeneous magnetic field background could be an advantage.

5 .2 Beamtime 2: ILL March 2018

The second beamtime with the Ramsey apparatus was at PF1b, ILL in 2018 from 07/03 to 27/03. The objectives of this beamtime were:

- to characterize the beam using the wavelength selector and a chopper in order to verify the wavelength of the neutrons as a function of the rotational frequency of the wavelength selector as well as the bandwidth of the wavelengths,
- to start the characterization of the spin flipper as a function of the wavelength as a premise of the modulated signal presented in [Section 3.3.4](#) with [Eq. \(3.2\)](#),
- to compare the effect of the optimized amplitude of the sinusoidal function with a fixed amplitude for several phase scan measurements when varying the vertical magnetic field.

A chopper was only used to characterize the spectrum of the wavelength selector. Afterwards, the measurements were performed with a continuous monochromatic beam. Moreover, the apparatus was upgraded from the previous beamtime: a new analyzer was used (see [Section 3.3.4](#) and [Fig. 3.21B](#)), and the end pieces of the aluminum structure were set to support the spin analyzer and the detector (see [Fig. 3.22](#)). The length of the apparatus is approximately 7 m from the first aperture to the front side of the detector. In comparison, for the previous beamtime, the distance from the chopper to the detector was 6 m.

5 .2.1 Characterization of the wavelength selector

To characterize the wavelength spectrum of the beam when using the wavelength selector, a time-of-flight measurement was performed. A chopper was placed at a fixed position downstream of the wavelength selector in the shielded area called the "casemate". The neutron detector was set in the experimental area, at different distances D from the chopper, defined by a laser measurement, as represented by the sketch in [Fig. 5.9](#). The chopper was running at 33 Hz and the rotation frequency of the wavelength selector was sampled according to [Table 5.4](#).

The time-of-flight measurement was preformed at four positions, $D = \{525; 1765; 3298; 4412\}$ mm, for each rotational frequency of the wavelength selector. An example of a time-of-flight spectrum is shown in [Fig. 5.10A](#), where the green square represents the position of the peak, i.e, the time-of-flight bin with the maximum counts. This time-of-flight position is recorded as a function of the distance, D , measured by the laser for each rotation frequency of the wavelength selector, as shown in [Fig. 5.10B](#), and fitted with a linear function.

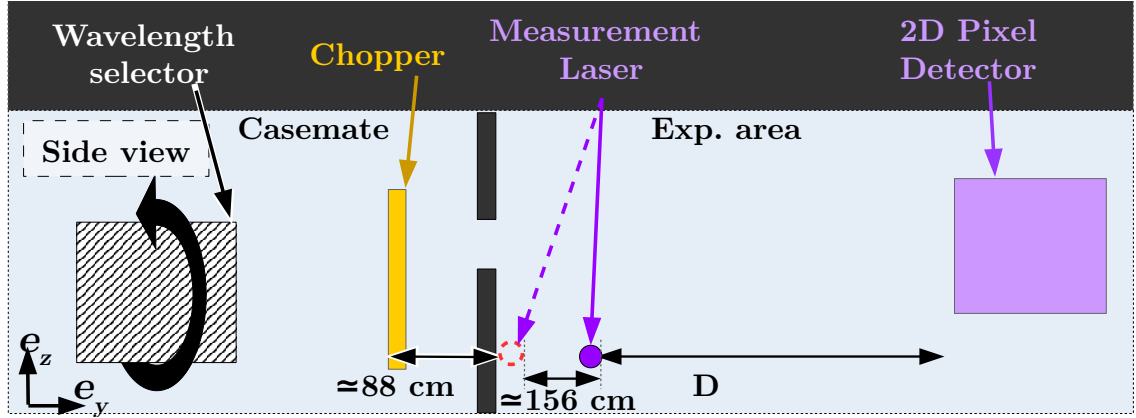


Fig. 5.9: Sketch of the measurement for the characterization of the wavelength selector (side view). The striped white rectangle represents the wavelength selector in the casemate, the black arrow superposed on it represents its rotation, the thin yellow rectangle is the chopper, the purple dot in the experimental area is the laser that measures the position of the detector represented by a purple square. The beam goes from left to right.

RPM	6'000	7'450	10'100	12'000	18'000	20'000	26'500	28'000
λ_N (Å)	21.2	17.1	12.6	10.6	7.07	6.36	4.8	4.55
α_W (ms/m)	5.39		3.18	2.71	1.801			1.158
$\sigma(\alpha_W)$ (ms/m)	0.09		0.02	0.01	0.004			0.003
λ_M (Å)	21.3		12.58	10.71	7.12			4.58
$\sigma(\lambda_M)$ (Å)	0.3		0.08	0.04	0.02			0.01
$\Delta\lambda/\lambda$			0.113	0.115	0.126			0.127

Table 5.4: Characteristics of the beam at different rotational frequencies of the wavelength selector in rotation per minute (RPM). λ_N is the nominal wavelength from the documentation, α_W is the slope from Fig. 5.10B, with $\sigma(\alpha_W)$ the associated error, λ_M is the wavelength calculated from α_W , and $\sigma(\lambda_M)$ is its associated error.

From their crossing point, one can extract the distance between the chopper and the laser $(2.62 - 0.05) \text{ m} = (2.57 \pm 0.01) \text{ m}$. The only line that does not fit to that description is the one at $\text{RPM} = 10100$, by approximately 11 cm, for an unknown reason. The value is corrected by $(5 \pm 1) \text{ cm}$ which is an educated guess of the distance from the detector front to the actual GEM foils of the detector. In comparison, the laser's position with regards to the chopper can be calculated from the logbook $\approx (0.88 + 1.56 + 0.11) \text{ m} = (2.55 \pm 0.01) \text{ m}$. This value is the result of a tape measurement between the chopper and the casemate wall of $(0.88 \pm 0.01) \text{ m}$ and the determination of the distance between the laser and the casemate wall of $(1563 \pm 2) \text{ mm}$. This latter distance was measured by subtracting the distance between the laser and detector at the initial position of the laser D displayed in Fig. 5.9 and the distance when the laser is against the casemate wall, represented

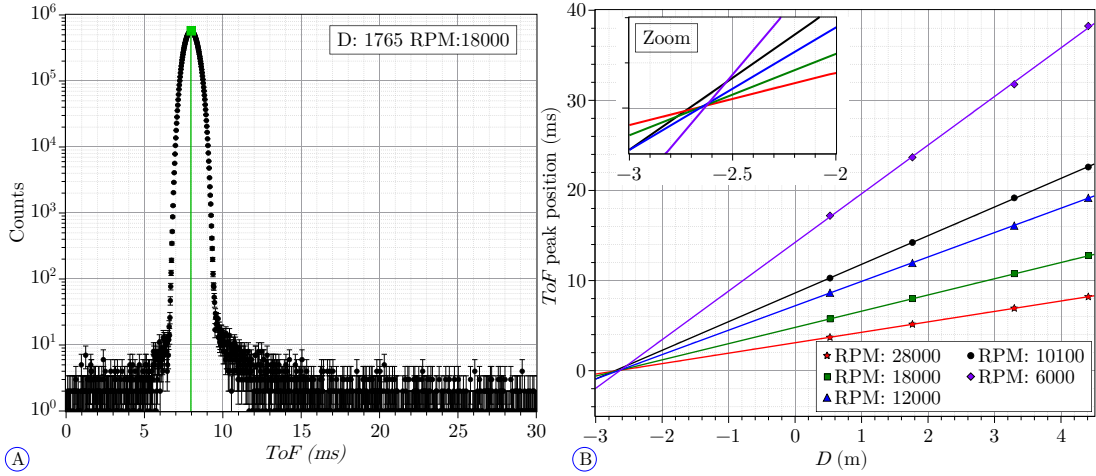


Fig. 5.10: A) Time-of-flight measurement with a distance $D = 1765$ mm and a wavelength selector frequency of 18000 RPM. The green line at 7.985 ms shows the maximum number of counts in that measurement. It corresponds to the green square at 1.765 m and 7.985 ms in B. B) Peak position vs. D for different wavelength selector frequencies in RPM. The straight lines are linear fits and a zoom around their crossing point is shown in the top left corner.

by red dashed circle in the same figure. The length of the laser, (110 ± 1) mm, was added to this measurement as it is assumed that the zero position of the laser is at the front. The distance between the chopper and the laser will be defined as the average of the two previously presented values $d_{CL} = (2.56 \pm 0.02)$ m.

From the slope of the fits in Fig. 5.10, one can extract the wavelength and compare it to the nominal one λ_N , extracted from the documentation available at the beamline. If the linear function follows $f(D) = \alpha_W D + \beta_W$, the wavelength is $\lambda_M = \alpha_W m_n / h$ using the de Broglie equations. The results are presented in Table 5.4. The stated errors are estimated from the standard deviation of the data points from the linear fits. One can conclude that the measured wavelengths λ_M are in agreement with the nominal ones λ_N found in the documentation available at the beamline.

Using the FWHM (full width half maximum) of the time-of-flight spectra at $D = 4412$ m, $\Delta\lambda/\lambda$ was measured for the selected wavelength selector frequencies, except 6000 RPM due to low statistics. This yields a $\Delta\lambda/\lambda$ between 0.11 and 0.13. The results are presented in Table 5.4. These values have an incidence on the Ramsey pattern presented afterwards.

5.2.2 Characteristics of the Ramsey apparatus

The following measurements were performed without chopper but with the wavelength selector. The selected wavelengths are summarized in Table 5.4. Their value was restricted by the mechanical resonance frequencies of the wavelength selector. They

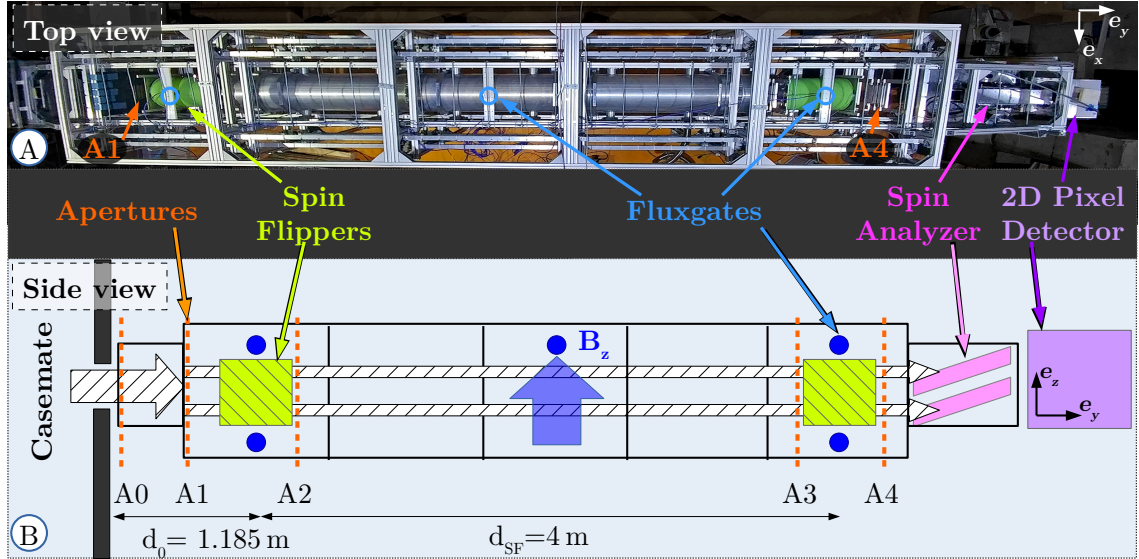


Fig. 5.11: A) Picture of the BeamEDM apparatus at PF1b in 2018 with indications for the apertures A1 and A4 and three visible fluxgates. B) Sketch of the apparatus with each $(1 \times 1 \times 1)$ m 3 cube of the structure (including the end pieces) represented by black rectangles, the different apertures represented by orange dashed lines, the position of the fluxgates denoted by the full blue circles, the spin flippers (striped green boxes), the analyzer (pink parallelograms) and the detector (purple cube). The neutron beam is coming from the casemate in the left, through an opening in the wall (full black rectangles) to the experimental area on the right.

cover the range from 4.55 Å to 21.2 Å which allows us to characterize the apparatus for this equivalent spectrum. In particular, the effect of the spin flippers and magnetic field on different wavelengths was studied.

A picture as well as a schematic of the Ramsey apparatus are shown in Fig. 5.11. The wavelength selector is not visible on the figure as it was in the shielded area: the casemate. The beams were defined by five apertures in the experimental area, additional ones were also installed in the casemate to reduce the radiation in the experimental area. The apertures A1 to A4 were cutting the beam into two, called

Name	A0	A1	A2	A3	A4
Type	I	II	II	II	II
Opening width (mm)	~ 40	30	30	30	30
Opening height (mm)	~ 70	2 × 10	2 × 15	2 × 15	2 × 10
Separation height (mm)		30	30	30	30
Distance to the casemate wall (m)	0	0.185	1.435	4.935	35.685

Table 5.5: Characteristics of the apertures at PF1b in 2018 shown in Fig. 5.11, with their type defined in Section 3.3.3, the width, height of the opening(s), the height of absorbing plates that cuts the beam in two, and the distance of the apertures to the casemate wall. The apertures A1 and A4 are the defining apertures in height.

top and bottom beams, in order to do relative measurements of the neutron phase. The apertures' geometry is summarized in [Table 5.5](#). The upstream spin flipper SF1 was placed in the middle of the first cube of the structure which corresponds to a distance from the casemate wall of (1185 ± 1) mm. The downstream spin flipper was placed in the middle of the fifth and last cube of the structure. This corresponds to a distance center-to-center between the spin flippers of $d_{SF} = (4000 \pm 1)$ mm. A sinusoidal signal was sent to the spin flippers to set the linearly oscillating magnetic field in the direction longitudinal to the beam. FLC3-70 fluxgates were placed on the top and the bottom of each spin flipper, monitoring the vertical gradient field $B_G = -1 \mu\text{T}$ over the vertical separation of the fluxgates $d_{FG} \approx 49 \text{ cm}$, and an additional one was placed in the middle of the third cube, at the same vertical position as the fluxgates above the spin flippers. All fluxgates were centered in the traversal and longitudinal axis with respect to their cube. The magnetic field was stabilized on the average of all five of them at $B_z = -125 \mu\text{T}$ for the vertical component and $B_x = B_y = 0 \mu\text{T}$ for the transversal and longitudinal components, as represented in [Fig. 5.11B](#). The vertical field gradient was not stabilized at zero due to a saturation of the power-supply. The vacuum pipe was placed in between the spin flippers in order to decrease the neutron scattering in air. It was approximately 3.4 m long and did not contain any electrodes yet. Therefore, there was no electric field in the free precession region defined by the spin flippers. The new, at the time, spin analyzer was installed in the 1 m long cuboid attached on the downstream side of the structure, reflecting vertically the neutrons into the detector, i.e. above or below the transmitted spots.

There are three possible configurations for the orientation of the spin analyzer mirrors. They are represented in [Fig. 5.12](#) and detailed hereafter:

- A: In the $>$ -shape configuration, the reflected beams are sandwiched in the middle of the two transmitted spots. This would have led to a complete overlap of the two reflected beams, therefore, this configuration was not considered.
- B: In the $<$ -shape configuration, the reflected spots are on the outside of the region defined by the two transmitted spots. The reflected spots would have triggered the edge pixels of the detector which were not considered reliable at that time and this configuration was rejected for this beamtime.
- C: In the parallel configuration, the reflected spots are always above (or below as it is symmetric) the transmitted spots. This was the configuration chosen for this beamtime. The incident angle of the top and bottom mirrors was set to ± 1 deg. This is because the reflected spot of the bottom beam was constricted by the transmitted top beam whereas the reflected top beam had

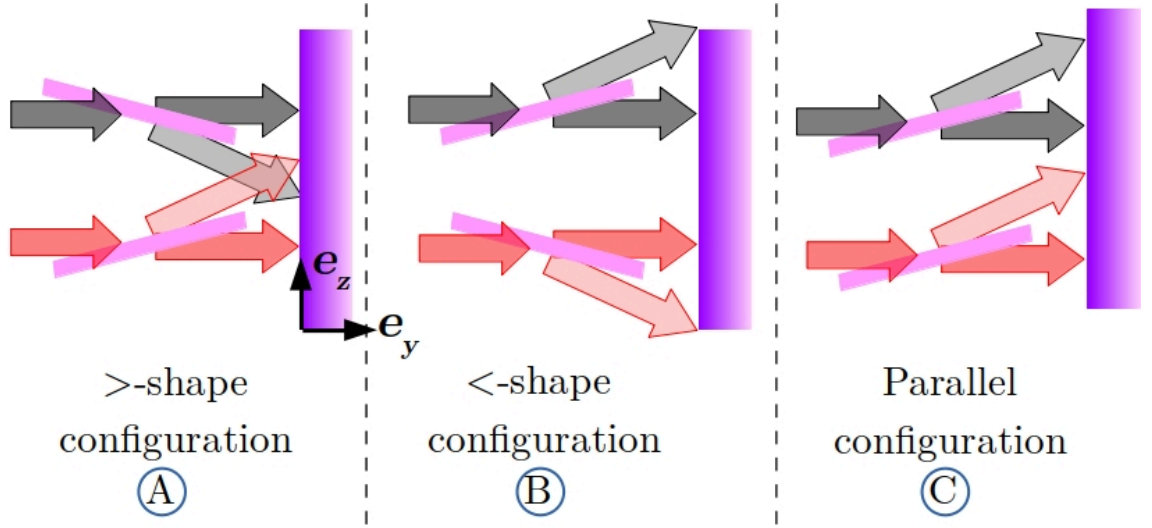


Fig. 5.12: Schematic representation from the side of the different configuration possible of the spin analyzer mirrors (pink rectangle), with the top beams represented by gray arrow, the bottom by red arrows and the detector by a purple gradient box. The reflected beams are always more transparent than the transmitted and incident beams. The position of the center of the mirrors is the same for all configurations.

more space as visible in Fig. 5.13. Therefore, the top mirror could have a higher angle. However, even in that case there is cross contamination between the transmitted and reflected spots, especially for the bottom beam.

We define the cross contamination as the overlap of one spot with another already defined for the previous beamtime, see Fig. 5.2. To reduce the effect of the cross contamination visible in Fig. 5.13 in the analysis, only one pixel line was chosen for each spot and they were defined according to Table 5.6. From Fig. 5.13 only, it is difficult to quantitatively disentangle the effect of cross contamination from the other effect presented in Fig. 5.2. They will be referred as the "overall spin analyzer" efficiency. This value is computed from the AFP asymmetry defined in Eq. (5.1). The results are shown in Fig. 5.13C and B.

Spot	Top Trans.	Top Ref.	Bottom Trans.	Bottom Ref.
Bottom left corner	(6;8)	(6;12)	(6;2)	(6;5)
Top right corner	(9;8)	(9;12)	(9;2)	(9;5)

Table 5.6: Definition of transmitted (Trans.) and reflected (Ref.) spots for the top and bottom beams. The squares are defined by the coordinate of their bottom-left and top-right corners in units of pixel.

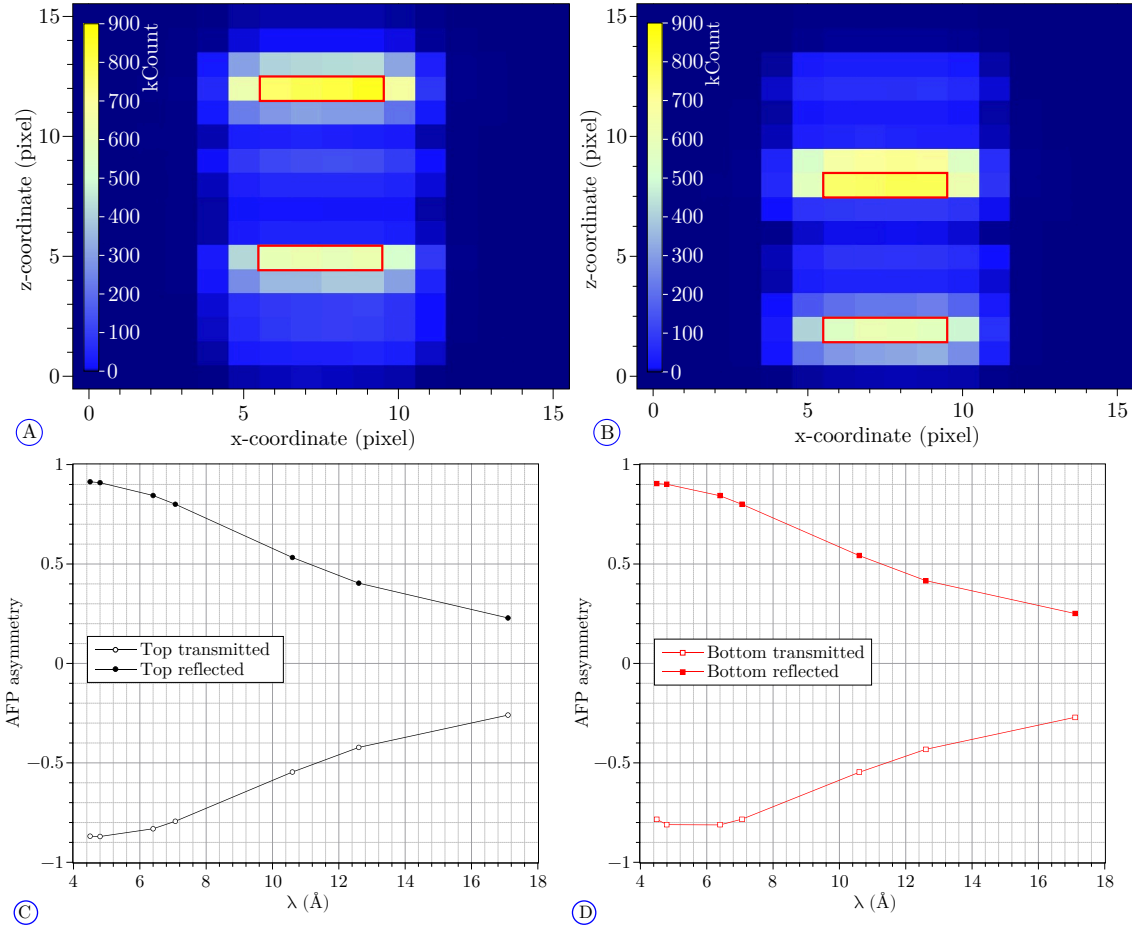


Fig. 5.13: A) Picture of the neutron count in the detector pixels with the adiabatic spin flipper off. B) Picture of the neutron count in the detector pixels with the adiabatic spin flipper on. The pixels used for the different spots are delimited by red rectangles. The measurement was performed with a monochromatic beam at $\lambda = 4.55 \text{ \AA}$. C) AFP asymmetry as a function of the neutron wavelength for the spots of the top beam. D) AFP asymmetry as a function of the neutron wavelength for the spots of the bottom beam.

5.2.3 Characterization of the spin flippers

From [Section 2.3](#), we know that a π flip is obtained on resonance when the amplitude of the oscillatory field $\omega_1 = -\gamma_n B_1$ matches τ the time that the neutrons spend in the spin flippers $\tau\omega_1 = \pi$. One of the goals of this beamtime is to determine the optimal amplitude of the sinusoidal signal sent to the spin flippers to achieve a π flip for a phase scan, on resonance, for each wavelength.

First, a Rabi frequency technique was performed on each spin flipper with a monochromatic beam at $\lambda = 10.6 \text{ \AA}$ and $\lambda = 4.8 \text{ \AA}$ to determine the resonance frequency of each spin flipper. These values of wavelength were chosen from a compromise between statistics and sensitivity of the linear regression that will determine the wavelength dependency of the optimal amplitude defined in the next paragraph.⁶ For these two measurements, the peak-to-peak amplitude of the sinusoidal signal sent to the spin flippers is 1 V_{pp} and $0.5 \text{ V}_{\text{pp}}$ respectively. From [Eq. \(2.21\)](#), we expect that the peak of the resonance frequency is the same for all wavelengths and indeed from the measurement we find 3325 Hz for SF1 and 3855 Hz for SF2, independently of the wavelength as shown in [Fig. 5.14A](#) for SF1. In addition, we know from [Eq. \(2.21\)](#) that the linewidth is bigger for a smaller value of $\tau/\omega_1 \propto \lambda/\omega_1$. Applied to our system, we expect the linewidth at 10.6 \AA to be smaller than the one at 4.5 \AA . This is what is observed in the measurement in [Fig. 5.14A](#). In order to compare the linewidth for the measurements at $\lambda = 10.6 \text{ \AA}$ and $\lambda = 4.5 \text{ \AA}$, the asymmetry was normalized to 1.

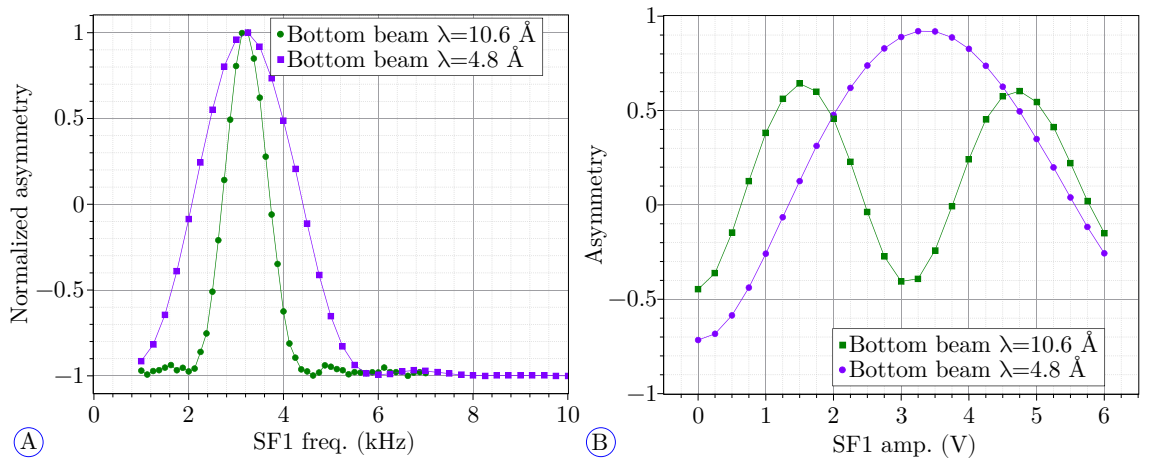


Fig. 5.14: A) Asymmetry normalized to expand from -1 to 1 vs. set frequency in SF1 for two configurations of the wavelength selector. B) Asymmetry vs. amplitude of the oscillating signal of SF1 for two configurations of the wavelength selector.

⁶To have the smallest error on the slope of the linear regression (for equivalent statistics) the measurement should be performed with wavelengths far apart. However the peak in statistics is towards short wavelengths $\approx 4.5 \text{ \AA}$, see [Table 3.2](#).

RPM	7450	10'100	12'000	18'000	20'000	26'500	28'000
λ (Å)	17.1	12.6	10.6	7.07	6.36	4.8	4.55
Optimal amplitude (V)	0.46	0.63	0.75	1.12	1.25*	1.65	1.74

Table 5.7: Optimal amplitude in volts for the spin flippers for different frequencies of the wavelength selector and corresponding neutron wavelengths. The "*" denotes the value used for the fixed amplitude measurements.

Then a Rabi amplitude scan, on resonance, with the same wavelengths was performed to characterize the "optimal amplitude" as a function of the wavelength for a $\pi/2$ flip. This value corresponds to half the voltage required of the maximum asymmetry in Fig. 5.14B. It is $(1.5 \pm 0.1)/2$ V at $\lambda = 10.6$ Å and $(3.3 \pm 0.1)/2$ V at $\lambda = 4.8$ Å, where the errors are estimated from the amplitude scan step size. From these two values, one can extrapolate that the amplitude should be equal to $7.9/\lambda$, where λ is in Angström and the amplitude in Volt. The value of this optimal amplitude is summarized in Table 5.7 for the wavelengths used in the following measurements.

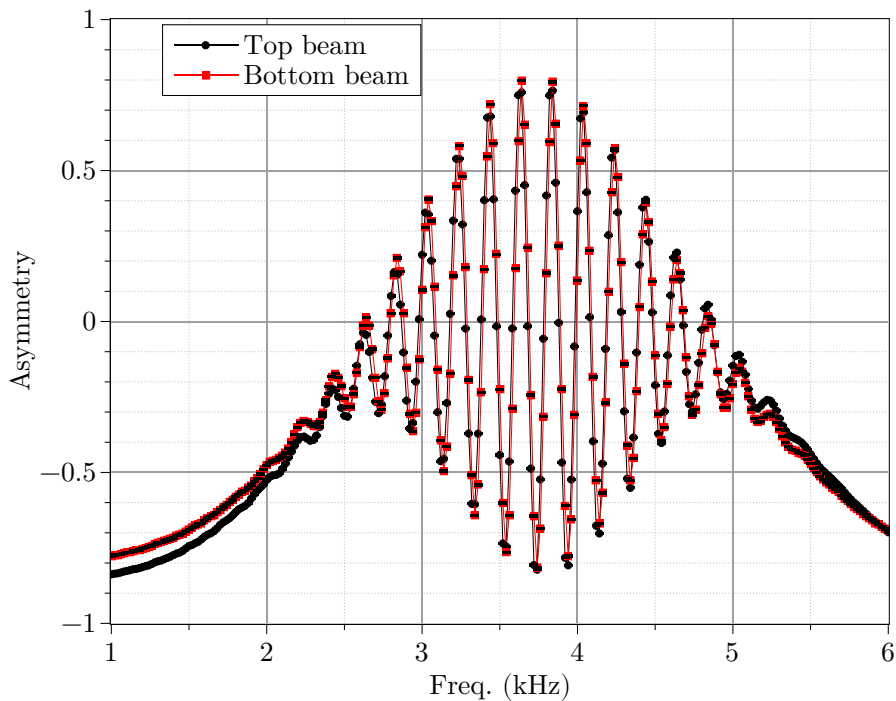


Fig. 5.15: Asymmetry vs. applied frequency for the spin flippers during a Ramsey technique on a beam at $\lambda = 4.8$ Å with an amplitude of 1.65 V for the top and bottom beam.

Finally, a Ramsey scan is performed with a monochromatic beam at $\lambda = 4.8$ Å and its optimal amplitude of 1.65 V to determine the resonance frequency of the

apparatus.⁷ The Ramsey pattern, displayed in [Fig. 5.15](#), has an amplitude of ≈ 0.8 instead of 1 in the ideal case, due to the following effects:

- The overall spin analyzer efficiency.
- The inhomogeneity of the magnetic field leading to a difference of about 500 Hz between the resonance frequencies for the spin flippers. This difference reduces the maximum achievable amplitude, see [Appendix A](#).
- The width of the spectrum. This is visible by the absence of oscillations further away from the resonance e.g. for $f_{RF} > 5$ kHz.⁸

In comparison with the Ramsey pattern measured in the previous beam time, several oscillations are visible. This is the result of a measurement performed with a monochromatic beam. The resonance frequency was estimated from the oscillation with the highest amplitude. It is (3750 ± 10) Hz where the error is estimated from the frequency scan step size.

5.2.4 Magnetic characterization

To evaluate the effect of the optimal amplitude of the spin flippers sinusoidal signal on the neutron phase, a similar characterization as in [Section 5.1.4](#) for the vertical component of the magnetic field was performed with the optimal amplitude of the spin flippers sinusoidal signal, see [Table 5.7](#), and compared with a fixed amplitude of 1.25 V.

The measurements were done as following: the wavelength selector was set at one wavelength, then the magnetic field was scanned from $B_z = -123$ μT to $B_z = -127$ μT with steps of $\Delta B_z = -1$ μT . For each value of the magnetic field, a phase scan measurement was performed with a fixed amplitude 1.25 V of the sinusoidal function sent to the spin flippers. This combination of magnetic field scan and phase scan was then repeated with the optimal amplitude of the sinusoidal signal sent to the spin flippers. This procedure was repeated for all seven wavelength given in [Table 5.7](#). At $\lambda = 6.36$ \AA , the measurement was done only once as the fixed and optimal amplitude of the sinusoidal signal are identical.

A linear behavior is expected for Φ_+ , as a function of λ and δB_0 , for the measurement with the optimal amplitude of the sinusoidal signal, as shown in [Eqs. \(4.12\)](#) and [\(5.3\)](#). The expected analytical value is:

⁷Measuring at another wavelength should only change the width of the Ramsey Pattern, see [Section 2.3](#).

⁸The mathematical derivation of the spin flip probability for a Ramsey technique with a generic wavelength distribution is developed in [\[Pie09\]](#).

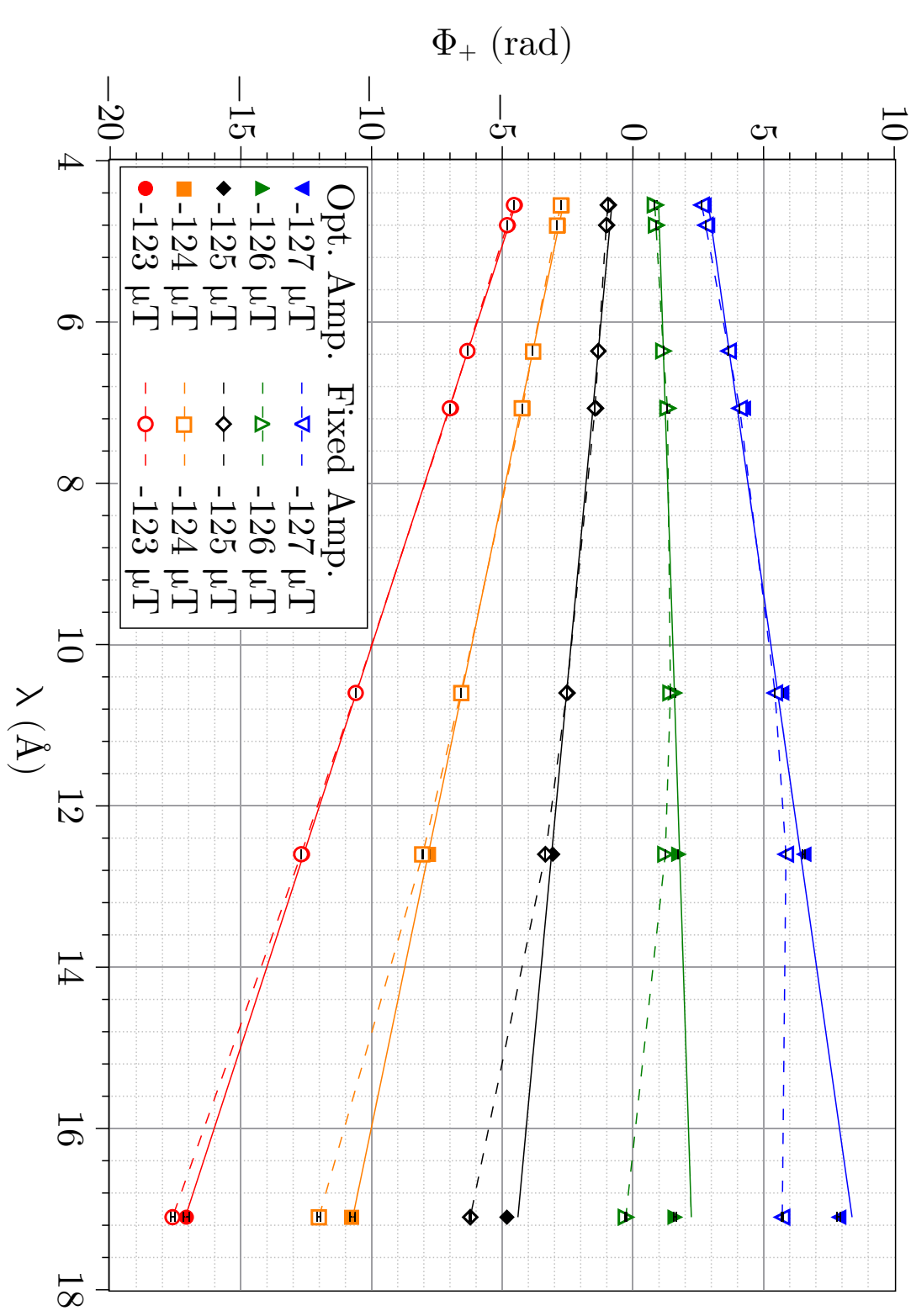


Fig. 5.16: Sum of the top and bottom phase vs. wavelength for different magnetic fields using the optimal amplitude for the full symbols and a fixed amplitude for the empty ones. The dashed lines are linking the data points for the fixed amplitudes and the full lines are linear fits of the data with the optimal amplitude send to the spin flippers.

$$\left. \frac{\partial^2(\Phi_+)}{\partial \lambda \partial(\delta B_0)} \right|_e = 2\gamma_n \frac{m_n d_{SF}}{h} = (370.6 \pm 0.1) \text{ mrad}\text{\AA}^{-1}\text{\mu T.}^{-1} \quad (5.18)$$

with as a reminder $d_{SF} = (4000 \pm 1)$ mm the distance center to center of the spin flippers and δB_0 is the deviation from the reference field B_0 which was used to determined $\omega_{RF} = \omega_0$. [Fig. 5.16](#) shows the sum of the neutron phases, determined by the fit function [Eq. \(4.6\)](#), as a function of the wavelength for different magnetic field strengths, indicated in the legend. The full and empty symbols represent the measurements with the optimized and the fixed amplitude of the sinusoidal signal respectively.

All measurements have a similar behavior: the phase sum Φ_+ of the fixed amplitude measurement deviates from the linear behavior of the optimal amplitude measurement for wavelengths far from $\lambda = 6.36 \text{ \AA}$. For the optimal amplitude measurement, the slope of the neutron phase vs. wavelength can be determined by a linear fit and plotted against the set magnetic field as displayed in [Fig. 5.17A](#). From this figure, one can extract the magnetic field for which $\delta B_0 = 0$ from the crossing at $d(\Phi_+)/d\lambda = 0$ of the linear fit function, $B_0 = -125.8 \text{ \mu T}$. The slope of this linear fit,

$$\left. \frac{\partial^2(\Phi_+)}{\partial \lambda \partial(B_z)} \right|_m = (367 \pm 2) \text{ mrad}\text{\AA}^{-1}\text{\mu T.}^{-1} \quad (5.19)$$

is two sigma away from the expected value with a reduced chi-square of $\chi^2/NDF = 17.5$. The error from the measurement value is coming from a combination of statistics and the standard deviation of the recorded values of the fluxgates over 256 s for each phase scan and a fixed error on the wavelength of 0.1 \AA . In addition, one would need to take into account the magnetic field drift in-between phase scans. Indeed, it was already mentioned that the measurement was performed in such an order to minimize the number of times that the wavelength was changed as this is a slow process. However, this means that the neutron phase measurements at two different wavelengths are more separated in time which makes this measurement sensitive to long term drift of the magnetic field background. In addition, PF1b is next to other beamlines with experiments that ramp magnetic fields up and down periodically, therefore, they influence this measurement's magnetic background, see [Appendix F](#).

On the other hand, the phase difference Φ_- should not have been affected by the spin flippers configuration (optimal amplitude or fixed one). Indeed, the effect linked to the amplitude of the spin flipper signal is the same for both beams and by taking the difference, the effect is suppressed. The phase difference for $B_z = -127 \text{ \mu T}$ for the optimal amplitude configuration and the fixed amplitude configuration was computed for a comparison, shown in [Fig. 5.17B](#). From the fit of the data with the

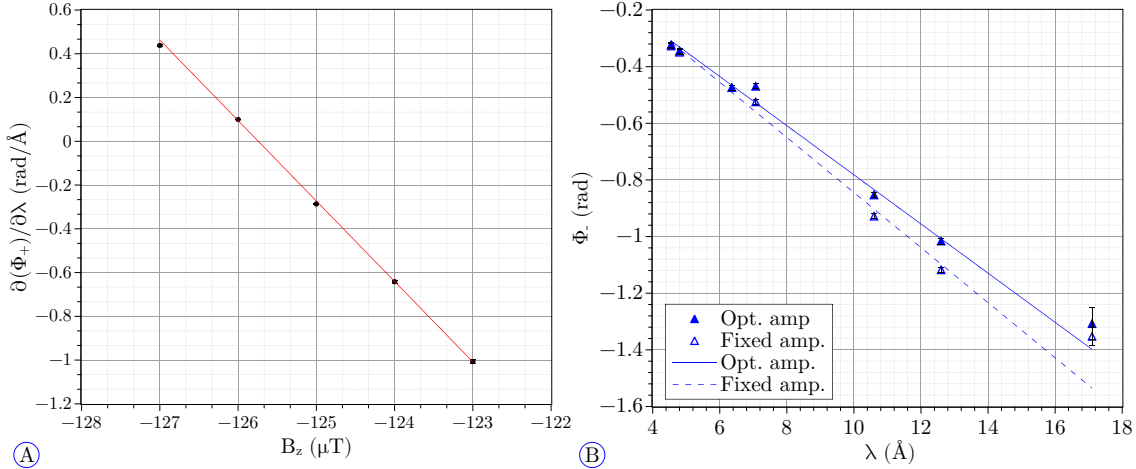


Fig. 5.17: *A)* Slope of the linear fit from Fig. 5.16 for the optimized amplitude of the spin flipper vs. applied magnetic field. A linear fit, red line, is used for the characterization of the setup in Eq. (5.19). *B)* Difference between the top and bottom phase vs. wavelength for $B_z = -127 \mu\text{T}$ for the measurements with optimized and fixed amplitude. The full line is the linear fit on the optimized amplitude measurement and the dash line is the one on the fixed amplitude measurement.

optimal amplitude, one gets

$$\frac{\partial(\Phi_-)}{\partial\lambda} = (86 \pm 4) \text{ mrad\AA}^{-1}, \quad (5.20)$$

which corresponds to a vertical magnetic field gradient of $B_g = (-0.47 \pm 0.02) \mu\text{T}$ over the two beams which are distant of $d_{bt} = 4 \text{ cm}$. This error is scaled with the chi-square, $\chi^2/NDF = 11$, in an attempt to take into account the already mentioned drift. The result for the fixed amplitude measurement is $d(\Phi_-)/d\lambda = (97 \pm 4) \text{ mrad\AA}^{-1}$ with $\chi^2/NDF = 13$. In comparison, the set gradient was $B_G = 1 \mu\text{T}$ over 49 cm which would correspond to a difference in the magnetic field of $0.08 \mu\text{T}$ for the top and bottom beams. This is not compatible with either measured value. The χ^2 also shows that the measurement was not conclusive.

In addition, one can look at the effect of an optimal amplitude on A_0 and A_1 defined by Eq. (4.6). For that, the measurement with $B_z = -126 \mu\text{T}$ is analyzed as it is the closest to resonance. One would expect A_1 closer to zero and a higher A_0 for the measurement with the optimal amplitude than for the measurement with a fixed amplitude. Experimentally, we observe a higher A_0 of the fit function Eq. (4.6) at wavelengths shorter than 6.36 \AA for the measurement with the optimal amplitude of the spin flipper sinusoidal signal with respect to the measurement with a fixed amplitude of the spin flipper sinusoidal signal. A_1 is also closer to 0 for these wavelengths. For the wavelengths longer than 6.36 \AA , it is the opposite. The reverse of behavior around 6.36 \AA cannot be attributed to spin analyzer as the measurement

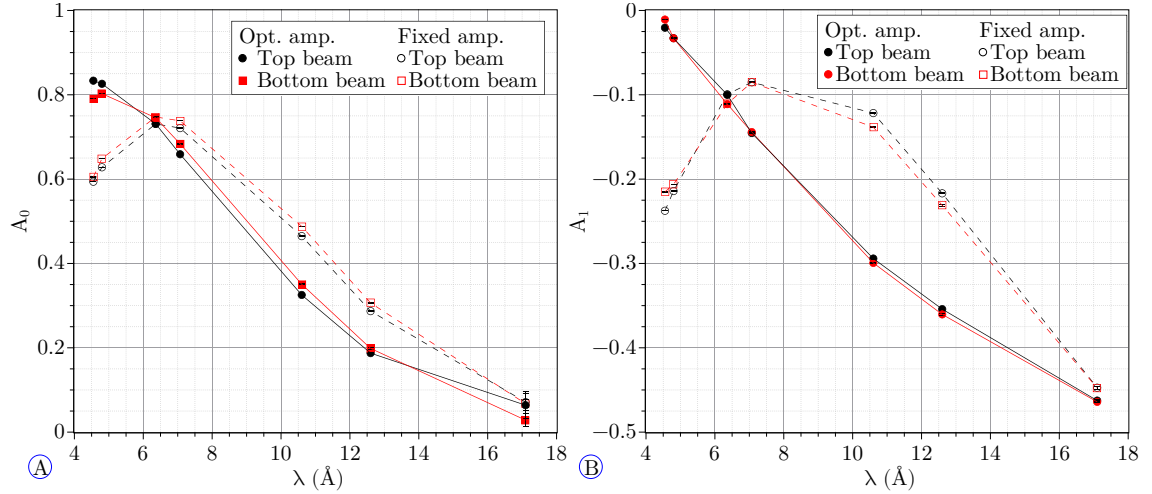


Fig. 5.18: A) Amplitude A_0 of the fit function Eq. (4.6) vs. wavelength for the top and bottom beam for the measurement with fixed and optimized amplitude. B) Offset A_1 of the fit function Eq. (4.6) vs. wavelength for the top and bottom beam for the measurement with fixed and optimized amplitude.

with a fixed amplitude for the sinusoidal signal does not display the same behavior as the measurement with the optimal amplitude.

In conclusion, the measurement was not conclusive. Using the optimal amplitude for the entire spectrum may increase the operational range of the apparatus wavelength-wise when looking at cumulative effects i.e. Φ_+ , and the effect of a non-optimized spin flip on Φ_- might be suppressed but the value of the chi-square prevent any strong claims. In addition, the effect of the optimal amplitude of the sinusoidal signal on the amplitude and offset of Eq. (4.6) is not understood.

5.2.5 Summary

During this beamtime the objectives were partially met. The wavelength selector was characterized and the wavelengths were corresponding to the documentation available during the beamtime. Rabi amplitude and frequency scans were performed on the monochromatic beam for several wavelengths allowing for a determination of the optimal amplitude of the oscillating magnetic field for all wavelengths. A Ramsey scan on a monochromatic beam was performed, with a peak-to-peak amplitude of 1.62 for $\lambda = 4.8 \text{ \AA}$. With the resonance frequency of the apparatus, a magnetic characterization of the setup was performed with a phase scan technique with the optimal and fixed amplitude of the spin flipper sinusoidal signal. However, the measurement was not conclusive due to drift of the magnetic field background. The investigation on the optimal amplitude of the sinusoidal signal sent to the spin flipper will be continued in the following beamtime at PSI where the magnetic field background should be more stable although more in-homogeneous. In addition, the

overall efficiency of the spin analyzer could be characterized at PSI with a pulsed white beam.

5.3 Beamtime 3: PSI 2018

The third beamtime with the Ramsey apparatus was at BOA, PSI in 2018 from 21/09 to the 24/10. The goals of this beamtime were:

- to characterize of the overall spin analyzer efficiency with a pulsed white beam,
- to implement the modulated signal of the spin flippers (detailed in [Sta19]) for a phase scan with a pulsed white beam in order to increase the working range of the apparatus wavelength-wise.
- the characterization of the apparatus with the modulated signal with several phase scan measurements when varying the vertical magnetic field value.
- and the measurement of the $v \times E$ effect as a proof-of-concept of BeamEDM.

The apparatus for this beamtime is 6.455 m long from the chopper to the detector. In comparison for the previous beamtime at PSI, the length was 6.04 m. The main changes in the apparatus for this beamtime are the additional fluxgates and the electrodes to set the electric fields.

A picture of the apparatus is shown in Fig. 5.19. The beam(s) was defined in shape and divergence by four apertures whose characteristics are summarized in Table 5.8. The apertures A3 and A4 were cutting the beam into two smaller ones, called top and bottom beam, in order to do relative measurements. The time-of-flight measurement was performed by a double-slit chopper disk with a rotational frequency of 25 Hz, i.e. a neutron pulse frequency of 50 Hz. The chopper was used for the measurements presented in Section 5.3.2. The measurements presented in Sections 5.3.3 and 5.3.4 were performed with a continuous white beam.

Name	A1	A2	A3	A4
Type	I	II	II	II
Opening width (mm)	40	60	30	30
Opening height (mm)	50	2×10	2×10	2×5
Separation height (mm)		30	30	40
Distance to chopper (m)	-2.12	-0.08	1.33	5.45

Table 5.8: Characteristics of the apertures at BOA in 2018 shown in Fig. 5.19, with their type defined in Section 3.3.3, the width and height of the opening, and the separation in height of the absorbing plate that cuts the beam in two. The aperture A4 initially with two openings of 10 mm height was reduced to 5 mm in order to reduce the neutron background in the detector.

The spin flippers were placed in the middle of the first and last cubes at a distance of (1984 ± 1) mm and (4984 ± 1) mm from the chopper. The signal send to them

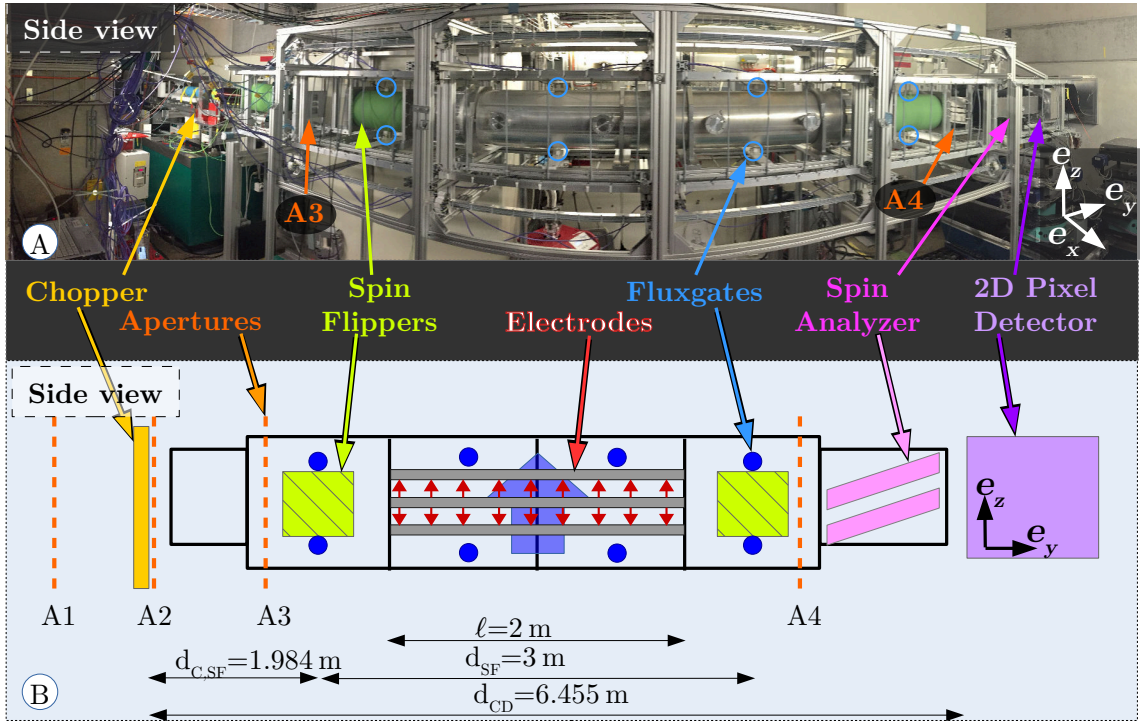


Fig. 5.19: A) Picture of the BeamEDM apparatus at BOA in 2018 with indications for the apertures A3 and A4 and the eight visible fluxgates. B) Sketch of the apparatus with each $(1 \times 1 \times 1) \text{ m}^3$ cube of the structure (including the end pieces) represented by black rectangles, the different apertures represented by orange dashed lines, the position of the fluxgates denoted by the full blue circles, the chopper (yellow box), the spin flippers (slashed green boxes), the electrodes (gray rectangles) with the electric field (red arrows), the analyzer (two parallel pink parallelograms) and the detector (purple cube). The beam goes from left to right. The top and bottom beams are traveling in between the central high voltage electrode and the top or bottom ground electrode, respectively as represented in Fig. 5.25.

was a modulated sinusoidal signal to set the linearly oscillating magnetic field in the direction longitudinal to the beam.

A FLC3-70 fluxgate was placed on the top and the bottom of each spin flipper, separated in height by about 36 cm. The idea was to monitor the field as close as possible to the spin flippers. Four additional ones were placed in the apparatus, with a height separation of about $d_{FG} = 49 \text{ cm}$, as represented in Fig. 5.19.B. The magnetic field was stabilized over the average of these four at $B_z = -125 \mu\text{T}$ for the vertical component and $B_y = B_x = 0 \mu\text{T}$ for the longitudinal and transversal component, and a gradient of $B_G = 0 \mu\text{T}$. All fluxgates were centered in the traversal and longitudinal axis with respect to their cube.

The vacuum pipe was placed in between the spin flippers in order to decrease the neutron scattering in air and to hold the high voltage stacks. Two stacks of mechanically polished electrodes were used, see Fig. 3.12. The inclusion of electrodes and the vacuum pipe increases the statistics by 50 %. We know from a similar relative

measurement at BOA in 2017, that adding the vacuum pipe alone increases statistics by 30 %. Thus, one can estimate that electrodes alone increase the statistics by 20 %.

The spin analyzer was installed in the last 1 m long cuboid of the aluminum structure. The mirrors were set in an almost parallel configuration, reflecting the neutrons vertically in the detector such that the reflected spots are always above transmitted spots of a same beam.

5.3.1 Characterization of the neutron spots in the detector

A time-of -flight measurement was performed with the adiabatic spin flipper (AFP) off and on without any additional spin flip from SF1 or SF2 in order to define the contours of the beam spots and their spectrum. We can define for this beamtime that AFP=off leads to reflection of the beam. Inversely, AFP=on leads to a transmission of the beam by the spin analyzer mirror. This is represented by the ideal case in [Fig. 5.2](#).

Spot	Top Trans.	Top Ref.	Bottom Trans.	Bottom Ref.
Bottom left corner	(3;12)	(3;9)	(3;6)	(3;3)
Top right corner	(13;13)	(13;10)	(13;7)	(13;4)

Table 5.9: *Definition of the beam spots by the coordinate of the bottom left and top right corners in units of pixel, with a parallel configuration of the spin analyzer.*

First, the spots for the different spin states of each beam are defined by a rectangular shape shown in [Fig. 5.3A&B](#) and summarized in [Table 5.9](#). It is interesting to note that the background level in the transmitted spot in [Fig. 5.20B](#) is not negligible. This can be due to the same reasons developed in [Section 5.1.1](#): the polarization of the beam, the efficiency of the spin analyzer at high and low wavelength, and potentially the cross contamination between the spots. In addition one can consider the case where the mirrors do not fully cover the beams. Part of the beam would not be analyzed and these neutrons would be counted in the transmitted spots independently of the AFP configuration. The effect of this would be the same as the one described for an asymmetric cross-contamination. This is what is observed in [Fig. 5.20C](#) and D. In the transmitted mode (AFP=on) the spectrum of the transmitted and reflected beam are similar to the ideal case with only 3 % of the counts in the reflected spot at $\lambda = 4 \text{ \AA}$. In the reflected mode, about 45 % of the counts is in the transmitted spot at $\lambda = 4 \text{ \AA}$. Here again, all the effect will be grouped under the name "overall spin analyzer" efficiency.

To quantitatively characterize the overall spin analyzer, the "AFP asymmetry" defined in [Eq. \(5.1\)](#) is then calculated with the result shown in [Fig. 5.20D](#) for

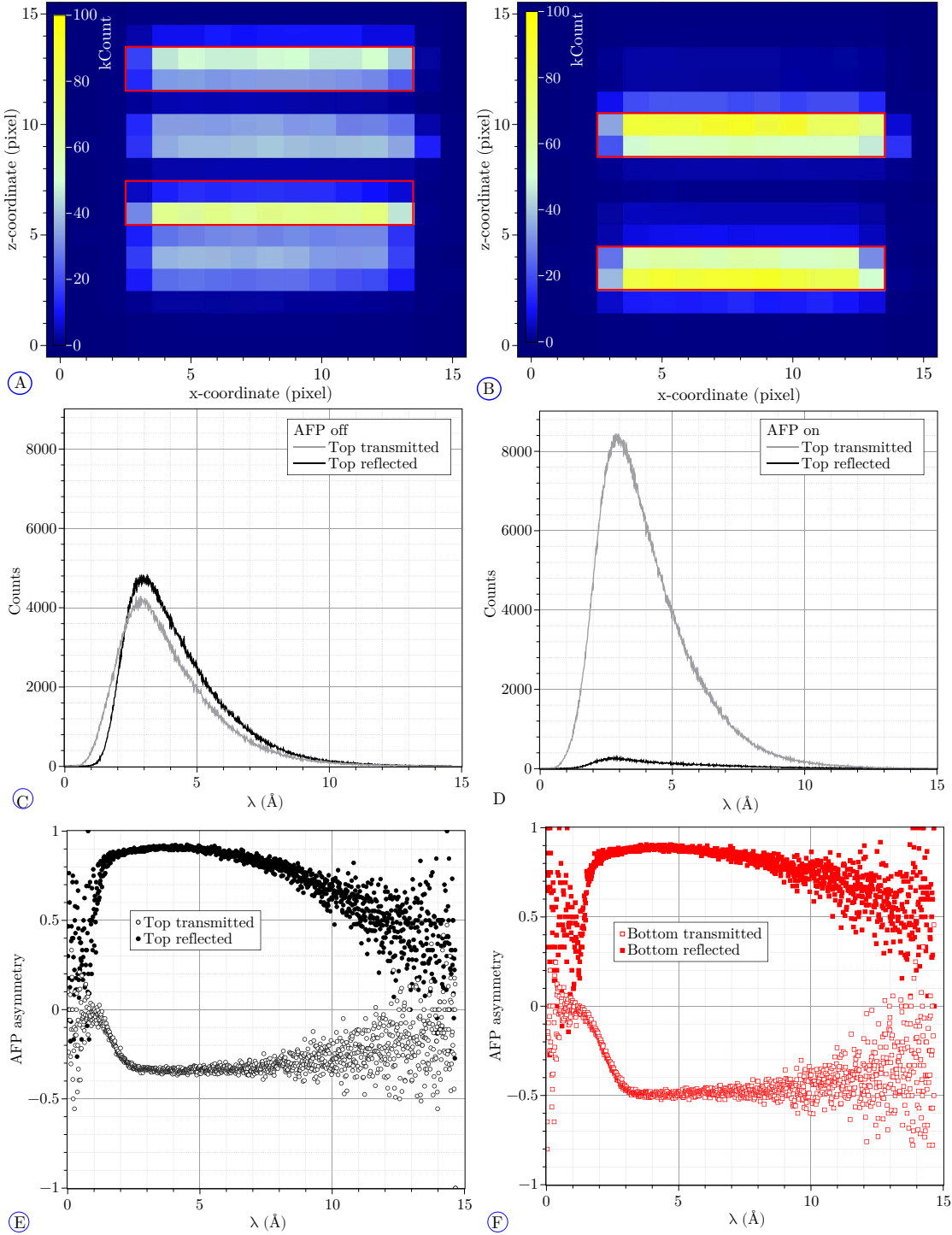


Fig. 5.20: *A and B) Neutron counts in the detector pixels integrated over wavelength with the adiabatic spin flipper off and on, respectively. The red rectangles represents the different spots. The same color scale was used for the two figures for a direct comparison. C and D) Number of integrated counts over the top reflected and top transmitted spots versus the neutron wavelength for the adiabatic spin flipper (AFP) off and on, respectively. The same scale was used for the two figures for a direct comparison of the numbers. E and F) AFP asymmetry for all spots versus the neutron wavelength for the top and bottom beams, respectively.*

each spot as a function of the wavelength. The maximum efficiency is around 0.9 for the reflected spots but only 0.3 and 0.5 for the top and bottom transmitted spots respectively. This will reduce the amplitude of the signal from the phase scan measurements. One can none-the-less estimate a working range of the spin analyzer from 2 Å or 3 Å to about 10 Å from the plateau in Fig. 5.20E and F.

5.3.2 Measurements with modulated signal

In continuation of the work at PF1b, ILL, a phase scan with optimal amplitudes of the spin flipper signal for a broad range of wavelengths was attempted with a pulsed white beam. To do so, a modulated sinusoidal function Eq. (3.2) and shown in Fig. 3.9 was programmed in the waveform generators with a different envelop for SF1 and SF2 to take into account the broadening of the spectrum with distance.

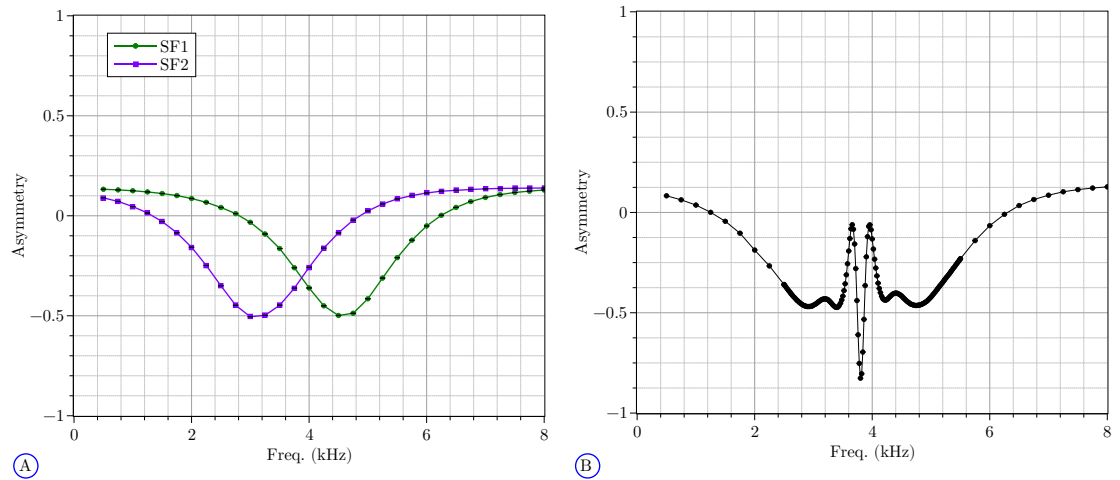


Fig. 5.21: A) Asymmetry of the top beam vs spin flipper frequency for the SF1 and SF2 for a Rabi measurement with a continuous white beam. B) Asymmetry of the top beam vs spin flipper frequency for a Ramsey measurement with a continuous white beam.

The signal sent to the spin flippers was triggered for each neutron pulse: the sinusoidal part of the signal always had the same phase with respect to the chopper pulse. Due to this complete synchronization, the neutrons of a given wavelength would always see the same portion of the sinusoidal signal. For example all the neutrons with a wavelength λ_0 will see a field generated by a sinusoidal function $\sin(x)$ for x between 10° to 190° . As the measurement is done with a pulsed white beam, the range x scans the sinusoidal function continuously as a function of the wavelength. This is important as it is visible in the neutron phase signal.

Configuration of the spin flipper signal

Before using the modulated signal the resonance frequency of each spin flipper was determined to be at 4.5 kHz for SF1 and at 3 kHz for SF2 from the Rabi frequency scans with a continuous white beam presented in [Fig. 5.21A](#). The resonance frequency of the Ramsey apparatus was measured at $f_0 = 3.8$ kHz from a Ramsey scan with a continuous white beam presented in [Fig. 5.21B](#). The configuration of the spin flipper and determination of the parameters of the modulated signal is documented in [\[Sta19\]](#). In this section, a summary of the measurement done to find the result is given.

First, a Rabi frequency technique was performed on each spin flipper with an amplitude of 0.15 V, but in this case, with a pulsed beam. The resonance frequency was measured to be 4.6 kHz for SF1 and 3.2 kHz for SF2. A Rabi amplitude scan was then performed on each spin flipper at their respective resonance frequency and was analyzed as a function of the wavelength. The optimal amplitude of each spin flipper was extracted for two wavelengths to extrapolate the parameters of the modulated signal for each spin flipper. A scan of each parameter of [Eq. \(3.2\)](#) was then performed with a Rabi technique on their respective resonance frequency to find the optimal set of parameters for each spin flipper individually. The goal was to have a set of parameters for which a broad part of the neutron spectrum undergo a $\pi/2$ flip characterized by $A_{AFP} = 0$ where A_{AFP} is defined in [Eq. \(5.1\)](#).

Finally, the scans of the parameters were repeated with a Rabi technique at 3.8 kHz, the resonance frequency of the Ramsey apparatus, to determine the optimal set of parameters for the full apparatus and the phase scan measurements. These parameters are summarized in [Table 5.10](#), and one can note that the p parameter does not correspond to the expected value of one. This is due to the inhomogeneity of the magnetic field, the optimal amplitude for the spin flippers follows [Eq. \(2.20\)](#) instead of $\tau\omega_1 = \pi$.⁹

	f_0 (Hz)	Amp. (V)	t_0 (ms)	t_1 (ms)	p
SF1	3800	1	0.58	0	0.45
SF2	3800	0.95	2.24	0	0.70

Table 5.10: Parameters of the modulated signal defined in [Eq. \(3.2\)](#), for each spin flipper. One should keep in mind that the frequency is the same for the two spin flippers in order to perform a Ramsey technique, however, it is only the resonance frequency of the apparatus and not of each spin flipper due to the magnetic inhomogeneity.

⁹Formula for a π flip on each spin flippers, a discussion about the formula for a $\pi/2$ flip is available in [\[Sta19\]](#).

During this beamtime, the change of the phase between the two spin flippers was done by adding a delay in the signal sent to SF2. This had the inconvenience of shifting the envelop of the modulated signal which is not optimal.

Working range of the apparatus

To define the working range of the apparatus, the phase scan close to resonance was analyzed according to [Chapter 4](#). It was performed with the characteristics of the spin flipper state in [Table 5.10](#), a vertical magnetic field of $B_z = -125 \mu\text{T}$, and no gradient field. The asymmetry A as a function of the phase between the spin flippers θ_{RF} is fitted by [Eq. \(4.6\)](#) for each wavelength.

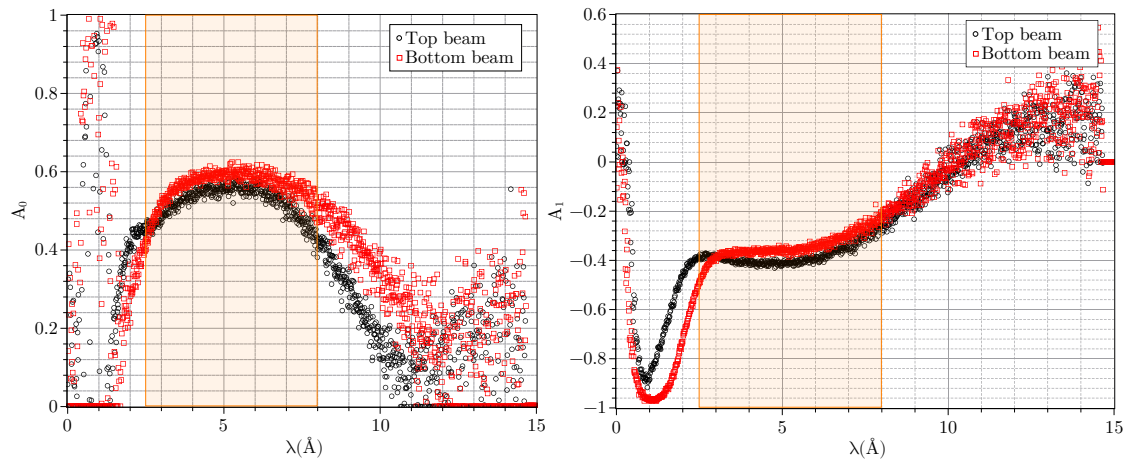


Fig. 5.22: *A)* Amplitude of the fit function [Eq. \(4.6\)](#) vs. wavelength *B)* Offset of the fit function [Eq. \(4.6\)](#) vs. wavelength. The orange squares define the working range.

The amplitude A_0 and the offset A_1 are displayed in [Fig. 5.22](#) as a function of the wavelength for the top and bottom beam. There are several key elements on these plots:

- The offset, A_1 , from the bottom beam is shifted horizontally with regards to the top beam. This is due to the different incident angle for the top and bottom mirrors of the spin analyzer. This is also visible in the A_0 figure and in [Fig. 5.20](#) where the maximum AFP asymmetry is achieved at lower wavelength for the top beam than for the bottom one.
- A plateau in the offset around -0.4 defines the working range of the apparatus, $\lambda = [2.5; 8] \text{ \AA}$. This range corresponds to an offset changing by less than 0.2.
- The value of the offset in that range is -0.4 ± 0.2 . This value is partially due to the efficiency of the spin analyzer, some neutrons are always transmitted

as it is visible in all the plots of [Fig. 5.20](#). But it is also due to an improper setting for the spin flippers due to the inhomogeneity visible in the difference of resonance frequency of the individual spin flippers. The maximum value for amplitude, A_0 , in that range is only 0.6, for the same reason.

- The behavior of A_0 and A_1 in [Fig. 5.17](#), determined from the beamtime at PF1b, ILL in 2018 with the optimal amplitude is not reproduced.

The phase sum Φ_+ is not linear with the neutron wavelength but shows a "long term oscillation" in the working range of the apparatus. This could be the result of two effects:

- Until this beamtime, it was always assumed that the data could be represented by a cosine or "improved" fit function, defined in [Eqs. \(4.5\)](#) and [\(4.6\)](#), whose phase is linear with the neutron wavelength. In practice this assumption corresponds to an off-resonance magnetic field of same magnitude but opposite sign at the position of the two spin flippers. A simulation in [Appendix A](#) shows that if the previously stated condition is not fulfilled and the amplitude of the spin flippers is not optimal, the neutron phase does not have a linear behavior as a function of the wavelength.
- The neutrons may see a different amplitude in SF1 and SF2 due to the difference in the p parameter and the delay in the signal sent to SF2 to perform a phase scan. To confirm this, a measurement or simulations should be performed.

This effect is suppressed by taking the phase difference, [Fig. 5.23B](#). A linear fit in the region of interest gives $\partial(\Phi_-)/\partial\lambda = (47.3 \pm 0.6)$ mrad/Å which is equivalent to a magnetic gradient of $B_g = 0.3$ µT over the distance center to center of the beams $d_{bt} = 40$ mm. The reduced chi-square $\chi^2/NDF = 576/447 = 1.29$ shows that the effect of the "long term oscillation" is reduced¹⁰.

In addition, one can see decaying fast oscillations at low wavelength in [Fig. 5.23A](#) zoom. As an empirical approach, the oscillations can be fitted with

$$\Phi_+ = (K_1 + K_2/\lambda) \cos(2\pi\lambda f_{\text{A}} + K_3) + K_4\lambda + K_5, \quad (5.21)$$

where K_i with $i \in [1; 5]$ and f_{A} are the fit parameters, recorded in [Table 5.11](#). The $1/\lambda$ modulation of these fast oscillations hint towards a time-of-flight dependent effect. Moreover, the approximate wavelength at which the signal faints away is $\lambda = 2.4$ Å, which is close to $\lambda_c = 2.6$ Å, the wavelength for which the neutrons see a full period of the oscillating magnetic field $T = 1/f_{RF} = 2.6 \times 10^{-4}$ s for a spin

¹⁰With 447 degrees of freedom, one would expect a reduced chi-squared between 0.8 and 1.1 for a two sigma band.

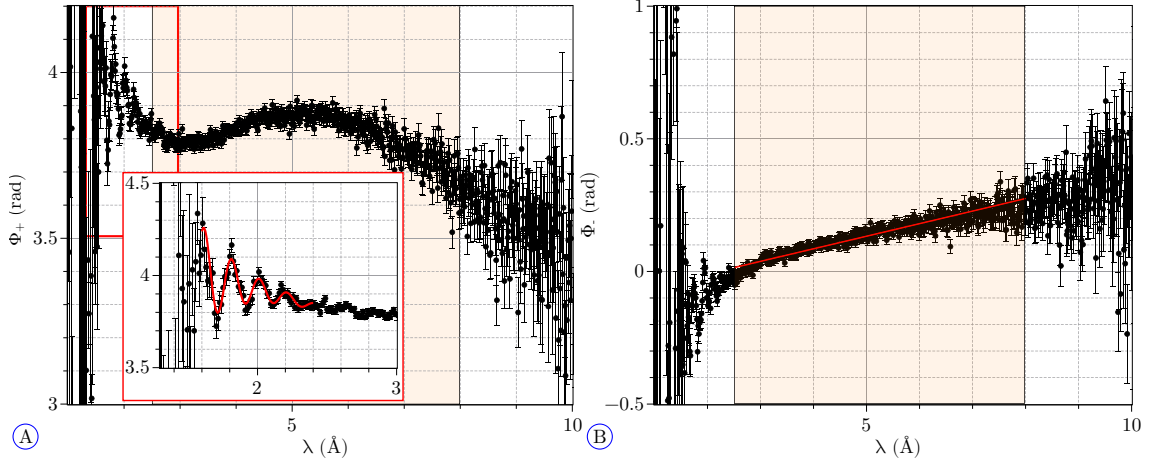


Fig. 5.23: A) Neutron phase sum between the top and bottom beam Φ_+ vs. wavelength. The insert in the middle is a zoom on the phase sum signal on the region represented by a red square. B) Neutron phase difference between the top and bottom beam Φ_- vs. wavelength. The orange squares define the working range defined from the amplitude and offset in Fig. 5.22

flipper length of $\ell_{SF} = 0.4$ m. In addition, the frequency from the fit corresponds to 3.84 ± 0.07 kHz, when converted in Hz at the position of SF2, i.e. where the final spin state is defined.¹¹ This analysis was actually performed with the unconverted time-of-flight data to avoid additional errors coming for the conversion from time-of-flight to wavelength and back to time or in this case frequency. As a reminder, the frequency of the sinusoidal signal sent to the spin flippers is $f_{RF} = 3.8$ kHz.

Parameters	$f_{\text{A}} (\text{\AA}^{-1})$	K_1	$K_2 (\text{\AA})$	K_3	$K_4 (\text{\AA}^{-1})$	K_5
Value	5.13	0.43	-1.0	21	0.22	4.35
Error	0.08	0.05	0.1	1	0.02	0.04

Table 5.11: Value of the fit parameters from Eq. (5.21) for the fast oscillation in the neutron phase at BOA in 2018.

The current hypothesis is that this effect is coming from an improper spin flip for the neutrons that see less than an oscillation. This is explained here after and compared to the already stated observation on the Fig. 5.23. The signal sent to the spin flippers was repeated for each neutron pulse. This synchronized the sinusoidal signal with the neutron pulses, therefore, the neutrons with wavelengths smaller than λ_c would always see the same incomplete portion of one oscillation. Because of the time-of-flight technique, two neutrons with different wavelengths would arrive at different times at the spin flippers and see a different starting point of the oscillations. Extending that consideration to a wide spectrum, the starting point of the oscillations

¹¹ f_{A} is measured in \AA^{-1} , to convert it into frequency one needs to use a distance: $f_{\text{A}} [\text{\AA}^{-1}] \times 3956 = d [\text{m}] \times f_0 [\text{Hz}]$

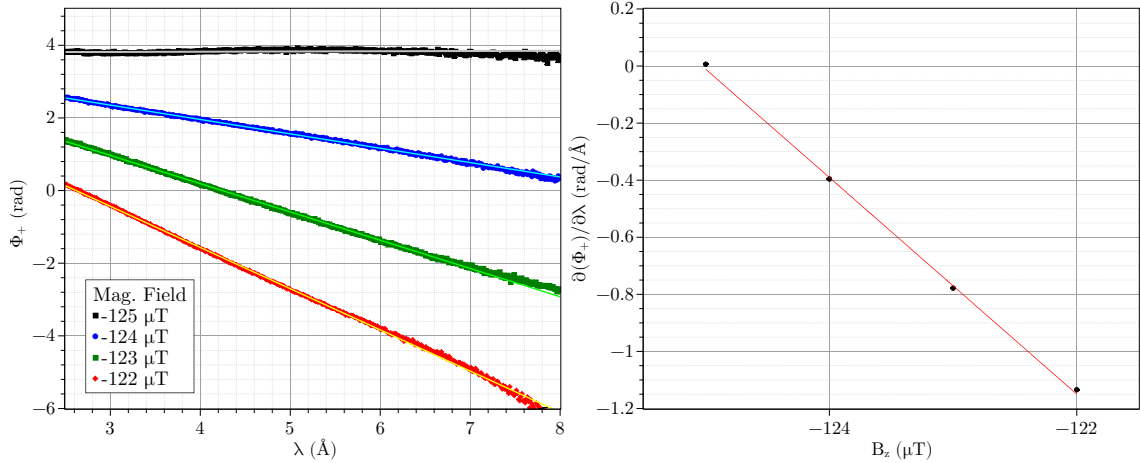


Fig. 5.24: A) Neutron phase sum vs. wavelength for different magnetic fields, using the modulated signal for the phase scan. B) Slope of the neutron phase difference as a function of magnetic field. The statistical error bars are included but not visible.

that the neutrons see would sample continuously the sinusoidal signal as a function of the neutron wavelength, which probably explains the fast oscillation on the neutron phase, hence the frequency of these oscillation of (3.84 ± 0.07) kHz when extracted at the SF2 position. The decay of the oscillations is also compatible with the idea of an improper spin flip due to the fact that the neutrons only see a partial oscillation of the spin flippers field. Indeed, the portion of the signal that the neutrons see is inverse proportional to their wavelength. This hypothesis is reinforced by the fact that these oscillations were not visible on other measurements, e.g. Fig. 5.6, where the sinusoidal signal is not synchronized with the neutron pulse.

Magnetic scan

Even if the neutron phase does not behave linearly, one can still take this assumption to evaluate the deviation for the expected behavior. This can be seen in some way as a proof by contradiction. This was done by scanning the magnetic field from $B_z = -122$ µT to $B_z = -125$ µT in steps of -1 µT and with $B_z = -125$ µT being our resonance configuration with no gradient. The phase sum Φ_+ was analyzed in a similar manner as in Section 5.1.4. Fig. 5.24A shows the result of the measurement. A linear fit has been performed and the slope recorded in Fig. 5.24B. From Eqs. (4.12) and (5.3), one would expect

$$\left. \frac{\partial^2(\Phi_+)}{\partial\lambda\partial(\delta B_0)} \right|_e = (-277.9 \pm 1) \text{ mrad}\text{\AA}^{-1}\text{\mu T}^{-1} \quad (5.22)$$

where δB_0 is the deviation for the off-resonance field common to the top and bottom beam. From the measurement, one gets

$$\left. \frac{\partial^2(\Phi_+)}{\partial \lambda \partial(B_z)} \right|_m = (-380 \pm 8) \text{ mrad}\text{\AA}^{-1}\mu\text{T}^{-1}, \quad (5.23)$$

where the error is the statistical error scaled by the chi-square to take into account the error coming for the linear fit model, where $\chi^2/NDF = 162$. The discrepancy between the two values and the chi-square clearly show that the analysis and/or the technique did not work properly. It is interesting to note that, the phase scans from the previous beamtime at BOA in 2017 gave a better result, Eqs. (5.7) and (5.8), although on a shorter range of wavelengths and on a measurement without modulated signal. This discrepancy did not occur either at PF1b in 2018, Eqs. (5.18) and (5.19).

5.3.3 vxE effect measurement with a white beam

One of the main challenges for measuring an EDM, that beam experiments have faced, is the $v \times E$ effect. In order to characterize this effect on the apparatus, the $v \times E$ effect was measured as a function of the applied electric field. This measurement was performed with a continuous white beam to gain in statistics, therefore, the signal sent to the spin flippers was not modulated but a simple sinusoidal signal. The main magnetic field was set to the transversal direction ($B_z = 0 \mu\text{T}$, $B_x = 120 \mu\text{T}$, $B_y = 0 \mu\text{T}$) in order to maximize the $v \times E$ effect on the neutron spin, as represented Fig. 5.25. Due to a saturation in the coil power supplies and a strong magnetic field background, the vertical gradient field could not be set to 0, therefore, it was stabilized at $B_G = +8 \mu\text{T}$. The resonance frequency for this field configuration was measured with a Ramsey technique at $f_0 = (4.1 \pm 0.1) \text{ kHz}$ where the error is estimated from the frequency scan step size. It is interesting to note that the transversal coil does not behave like the vertical coil: for a lower set field in the transversal direction than the vertical one, the neutrons have a higher Larmor frequency. The geometry of the coils and fluxgates is optimized for the vertical direction.

The delivered voltage to the central electrode was scanned from -30 kV to +30 kV with intermediate steps at 0 kV, $\pm 15 \text{ kV}$, and $\pm 25 \text{ kV}$ with the outside electrodes at ground with a 1 cm separation (surface to surface) from the high voltage electrode. For each high voltage configuration, several phase scans were performed in order to have high enough statistics. Making a single long measurement was not optimal as one could not correct for magnetic drifts. Assuming that all other fields are negligible compared to the transversal magnetic field: $B_x \gg B_{v \times E}$ where $B_{v \times E}$ is the pseudo magnetic field from the $v \times E$ effect defined in Eq. (2.17), and $B_x \gg B_g$, the neutron phase of the top and bottom beam can be derived from Eqs. (4.15) and (4.16) into:

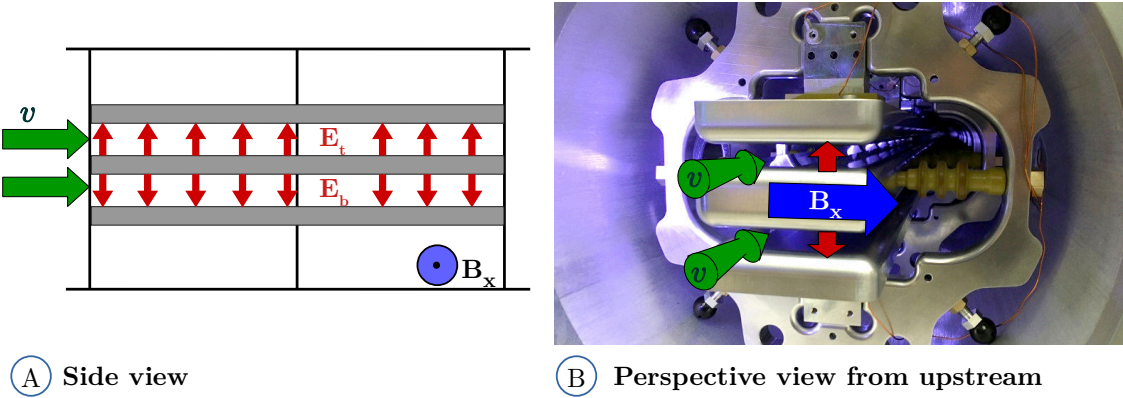


Fig. 5.25: A) Sketch of the central part of the apparatus with the electrodes, the electric field, magnetic field, and the neutron velocity v for the two beams. The two cubes that hold the electrodes are presented by black lines. B) Picture of the electrodes inside a vacuum pipe with the same labels for the fields and velocity as in A.

$$\begin{aligned}\varphi_t(\delta B_0, B_g, E) &\approx \gamma_n \left(\delta B_0 + \frac{B_g^2}{6B_x} \right) T + \gamma_n \frac{\ell E_t}{c^2}, \\ \varphi_b(\delta B_0, B_g, E) &\approx \gamma_n \left(\delta B_0 + \frac{B_g^2}{6B_x} \right) T + \gamma_n \frac{\ell E_b}{c^2},\end{aligned}\quad (5.24)$$

with δB_0 the deviation from the resonance field common to the top and bottom beam, B_g is the vertical field gradient over the distance of the top and bottom beam, E_t the electric field seen by the top, E_b the electric field seen by bottom beam, $\ell = (2000 \pm 1)$ mm the length of the electrodes, and T the interaction time within the magnetic field. For this calculation, it is assumed that the top and bottom beam are sensing an opposite electric field of same strength $E_t = -E_b = E$. The difference between the two phases, Φ_- , should be proportion to the electric field with the expected value:

$$\left. \frac{\partial(\Phi_-)}{\partial E} \right|_e = \frac{\partial(\varphi_t - \varphi_b)}{\partial E} \approx -\gamma_n \frac{2\ell}{c^2} \approx (-815.6 \pm 0.4) \mu\text{rad}/(\text{kV}/\text{cm}) \quad (5.25)$$

where the error is coming from the error on ℓ .

Each phase scan of the measurement with a given electric field was analyzed independently, in order to correct for magnetic drifts that happen on a time scale longer than a phase scan. The result in Fig. 5.26 is the (non-weighted) average of the phase difference for each electric field. The dominant error of the measurement is not coming from statistics but from random shift of the neutron phase probably due to magnetic field gradient drifts. The assumption of a random behavior for these drifts is important as it is the base of the following error calculation. The error of each data point was computed as the standard error of the mean of the dataset

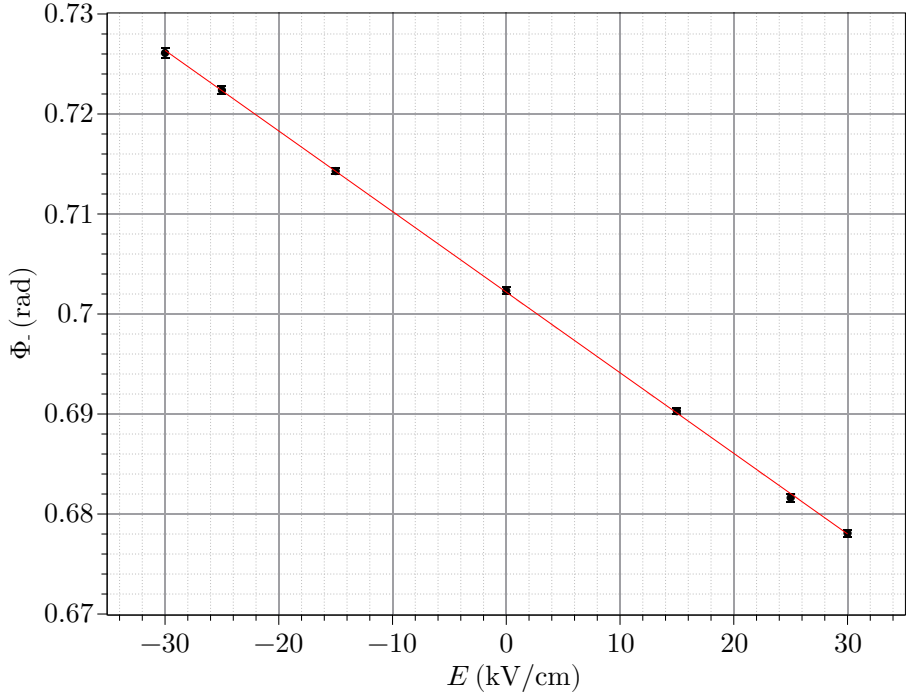


Fig. 5.26: Φ_- vs. applied electric field E for a continuous white beam and a non-modulated sinusoidal signal sent to the spin flippers for the phase scans.

used to compute the average.¹² The slope of the linear fit of the phase difference vs. electric field gives

$$\left. \frac{\partial(\Phi_-)}{\partial E} \right|_m = (-805 \pm 6) \mu\text{rad}/\text{kV}, \quad (5.26)$$

with a $\chi^2/NDF = 2.043/5 = 0.409$.¹³ The central value differs from the expected value by less than two sigma. This could be due to statistical effect or can be explained by a misalignment between the magnetic and electric field of $\beta = 0.6^\circ$. The offset of the linear fit is due to the magnetic field gradient.

5.3.4 Investigation on the EDM measurement procedure

The current procedure of an EDM measurement is a repeated phase scan. The new idea investigated here is the measurement of the asymmetry at a fixed phase. Any change in the asymmetry value is converted into a neutron phase using the amplitude,

¹²The standard error of the mean (STM) is an indicator of the possible discrepancy between the mean value of a finite number of elements and that of an infinite number of elements. It is related to the standard deviation (STD) by $STM = STD / \sqrt{N}$, where N is the number of sample averaged over.

¹³The reduced chi-square distribution has an expected standard deviation of $2/\sqrt{NDF}$ which here is 0.63.

offset, and distortion parameters of Eq. (4.6), determined by a fit of a reference phase scans.

The measurement would start and end with one or several reference scans in order to get the fit parameters from Eq. (4.5) or Eq. (4.6). In between, the neutron asymmetry would be measured at a fixed phase between the two spin flippers, chosen at the most sensitive point (usually around $\theta_{RF} = \pi/4$). Any change in the neutron precession frequency would change the recorded asymmetry. This change in asymmetry is then converted in neutron phase φ with the fit parameters from the phase scans.

This could be done with the datasets from the $v \times E$ effect as it is composed of several phase scans that will be considered here as a succession of individual measurements at one phase. In order to be independent of the electric field, the analysis was performed on the data with a zero field. The fit parameters from Eq. (4.6) were determined either on the first or last phase scan for comparison. Then the value of the neutron phase was determined using the fit parameters from the first phase scan shown in Fig. 5.27A and the last phase scan, shown in Fig. 5.27B. If the procedure is successful they should have the same behavior, reproducing the magnetic field fluctuations. This is not the case. An overall trend is common to the two plots and shows a jump in magnetic field during the first two phase scans but the plots differs by an oscillation mostly visible in Fig. 5.27A. To characterize it, the difference of the phase from the two plots was computed and is shown in Fig. 5.27C. The oscillation is clearly visible in this figure. It has a periodicity of 1 phase scan and a decaying amplitude. As the initial data are the same the only cause of these oscillation is the analysis. The already mentioned important drift in magnetic field during the first (and second) phase scan distorted the signal of asymmetry vs θ_{RF} from which the fit parameters are estimated. Indeed, each datapoint of this phase scan corresponds to a cosine function with a different phase. Thus, the parameters extracted from this phase scan do not represent the rest of the dataset correctly and induced the described artifact. It seems that the artifact is only present for Fig. 5.27A. The parameters extracted from the last phase scan seems to represent the data correctly when the magnetic field is stable (phase scan number > 2) as no oscillation is visible in that region of Fig. 5.27B.

In conclusion, this type of analysis or measurement is possible. However, if the magnetic field is not stable over the phase scan that determines the fit parameters, then they (i.e. the fit parameters) do not correspond to the data and an artifacts might add an offset in the signal. If this is not fully compensated by the subtracted the signal from the bottom beam, it could lead to a systematic effect if it is correlated to an electric field reversal.

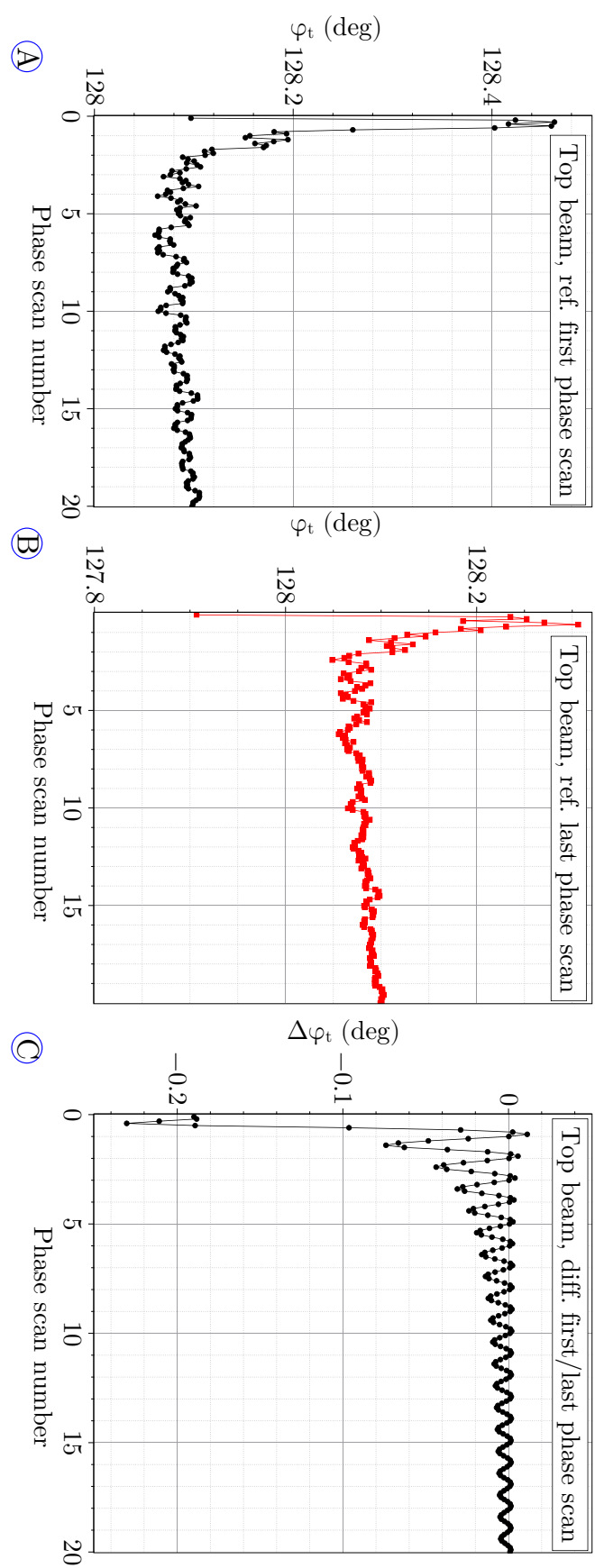


Fig. 5.27: A) Neutron phase for the top beam vs. phase scan iteration number when the fit parameters are estimated from the first phase scan. B) Neutron phase for the top beam vs. phase scan iteration number when the fit parameters are estimated from the last phase scan. C) Difference of the neutron phase of the top beam determined in A) and B).

5 .3.5 Summary

This beamtime was the most challenging one and not all the goals were met. The group had to face a lot of issues and unexpected equipment break downs. However, for the first time, a measurement was done with high voltage electrodes in the system. The addition of the electrodes led to an increase in statistics of about 20 %. A stable field of 30 kV over 1 cm could be achieved. A first characterization of the $v \times E$ with a continuous white beam was performed by ramping the electric field in an orthogonal configuration with the magnetic field. In addition, from the $v \times E$ measurement, a preliminary investigation on a different measurement technique for the EDM, involving a measurement at a fixed phase between the spin flippers, was started for the next beamtime. Besides, even if the modulated signal technique did not give the expected result due to the inhomogeneity of the magnetic field, experience has been gained. To solve the inhomogeneity of the magnetic field, a magnetic shielding will be installed in the following beamtime. To reduce the fast oscillation seen in [Fig. 5.24](#), a different technique to generate the modulated signal was developed and a higher magnetic field will be set so that no neutrons in the working range of the analyzer will see less than one period of the oscillating magnetic field.

5.4 Reflectivity measurement: PSI 2018

To characterize the neutron reflectivity of the electrodes and define their angular acceptance, a measurement was performed at the Narziss beamline, PSI, on the 06/12/2018.

Narziss is a reflectometer with (potentially polarized) neutrons of $\lambda = 5 \text{ \AA}$. It has an integrated monitor counter, its own neutron detector, a support to install a sample in the center of the beamline, and several apertures to define the angular acceptance of the beam. The detector is on a support that can rotate around the central point of the beam line i.e. around the sample, see Fig. 5.28. The sample support can also rotate around that central point. A picture of the setup is displayed in Fig. 5.28.

We define in this section: θ_S the angle between the sample and the beam, θ_D the angle between the detector and the beam, and θ_c the critical angle of the material.

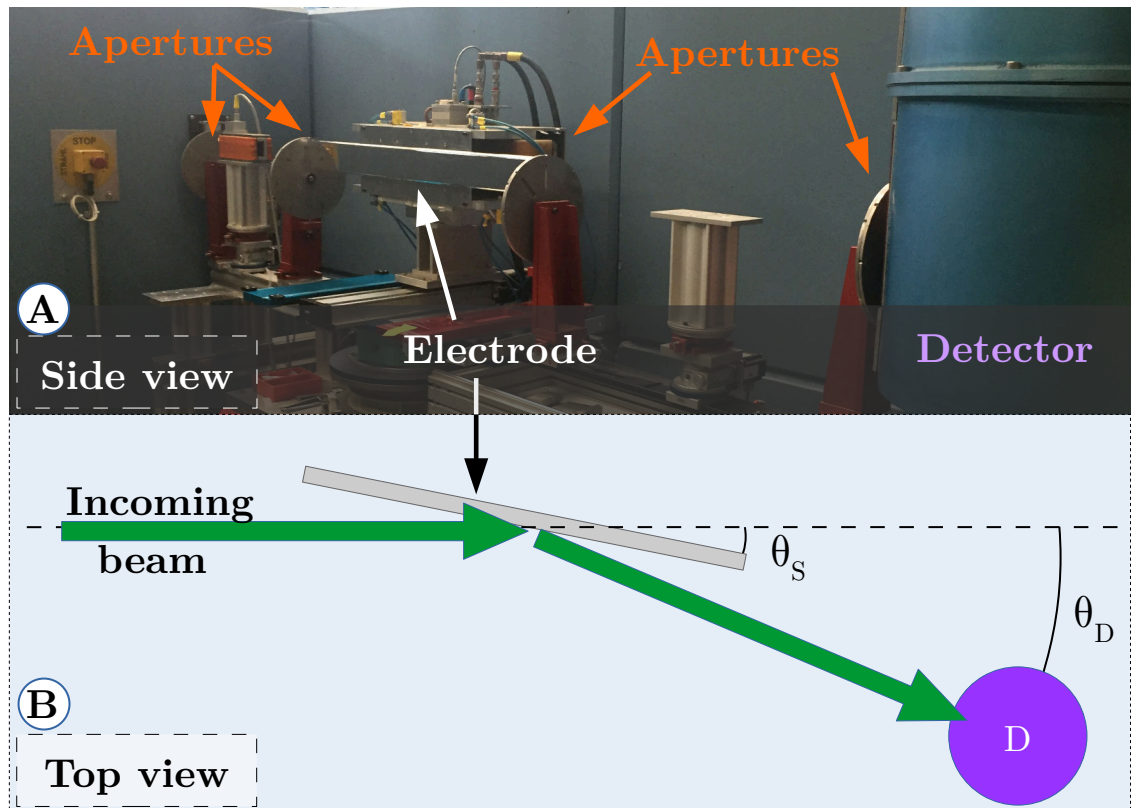


Fig. 5.28: A) Picture of the Narziss beamline during the reflectometry measurement with labels for the apertures, the electrode, and the detector. B) Schematic of the measurement seen from the top, where the green arrows represent the neutron beam, the gray rectangle is the electrode, and the purple circle is the detector. The incident angle between the incoming neutron beam and the electrode is denoted by θ_S and the angle between the incoming neutron beam and the detector is denoted by θ_D .

Several samples were measured:

- a $m=3$ super-mirror¹⁴ from the Swiss Neutronics (SN 17040/16088) whose length is shorter than the other samples,
- a float glass plate, i.e. un-coated, from the beamline,
- BeamEDM electrode (Al, $V_F = 50\text{neV}$) without surface finishing , i.e. rough surface,
- BeamEDM electrode (Al, $V_F = 50\text{neV}$) after mechanical polishing.

Each of them was measured in two modes.

$\theta - 2\theta$ mode

In this measurement mode, the angle between the detector and the incoming beam is twice the angle between the sample and the incoming beam, i.e. $\theta_D = 2\theta_S$. In such a situation, assuming total, specular reflections, the beam is reflected into the detector and the number of counts, normalized by the monitor count, is high. By scanning θ_S , one measure the critical angle θ_c of the material at 5 Å, defined in Eq. (2.5).

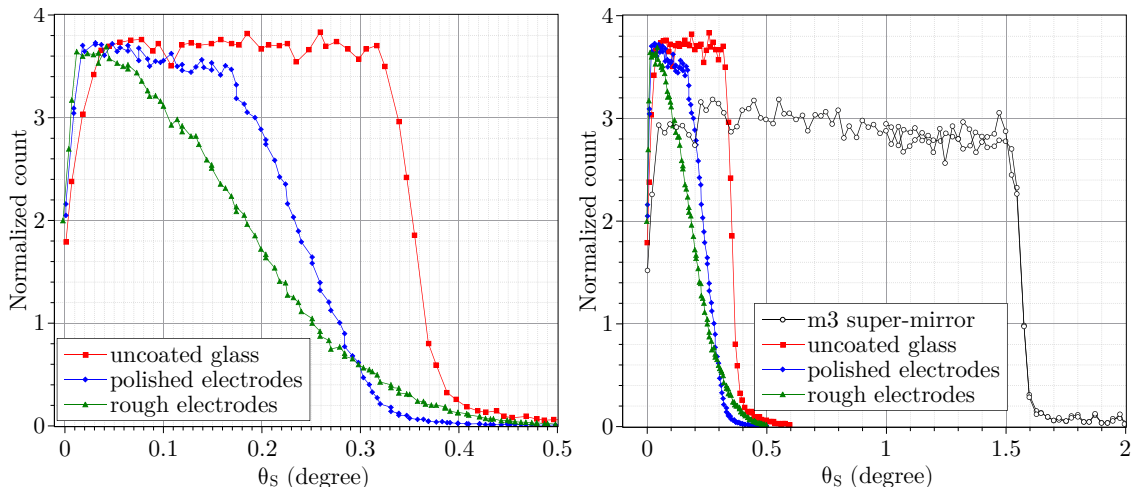


Fig. 5.29: A) Normalized number of counts vs θ_S for the different samples for a measurement in $\theta - 2\theta$ mode without the $m=3$ super-mirror for visibility. B) Same plot with the $m=3$ super-mirror for comparison.

The four samples have different behaviors and Fig. 5.29 can be analyzed via several parameters:

- The maximum number of counts: The glass sample and both electrodes have the same normalized maximum number of counts which means that the full beam is reflected (total-reflection). The $m=3$ super-mirror has a lower number

¹⁴The m-value is defined in Eq. (2.8).

of counts. This is due to a smaller aperture setting for this sample because of its shorter length.

- The slope of the drop in number of counts: The glass plate and the super-mirror have a very steep drop in their normalized counts close to their critical angle whereas the electrodes have an elongated one. This is due to the surface quality of the material. On a microscopical scale, part of the material has a different incident angle with respects to the beam which decreases the effective specular reflection observed in the detector. This elongated drop makes the determination of the critical angle more difficult.
- The half-maximum intensity: It corresponds to the critical angle for the sample. It is difficult to define for the rough electrodes and can be considered close to $\theta_c \approx 0.19^\circ$. For the polished electrodes, $\theta_c \approx 0.24^\circ$. In comparison, the critical angle for the $m=3$ super-mirror is $\theta_c \approx 1.55^\circ$, and $\theta_c \approx 0.36^\circ$ for the glass plate. These numbers are summarized in [Table 5.12](#).

Sample	super-mirror	Glass	Polished electrode	Rough electrode
θ_c from Fig. 5.29	1.55°	0.36°	0.24°	0.19°
$\theta_D/2$ for rocking mode	1.525°	0.375°	0.225°	0.225°
Deviation in Fig. 5.30	0.04°	0.08°	0.04°	0.08°
FWHM in Fig. 5.30	0.13°	0.14°	0.15°	0.17°

Table 5.12: Approximate critical angle defined in the $\theta - 2\theta$ mode, angle $\theta_D/2$ used in the rocking mode to define the position of the detector, deviation from 0 of the maximum number of counts, and FWHM in [Fig. 5.30](#).

With the measurement of the critical angle for the super-mirror, we retrieve the m -value : $m = \sin(\theta_c)/\sin(\theta_{c,Ni}) = 3.1 \pm 0.2$.

Rocking mode

This measurement depicts the diffuse scattering of the sample. One of the two angles is kept constant and the other one is scanned. In our case, the angle between the detector and the beam θ_D was kept constant, and θ_S scanned. The maximum number of counts is expected to be for $\theta_S = \theta_D/2$.

For this measurement, θ_D was defined to correspond approximately to the critical angle $\theta_D \approx 2\theta_c$, see [Table 5.12](#). One can estimate the maximum angle for diffuse scattering from the FWHM and a possible systematic error on the critical angle from the deviation of the maximum from $\theta_D = 2\theta_S$. These values are recorded in [Table 5.12](#). The peak is broader for the rough electrode than the polished one as expected.

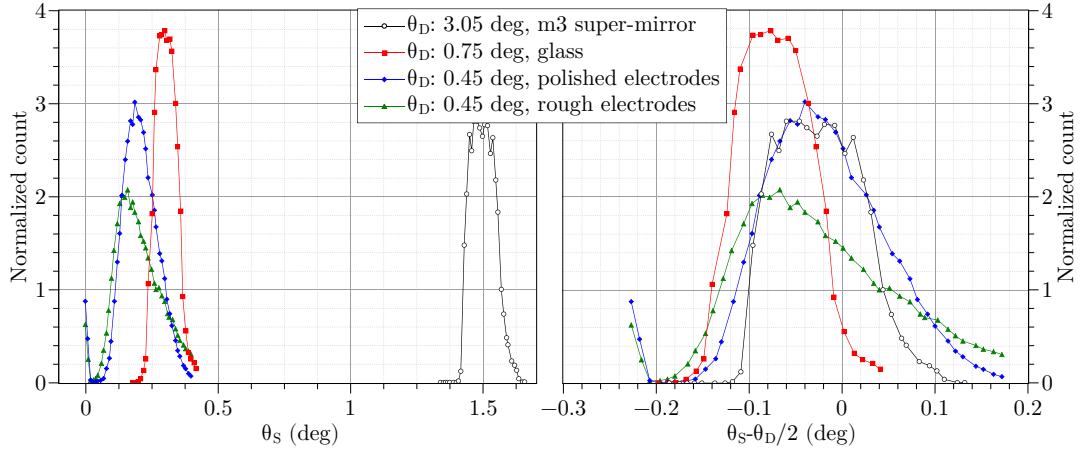


Fig. 5 .30: Normalized number of counts vs θ_S and $\theta_S - \theta_D/2$ for the different samples for a measurement in rocking mode.

Considering $\theta_c = 0.25^\circ$ at 5\AA for the electrodes, the critical angle at 15\AA can be extrapolated with Eq. (2.7) to $\theta_c(15\text{\AA}) = 0.75^\circ$ which defines the angular acceptance of the electrodes at 15\AA which is higher than the wavelengths that are analyzed in a phase scan. A divergence of this angle corresponds to an increased distance from a horizontal path of 0.7%, neglecting gravity. In comparison, the angular acceptance of the apertures defined in Table 5.8 was 0.41° . This is important as it increase the number of neutrons that are detected therefore the statistical sensitivity of the apparatus. However, it also increases the divergence of the beams and potentially increase the cross contamination between the beams. To solve this problem, additional apertures are mounted onto the spin analyzer.

5.5 Beamtime 4: ILL 2020

The last beamtime to date of BeamEDM with the Ramsey apparatus was at PF1b, ILL in 2020 from 06/08 to 15/09. The goals of this beamtime were:

- the characterization of the new BeamEDM chopper ([CAZ⁺]),
- the magnetic field characterization of the apparatus on a pulsed white beam with a modulated signal in the spin flippers following the same principle as in [Section 5.1.4](#). The measurements of this characterization are summarized in [Table 5.13](#).
- the $v \times E$ effect measurement on a pulsed white beam with a modulated signal in the spin flippers as a proof-of-concept for the BeamEDM experiment. Only the measurement principle is presented in this thesis in [Section 5.5.5](#),
- a stability measurement with full phase scan and at one fixed phase to determine the optimal measurement procedure to follow, presented in [Section 5.5.6](#),
- the EDM measurement with full phase scan and at one fixed phase on a pulsed white beam with a modulated signal in the spin flippers as a proof-of-concept for the BeamEDM experiment. Only the measurement principle is presented in this thesis from the previously mentioned stability measurement.

Field	B_z	B_G	B_x	B_y
Ref. value (μT)	220	0	0	0
Number of configurations	9	9	9	9
Graphs	Fig. 5.36A	Fig. 5.36B	Fig. 5.37A	Fig. 5.37B

Table 5.13: Characteristics of the measurement performed at PF1b in 2020 for the characterization of the field sensed by the neutrons. It records, the fields that are scanned, the reference value for this field, how many values are scanned (num. configuration), and the reference to the graphs where the results are displayed.

During this beamtime the length of the apparatus from the chopper to the detector was 10.75 m compared to 6.4 m in the previous beamtime at BOA. The length from the casemate wall to the detector was 8.73 m compared to ≈ 7 m during the beamtime at PF1b in 2018, see [Section 5.2](#). The main improvements are the passive magnetic shield, the higher achievable magnetic field thanks to the low resistivity coils and the new fluxgates, and the automation of most of the measurements thanks to the new DAQ system.

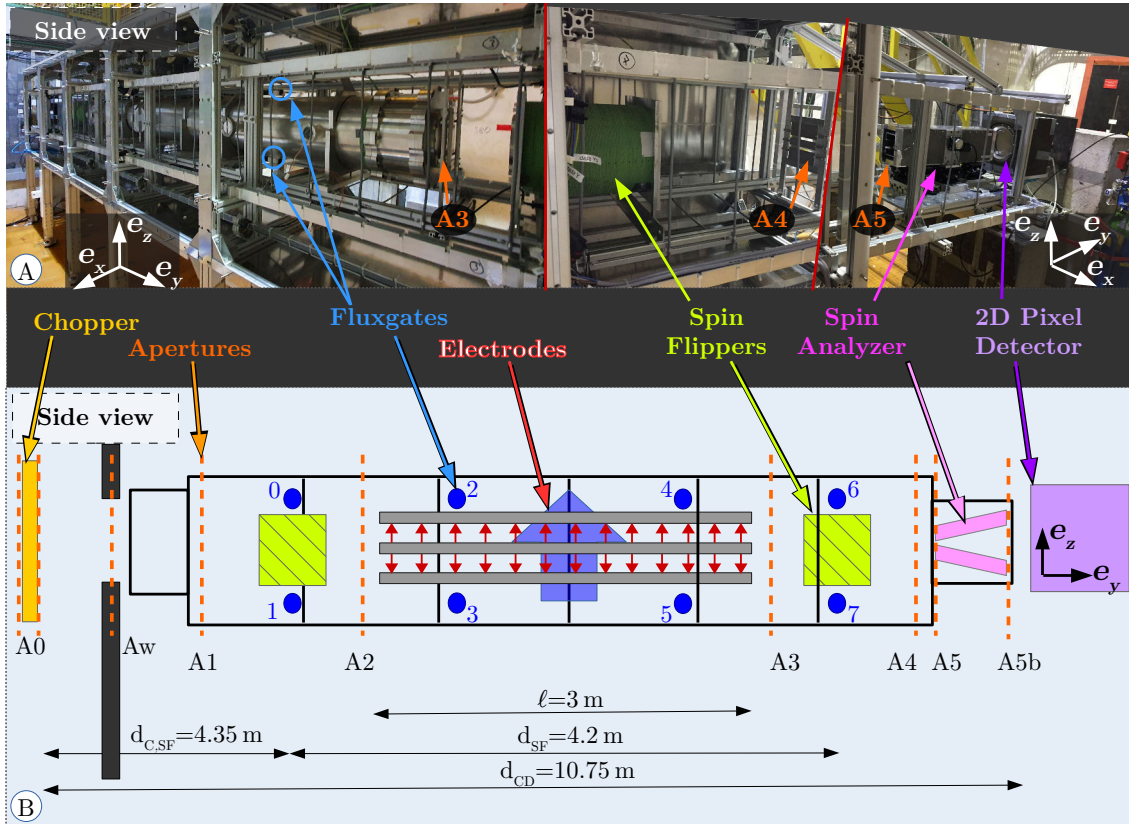


Fig. 5.31: A) Reconstructed side view from 3 pictures with indications for the apertures A3, A4, A5, and the two visible fluxgates. B) Sketch of the apparatus with each cube of the structure including the end pieces (black squares), the different apertures (orange dashed lines), the chopper (yellow box), the position of the fluxgates denoted by the full blue circles, the spin flippers (green boxes), the electrodes (gray rectangles) with the electric field (red arrows), the analyzer (two <-shape pink parallelograms), and the detector (purple cube). The beam is coming from the casemate on the left, through an opening in the wall (full black rectangles) to the experimental area. The top and bottom beams are traveling in between the central (high voltage) electrodes and the top or bottom ground electrodes, respectively, as represented for the previous beamtime in [Fig. 5.25](#).

The apparatus for this beamtime is the state-of-the-art of the BeamEDM experiment at the time of writing. A scheme of the apparatus is displayed in [Fig. 5.31](#) as well as pictures from the beamtime.

The beams were defined in shape and divergence by a set of apertures whose characteristics are summarized in [Table 5.14](#). The first three apertures (A0, A0* and Aw) in the casemate, and the aperture A3 in the experimental area were installed to reduce the radiation level from neutron scattering. Four other apertures (Aw, A1, A2, A4) in the experimental area were cutting the beam in two smaller ones, called top and bottom beam in order to perform a relative measurement. A last aperture on the spin analyzer absorbed the neutrons that would not hit the mirrors, reducing the neutron background in the detector.

Label	A0	A0*	Aw	A1	A2	A3	A4	A5	A5b
Type	I	I/ II	II	II	II	I	II	III	III
Inside width (mm)	70	70	70	70	70	80	70	70	70
Inside height (mm)	70	2×20	2×10	2×15	2×10	75	2×10	2×10	2×10
Separation height (mm)		20	30	25	30		30	30	30
Distance to chopper (m)	-0.150	0.160	2.02	3.29	4.44	7.94	9.21	~ 9.93	10.38

Table 5.14: Characteristics of the apertures at PF1b in 2020 shown in Fig. 5.31, with their type defined in Section 3.3.3, the width and height of the opening, and the separation in height between the two holes when divide the beam in two. The aperture A0* is of a mixed type as it has the geometrical characteristics of a type II, i.e., two openings for the beam, but the purpose of a type I, i.e., reducing the radiation level in the experimental area.

The chopper was upgraded from last beamtime to the Fermi type chopper which allowed for a larger beam area and, assuming a similar duty cycle, an increase in statistics. The chopper was run at a frequency of 19 Hz.

The homogeneity of the magnetic field over the length of the apparatus was improved by the installation of two layers of mumetal on the cubes of the structure. Due to time constraints from the production, there was no mumetal plates on the cuboids attached to the upstream and downstream end of the structure. To prevent picking up high frequency signal in the coils aluminum plates were installed on the cuboids. A picture of the apparatus with the mumetal shielding and the aluminum plates is shown in Fig. 5.32A&B.

For this beamtime, the spin flippers were re-designed to be under vacuum in order to reduce the neutron scattering on air. In addition layers of B4C were installed on top of the apparatus, partially visible in Fig. 5.32A&B.

The spin flippers were not placed in the middle of the first and last cubes as done previously but closer to the middle of the structure in order to improve the homogeneity at the spin flipper position as this was a problem for the previous beamtime ("long oscillation" in Fig. 5.23). SF1 was placed at a distance of $d_{C,SF} = 4.35$ m from the chopper and SF2 was placed at a distance of $d_{SF} = 4.2$ m from SF1.

Moreover, the modulated signal for the spin flippers was generated in a different way, see Fig. 3.10, to avoid fast oscillation in the neutron phase seen in Fig. 5.23. The envelop of the signal was generated by a first waveform generator. The second waveform generator generated the sinusoidal pattern that fills the envelope. At each chopper pulse, only the modulation from the first waveform generator was trigger without triggering the sinusoidal part of signal. By choosing prime numbers for the chopper frequency and spin flipper frequency, the sinusoidal part of the signal was

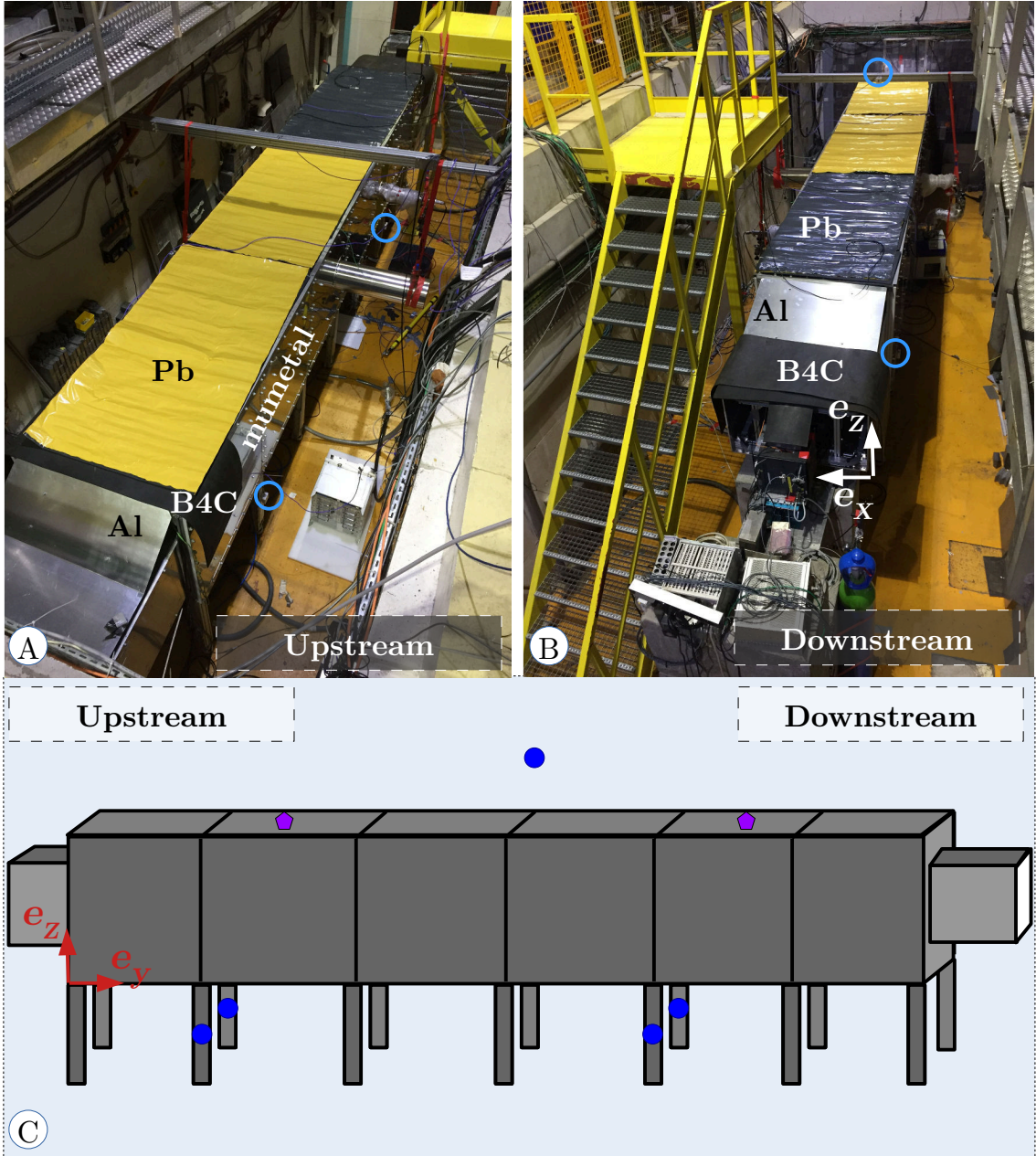


Fig. 5.32: A) Picture of the apparatus taken from upstream at PF1b in 2020 with the aluminum and mumetal shielding, the B4C and the lead sheets. Denoted by blue circles are the visible FLC3-70 fluxgates that measure the background field. B) Picture from downstream with the same characteristic as in A. C) Sketch of the apparatus at PF1b, ILL in 2020 with the full blue circles are the FLC3-70 fluxgates and the purple pentagons the temperature sensors.

fully de-synchronized from the chopper pulse. This was monitored by measuring the phase of the upstream (SF1) and downstream (SF2) spin flipper signal with respects to the chopper pulse. Besides, with this systems, one can scan the relative phase between the two sinusoidal signals, $\theta_{RF} = \theta_{SF2} - \theta_{SF1}$, without changing the envelope, unlike for the last beamtime.¹⁵

¹⁵The phase recorded in the root file is actually the opposite.

New low resistance coils were used to generate a higher vertical magnetic field than during the previous beamtimes. A higher field corresponds to a higher Larmor frequency, and thus, a higher resonance frequency for the spin flippers. The idea is to diminish the wavelength threshold for which the neutrons do not see a full oscillation of the oscillating field. The vertical component of the field was set at $B_z = 220 \mu\text{T}$, and the transversal, longitudinal components, and vertical gradient fields were stabilized at $B_x = B_y = 0 \mu\text{T}$ and $B_G = 0 \mu\text{T}/\text{m}$.¹⁶ To monitor this field, eight FGM3D-250 fluxgates were placed inside the apparatus as represented in Fig. 5.31. Their longitudinal position is recorded in Table 5.15, they were centered in the transversal direction and separated by $d_{SF} = 36.1 \text{ cm}$ in the vertical direction, center-to-center. The four middle ones were used for the stabilization. Five FLC3-70 fluxgate were set on the outside to monitor the magnetic background, as represented in Fig. 5.32C. Also represented in this figure, the temperature sensors that monitored the temperature of the mumetal.

FG	0	1	2	3	4	5	6	7
Distance to adjacent cube (mm)	-114.5	-114.5	85.5	85.5	-114.5	-114.5	85.5	85.5
Vertical position	top	bottom	top	bottom	top	bottom	top	bottom

Table 5.15: Longitudinal position of the fluxgates at ILL in 2020. It is defined with respects to the closest adjacent cube. For the fluxgates 0, 1, 4, and 5, the value is negative meaning that are upstream with respect to cube as represented in Fig. 5.31.

The vacuum pipe, placed in between the spin flippers, was 3.4 m long. It carried three electrode stacks which were used to generate the electric field. The HV electrodes (in the center) were run up to $\pm 40 \text{ kV}$ with the ground electrodes (the outer ones) at a 1 cm distance surface-surface. Discharges were monitored by the leakage current monitor according to the diagram in Appendix C. A lead shielding, visible in Fig. 5.32A&B, was placed on top of the experiment in order to reduce the X-ray radiation from potential breakdowns.

The spin analyzer mirrors were position in a V-shape configuration leading to a top reflected spot above the top transmitted one and a bottom reflected spot below the bottom transmitted one. This had the advantage to have a larger gap between the spots of the top and bottom beams, decreasing the cross contamination between them, but the inconvenience of using the pixels on the edges of the detector which were considered unreliable previously due to some unknown in the event reconstruction program of the Cascade detector. Two apertures, A5 and A5b were

¹⁶For this beamtime, the vertical field gradient was recorded in $\mu\text{T}/\text{m}$ this was not the case for any previous beamtime.

also installed on each side of the spin analyzer in order to absorb the neutrons that would not pass through the spin analyzer mirrors.

The detector was placed at a distance $d_{CD} = (10.75 \pm 0.01)$ m from the chopper. It was covered by B4C layers on all sides with the exception of the measurement window and the bottom face. This was done to minimize neutron background in the detector that would come from scattering in air and trigger the detection mechanism of the detector from the side.

5 .5.1 Characterization of the neutron spots in the detector

A time-of-flight measurement was performed with the adiabatic spin flipper (AFP) off and on without any additional spin flip from SF1 or SF2 in order to define the contours of the beam spots and measure their spectrum. We can define for this beamtime that AFP=off leads to reflection of the beam. Inversely, AFP=on leads to a transmission of the beam by the spin analyzer mirror. This is represented by the ideal case in [Fig. 5.2](#).

Spot	Top Trans.	Top Ref.	Bottom Trans.	Bottom Ref.
Bottom left corner	(0;10)	(0;13)	(0;4)	(0;0)
Top right corner	(15;12)	(15;15)	(15;6)	(15;3)

Table 5 .16: Definition of the transmitted (Trans.) and reflected (Ref.) spots for the top and bottom beams by the coordinate of the bottom left and top right corners in units of pixel at PF1b in 2020 with a V-shape configuration of the spin analyzer.

First, the spots for the different spin states of each beam are defined by a rectangular shape shown in [Fig. 5.3A&B](#) and summarized in [Table 5.9](#). Then one can analyze the spectrum of each spot individually in [Fig. 5.33C](#) and D which has a characteristic behavior of the spin analyzer efficiency described in [Fig. 5.2D](#). The configuration AFP off corresponds to the spin state where the neutrons are reflected. At low wavelength $\lambda < 2 \text{ \AA}$, the transmitted spot contains all the counts and the reflected spots none. This is due to the efficiency of the spin analyzer, the wavelength of the neutron is lower than the critical one defined in [Eq. \(2.7\)](#) and the neutrons are always transmitted independently of their spin state. The number of counts in the transmitted count decreases when the efficiency of the analyzer increases.

To quantitatively characterize the overall spin analyzer, the "AFP asymmetry" defined in [Eq. \(5.1\)](#) is then calculated with the result shown in [Fig. 5.33E](#) and F for each spot as a function of the wavelength. The maximum efficiency is around 0.95 for all spots. One estimates the working range of the spin analyzer from 2.9 \AA to 14.7 \AA from the region where $A_{\text{AFP}} \geq 80\%$ for all spots.¹⁷ The improvement from the

¹⁷This value was chosen to match the plateau in the AFP asymmetry in [Fig. 5.33E](#) and F.

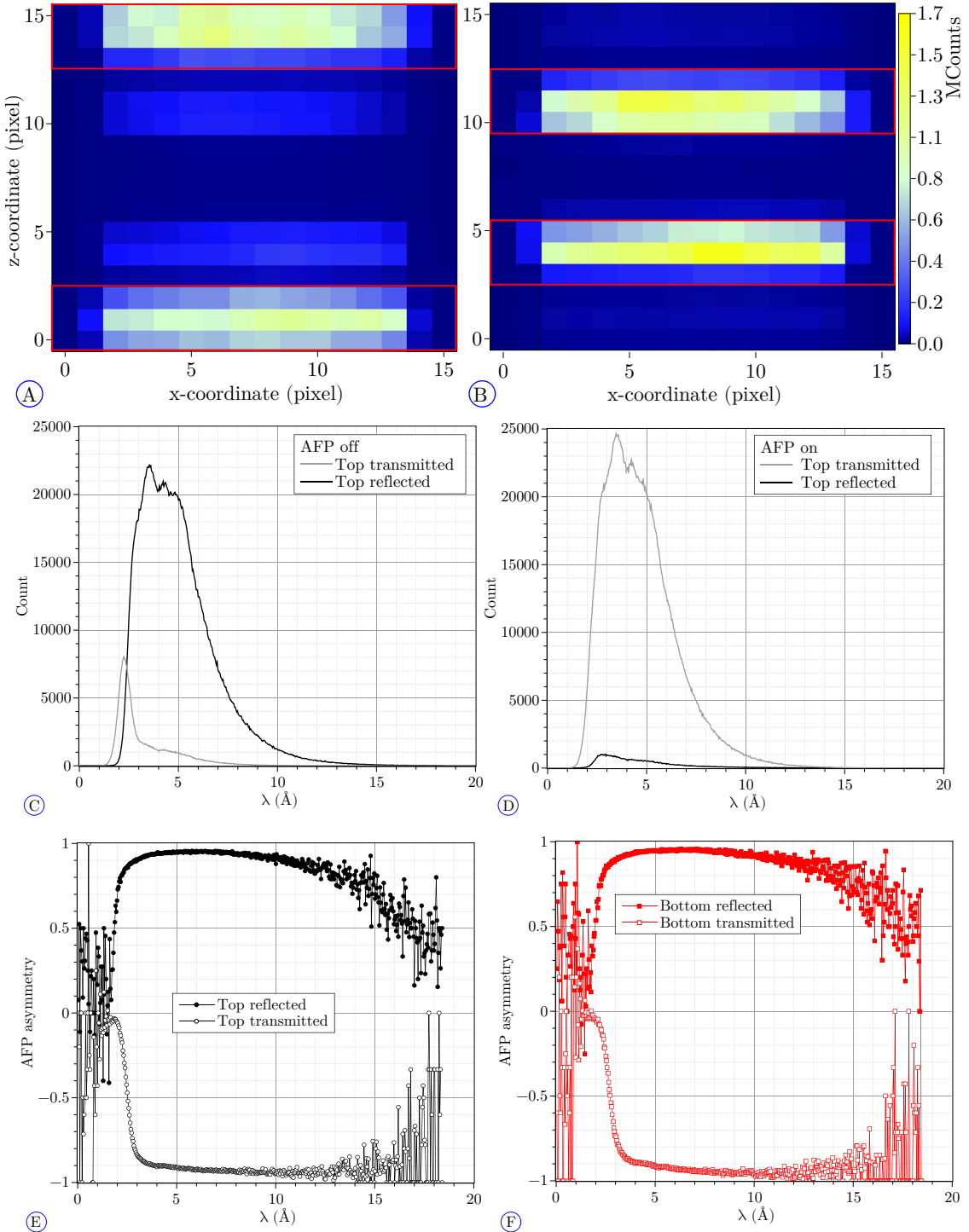


Fig. 5.33: *A and B) Neutron counts in the detector's pixels integrated over wavelength for the adiabatic spin flipper off and on, respectively. The color scale was used for the two figures for a direct comparison. C and D) Neutron count integrated over the transmitted and reflected spots of the top beam as a function of the neutron wavelength for the adiabatic spin flipper off and on, respectively. The same scale was used for a direct comparison of the numbers. E and F) AFP asymmetry of each spots defined in Eq. (5.1), as a function of the neutron wavelength for the top and bottom beams, respectively*

previous beamtime can be attributed to the V-shape configuration of the analyzer mirror and the apertures A5 and A5b.

5 .5.2 Configuration of the spin flipper signal

The resonance frequency of the individual spin flippers was determined from a Rabi measurement, (6391 ± 1) Hz and (6384 ± 1) Hz for top and bottom beam for SF1 and (6389 ± 1) Hz and (6384 ± 1) Hz on the top and bottom beam for SF2. Due to the mumetal, the difference in magnetic field at both spin flippers is negligible compared to all previous beamtimes. The resonance frequency for each of them is nearly identical which give an almost perfect Ramsey pattern for both the top and bottom beam, displayed in Fig. 5 .34. In comparison, in 2018 at PF1b, ILL, the difference in resonance frequency between the two spin flippers was about 500 Hz. The frequency of the spin flippers was chosen to $f_0 = 6397$ Hz, as it is a prime number close to the actual resonance frequency of the apparatus.

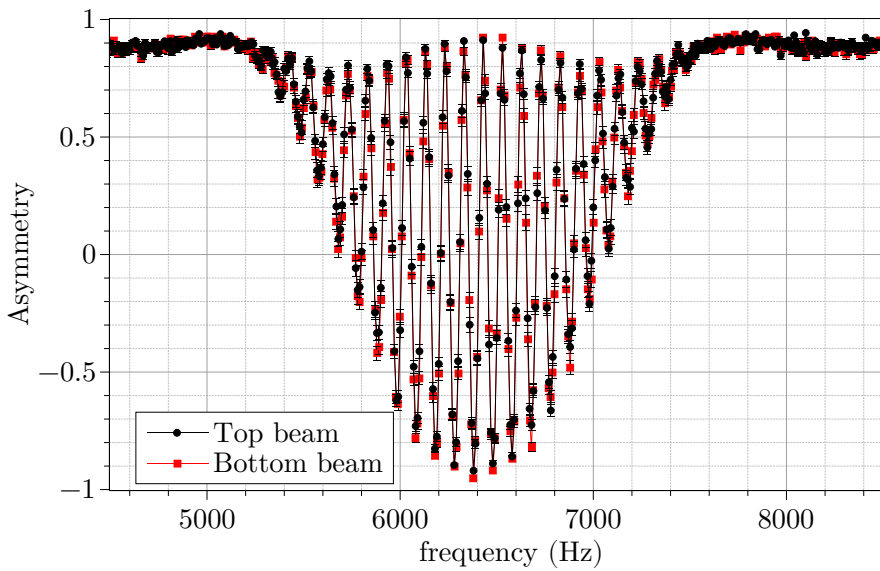


Fig. 5 .34: Ramsey pattern for the top and bottom beam at $\lambda = 9.2 \text{ \AA}$ with the AFP on.

With the Rabi amplitude measurement at this frequency, the initial parameters for the modulated signal were estimated during beamtime. This was done by extracting the optimal amplitude to perform a π flip for each wavelength. The shape of the modulated signal could then be extracted by fitting this result with the modulated signal function defined by Eq. (3.2). The result of the fit provided the initial values for the modulated signal with the small change that t_0 (or equivalently S_0) was divided by two in order to represent a $\pi/2$ flip instead of a π flip. Then, each parameter was scanned independently for each spin flipper to find the optimal set of parameters. The goal was to have a set of parameters for which a broad part of

the neutron spectrum undergo a $\pi/2$ flip characterized by $A_{AFP} = 0$ where A_{AFP} is defined in [Eq. \(5.1\)](#). The optimal set of parameters used for the following are summarized in [Table 5.17](#).

	f_0 (Hz)	Amp. (V)	t_0 (ms)	t_1 (ms)	p
SF1	6379	3.5	3.16	0	1
SF2	6379	3.5	6.26	0	1

Table 5.17: Parameters of the modulated signal for the upstream spin flipper (SF1) and the downstream spin flipper (SF2) for the phase scans and Ramsey technique extracted from the logbook.

5.5.3 Working range of the apparatus

As stated previously, the angle of the spin analyzer mirrors were optimized to have a high efficiency, $A_{AFP} \geq 80\%$ for the neutrons of wavelength between 2.9 Å and 14.7 Å.

The modulated signal sent to the spin flippers [Eq. \(3.2\)](#) was defined with t_0 corresponding to a wavelength $\lambda_0 \approx 2.87 < 2.9$ Å. In that case, the modulation range of the spin flipper covers the high efficiency range of the spin analyzer. In addition, the frequency of signal was $f_0 = 6397$ Hz which corresponds to a period $(2\pi f_0)^{-1} = 156.3$ µs and a critical neutron wavelength of $\lambda_c = 1.55$ Å < 2.9 Å defined in [Eq. \(3.1\)](#). Hence, the neutrons in the range [2.9; 14.7] Å would see at least one full period of the oscillating magnetic field, i.e. this range is limited by the spin analyzer and statistics.

To confirm this range with a measurement, the data from a phase scan was analyzed according to [Chapter 4](#). The fit function defined by [Eq. \(4.5\)](#) was used for a preliminary analysis of the neutron phase during beamtime. The fit parameters and the χ^2/NDF are displayed in [Fig. 5.35](#). On the presented range, one achieves :

- An amplitude A_0 of [Eq. \(4.5\)](#), of 0.8 to 0.9.
- An offset A_1 centered around 0, spread between -0.2 and 0.3. The tail at high wavelength is probably due to the spin analyzer efficiency reduced to 0.8 at that point. In a detailed analysis, one could consider restricting further the range e.g. $A_1 \in [-0.05; +0.05]$.
- A constant neutron phase. A linear fit actually measures a slope of (3.5 ± 0.1) mrad/Å with a chi-squared of $\chi^2/NDF = 4220.3/3204 = 1.32$. The value of reduced chi-square could be reduced by the stricter cut on the wavelength range stated above but this value is considered adequate for the preliminary analysis performed here.

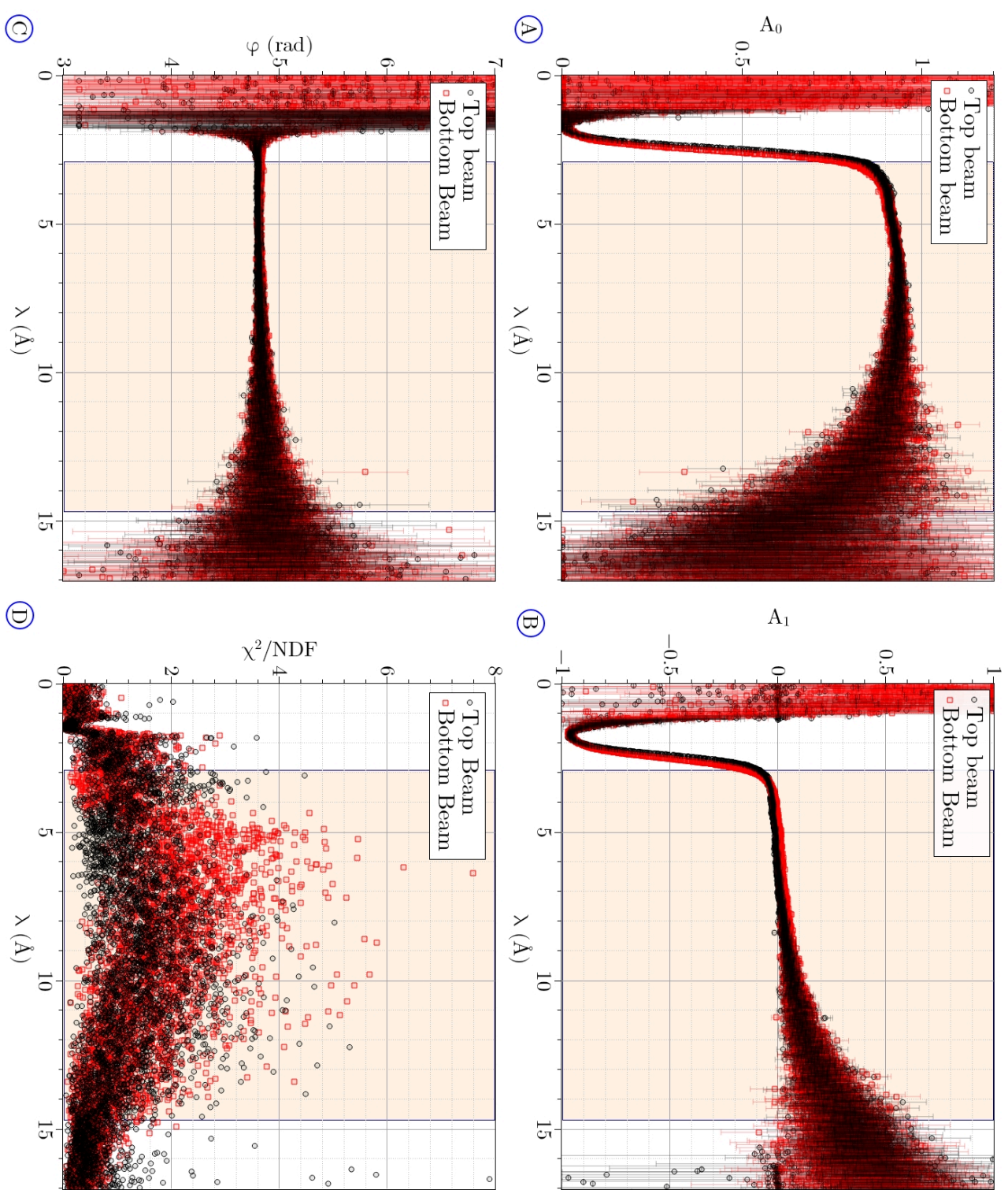


Fig. 5.35: A) Amplitude, A_0 , of the fit function Eq. (4.5) vs. wavelength. B) Offset, A_1 , of the fit function Eq. (4.5) vs. wavelength. C) Phase, φ , of the fit function Eq. (4.5) vs. wavelength. The value of the top beams are always represented by black circles and the bottom beam one by red squares. The transparent orange rectangle defines the working range of the apparatus.

- A χ^2/NDF centered around 1.2 for the top beam and 1.4 for the bottom beam estimated by a Gaussian fit of the distribution of the defined range.

This range cannot be increased at low wavelength due the efficiency of the spin analyzer. At high wavelength, the statistics is low and the AFP asymmetry is lower, thus, these points are not included in the working range.

5.5.4 Magnetic field characterization

During this beamtime, scans of the vertical, transversal, longitudinal, and vertical gradient field were performed with modulated signal in the spin flippers and a pulsed beam. The neutron phase sum should follow the same behavior as in the previous beamtime, Eqs. (4.11) and (5.3).

The measurement with the vertical magnetic field was performed by scanning from $B_z = 216 \mu\text{T}$ to $B_z = 224 \mu\text{T}$. As already mentionned in the previous beamtimes, the interaction range is not necessary the distance center to center between the spin flippers. Thus a new definition is used for this beamtime: one can define the interaction length by the distance between the spin flippers including about $(60 \pm 10) \%$ of their length: $d_{Int} = d_{SF} + (0.6 - 0.5) \times \ell_{SF} = (4280 \pm 80) \text{ mm}$.¹⁸ Using the same formula as in the previous beamtimes, the expected value of the neutron phase sum over the top and bottom beam is

$$\left. \frac{\partial^2(\Phi_+)}{\partial \lambda d(\delta B_0)} \right|_e = 2\gamma_n \frac{m_n d_{Int}}{h} = (-397 \pm 7) \text{ mrad}\text{\AA}^{-1}\mu\text{T}^{-1} \quad (5.27)$$

where δB_0 is the off-resonance field common to the two beams. To estimate the accuracy on the variation of the set field, the deviation of the value of each fluxgates from the set field is corrected by the static background.¹⁹ The standard error of these calculations at a given target field acts as the error on the magnetic field in Fig. 5.36. It is of the order of 4 nT. A fit on these data yields:

$$\left. \frac{\partial^2(\Phi_+)}{\partial \lambda d(B_z)} \right|_m = (-408.4 \pm 0.2) \text{ mrad}\text{\AA}^{-1}\mu\text{T}^{-1}. \quad (5.28)$$

with $\chi^2/NDF = 3.96/8 = 0.495$ which is an acceptable value according to the theoretical chi-square distribution. The discrepancy between the two values is less than three sigma away.

Instead of considering an error of 80 mm in the interaction length, one could compute the equivalent value when assuming the correct evaluation of the magnetic

¹⁸This value was motivated by the definition of the interaction time in [AAA+20].

¹⁹The considered static background is the field in homogeneity for the reference measure, see Table 5.1.

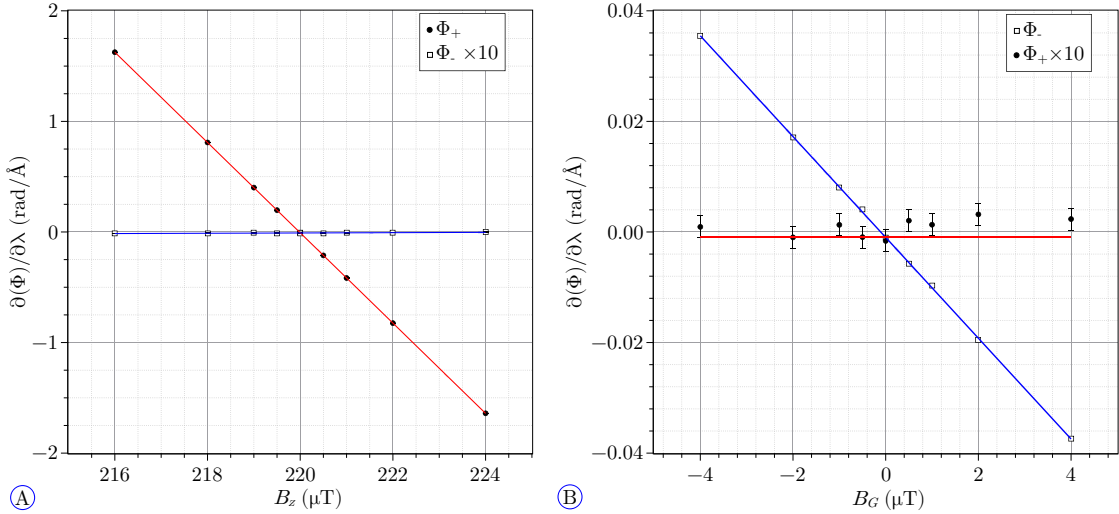


Fig. 5.36: *A.* Slope of the neutron phase sum and difference over wavelength vs. vertical magnetic field. The value for the difference Φ_- is scale by a factor 10 for visibility. *B.* Slope of the phase sum and difference over wavelength vs. vertical magnetic field gradient in $\mu\text{T}/\text{m}$. The value for the sum Φ_+ is scale by a factor 10 for visibility.

field in Eq. (5.28). This would yield $d_{Int} = (4401 \pm 0.2) \text{ mm}$ which corresponds to the distance between the spin flippers including about 75 % of their length. In comparison, [AAA⁺20] includes 2.5 s of the 4 s of the flipping pulses in the interaction time. For a direct comparison this represents 62.5 % of the flipping pulse duration.

One could also analyze the phase difference in Fig. 5.36. A linear fit yields:

$$\left. \frac{\partial^2(\Phi_-)}{\partial \lambda d(B_z)} \right|_m = (-13 \pm 3) \times 10^{-5} \text{ rad}\text{\AA}^{-1}\mu\text{T}^{-1}, \quad (5.29)$$

with $\chi^2/NDF = 9.00/8 = 1.12$. The value in Eq. (5.29) can be interpreted as an increase of the vertical gradient field of $\Delta B_g / \Delta B_z = (1.6 \pm 0.4) \times 10^{-4}$ of the increase of the vertical magnetic field ΔB_z . This is important as a change in the vertical gradient field would mimic an EDM if it is correlated to the electric field reversal. For example a shift of 160 pT in the field gradient corresponds to an EDM of $|d_n| = 1 \times 10^{-24} e \text{ cm}$ for an electric field of 100 kV/cm on a 3 m long section using Eq. (4.10).

The measurement with the vertical magnetic field gradient was performed by scanning from $B_G = -4 \mu\text{T}/\text{m}$ to $B_G = 4 \mu\text{T}/\text{m}$. It was the first time that this measurement was performed with a pulsed beam. This allows to compute the

expected value of the neutron phase difference with

$$\begin{aligned} \frac{1}{d_{bt}} \times \frac{d^2(\Phi_-)}{\partial \lambda \partial (B_G)} \bigg|_e &= \gamma_n \frac{m_n d_{Int}}{h} = (199 \pm 3) \text{ rad}\text{\AA}^{-1}\text{\mu T}^{-1} \\ \frac{d^2(\Phi_-)}{\partial \lambda \partial (B_G)} \bigg|_e &= (-0.040 \times 0.199) \text{ rad}\text{\AA}^{-1}(\text{\mu T}/\text{m})^{-1} \\ &= (7.9 \pm 0.1) \text{ mrad}\text{\AA}^{-1}(\text{\mu T}/\text{m})^{-1} \end{aligned} \quad (5.30)$$

considering the distance between the top and bottom beam $d_{bt} = (40 \pm 1)$ mm. One can use the same technique to evaluate the error on the magnetic field as previously which yields an error equivalent to 4 nT. A fit of the data in Fig. 5.36B yields:

$$\frac{d^2(\Phi_-)}{d \lambda d(B_G)} \bigg|_m = (-9.1 \pm 0.1) \text{ mrad}\text{\AA}^{-1}(\text{\mu T}/\text{m})^{-1}. \quad (5.31)$$

with a $\chi^2/NDF = 2.1/7 = 0.30$ which means that the error relative to the precision of precision might be overestimated. However, the discrepancy between Eq. (5.30) and Eq. (5.31) hints toward a systematic underestimation of the magnetic field gradient or of the interaction length. Assuming that the interaction length is correct, the magnetic field gradient sensed by the neutrons would always be $(11.5 \pm 0.2)\%$ higher than what is set.

One can also analyze the phase sum in order to measure the vertical magnetic field generated with the gradient field. The fit in Fig. 5.36 shows no dependency between the vertical field and the field gradient.

The measurement with the transversal, B_x , and longitudinal, B_y , component of the magnetic field was performed with a pulsed beam and the modulated signal for the spin flippers²⁰. Each component was scanned from -40 \mu T to 40 \mu T . Like in Section 5.1.5, the neutron phase for the top and bottom beams should follow Eq. (5.14) and the sum of phase from both beams should follow Eq. (5.15) assuming $B_z^2 \gg B_x^2 + B_y^2$. In terms of wavelength, for this configuration of the apparatus, we expect from a third order Taylor expansion:

$$\frac{\partial(\Phi_+)}{\partial \lambda} \bigg|_e \approx \gamma_n \frac{m_n d_{SF}}{h} \times \left[2\delta B_0 + \frac{B_y^2 + B_x^2}{B_z} - \frac{(B_y^2 + B_x^2)^2}{4B_z^3} + \frac{(B_y^2 + B_x^2)^3}{8B_z^5} \right], \quad (5.32)$$

where δB_0 is the deviation of B_z from the resonance field common to the top and bottom beams. The third order was chosen due to the weakness of the assumption $B_z^2 \gg B_x^2 + B_y^2$ (in the extreme case $(B_x^2 + B_y^2)/B_z^2 \approx 1/30$). Assuming δB_0 does not increase with B_x or B_y , the data with the variation of the transversal and longitudinal

²⁰As a reminder, the characterization of the transversal and longitudinal field were always performed with a continuous white beam in the previous beamtimes.

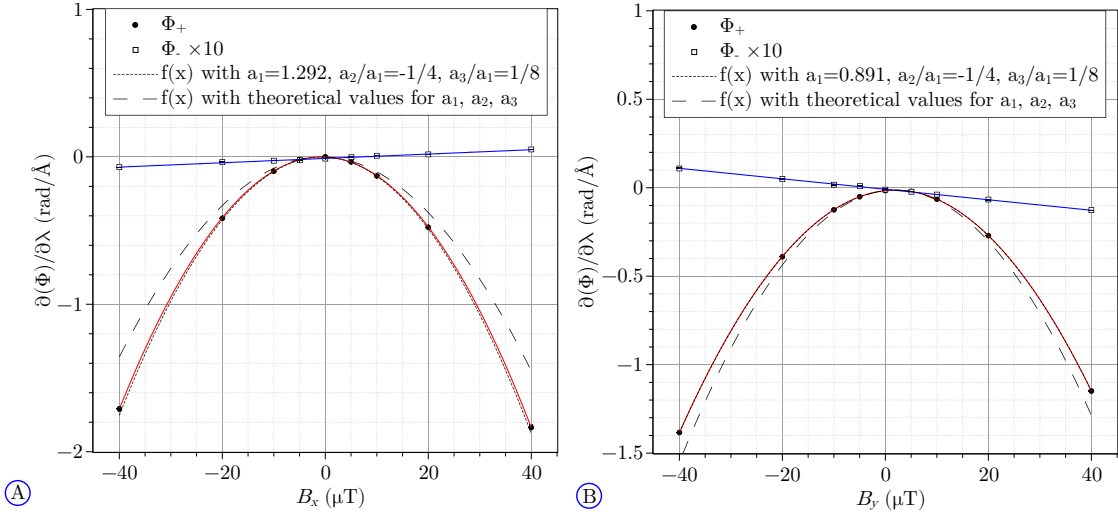


Fig. 5.37: A) Slope of the neutron phase sum and difference over wavelength vs. transversal magnetic field. The value for the difference Φ_- is scale by a factor 10 for visibility. B) Slope of the neutron phase sum and difference over wavelength vs. longitudinal magnetic field. The value for the difference Φ_- is scale by a factor 10 for visibility. The red lines are the representation of the fit described in the text and the blue lines are linear fit of the phase difference in order to see the contribution of the transversal and longitudinal coils to the gradient fields. For both graph, the dot and dash lines represent the function in Eq. (5.33) with the theoretical parameters for a_i for $i \in \{1; 3\}$ and the theoretical parameters for a_2 and a_3 normalized to a_1 .

magnetic field scan in Fig. 5.37 were fitted by:

$$f(x) = K \times \left[\sum_{i=1}^3 a_i \times \frac{(x+b)^{2i}}{(B_z)^{2i-1}} + c \times 1000 \right], \quad (5.33)$$

where x is the function variable, $K = \gamma_n \frac{m_{nd} I_{nt}}{h} = (-195 \pm 1) \text{ mrad}\text{\AA}^{-1}\mu\text{T}^{-1}$ is fixed for the fit, a_i , with $i \in [1; 3]$, are the parameters of the fit which the numerical factor of the Taylor expansion in Eq. (5.32), b represents the offset of the magnetic field for this component, and c is the off-resonance value when $x + b = 0$. The result for the parameters are available in Table 5.18 as well as their expected value. The error on the data points in Fig. 5.37 is coming from statistics and the error on the magnetic field estimated the same way as for the vertical field and field gradient. The value of the error is not constant for all data points: it is of the order of $0.2 \mu\text{T}$ for the measurement at extreme points ($B_x = \pm 40 \mu\text{T}$) and around 5 nT for the other value of the transversal field. Only the error at $\pm 40 \mu\text{T}$ are dominant with respect to the statistical error.

The $\chi^2/NDF = 80.5/4 = 20.1$ suggests that the errors on the slope and/or on the magnetic field are underestimated or the model does not corresponds to the data. First, a different model was considered by fitting the data with an additional term in Eq. (5.33) linear with B_x , i.e. $K \times d \times (B_x + b)$. This term would correspond

parameter	value	expected
a_1	1.292 ± 0.002	1
a_2	-3.6 ± 0.4	$-1/4$
a_3	72 ± 18	$1/8$
b	0.685 ± 0.004	0
c	4.6 ± 0.3	0
χ^2/NDF	84.3/4	

Table 5.18: Values for the fit parameters and reduced chi-square for the scan of the transversal field, as well as the expected value from the Taylor expansion.

to a linear offset in the vertical component of the magnetic field proportional to the transversal field. The value of the additional free parameter was compatible with zero at less than one sigma and only decreased the number of free parameter. In addition, the error coming from the approximation associated with the Taylor expansion was investigated. The slope $\partial(\Delta\phi_+)/\partial\lambda$ was analyzed as a function of the norm of the magnetic field, $\|B\| = \sqrt{B_z^2 + (B_x - b)^2}$, where the transversal component is corrected by $b = 0.7 \mu\text{T}$. In that case, the reduced chi-square does not improve, $\chi^2/NDF = 532/7 = 76.7$. An extensive study of the magnetic field should be performed to understand this measurement like Comsol simulations of the coils with mumetal, mapping of the magnetic field with different values for the transversal magnetic field, etc. This is especially important as it is a key point in the analysis of the $v \times E$ measurement. In conclusion, the measurement with the variation of the transversal field shows a quadratic behavior whose shape is close to the expected one (using $a_1 = 1.292$) but the coefficients are not the expected ones possibly due to a wrong estimate of the error on the magnetic field.

The same analysis is performed with the longitudinal field and the result of fit is presented in [Table 5.19](#). The Taylor expansion was limited to order 4 due to a lack of sensitivity for the higher orders. The measurement matches the expected result when considering a linear offset of about $(a_1 - 1)/1 = -11\%$ when setting the magnetic field and a fixed offset of $b = -1.9 \mu\text{T}$. A linear analysis with the magnetic field norm has also been done for this scan, the result of this analysis is compatible with the Taylor expansion analysis and the reduced chi-squares are similar and in an acceptable range²¹.

The main difference between the longitudinal and transversal field is the position of the fluxgates relatives to the coils as represented in [Fig. 5.38](#) which could explain

²¹As a reminder the distribution of the χ^2 has a standard deviation of $\sqrt{2NDF}$, here, with $NDF = 5$ the expected variance is 3.16 for the χ^2 distribution and 0.63 for the reduced chi-square distribution.

parameter	value	expected
a_1	0.891 ± 0.002	1
a_2	-0.26 ± 0.2	$-1/4$
a_3	NF	$1/8$
b	-1.905 ± 0.005	0
c	67.5 ± 0.7	0
χ^2/NDF	1.9/5	

Table 5 .19: Values for the fit parameters and reduced chi-square for the scan of the longitudinal field, when the error on the magnetic field is negligible, $\sigma_B = 0.17 \text{ nT}$, and the expected value from the Taylor expansion. NF stands for "not fitted" when fitting with this parameter would not make sens.

the difference the presented results. In a future beamtime, one could consider adding fluxgates on the left and right of the beams as shown by crosses in Fig. 5 .38.

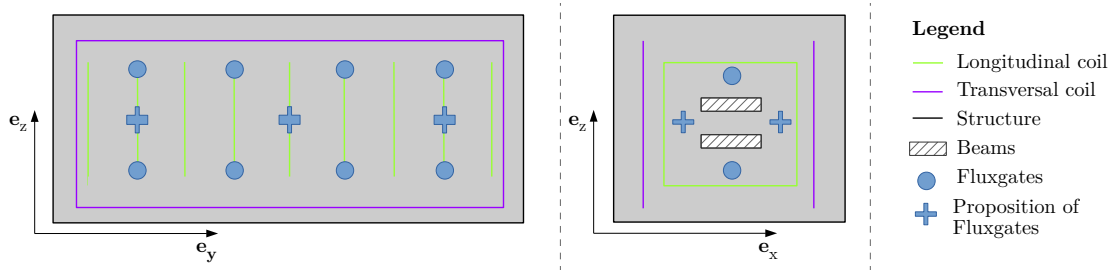


Fig. 5 .38: Cross sections of the apparatus where the white rectangles represent the beams, the purple and green lines are the transversal and longitudinal coils, the black line represent the aluminum structure on top of which the mumetal has been set, the blue circles are the fluxgates as they were during the beamtime, and the blue crosses are the position of potentially additional fluxgates in order to monitor better the transversal component of the magnetic field.

From the slope of phase differences $\partial(\varphi_-)/\partial\lambda$ vs B_x or B_y , one can see a vertical gradient of $-0.8 \times 10^{-3} \mu\text{T}/3\text{cm}$ and $1.5 \times 10^{-3} \mu\text{T}/3\text{cm}$ of the applied transversal and longitudinal field respectively.

5 .5.5 $v \times E$ measurement

In continuation from the previous beamtime and as a characterisation of the systematic effect for the BeamEDM experiment, the measurement of the $v \times E$ effect was performed with a pulsed beam and continuous beam. The electric field was generated by the electrodes along the vertical direction and the magnetic field was tilted by an angle β in the transversal direction. The different configurations of the magnetic field summarized in Table 5 .20. For each of these configurations, the applied voltage was scanned from -40 kV to $+40 \text{ kV}$ by steps of 20 kV with a distance between the electrodes of 1 cm for the measurement with a pulsed beam.

B_z (µT)	B_x (µT)	B_y (µT)	B (µT)	β (deg)
220	40	0	223.6	10.3
220	-40	0	223.6	-10.3
214	50	0	219.8	13.2
214	-50	0	219.8	-13.2

Table 5.20: Configuration of the field for the different $v \times E$ measurements. The magnetic field components are in µT and the angle is in degree. B is the norm of the magnetic field.

There are two ways to analyze the data:

- One can consider the magnetic field axis as the angle of reference e.g. $\mathbf{B} = B \mathbf{e}_B$, where B is the magnitude of the magnetic field, and use Eq. (4.16) with the appropriate change of coordinate.
- An alternative analysis could be done with the coordinate system of the coils. The pseudo magnetic field $B_{v \times E}$ is in the transversal direction, and therefore, it is added to the transversal component of the set magnetic field B_x . The phase should follow:

$$\begin{aligned}
 \varphi &= \omega_{RF} \pm \gamma_n \sqrt{B_z^2 + (B_x + B_{v \times E})^2 + B_y^2} \\
 &\approx \omega_{RF} + \gamma_n B_z + \frac{(B_x + B_{v \times E})^2 + B_y^2}{2B_z} \\
 &\approx \omega_{RF} + \gamma_n B_z + B_{v \times E} \tan(\beta) + \frac{B_x^2 + B_{v \times E}^2 + B_y^2}{2B_z}
 \end{aligned} \tag{5.34}$$

This formula is only the first order Taylor expansion in β and it might be interesting to go higher for the analysis as the assumption $B_z^2 \gg (B_x + B_{v \times E})^2$ is weak. In the first configuration presented in Table 5.20, $\omega_{RF} + \gamma_n B_z = 0$, in the second $\omega_{RF} + \gamma_n B_z = 0$ can be replaced in Eq. (5.34).

However, for both analysis one should consider the uncertainty on the transversal field (equivalently the angle β) as it has been seen previously that the precision of the set value for the transversal field is off.

For the measurement with a continuous white beam, the high voltage scanned followed a sequence of +35 kV, 0 kV, -35 kV, 0 kV, in order to be able to correct for drifts.

5 .5.6 Stability measurement for EDM procedure

One of the goals of the beamtime was to compare two procedures: always measuring a phase scan or measuring at a fixed, high sensitivity phase and making one or several phase scan at the beginning and at the end to get the amplitude and offset.

For both procedures, a stability measurement without electric field has been performed, over night (10 to 12 hours) and each phase scan is about 3 min long. The idea is to see any shifts in the fit parameters for the phase scan procedure and in the neutron phase for the phase scan and fixed phase procedures.

For the phase scan procedure, one has to go through the entire analysis described in [Chapter 4](#) , i.e. compute the neutron phase to determine the stability of the phase. [Fig. 5 .39](#) shows the evolution of the phase, offset, and amplitude for both top and bottom beam for a wavelength range of $\lambda \in [2.94; 14.72]\text{\AA}$. The initial value, recorded in [Table 5 .21](#), was subtracted for amplitude and offset in order to see the drift of the top and bottom beam in the same graph. The same was done for the phase to directly compare the drifts for the two beam. The amplitude and offset are stable on the order of 10^{-4} and 10^{-3} respectively. The neutron phase drifts by $\sim +1.5 \text{ mrad/h}$ for the first 8 hours of measurement and by $\sim -3.3 \text{ mrad/h}$ for the last two hours of measurement. Thus, this drift is not correlated to the parameter of the cosine fit. To explain its origin, correlation calculations have been performed for several values including the temperature of the mu-metal whose data are presented in [Fig. 5 .39D](#). The correlation factor is $-0.3 \text{ mrad/}^{\circ}\text{C}$ when considering a delay of 1 h 40 min.

Beam	$A_{0,0} (\times 10^{-4})$	$A_{1,0} (\times 10^{-4})$	$\varphi_0 (\text{mrad})$
Top	9118 ± 1	-114 ± 1	-1466.9 ± 0.2
Bottom	9061 ± 1	-28 ± 1	-1457.8 ± 0.2

Table 5 .21: Initial value for the amplitude, offset, and phase for the top and bottom beam in [Fig. 5 .39](#)

In that case, the actual stability of the fit parameters is good enough to avoid oscillating artifacts in the neutron phase. One can compare the stability of the phase with the stability of the asymmetry for the measurement at one fixed phase ($\theta_{RF} = 95^\circ$) in [Fig. 5 .40](#).

For both measurements, there is a cyclic change in the temperature with a period of about one day. The asymmetry and the phase scan both follow the temperature drift with a delay of approximately 1 hour 40 min. The opposite slope for the asymmetry is due to the working point in phase: $\theta_{RF} = 95^\circ$. This drift correlated to the temperature is the dominant effect.

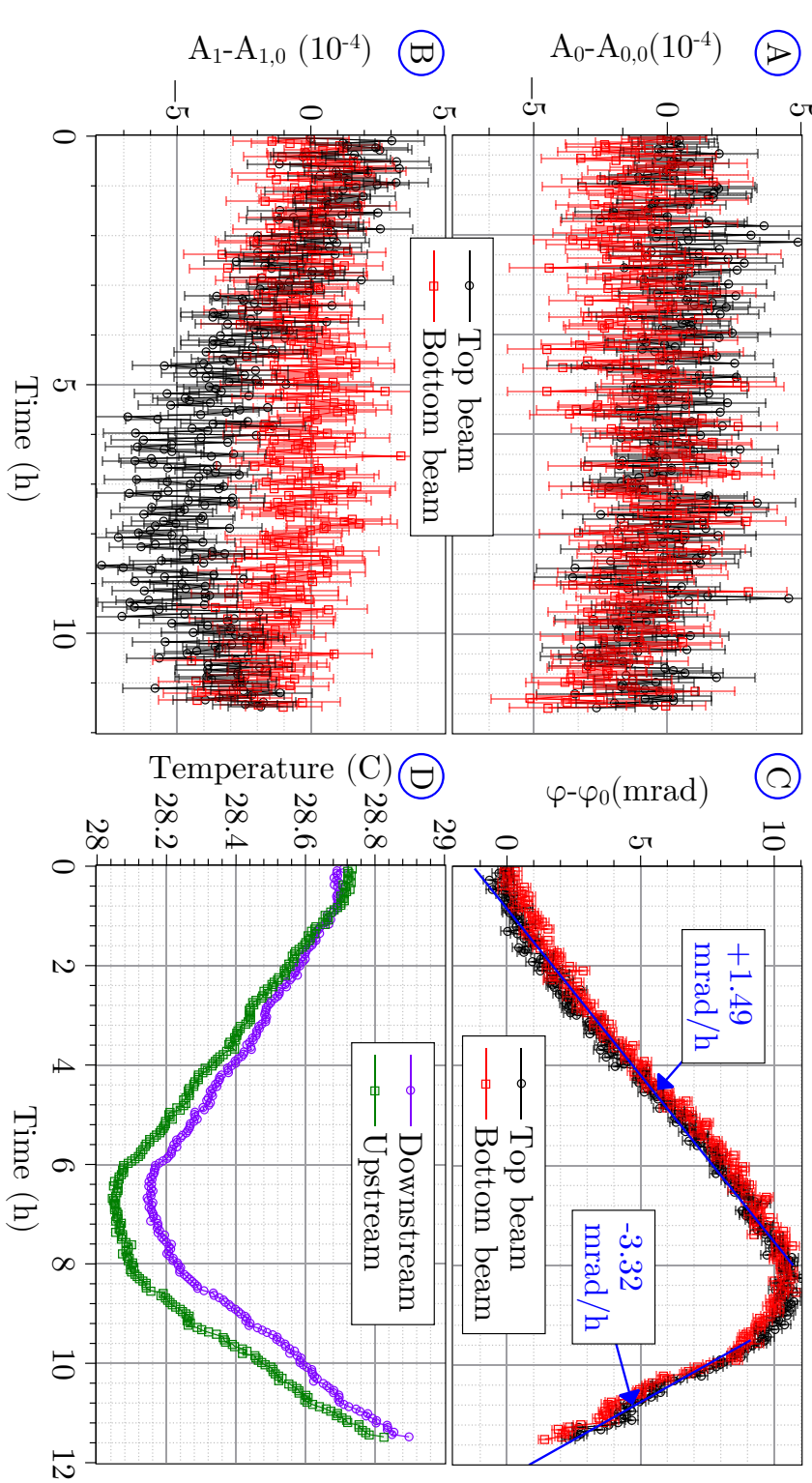


Fig. 5.39: A) Amplitude of Eq. (4.5) corrected by the first value vs. time. B) Offset of Eq. (4.5) corrected by the first value vs. time. C) Neutron phase of Eq. (4.5) corrected by the first value vs. time. D) Temperature from the downstream and upstream sensor vs. time. The values from the fit are for an asymmetry calculated from the integrated count in the range $\lambda \in [2.94; 14.72]\text{\AA}$

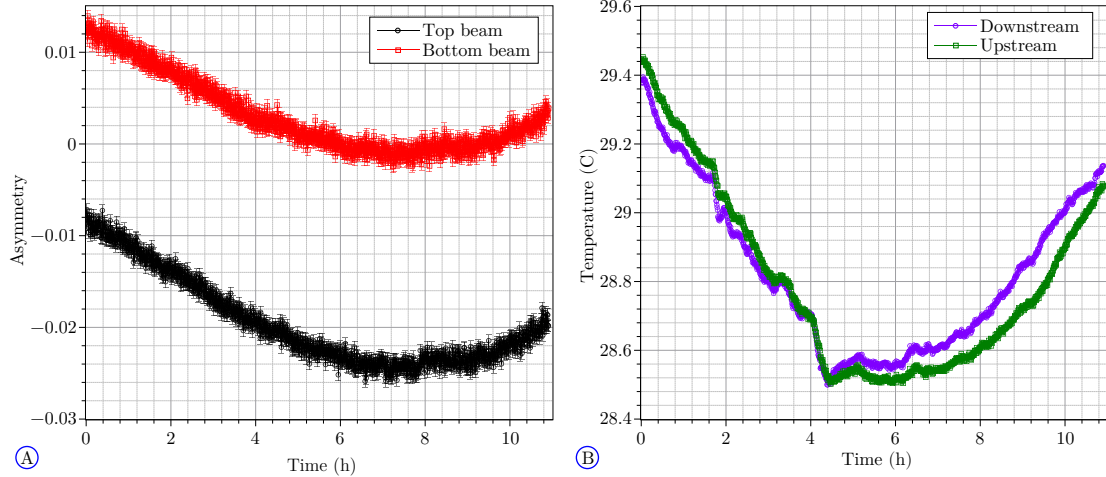


Fig. 5.40: A. Asymmetry vs. time for the top and bottom beam calculated from the integrated number of count for the wavelength range $\lambda \in [2.94; 14/72] \text{ \AA}$. B) Temperature from the downstream and upstream sensor vs. time.

5 .6 Summary

This beamtime was the last as one at the time of writing. In the two years that separates it from the previous beamtime, important changes in the apparatus were implemented.

The new chopper allowed to increase the beam cross-section, which means an increase in the overall statistics from geometric consideration, assuming an identical duty cycle.

The magnetic shielding homogenized the field to the point that the two spin flippers would see a nearly identical field, leading to the measurement of a close to ideal Ramsey pattern. This was crucial for the modulated signal of the spin flippers. And indeed the long drift in the neutron phase as a function of the wavelength, seen in the previous beamtime, Fig. 5.23, did not appear in this beam.

In addition, the new type of fluxgates, the FGM3D-250, and the low resistivity coils for the vertical field allowed us to measure at a higher magnetic field and thus at a higher Larmor frequency, to avoid the fast oscillation in the neutron phase from the neutrons that do not see a full period of the oscillation field. This was combined with a new way to generate the spin flippers signal so that no synchronization between the neutron pulses and the signal was possible.

Despite the loss of a few days due to the breaking down of the detector, many measurements could be taken successfully with the modulated signal. From the magnetic characterization of the setup with neutrons, we have evaluated that the vertical component of the magnetic field measured with fluxgate corresponds to what the neutrons are sensing. Ramping the vertical magnetic field increases the gradient by about 1 per 10 000, $\Delta B_G / \Delta B_z \approx 10^{-4}$. In addition, when ramping the magnetic

field gradient, the neutrons are sensing a field of about 18 % higher than what would be expected from the fluxgate values. This is assuming a linear behavior of the field with the height separation. They also sense a 28 % higher transversal component of the magnetic field and a 12 % lower longitudinal component of the magnetic field than what is measured by the fluxgates at their current position. This is probably due to the geometry of the coils and the position of the fluxgates and should be taken into account when analyzing the $v \times E$ measurement. Moreover, the two measurement procedures for the EDM were characterized by stability measurement of about 12 h each. The amplitude and offset of the fit function are stable on the 10^{-4} and 10^{-3} level respectively. However, the influence of this on the neutron phase could not be estimated as the neutron phase drifted of 10 mrad over an eight hour measurement range. This drift is correlated with the temperature of the mumetal with a 1h 40 min delay. If this effect is caused by the fluctuation of the temperature of the mumetal or the internal fluxgates, a solution could be to add a thermal insulation around the apparatus. On the other hand, if it is coming for a drift of the electronics outside the apparatus, the proposed thermal insulation would not reduce the drift. This should be investigated in the future.

Chapter 6

Conclusion

This chapter summarizes the evolution and improvement of the BeamEDM experiment with regards to the measurements performed during beamtimes from the magnetic fields characterizations to the EDM measurement procedure. In addition, the future of the experiment at the ESS is presented with some of the possible challenges it may face.

6.1 Magnetic Scan

In 2017 at BOA, the objective was to perform a first characterization of the apparatus with respects to the magnetic field. A characterization of the vertical component was performed with a pulsed white beam and a non-modulated sinusoidal signal sent to the spin flippers. The effect of the magnetic field on the neutron phase as a function of the wavelength in [Fig. 5.6](#) corresponds to the expectation when including an error of $0.2 \mu\text{T}$ from the magnetic field. A similar characterization of magnetic field was performed on the vertical field gradient, the transversal, and the longitudinal but with a continuous white beam. To estimate the theoretically expected behavior of the neutron phase as a function of the magnetic field, an effective wavelength was computed so that it would correspond to the average wavelength of the neutrons that contributes to the signal. The neutron phase in [Fig. 5.7](#) displays a linear behavior as expected but with a three sigma discrepancy which could be interpreted as a wrong estimation of B_G over the full length of the apparatus. The measurements for the transversal and longitudinal field both show a quadratic behavior of the phase as a function of the magnetic field compatible with the theoretically expected one. However, the two measurements are not compatible with each other, due to the difference in accuracy when setting the transversal and longitudinal magnetic fields.

The beamtime at PF1b in 2018 started the investigation of the modulated signal for the spin flippers. Measurements with a monochromatic beam were performed to compare the result of a phase scan with an optimal amplitude of the spin flipper

signal with respects to neutron wavelength and with a defined, reference amplitude corresponding to the wavelength of 6.8 Å. Drifting of the magnetic field shown in [Fig. F.1](#) increased the χ^2 related to the measurement in [Fig. 5.17](#). Such χ^2 prevented us from demonstrating that the working range of the apparatus can be expanded due to the modulated signal.

In 2018 at BOA, a pulsed white beam was employed in order to investigate further the effect of the modulated signal on the working range of the apparatus. It was discovered that the non-uniformity of the magnetic field at the position of the spin flippers could distort the neutron phase from its expected linear behavior as a function of the wavelength. It also prevented the correct use of a modulated signal for the spin flippers as the optimal amplitude did not follow a $1/\tau$ description. Additionally, a flaw was found in the modulation technique due to the synchronization of the spin flipper signal with the neutron pulses. At the wavelengths where the neutrons do not see a full period of oscillating field, fast oscillations in the neutron phase were visible with a frequency compatible to that of the sinusoidal part of the signal sent to the spin flippers.

These issues were resolved for the beamtime in 2020 at PF1b. A magnetic shield was added to improve the magnetic homogeneity, and the spin flippers were placed closer to the vacuum pipes, i.e. closer to center of the most uniform region of the magnetic field. The modulated signal was generated in such way that its sinusoidal part was not synchronized with the neutron pulse. The vertical coils and fluxgates were changed to measure at a higher magnetic field, i.e. with a higher neutron Larmor frequency, so the neutrons that do not see a full period of the oscillating field are outside the working range of the apparatus.

These improvements and the high neutron flux of the ILL allowed us to perform high statistics measurements in all magnetic field directions, including the vertical field gradient, using the modulated signal. The fast oscillation in the neutron phase did not appear, nor did the long drift as a function of the wavelength.

The neutron phase as a function of the wavelength and applied vertical magnetic field followed expected behavior in [Fig. 5.36](#). The expected behavior was computed using an interaction length of (4280 ± 80) mm. The error of the measurement is smaller than that of the corresponding theoretically expected value. One can compute back the interaction length to be (4401 ± 0.2) mm if one considers that the measured magnetic field is accurate. In [Section 5.5.4](#), it was stated that the magnetic field was stable enough to estimate the variation with an error of ≈ 4 nT at the fluxgates' position, compared to an error of 200 nT from the first beamtime evaluated in [Section 5.1.4](#).

In the measurements for the vertical field gradient, presented in [Fig. 5.36B](#) and longitudinal field, presented in [Fig. 5.37](#), the field probed by neutrons was found

to be systematically $(11.5 \pm 0.2)\%$ higher and $(10.9 \pm 0.2)\%$ lower than the field recorded by the fluxgates, respectively, when considering the interaction length of (4.28 ± 0.08) m.

The result of the measurement for the transversal field was not conclusive due a high χ^2 which is probably from the low accuracy when setting the transversal field. To solve this problem additional fluxgates positioned according to Fig. 5.38 should be considered as well as a simulation of the magnetic field generated by the coils with the mumetal shielding.

6.2 Stability of the neutron phase

The stability of the neutron phase has improved with time and especially with the introduction of mumetal. One can compare the stability of the neutron phase over time from section 5.3 evaluated from the $v \times E$ measurement and section 5.5. In 2018 at BOA, the phase was shifting by 5 mrad over a few minutes, whereas in 2020 at PF1b, a similar phase shift occurred over several hours.

One can assume that the variation occurred due to a change of an external magnetic field at BOA in 2018, shown in Fig. 5.27. In 2020, on the contrary, the mumetal suppressed this direct effect from the external magnetic field. Indeed, the observed, long term drift shown in Fig. 5.39 is correlated with the temperature of the mumetal hinting toward a thermal effect.

6.3 $v \times E$ effect

In 2018 at BOA, the $v \times E$ measurement has been done with a continuous beam due to time constraint. It had the advantage of increased statistics, however, the offset of the phase vs. wavelength could not be directly demonstrated as there was no time-of-flight measurement. Additionally, the magnetic field was stabilized at $120 \mu\text{T}$ in the transversal direction and $0 \mu\text{T}$ in the vertical and longitudinal ones to maximize the $v \times E$ effect. The result from the measurement shown in Fig. 5.26 is in agreement with the theoretically expected value defined in Eq. (5.25).

In 2020 at PF1b, the measurement was performed with a pulsed white beam and with a magnetic field tilted up to $\pm 13.2^\circ$ from the vertical axis. This reduced the sensitivity of the measurement, but it is a more realistic configuration to reproduce the systematic effect. The analysis of this data was not presented in this thesis.

6 .4 EDM measurement

Two procedures were considered for the EDM measurement. One where we measure the asymmetry as a function the phase between the spin flipper, and the second one where we measure the asymmetry at a fixed phase. In the case of the fixed phase procedure, reference phase scan measurements were performed at the beginning and at the end of the procedure in order to determine the fit parameters of the cosine. Any change in the asymmetry value is converted into a neutron phase as shown in [Fig. 5.27](#) using the amplitude, offset, and distortion parameter, determined from the previously mentioned reference measurement.

From the $v \times E$ measurement in 2018, one investigated the fixed phase procedure. The measurement was a repeated phase scan, however, it was interpreted as fixed phase measurement: each asymmetry value was converted into a neutron phase using as reference the first phase scan.

The instability of the magnetic field during the reference scan used to determine the fit parameters created an oscillation artifact in the neutron phase whose period corresponds to one phase scan as shown in [Fig. 5.27](#). This artifact would have added an offset in the neutron phase if it was really performed at a single phase. The artifacts disappears when using a more stable phase scan as a reference for the fixed phase procedure.

This investigation was continued in 2020 at PF1b where EDM measurements with both techniques were performed. However, during this beam time, the conditions were not optimal either. Indeed, from a stability measurement with a repeated phase scan, it was found that the amplitude and offset of the fit function were stable to 10^{-4} and 10^{-3} level respectively, but the difference between the two procedures could not be seen due to the neutron phase drift correlated to the temperature of the mumetal.

6 .5 Outlook

BeamEDM is currently in a proof-of-principle stage. The full scale experiment would be similar but with 50 m long electrodes, which defines approximately the length of the full apparatus, [\[EZR⁺19\]](#). These electrodes would produce a field of ± 100 kV/cm for the two beams.

The apparatus would be install at the ANNI beamline at the European Spallation Source (ESS) in Sweden, currently under construction. In the proposal [\[TAK⁺19\]](#), ANNI will be a beamline of pulsed cold neutrons. For the first iteration, the experimental area would be 25 m long, extendable to 50 m for the second iteration. The current estimate of the flux is 2.0×10^{10} n cm⁻² s⁻¹ with a spectrum of 2.5 Å to

8 Å with a peak at ~ 3 Å. The beam would have a divergence of 10 mrad and 15 mrad for the horizontal and vertical angle respectively, and neutron pulse frequency of 14 Hz.

Several consideration should be investigated if/when the BeamEDM apparatus will be installed there. A non-ordered, non-exhaustive list is given hereafter:

- Increasing the length of the experiment means increasing the length of the magnetic field coils, which would result in a higher resistance. This could be a problem in trying to drive current through them to generate the set magnetic fields. A redesign could be considered, e.g. increasing the diameter of the wires, separating the coils into smaller ones powered by different power supplies.
- The requirement on the stability of the neutron phase difference $|\Delta\Phi_-| < 20$ nrad/Å equivalent to a 10 fT magnetic gradient drift stated in [EZR⁺19] should also be addressed. Indeed, the neutron phase average over the spectrum has a correlation with the temperature of the apparatus of ≈ -0.30 mrad/°C. Additionally, to stabilize the field on the femto Tesla level, one needs magnetic sensors that can measured down to that same level which is not the case for the currently available fluxgates. However, for this drift to cause a systematic effect it needs to be correlated to the electric field reversal which makes it more realistic.
- In order to maintain a homogeneous magnetic field over the 50 m that would separate the spin flippers, the development of a sufficiently long shield, capable of orders of magnitude improvement in the shielding factor to the current setup is required. This new shield would need additional mumetal layers compared to the current one, this presents mechanical challenges with installation and construction.
- Generating an electric field of 100 kV/cm over a 50 m length would be a challenge. The dielectric strength of vacuum is known to be order of MV/cm, however, its a question of scale. The achievability of high electric fields in a vacuum is dependent on the quality of the electrode surface, as this is increased, more asperities are introduced, resulting in a lower electric field, [BDJ⁺95]. To reduce the asperities from the material itself, diamond milled electrodes could be a solution. This should be combined with a high standard cleaning procedure and an improved vacuum inside the vacuum pipe.
- The capacity of the electrodes stacks will be increased linearly with the length which could pose some safety issues, increase ramping time to a defined voltage, and possibly result in more damage to the electrodes in case of discharge.

- A horizontal divergence of 10 mrad would mean that for a 50 m length, the neutrons would diverge by 0.5 m. Currently the electrodes are 9 cm wide. Increasing their width to 0.5 m would avoid the loss in statistic due to falling out of the interaction region.¹ However, this solution has an issue, the spread could diminish the visibility of the phase scan due to the pseudo-magnetic field from the $v \times E$ effect. If the loss in statistics due to the divergence is acceptable without reflectors, absorbing materials should be install to decrease unwanted radiation and neutron background in the detector.
- A vertical divergence of 15 mrad, the neutrons will experience around 75 or 25 reflections on the electrodes for an electrode separation of 1 cm or 3 cm, respectively if the angular acceptance of the electrodes is high enough. From the reflectivity measurement, the acceptance of the manually polished electrodes was estimated to be 4 mrad at 5 Å and extrapolated to be 13 mrad at 15 Å. In that case where the reflectivity is high enough, the depolarization, losses and π flip from scattering should be considered carefully. However, this divergence angle should not contribute to the $v \times E$ effect as the additional displacement is along the electric field.
- The frame overlap from such a long experiment may also be an issue that is currently under investigation. To avoid it, the wavelength spectrum should be contained in a band of 3 Å and 6.5 Å for example.

The challenges could be faced and the solutions determined if/when BeamEDM will be setup at the ESS on the 25 m long iteration. If the challenges are overcome, the expected sensitivity of BeamEDM in its full scale configuration, i.e. 50 m long, is estimated to be $5 \times 10^{-27} e \text{ cm}$ for 100 days of data taking [EZR⁺19].

¹Not only the electrodes should be increased in width but the entire apparatus.

Part 2 :

**Measurement of the neutron
incoherent scattering length of
Mercury 199**

Chapter 7

Theory of the incoherent scattering length

This chapter describes the neutron–nucleus interaction governed by the strong nuclear forces for the case of slow neutrons, i.e., when the spatial range of neutron–nucleus interactions is negligibly with respects to the neutron wavelength. The theoretical background of neutron scattering lengths is developed with a particular focus on the spin dependent interaction. A similar development can be found in the following books [DGS⁺13][CL15].

7.1 Scattering length

We start by considering an elastic scattering process between a nucleus and neutrons and we assume the neutrons to have an energy E with a relative wave vector \mathbf{k} of modulus k as represented in Fig. 7.1 in the center of mass frame. The distance between the neutron and the nucleus is denoted by \mathbf{r} . The Schrödinger equation of this system is

$$\begin{aligned}\hat{H}\psi(\mathbf{r}) &= \left[-\frac{\hbar^2\Delta}{2m} + V(\mathbf{r}) \right] \psi(\mathbf{r}) = \frac{\hbar^2k^2}{2m}\psi(\mathbf{r}), \\ (\Delta + k^2)\psi(\mathbf{r}) &= \frac{2m}{\hbar^2}V(\mathbf{r})\psi(\mathbf{r}).\end{aligned}\tag{7.1}$$

where V is the potential of the interaction and m is the reduced mass $m = m_N m_n / (m_n + m_N)$ in which the neutron mass is $m_n = 1.675 \times 10^{-27}$ kg, and the nucleus mass is denoted by m_N .

In the case where the mass of the neutron is small relative to the mass of the nucleus, the wave vector of the neutron in the laboratory $k_0 \sim k$, and the formal

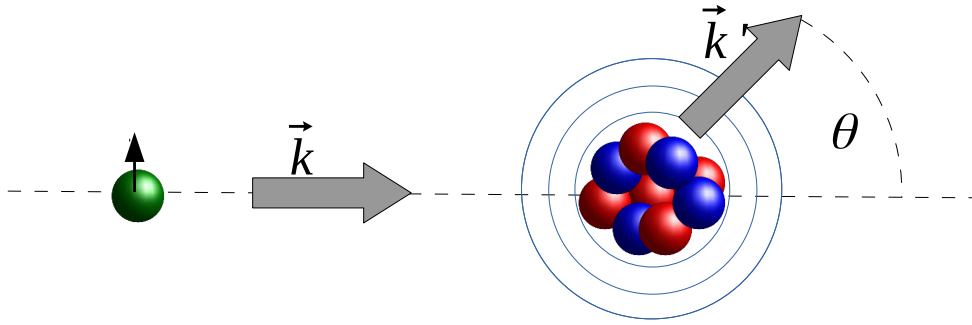


Fig. 7.1: Schematic of the neutron scattering on a nucleus in the center of mass system

solution of Eq. (7.1) is the wave function:

$$\psi(\mathbf{r}) = e^{i\mathbf{k} \cdot \mathbf{r}} - \frac{m}{2\pi\hbar} \int_{-\infty}^{+\infty} V(\mathbf{r}') \psi(\mathbf{r}') \cdot \frac{e^{i\mathbf{k} \cdot |\mathbf{r} - \mathbf{r}'|}}{|\mathbf{r} - \mathbf{r}'|} d^3 r' \quad (7.2)$$

developed in appendix A.1 of [Pie09], where the first part $e^{i\mathbf{k} \cdot \mathbf{r}}$ represents the incoming wave and the second term represents the scattered wave arising from the interaction with the nuclei over the region denoted by \mathbf{r}' .

Far from the scattering center $|\mathbf{r}| \gg |\mathbf{r}'|$, one can solve asymptotically Eq. (7.2) with the approximation $|\mathbf{r} - \mathbf{r}'| \simeq r - (\mathbf{r} \cdot \mathbf{r}')/r$.¹ The scattered wave is then spherical and Eq. (7.3) becomes:

$$\psi(\mathbf{r}) \simeq e^{i\mathbf{k} \cdot \mathbf{r}} + f(\theta) \frac{e^{ikr}}{r}, \quad (7.3)$$

where $f(\theta)$ is called the scattering amplitude and is defined by:

$$f(\theta) = -\frac{m}{2\pi\hbar^2} \int V(\mathbf{r}') \psi(\mathbf{r}') \cdot e^{-i\mathbf{k}' \cdot \mathbf{r}'} d\mathbf{r}', \quad (7.4)$$

with $\mathbf{k}' = kr/r$ the wave vector of the scattered neutron in the direction of \mathbf{r} and θ is the angle between \mathbf{k} and \mathbf{k}' , i.e. the angle of the scattering.

For slow neutrons, the range of nuclear forces is negligible compared to the neutron wavelength $\mathbf{k} \cdot \mathbf{r}' \ll 1$, therefore, $e^{-i\mathbf{k}' \cdot \mathbf{r}'} \sim 1$. The scattering amplitude becomes independent of θ :

$$f = -\frac{m}{2\pi\hbar^2} \int V(\mathbf{r}') \psi(\mathbf{r}') d\mathbf{r}'. \quad (7.5)$$

This corresponds to an isotropic scattering, also called s-wave scattering with orbital momentum $l = 0$.

¹the scattering is a short range interaction

Using the partial wave expansion, the scattering amplitude $f(\theta)$ can be expressed using Legendre polynomials, $P_\ell(\cos(\theta))$, [Gri95]. For $\ell = 0$, the scattering amplitude can be express as:

$$f = \frac{1}{2ik} (e^{2i\delta_0(k)} - 1) = \frac{1}{2ik} \left(2i\delta_0(k) + \frac{(2i\delta_0(k))^2}{2!} + O\left(\frac{(2i\delta_0(k))^3}{3!}\right) \right) \quad (7.6)$$

where $\delta_0(k)$ is the scattering phase of the partial wave which is proportional to k for low energy scattering [Pie09]. The proportional factor is usually denoted by a and called the free scattering length due to its length dimension. Using this notation, Eq. (7.6) becomes:

$$f = a + ia^2k + \mathcal{O}(k^2). \quad (7.7)$$

The free scattering length is a complex number, $a = a' - ia''$, where the imaginary part a'' describes the absorption process [CL15]. It is called the free scattering length because it describes the scattering on unbounded atoms, e.g. scattering on the nuclei of a gas. On the contrary, the bound scattering length b describes the scattering of neutrons on bound nuclei e.g. scattering on the nuclei of crystal. It relates to free scattering length, a , with the following proportional factor

$$b = \frac{A+1}{A}a \quad (7.8)$$

and can be described with a similar structure $b = b' - ib''$.

7.2 Incoherent scattering length

The discussed scattering length does not take into account any spin-dependent effects so far. To address these effects we take the notation \mathbf{I} for the nucleus spin and $\frac{1}{2}\boldsymbol{\sigma}$ for the neutron spin. In the case of an s-wave, the spins couple into the total spin $\mathbf{J} = \mathbf{I} + \frac{1}{2}\boldsymbol{\sigma}$. This coupling affects the scattering by an additional term in $\boldsymbol{\sigma} \cdot \mathbf{I}$. It can be described by the operator \hat{b} :

$$\hat{b} = \frac{(I+1)b^+ + Ib^-}{2I+1} + \frac{b^+ - b^-}{2I+1}\boldsymbol{\sigma} \cdot \mathbf{I} \quad (7.9)$$

where b^\pm are the two eigenvalues of \hat{b} considering the two states for J , [DGS⁺13]. The first term,

$$\bar{b} = \frac{(I+1)b^+ + Ib^-}{2I+1}, \quad (7.10)$$

is independent of the neutron spin and is historically called the coherent scattering length, in contrast to the incoherent scattering length is defined by

$$b_i = \frac{\sqrt{I(I+1)}}{2I+1}(b^+ - b^-). \quad (7.11)$$

One can use these notations in [Eq. \(7.9\)](#) and this yields :

$$\hat{b} = \bar{b} + \frac{1}{\sqrt{I(I+1)}}b_i\boldsymbol{\sigma}I \quad (7.12)$$

7.3 Pseudomagnetic Method

Using the Born approximation, the potential from [Eq. \(7.5\)](#) can be described by the pseudo Fermi potential V_F [[F+36](#)]

$$V_F(\mathbf{r}) = \frac{2\pi\hbar^2}{m_n}\hat{b}\delta(\mathbf{r}) \quad (7.13)$$

with

$$\delta(\mathbf{r}) = \begin{cases} +\infty, & \mathbf{r} = 0 \\ 0, & \mathbf{r} \neq 0 \end{cases} \quad (7.14)$$

and $\int_{-\infty}^{+\infty} \delta(\mathbf{r}) d\mathbf{r} = 1$,

which is dependent on the scattering length. Combining [Eq. \(7.13\)](#) and [Eq. \(7.12\)](#), one can describe the Fermi potential as function of the spin state of the neutron and nuclear spin:

$$V_F(\mathbf{r}) = \frac{2\pi\hbar^2}{m_n}\delta(\mathbf{r}) \left(\bar{b} + \frac{b_i}{\sqrt{I(I+1)}}\boldsymbol{\sigma} \cdot \mathbf{I} \right) \quad (7.15)$$

This only consider one nucleus, but in the reality of an experiment, the neutron sample has N nuclei distributed in a volume V . We assume the distribution to be homogeneous and defined by the density $\rho = N/V$. The overall polarization of the nuclei \mathbf{P} is given by the average of the spin of all nuclei \mathbf{I}_i , normalized by the modulus I :

$$\mathbf{P} = \frac{\langle \mathbf{I}_i \rangle}{I}. \quad (7.16)$$

Integrating [Eq. \(7.15\)](#) over the space parameter (i.e. over the N nuclei) give the macroscopic Fermi potential:

$$V_F(\mathbf{r}) = \frac{2\pi\rho\hbar^2}{m_n} \left(\bar{b} + b_i \sqrt{\frac{I}{(I+1)}} \boldsymbol{\sigma} \cdot \mathbf{P} \right) \quad (7.17)$$

The spin dependent part of the Fermi potential could be written as:

$$V_{F,i} = \rho b_i \frac{4\pi\hbar}{m_n \gamma_n} \sqrt{\frac{I}{I+1}} \boldsymbol{\mu}_n \cdot \mathbf{P}, \quad (7.18)$$

using the relation $\boldsymbol{\mu}_n = \gamma_n \frac{\hbar}{2} \boldsymbol{\sigma}$ with $\boldsymbol{\mu}_n$ the neutron magnetic moment and γ_n the gyromagnetic ratio.

This has a similar structure as a magnetic potential

$$V_{F,B} = -\boldsymbol{\mu}_n \cdot \mathbf{B}, \quad (7.19)$$

where the equivalent to the magnetic field can be expressed by

$$\mathbf{B}^* = -\frac{4\pi\hbar}{m_n \gamma_n} b_i \rho \sqrt{\frac{I}{I+1}} \mathbf{P}, \quad (7.20)$$

using the formula $V = -\boldsymbol{\mu}_n \cdot \mathbf{B}^*$, known from electromagnetism. Because of it dimension B^* is called pseudo-magnetic field [BP65]. This induces a shift in the neutron Larmor frequency of

$$\omega^* = \frac{4\pi\hbar}{m_n} b_i \rho P \sqrt{\frac{I}{I+1}} \quad (7.21)$$

which is usually measured to determine incoherent scattering lengths with a Ramsey apparatus e.g. [AGH⁷³].

Chapter 8

The measurement

This chapter details the measurement of the neutron incoherent scattering length of ^{199}Hg performed in 2017 with the nEDM apparatus. It will start with the motivation for such a measurement, then the apparatus with a focus on the mercury magnetometer. Finally, the measurement with the analysis and the result are presented with the possible outlooks.

8.1 Motivation

In 1947, Fermi and Marshall published the first extensive set of scattering length measurements of the neutron [FM47]. Since then, measurements and calculations have extended this list, and tables of scattering lengths have been published [Sea86], [KRS91]. In 1965, Baryshevskii and Podgortskii formalized the idea of a pseudo-magnetic field for neutrons in a polarized target [BP65], leading to the definition of spin-dependent, incoherent, scattering length. A few years later, Abragam et al. started a series of incoherent scattering length measurements using a neutron Ramsey apparatus [AGH⁺73]. A recent table of scattering lengths can be found in [Mug18].

This part of the thesis presents the first direct measurement of the neutron incoherent scattering length of ^{199}Hg . Thus far, the literature provides the absolute value: $|b_{i,lit}| = (15.5 \pm 0.8) \text{ fm}$ [Sea92]. A first direct measurement of this quantity has now been performed in 2017 by the nEDM collaboration at the Paul Scherrer Institute with its neutron Ramsey apparatus [AAB¹⁹].

The motivation for this measurement, besides the determination of the incoherent scattering length sign per say, is related to neutron electric dipole moment experiments.

Indeed, the mercury incoherent scattering length can affect neutron electric dipole moment experiments that use mercury as a co-magnetometer [AAB¹⁹] [Mar13] as they are highly sensitive to pseudo-magnetic fields. A correlation between the

pseudo-magnetic field resulting from the incoherent scattering length and the electric field reversal would mimic an electric dipole moment. This was only considered during the analysis of [AAA⁺20], and due to the unknown sign of b_i , the result could not be corrected for it. However, the knowledge of the absolute value of b_i allowed an estimation of the magnitude of this effect, leading to a systematic uncertainty contribution of $7 \times 10^{-28} e \text{ cm}$. This represents one third of the total systematic error ($2 \times 10^{-27} e \text{ cm}$) which is why efforts have been put in the determination of the sign of b_i for future measurements.

8 .2 nEDM Apparatus

The presented measurement uses the nEDM apparatus, designed for the neutron electric dipole moment experiment with a mercury co-magnetometer [BCC⁺14]. It uses neutrons with a energy smaller than $< 300 \text{ neV}$, called Ultra-Cold neutrons. Due to their low energy, these neutrons can be stored in material containers which allows for storage type of experiments. The nEDM experiment is one of them. The relevant components of the apparatus used for the incoherent scattering length measurement are presented in [Fig. 8.1a](#).

The PSI UCN source [LT12] produces bunches of the neutrons approximately every 5 minutes. The neutrons are guided through glass vacuum guides (G) which are coated with nickel molybdenum (NiMo) alloy to achieve a high transmission rate. A mechanical switch (S) directs the neutrons to the different parts of the apparatus. The fill position connects the source to the precession chamber (C). The empty position connects the chamber to the neutron spin analyzer and detectors (D1, D2). The monitoring position directly connects the source to the neutron spin analyzer and detectors.

The precession chamber is a cylindrical container of diameter $L = 470 \text{ mm}$ and height $H = 120 \text{ mm}$. It is closed at the top by the high voltage electrode and at the bottom by the ground electrode, both made of aluminum and coated with diamond-like-carbon to increase the storage property of the chamber. The side wall that separates the electrodes is made of polystyrene, coated with deuterated polystyrene for the storage property of the chamber. Additionally, two quartz windows are placed in a parallel configuration on the side wall to allow a UV light to travel through the chamber for the mercury system. The precession chamber is placed in a vacuum tank inside a magnetic shielded room where a set of coils generates a vertical magnetic field $B_0 = 1 \mu\text{T}$. This field is monitored by a mercury co-magnetometer in order to correct for magnetic drifts during the precession measurement as they precess in the chamber with the neutrons during this time.

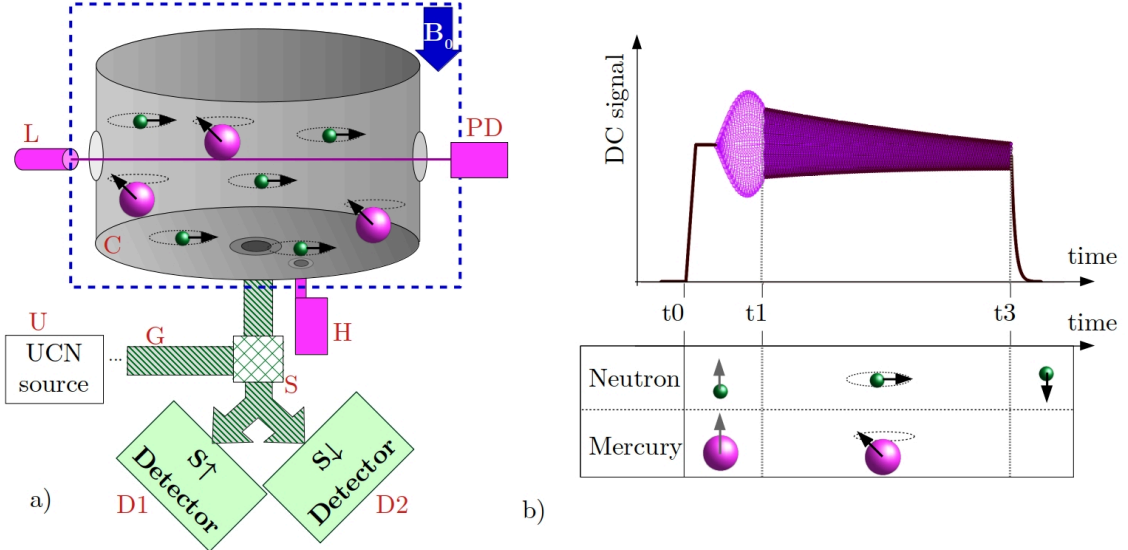


Fig. 8.1: a) A sketch of the Ramsey apparatus to measure the neutron EDM at the Paul Scherrer Institute. The spheres represent the neutrons (small size and green color) and the mercury atoms (large size and pink color). The incoming Ultra Cold Neutrons (UCNs) are transported from the source (U) to the switch (S) which guides them to the precession chamber (C), via neutron guides (G). After a neutron precession measurement, the neutrons are transported from the precession chamber (C) to the switch and the detectors (D1, D2). The mercury system indicates in pink colors the source (H) below the precession chamber, the read-out laser (L) on one side, and photo-detector (PD) on the opposite side. The blue dashed line represents the area where a magnetic field of $1 \mu\text{T}$ was applied. The magnetic field was shielded from the outside field by a room made of mumetal. The orientation of the field in the presented scattering length measurement is represented by a blue arrow. The neutrons and mercury atoms are represented with their spins (black arrow) during the free precession time. b) A representation (not to scale) of one cycle as a function of time and below the spin states of the mercury atoms and the neutrons.

The mercury atoms are produced in a gaseous form by a vaporization process of the ^{199}Hg source (H), at the chamber's bottom. The source's temperature, T_{Hg} , influences the mercury gas density as a higher temperature increases the evaporation rate of mercury [VL99]. An optical pumping by a circular light in the right direction ($H=+1$) polarizes the mercury atoms upwards, i.e., anti-parallel to the main magnetic field in the case of this measurement. Then, the atoms are released in the precession chamber where they are used for their co-magnetometer property and the incoherent scattering measurement simultaneously.

The spin state of the mercury atoms is monitored via a light signal. This signal is coming from a read-out laser (L) on one side of the precession chamber. The light passes through the mercury gas in the chamber to a photo-detector (PD) on the opposite side. The DAQ cards associated with the photo-detector record two signals that are used for the determination of the mercury density and polarization: a DC

signal with a sampling rate of 10 to 50 Hz, which is represented in [Fig. 8.1b](#), and an AC signal with a sampling rate (100 Hz) that went through a bandpass filter centered around ~ 7.85 Hz to match the Larmor frequency of the mercury. The data from the filtered signal, expressed in channels, can be converted into volt via a conversion factor $C_f = 44325.6$ V/channel, determined via a calibration measurement. The laser is tuned to the $6^1S_0 \rightarrow 6^3P_1$ transition of the electronic states of ^{199}Hg . Ref.[\[BBB⁺18\]](#) presents a detailed description of the mercury system.

A set of radio-frequency coils that surrounds the apparatus produces oscillating magnetic fields with matching amplitudes and frequencies, in the plane perpendicular to \vec{B}_0 , in order to sequentially flip the spins of the neutrons and mercury atoms respectively.

8 .3 Mercury co-magnetometer

As stated before ^{199}Hg is the co-magnetometer for the nEDM experiment. The modulation of light due to the precessing mercury atom measures the Larmor frequency of the atoms, and therefore, the magnetic field they sample. Indeed, polarized mercury atoms interact with the magnetic field in the same manner as the neutrons:

$$\omega_{Hg} = -\gamma_{Hg}B, \quad (8.1)$$

with γ_{Hg} the mercury gyromagnetic ratio, ω_{Hg} the mercury Larmor precession and B the value of the magnetic field. This value is then normalized by $\gamma_n/\gamma_{Hg} = -3.8424574(30)$ [\[ABB⁺14\]](#) to estimate the neutron precession frequency due to the magnetic field. A drift in the magnetic field would affect both the neutron and the mercury precession frequencies. By taking the difference of the two frequencies, one suppresses the effect of these drifts.

8 .3.1 Advantages of mercury

From the magnetic sensing point of view, mercury atoms have several advantages:

- Mercury has a non zero magnetic moment. That allows to track the magnetic field.
- Mercury is a diamagnetic atom as its electron ground state is paired, 6^1S_0 , hence, it does not have an electronic spin J , and therefore, does not play a role in the total angular momentum $F = I + J$
- The mercury ^{199}Hg and ^{201}Hg are the fermionic isotopes of mercury, $I = 1/2$ and $I = 3/2$ respectively, i.e. their nuclear spin can be manipulated and probed by optical means (optically detected nuclear magnetic resonance - ODNMR).

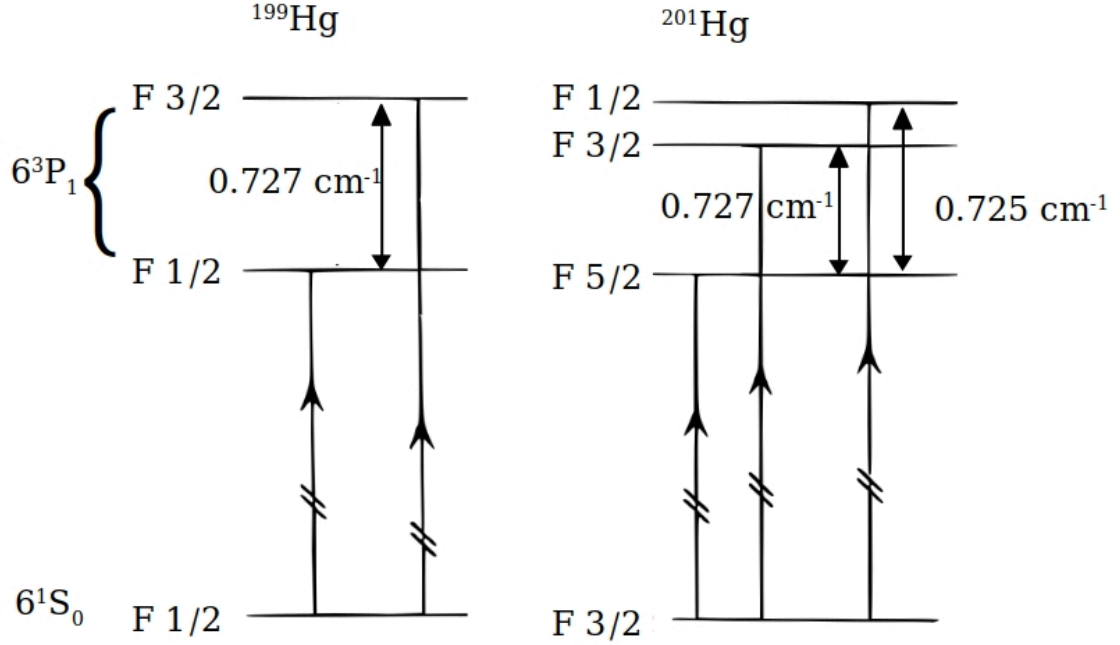


Fig. 8.2: Representation of the hyperfine structure of ^{199}Hg and ^{201}Hg , [Fer13].

- The electric dipole moment of ^{199}Hg is less than $7.4 \times 10^{-30} \text{ ecm}$ [GCLH17]. It is much smaller than the current limit for the neutron EDM, therefore, it should not influence the results.

In addition, the mercury has technical advantages:

- The neutron absorption cross section of mercury at room temperature is relatively low for abundant isotopes (see Table 8.2). Assuming a ^{199}Hg density of $\rho = 5 \times 10^{10} \text{ cm}^{-3}$ and a relative velocity of $v = 150 \text{ m/s}$, the neutron absorption rate is $R = v\rho\sigma_{n,a}(v_{UCN}) = 2 \times 10^{-5} \text{ s}^{-1}$. This effect is negligible for an interaction neutron-mercury of about 200 s.
- The close proximity of the energy lines for ^{204}Hg and ^{199}Hg makes it more easy to optically pump on it with a mercury lamp. These energy lines are summarized in Table 8.1.

In addition, the ^{199}Hg had the advantage to have a better separation of the hyperfine energy band compared to ^{201}Hg . A schematic of the hyperfine structure for both the ^{199}Hg and ^{201}Hg is shown in Fig. 8.2. These are the historical reasons for the choice of ^{199}Hg as co-magnetometer.

8.3.2 Mercury System

A mercury source releases mercury vapor through a capillarity to the polarization cell when heated. The polarization cell is illuminated with right handed circular polarized

Isotope	excited level number	energy band [GHz]
^{199}Hg	1/2	-15.409(13)
^{204}Hg	1	-15.313(13)
^{201}Hg	5/2	-14.6587(99)
^{202}Hg	1	-10.1018(45)
^{200}Hg	1	-4.8054(45)
^{201}Hg	3/2	-0.6763(27)
^{198}Hg	1	0
^{199}Hg	3/2	6.7273(69)
^{201}Hg	1/2	6.872(15)

Table 8 .1: Excited level number and energy level of the first transition of the mercury isotopes. The reference for the energy level is taken from ^{198}Hg , [Kom17]

light to polarize the mercury atoms. At the beginning of a cycle, the mercury atoms are released in the precession chamber. A probing light shoots through the precession chamber to monitor the mercury spin state. The light is collected in a photodetector. The setup is represented in [Fig. 8 .3](#).

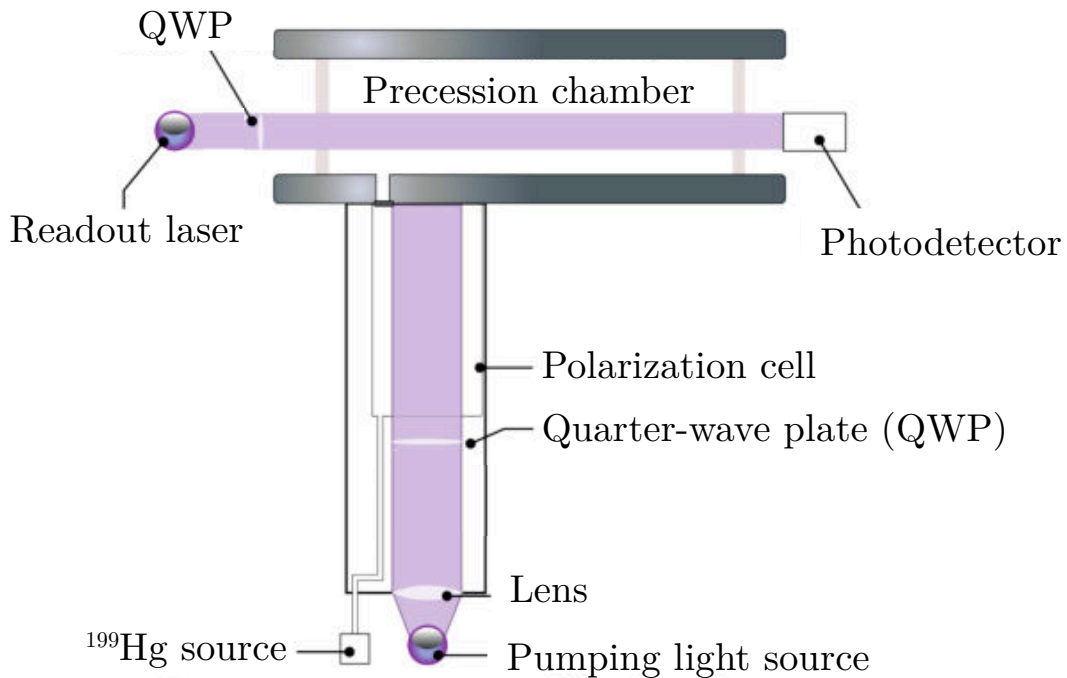
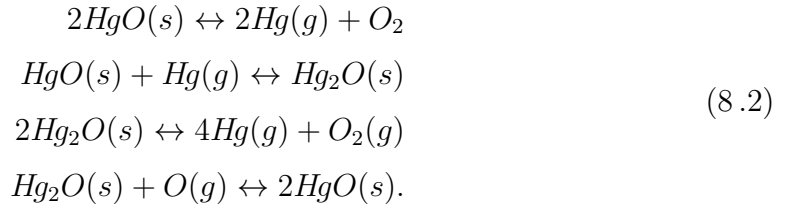


Fig. 8 .3: Sketch of the mercury co-magnetometer designed for the nEDM experiment. The purple areas represent the probing and pumping light. This picture is a modified version of Figure 2.9 in [Kom17]

The mercury source

The mercury source is a source of mercury oxide II, HgO , (also called red oxide due to its color) with a composition described in [Table 8 .2](#) from its seven stable isotopes.

The mercury oxide II has negligible evaporation at 20°C which allows to control the density of mercury atoms released in the magnetometer system with temperature. The production mechanism can be decomposed through the following reactions:



At a temperature range of 160–220 °C, the direct conversion of the red oxide to atomic is low and mainly contribute to the production of black oxide, Hg_2O , in a solid form. It is this lower mercury oxide that produces the atomic mercury [VL99].

Isotope	nEDM source [%]	nature [%]	$\sigma_{n,a}$ [b]
¹⁹⁶ Hg	<0.5	0.15	3080.(180.)
¹⁹⁸ Hg	1.2	10.1	2
¹⁹⁹ Hg	91.09	17.0	2150.(48.)
²⁰⁰ Hg	4.22	23.1	<60.
²⁰¹ Hg	0.92	13.2	7.8(2.0)
²⁰² Hg	1.89	29.65	4.89
²⁰⁴ Hg	0.68	6.85	0.43

Table 8.2: Isotopic composition of the enriched mercury source and of the natural sample with the thermal neutron absorption cross section $\sigma_{n,a}$ for each of the isotope at room temperature, [Fer13].

Polarization of mercury

The polarization of the mercury atom is done by optical pumping [Kas50]. The principle is to illuminate the atoms with a circularly polarized light with a wavelength equal to the energy band of the targeted transition. Due to the conservation of the angular momentum, when the light is absorbed, the light angular momentum is transferred to the mercury atom.

The resonant light is produced either by a mercury bulb lamp using the light emission of ²⁰⁴Hg to target the F=1/2 transition of the ¹⁹⁹Hg or by a UV laser tuned to the same transition. In both case, the circular polarization of the light is performed by shooting through a quarter-wave plate (QWP). In the case of the bulb lamp, the a preliminary stage is used with linear polarizer (LP).

In the case of the thereafter presented measurement, the pumping light is coming from a lamp. It produces right handed circularly polarized photons, i.e. photons with a spin projection along their propagation direction. This leads positive vertical

polarization of the mercury considering a fix axis opposite to gravity. As the helicity of the light is independent of the magnetic field so is the polarization of the mercury atoms.

Probing light source

The probing light source has evolved since the beginning of the data taking with the nEDM apparatus. At the beginning, the probing light was a bulb ^{204}Hg discharge lamp. The atoms of ^{204}Hg are excited to their first state with a 2.5 GHz microwave radiation. When the atoms relax to their ground state, they emit photon with a wavelength of 253.7 nm. This spectrum is broadened due to the Doppler effect and allows to target the near by $F=1/2$ transition of the ^{199}Hg .

However, the lamp has some disadvantages/ drawbacks. They are studied in [Kom17] and [Fer13]. A non exhaustive list is summarized bellow:

- Due to the Doppler effect, the effective cross section of the light absorption by mercury is reduced by a factor $\sqrt{2}$
- The light produced inside the lamp is reabsorbed by the mercury plasma which reduce the available light intensity. This reduction is dependent of several parameter such as the temperature of the lamp, the geometry of the bulb, composition of the lamp etc. [Roc09] [BR03]
- The light from the lamp is divergent, its spacial coherence is low which is a problem for optical fiber guiding and background light.

A laser system has been developed by [Kom17] and [Fer13] which overcomes the problems of the lamp. The laser itself is a commercial one (TA FHG pro). Because of the damage that the UV light causes optical fibers, a free space beam option has been preferred and a dedicated laser hut has been built next to the experiment.

8 .3.3 Interpretation of the mercury signal

The mercury density, polarization and precession frequency are measured via the quantity of light absorbed by the nuclei on resonance with the $6^1S_0 \rightarrow 6^3P_1$ transition. Indeed, the absorption rate Γ has a scalar Γ_0 and a vector component Γ_1 :

$$\Gamma = \Gamma_0 + \boldsymbol{\mu} \cdot \boldsymbol{\Gamma}_1, \quad (8.3)$$

with μ the nuclear magnetic moment. In the case of the ^{199}Hg , the possible contribution of the quadratic dipole moment vanishes because it has a nuclear spin $I = 1/2$ and no electron spin (Wigner-Eckart-theorem).

The scalar component relates to the absorption of unpolarized light and is given by [HM67]

$$\Gamma_0 = \frac{I_0 G}{6\hbar} \text{Im}Z \cdot \frac{2F_e + 1}{2I + 1}. \quad (8.4)$$

The vector component describes the spin dependent or orientation dependent absorption for circularly polarized light [HM67], given by

$$\Gamma_1 = \frac{I_0 G}{8\hbar\gamma_{\text{Hg}}} \text{Im}Z \cdot \left[\frac{\mathbf{e} \times \mathbf{e}^*}{i} \right] \cdot \frac{2F_e + 1}{(2I + 1)(I + 1)} \cdot [2 + I(I + 1) - F_e(F_e + 1)] \quad (8.5)$$

where Z is the complex Voigt-profile that takes into account the Doppler broadening and the line shape of the transition, I_0 is the intensity of a weak light beam, $F_e = 1/2$ is the fine element splitting of the transition, and G is a constant following

$$G = \frac{\lambda^2 e^2 f}{2\pi^2 m_e c^2 \epsilon_0} \frac{1}{v_p}, \quad (8.6)$$

with λ the wavelength of the given transition, f its oscillator strength, v_p the most probable speed of the atoms in the case of an ideal gas, and \mathbf{e} and \mathbf{e}^* are complex polarization vectors which are a combination of

$$\mathbf{e}_\pm = \frac{1}{\sqrt{2}} \begin{pmatrix} 1 \\ \pm i \\ 0 \end{pmatrix} \quad (8.7)$$

for right and left circularly polarized light. This latter is the element that carries the nuclear spin dependent effect. The absorption is maximized when the nuclear spin is aligned anti-parallel with the incoming light beam (i.e. its \mathbf{k} vector), and it is minimized for a parallel orientation.

Because the laser is shooting cross the precession chamber, only the radial polarization of the mercury spin is monitored. When the mercury atoms precess around the vertical magnetic field, the mercury spin alternates between the two eigenstates defined in Eq. (8.7) leading to an oscillation in the light absorption during the mercury precession time.

To determine the density and polarization of the mercury gas, a model was developed in [BBB¹⁸]. It is based on the assumption that the amplitude of the oscillation $a_s(t)$ in the light absorption due to the precession of the mercury spin is small compared to the light level $I(t)$ when the chamber is empty, $t = t_0$. In addition, we assume here that there is no offset in $I(t)$, i.e., the laser is exactly tuned on the $6^1S_0 \rightarrow 6^3P_1$, $F=1/2$ transition. With these assumptions, the light level for

unpolarized atoms follows

$$\forall t, \quad I(t) = I(t_0) \exp(-\rho(t)\sigma_a L), \quad (8.8)$$

where $\rho(t)$ is the mercury density in the chamber at the time t , $\sigma_a = 2 \times 10^{-17} \text{ cm}^2$ is the light absorption cross section of unpolarized mercury, and $L = 47 \text{ cm}$ is the diameter of the precession chamber. The absorption is then given by

$$\forall t, \quad A(t) = \frac{I(t_0) - I(t)}{I(t_0)} = 1 - e^{-\rho(t)\sigma_a L}. \quad (8.9)$$

If the chamber is empty, $\rho(t) = 0$, therefore, $I(t) = I(t_0)$ and $A = 0$. The amplitude of the oscillation described earlier is calculated the difference between the minimum and maximum light level due to polarized mercury gas,

$$\begin{aligned} a_s(t) &= \frac{I(t_0)}{2} \left(e^{-\rho(t)[1-P(t)]\sigma_a L} - e^{-\rho(t)[1+P(t)]\sigma_a L} \right) \\ &= \frac{I(t_0)}{2} e^{-\rho(t)\sigma_a L} \times \left[e^{\rho(t)P(t)\sigma_a L} - e^{-\rho(t)P(t)\sigma_a L} \right] \\ &= I(t_0)e^{-\rho(t)\sigma_a L} \times \sinh(\sigma P(t)\rho(t)) \\ &= (1 - A(t)) \sinh(\sigma P(t)\rho(t)) \\ &= \frac{I(t)}{I(t_0)} \sinh(\sigma P(t)\rho(t)), \end{aligned} \quad (8.10)$$

where $P(t)$ is the polarization of the mercury atoms along the path of the readout laser light at the time t . In the case of $P(t) = 0$ or if $\rho(t) = 0$, we retrieve $a_s(t) = 0$. Inverting this equation gives the product of the density and polarization of the mercury gas as function of time

$$\rho(t) \times P(t) = \rho P(t) = -\frac{1}{L\sigma} \operatorname{arcsinh} \left(\frac{a_s(t)}{I(t)} \right). \quad (8.11)$$

8.3.4 Meta file, PMT signal, precession signal

The signal from the photo-detector is split by a T-piece after a current-to-voltage converter [PXI]. One part of the signal is directly recorded with a variable sampling frequency (usually 10 Hz) in a file called "****PMT-readout.edm". This file contains the unfiltered data from the photo-detector for a full Ramsey measurement, i.e. several filling and pumping out of mercury gas. From this file, one can extract the light level for unpolarized atoms at different times represented in Fig. 8.1b and shown on data in Fig. 8.4.

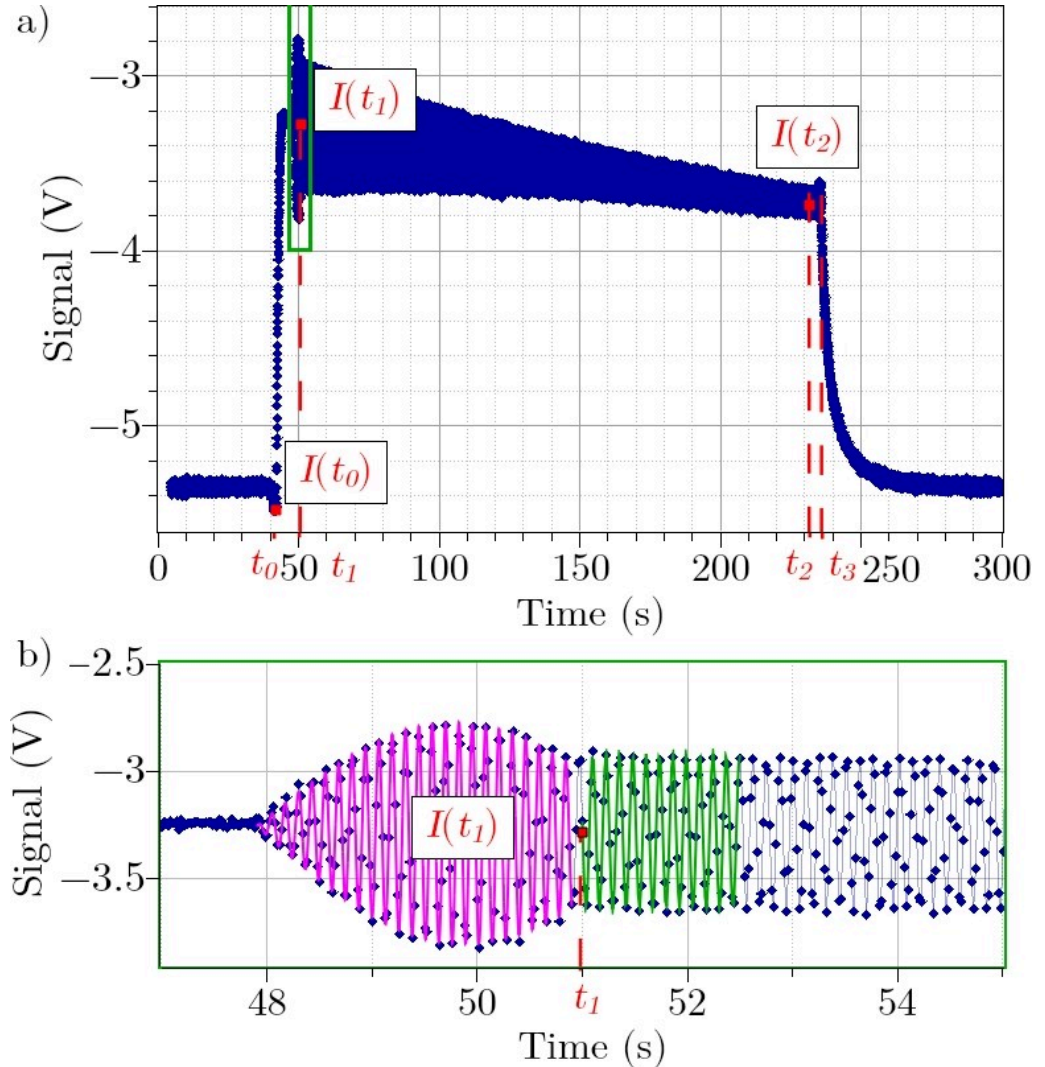


Fig. 8.4: a) An example of a DC signal of the ^{199}Hg co-magnetometer during a measurement cycle with a $7/4\pi$ configuration. The value for $I(t)$ is indicated by a red squares for several time stamps (t_0 , t_1 , and t_2). b) A zoom of the green squared region in a). The signal is fitted by a sinusoidal function modulated by a $\sin(x)$ in pink. This section of the signal corresponds to the mercury spin flip. The value of $I(t_1)$ is determined from this fit. The green line is a guide for the eyes in order to see the oscillation in the mercury signal. For this cycle, $a_s(t_1) = 0.36$ V, $I(t_0) = -5.48$ V, $I(t_1) = -3.28$ V, $T_2 = 101$ s, and $T_3 = 810$ s.

- t_0 is the starting time of the mercury gas filling into the chamber. $I(t_0)$ is evaluated by a constant fit of 1.5 s before t_0 . It corresponds to the light level for $\rho = 0$.
- t_1 is the time when the mercury spin flip has ended. It is computed from t_0 and the time it takes to fill the precession chamber with the mercury gas and perform the mercury spin flip. $I(t_1)$ is evaluated from the offset of a double sinusoidal fit (a sinusoidal function modulated by another sinusoidal function) for 1.5 s before t_1 .
- t_2 is defined about 170 s after t_1 which is still during the free precession period of the mercury. $I(t_2)$ is evaluated from the offset of a sinusoidal fit for 1.5 s before t_2 . $I(t_2)$ and t_2 are only used to compute the exponential decay constant of the light level for unpolarized mercury during the measurement, the position of their evaluation is therefore only constrained by the free precession time of the mercury.
- t_3 is the time when the mercury is pumped out of the chamber.

A drop in the signal is visible around t_0 , when the neutron shutter was being closed. The shutter is based on a rotation of an element in front of the guide. As the rotation axis is fixed on the precession chamber, the rotation of the piece also leads to a rotation of the precession chamber. From this rotation, the alignment between the chamber and the laser system is changed. This specific alignment is maintained for the entire duration of the precession measurement which is why $I(t_0)$ is measured in the drop. This effect is also visible when the shutter opens again to empty the chamber by a bump in the signal. Because of this change of alignment when opening the shutter, $I(t_2)$ is measured before the bump.

The second part of the signal was sent to DAQ board [Raw14] which includes a band-pass filter centered around 7.85 Hz with the cut-off frequencies at 7.125 Hz and 8.68 Hz. The data from this signal is usually sampled with a frequency of 100 Hz and recorded only during the free precession of the mercury, i.e. between the mercury flipping pulse and the pumping out. This gives a signal in channel, a conversion factor of 44325.6 channel/V is used to compare this signal with the PMT signal, see appendix I. The amplitude of the oscillations and its decay time constant over time are extracted from these data. An example is shown in Fig. 8.5.

A last file that contains all the meta data of the experiment also contains the information about the mercury signal. It is a summary of the pre-analysis of the precession and PMT files but the accuracy is less than 10% for the light levels as shown in Fig. I.3 and no uncertainty is given for these values. Therefore, the data have been extracted from the filtered and un-filtered photo-detector signals.

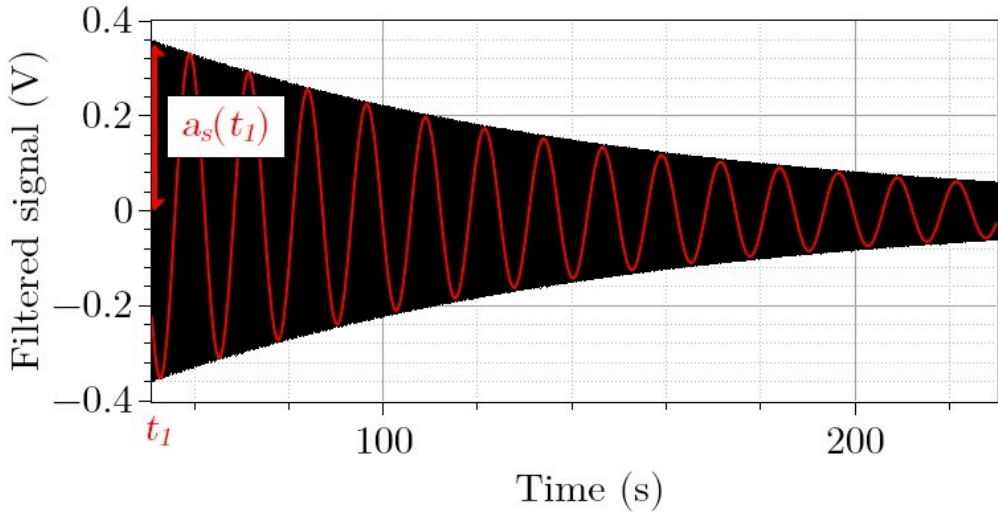


Fig. 8.5: An example of the filtered signal (black curve) of the photo-detector of the same cycle between t_1 and t_3 . The red curve is a representation of the decay \sin function used to fit the data but with an frequency scale by a factor 100 so that the oscillations are visible. For this cycle, $a_s(t_1) = 0.36$ V, $I(t_0) = -5.48$ V, $I(t_1) = -3.28$ V, $T_2 = 101$ s, and $T_3 = 810$ s.

8.4 Mercury incoherent scattering length measurement

The incoherent scattering length of ^{199}Hg is measured with the described before mentioned apparatus, using the mercury co-magnetometer as the polarized nuclei. The measurement, done in august 2017, involves the separated oscillating fields method [Ram50] to determine the neutron precession frequency for different densities and polarizations of the mercury gas.

The frequency shift due to the incoherent scattering length would be maximal by having a pure eigenstate of the mercury spin (parallel or anti-parallel to the magnetic field). However, the visibility of the co-magnetometer signal is maximal for the mercury spin precessing in the plane perpendicular to the magnetic field, \mathbf{B}_0 . A compromise was chosen by setting the mercury spin in a superposition state corresponding to a $3\pi/4$ or a $7\pi/4$ spin flip from the initial spin state. This reduces the strength of the incoherent scattering length effect and of the visibility of the co-magnetometer signal by a factor $\sqrt{2}$.

The measurement was performed over several days in different configurations for the mercury polarization and density, summarized in [Table 8.3](#) and explained hereafter. We define as "cycle" a set of steps that lead to the measurement of the neutron spin state, detailed below :

- **Filling:** At the beginning of each cycle, the neutrons and mercury atoms are both polarized in the magnetic field axis. The UCNs are filled into the precession chamber first. In a second step, the mercury atoms are introduced.
- **Spin-flips:** A first oscillating magnetic pulse is applied to flip the mercury spins. Its frequency is set to the mercury resonance Larmor frequency, f_{Hg} , of about 8 Hz at 1 μT . Then, a second pulse is applied to flip the UCN spins to a $\pi/2$ configuration. Its frequency, f_{RF} , is close to the neutron Larmor resonance frequency of approximately 30 Hz at 1 μT and its duration is about 2 s.¹
- **Free precession:** The UCNs' and mercury atoms' spins start to precess freely around the main magnetic field axis after their respective flipping pulses. The free precession time of the neutrons lasts for $T_0 = 180$ s.
- **Spin-flip:** After the 180 s, a third oscillating magnetic pulse is applied to flip the UCN spins again by $\pi/2$. Besides having the same amplitude, duration, and frequency, the phase of this pulse is coherent with the previous one.

- **Emptying:** The precession chamber is emptied by guiding the neutrons to the spin analyzer and detectors and then pumping out the mercury gas. The analyzer separates the neutrons according to their spin to detector (D1) or detector (D2). From the integrated counts in each detector, the asymmetry is computed,

$$A = \frac{N_1 - N_2}{N_1 + N_2}, \quad (8.12)$$

where N_1 and N_2 corresponds to the counts in the detector D1 and D2 respectively.

The process is repeated twelve times with different f_{RF} settings to obtain a Ramsey pattern with one mercury polarization e.g. $3\pi/4$ polarization. A Ramsey pattern was then measured with the opposite polarization, $7\pi/4$ polarization. These two measurements form a group of opposite polarization called "polarization group" in [Table 8 .3](#). Then, a second polarization group is measured starting by a $7\pi/4$ polarization. This sequence was repeated several times, alternating the $3\pi/4$ and $7\pi/4$ mercury polarization with a stable density of mercury. The regular changes help to correct for systematic effects from drifts in the magnetic gradient.

In addition, the temperature of the mercury oven was changed to repeat the measurement at a different density for the mercury gas.

¹The frequency of the flipping pulses for the two species are far enough apart so that they do not influence the other species.

Batch number	1	2	3	total
Nb of cycles	240	228	204	672
Nb of Ramsey pattern	20	19	17	56
Nb of polarization group	10	8	8	26
T_{Hg} (C)	225	225	210	
Sampling rate of the Hg signal (Hz)	10	10	50	
Averaged measured polarization	0.13	0.12	0.20	
Averaged measured absorption	0.66	0.66	0.41	
Averaged measured density (mol/mm ³)	0.19	0.19	0.10	

Table 8 .3: *Attributes of each batch with the number of cycles, the number of Ramsey patterns taken, the number of groups with opposite polarization for the linear regression, the temperature of the mercury source and sampling rate of the photo-detector for the mercury signal. In addition, the averaged metafile values of the polarization, density, and absorption are summarized.*

8 .5 Data Analysis

Using Eqs. (7.8) and (7.21), one can derive the free scattering length to be

$$b_i = \frac{m_n}{2\hbar} \sqrt{\frac{I+1}{I}} \frac{\Delta f_n^*}{\rho P}, \quad (8.13)$$

where Δf_n^* is the frequency shift in the neutron precession frequency due to the pseudo-magnetic field B^* . As one cannot insure that the neutron frequency shift Δf_n of a single measurement is the result of the incoherent scattering length effect only, a relative measurement was performed as previously explained and the data of each polarization group were analyzed together in order to determine the slope $\partial(\Delta f_n)/\partial(\rho P)$. As the neutron frequency shift and product of the mercury density and polarization are calculated from different subsection of the data, the determination of these two value can be done independently.

The neutron frequency is determined for each cycle through the evaluation of the asymmetry Eq. (8.12) and the difference between the first estimate of the neutron frequency and the frequency of the oscillating magnetic field is given by

$$\Delta\nu = \left| \frac{\gamma_n}{\gamma_{\text{Hg}}} \right| f_{\text{Hg}} - f_{\text{RF}}, \quad (8.14)$$

where f_{RF} is the set frequency of the neutron flipping pulse, f_{Hg} is the measured precession frequency of mercury, γ_{Hg} is the mercury gyromagnetic ratio. During the measurement, f_{RF} is the range of the central fringe of the Ramsey pattern, where the asymmetry has a cosine behavior as a function of $\Delta\nu$,

$$A = A_0 - |\alpha| \cos[2\pi T(\Delta\nu + \Delta f_n)], \quad (8.15)$$

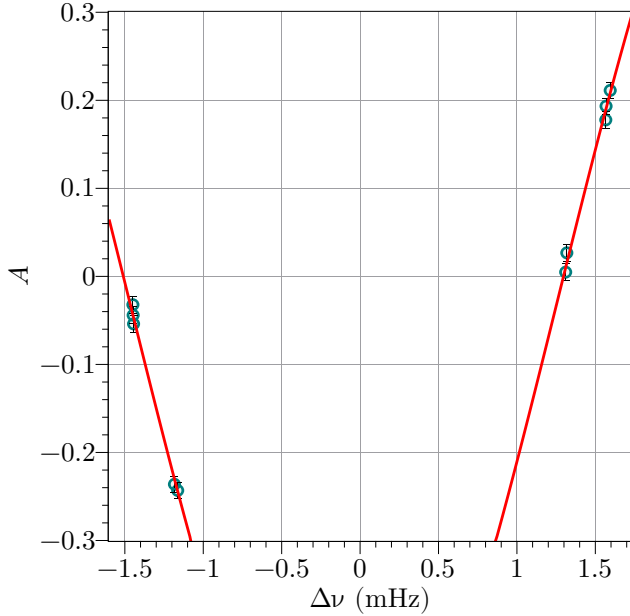


Fig. 8.6: Example of asymmetry A vs. $\Delta\nu$ plot from the batch 3. Here, only ten data points are used for the fit with Eq. (8.15) (red curve) because two cycles are excluded.

of amplitude α , offset A_0 , and where $\Delta f_n = f_n - |\gamma_n/\gamma_{Hg}|f_{Hg}$ is the neutron frequency shift from the normalized mercury frequency, and $T = T_0 + 2 \times 2/\pi T_{SF} = 182.5$ s is the interaction time. This time includes the precession time T_0 , and the interaction between the neutron and mercury spin during the neutron spin flips T_{SF} .² A Ramsey pattern is reconstructed by grouping together 12 successive cycles with the same mercury configuration as displayed in Fig. 8.6. The parameters A_0 , α , and Δf_n are determined via a cosine fit over the Ramsey pattern with the assumption that their values do not change over the cycles.

Then, by inverting Eq. (8.15) with the value of A_0 , α obtained by previously stated fit, one can compute the individual cycle neutron frequency shift with

$$\Delta f_{n,j} = f_{n,j} - |\gamma_n/\gamma_{Hg}|f_{Hg,j} = \frac{\text{sgn}(\Delta\nu_j)}{2\pi T} \arccos\left(\frac{A_a - A_j}{|\alpha|}\right) - \Delta\nu_j, \quad (8.16)$$

where the j index runs over the cycle of one Ramsey pattern and $\text{sgn}(\Delta\nu_j)$ give the sign of $\Delta\nu_j$. This sign is used in Eq. (8.16) to expand the range of arccos-function from $[0;\pi]$ to $[-\pi;\pi]$. If a drift in the magnetic field affects the neutrons and the mercury spin equally, the resulting frequency shift does not alter Δf_n . As the pseudo-magnetic field from the incoherent scattering length only affect the neutron spin, its effect remains in Δf_n .

²The factor $2/\pi$ takes into account the reduced contribution of the interaction during this period.

From Eq. (8.11), we know the density and polarization as function of time. However, we need it averaged over the interaction time T for each cycles:

$$\rho P = \frac{1}{T} \int_{t_1}^{t_1+T} \rho P(t) dt = \frac{1}{L\sigma T} \int_{t_1}^{t_1+T} \operatorname{arcsinh} \frac{as(t)}{I(t)} dt. \quad (8.17)$$

From Figs. 8.4 and 8.5, one can see an exponential decrease in $I(t)$ and $as(t)$ between $t = t_1 \approx 51$ s and $t = t_3 \approx 230$ s. This is due to the leaking of the mercury gas out of the chamber in the vacuum tank and the depolarization of the mercury spin with wall collisions. It can be parametrized as

$$I(t) = [I(t_1) - I(t_0)] \cdot \exp(-t/T_3) + I(t_0) \quad (8.18)$$

and

$$as(t) = as(t_1) \cdot \exp(-t/T_2), \quad (8.19)$$

where T_2 is the depolarization time constant, and T_3 is the leaking time constant which is computed from

$$\forall t_2 \in]t_1; t_3], \quad T_3 = \frac{t_2 - t_0}{\ln \left(\frac{I(t_1) - I(t_0)}{I(t_2) - I(t_0)} \right)}. \quad (8.20)$$

The absolute value of the density and polarization for each cycle is then compute via a numerical integration as the combination of Eqs. (8.17) to (8.19) does not have an analytical solution. We define the sign of ρP according to its spin direction with respect to the magnetic field: the $3\pi/4$ configuration is with the spin in the direction of the main magnetic field, therefore, has a positive value, the $7\pi/4$ configuration has a negative one.

8.6 Data selection criteria

From an initial sample of 672 cycles, data were cut based on the following considerations:

Firstly, 24 cycles were removed due to exceptional events like a pause in the middle of a Ramsey pattern.

The second set of criteria is applied during the data extraction on the following parameters:

- Waiting time: the time between the end of the previous cycle and the beginning of the current one. Fluctuations can happen as this waiting time is dependent on the time between UCN pulses which is not fixed. The acceptable values for these times are between 10 s and 21 s. Outside the defined range, the mercury

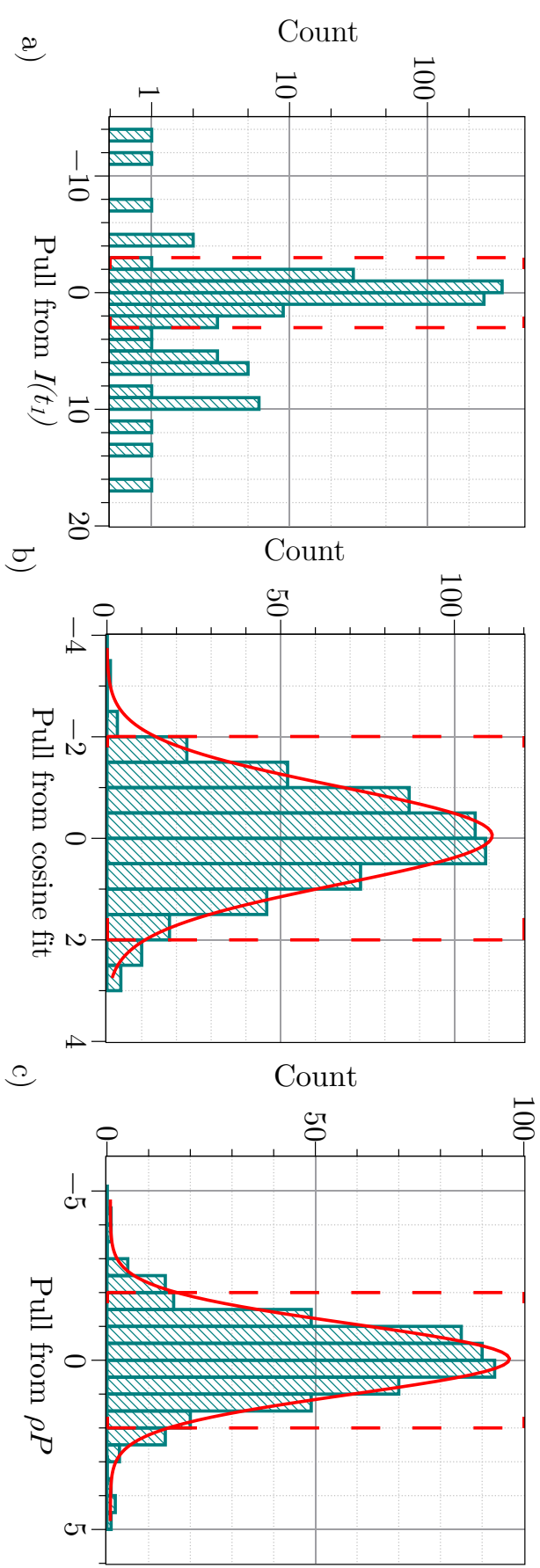


Fig. 8.7: a) Pull distribution of $I(t)$ at $t = t_1$ as defined in the text. The red dashed lines represent the exclusion limits Eq. (8.15). The red dashed lines represent the exclusion limits and the continuous red line is a density-polarization factor as defined in the text. The red dashed lines represent the exclusion limits and the continuous red line is a Gaussian fit.

inside the source increases or decreases in pressure, leading to a higher or lower density compared to adjacent cycles. Therefore, the waiting time is an indicator of the initial pressure build up in the source but not its effects on the following cycles. From this criteria, 90 cycles were excluded additionally.

- The value of $I(t_1)$ of each batch: stated in the previous section, this parameter is directly linked to the density of mercury inside the chamber. It is an indicator of both the pressure build up in the mercury source and its effect on the following cycles. The acceptable value for $I(t_1)$ is determined for each batch individually from the mean value $\langle I(t_1) \rangle$ and the standard deviation $\sigma(I(t_1))$ calculated after the initial cuts in the data. 7 cycles outside a three sigma range are rejected additionally. The cut on the full data set is represented on the pull distribution in [Fig. 8.7a](#) where the pull value defined by

$$\frac{\langle I(t_1) \rangle - I(t_1)}{\sigma(I(t_1))}.$$

- The neutron statistics: the low statistic measurement $N < 4000$ are removed. This leads to a rejection of 10 cycles additionally.

A final set of criteria is applied before the final stage of the analysis on a Ramsey pattern level.

- During the determination of the neutron frequency shift, the stability of the fit parameters over a Ramsey pattern is estimated from the pull value of each cycle. This latter is defined by the difference between the expected value, i.e., the value of [Eq. \(8.15\)](#) at $\Delta\nu_j$, and the asymmetry A_j of the cycle j over the error of A_j . 18 cycles further than two sigma from their fit function were rejected during the frequency shift determination, as depicted in [Fig. 8.7b](#).
- During the determination of density and polarization of mercury, the stability of the production over each Ramsey pattern is estimated from the deviation between the data and the mean value $\langle \rho P \rangle$. 33 cycles outside a two sigma range from their mean are rejected. The cut on the data is represented on the pull distribution in [Fig. 8.7c](#) where the pull value is defined by

$$\frac{\langle \rho P \rangle - (\rho P)}{\sigma(\rho P)}.$$

In total, 490 cycles out of 672 are used in the final stage of the analysis and are used to determine the slope the neutron frequency shift as a function of the mercury density and polarization $\partial(\Delta f_n)/\partial(\rho P)$.

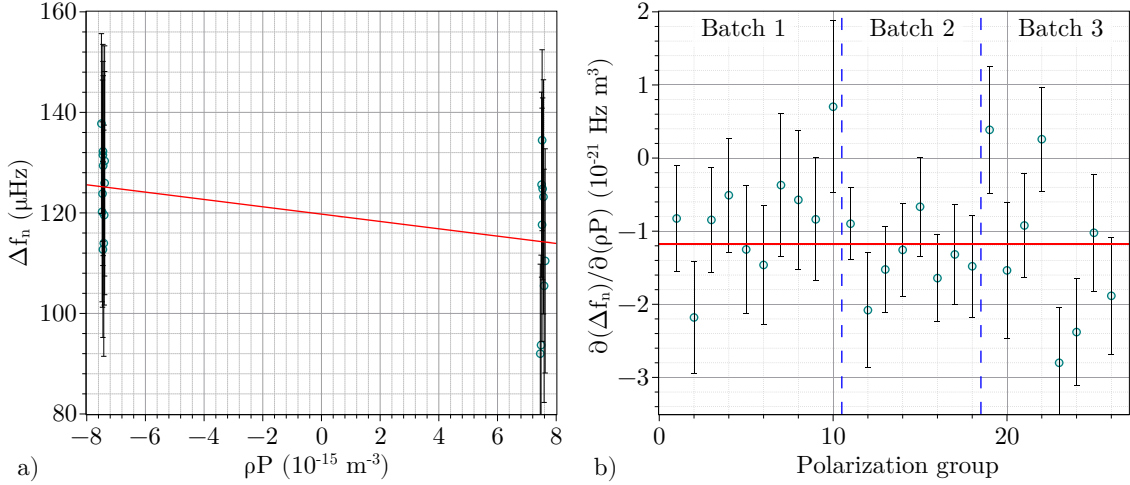


Fig. 8.8: a) An example of the linear regression for the one polarization group. b) Result of the linear regression between Δf_n and ρP for group of successive Ramsey pattern with opposite polarization. The data of the batch 1, 2, and 3 are delimited by dashed blue lines. The red line represents the weighted mean $\langle \partial(\Delta f_n)/\partial(\rho P) \rangle = (-1.2 \pm 0.1) \times 10^{-21} \text{ Hz m}^3$.

8.7 Results

In the final stage of the analysis, the neutron frequency shift Δf_n is plotted versus the density-polarization factor ρP as shown in Fig. 8.8a for each polarization groups, i.e., group of two consecutive Ramsey patterns with opposite mercury polarization. The slope, $\partial(\Delta f_n)/\partial(\rho P)$, is calculated from a linear regression of the data and recorded as function of the polarization group number in Fig. 8.8a. A weighted average gives

$$\langle \partial(\Delta f_n)/\partial(\rho P) \rangle = (-1.2 \pm 0.1) \times 10^{-21} \text{ Hz m}^3. \quad (8.21)$$

By inserting this value into Eqs. (7.8) and (8.13), we obtain

$$b_i = (-16 \pm 2) \text{ fm}. \quad (8.22)$$

This value is in agreement with the literature value $|b_{i,lit}| = (15.5 \pm 0.8) \text{ fm}$ and the negative sign of the neutron incoherent scattering length of ^{199}Hg has been determined.

The nEDM experiment is over and the data analyzed. The result of this measurement will only slightly change the result in [AAA⁺20]. The reason for this is the low sampling rate of the mercury signal leading to a difficult determination of the net polarization of the mercury along the magnetic field. The limiting factor for the correction is due to the determination of the polarization. This could be

improved for the n2EDM experiment which is the upgrade of nEDM by having a higher sampling rate for the mercury system during the flipping pulse.

Other EDM experiments are using co-magnetometers such as ^{129}Xe [Mar13] and would be subject to the same effect. Therefore, a measurement of the neutron incoherent scattering length of this nuclei could be relevant.

References

- [AAA⁺19] MW Ahmed et al. A new cryogenic apparatus to search for the neutron electric dipole moment. *Journal of Instrumentation*, 14(11):P11017, 2019.
- [AAA⁺20] C. Abel et al. Measurement of the permanent electric dipole moment of the neutron. *Phys. Rev. Lett.*, 124:081803, 2020.
- [AAB⁺19] C. Abel et al. nEDM experiment at PSI: Data-taking strategy and sensitivity of the dataset. In *European Physical Journal Web of Conferences*, volume 219 of *European Physical Journal Web of Conferences*, page 02001, 2019.
- [ABB⁺80] I.S. Altarev et al. A search for the electric dipole moment of the neutron using ultracold neutrons. *Nuclear Physics A*, 341(2):269–283, 1980.
- [ABB⁺81] I. S. Altarev et al. A new upper limit on the electric dipole moment of the neutron. *Physics Letters B*, 102(1):13–16, 1981.
- [ABB⁺92] I.S. Altarev et al. New measurement of the electric dipole moment of the neutron. *Physics Letters B*, 276(1):242–246, 1992.
- [ABB⁺96] I. S. Altarev et al. Search for the neutron electric dipole moment. *Physics of Atomic Nuclei*, 59(7):1152–1170, 1996.
- [ABB⁺14] S. Afach et al. A measurement of the neutron to ^{199}Hg magnetic moment ratio. *Physics Letters B*, 739:128–132, 2014.
- [ABB⁺21] N. J. Ayres et al. The design of the n2EDM experiment. *The European Physical Journal C*, (512):80, 2021.
- [AD5] Ad5791 datasheet. <https://www.analog.com/media/en/technical-documentation/data-sheets/ad5791.pdf>. Accessed: 2021-04-06.
- [ADH⁺06] H. Abele et al. Characterization of a ballistic supermirror neutron guide. *Nuclear Instruments and Methods in Physics Research Section A: Accelerators, Spectrometers, Detectors and Associated Equipment*, 562(1):407–417, 2006.
- [AFS20] Apriadi S. A., Akmal F., and Mirza S. A new left-right symmetry model. *Advances in High Energy Physics*, 2020:3090783, 2020.
- [AGH⁺73] A. Abragam et al. Pseudo magnetic moments of ^1H and ^{51}V measured by a new method. *Physical Review Letters*, 31(12):776–779, 1973.
- [B.14] Csaba B. Baryogenesis: A small review of the big picture, 2014.

- [BB13] W.H. Bragg and W.L. Bragg. The reflection of x-rays by crystals. *Proceedings of the Royal Society of London. Series A, Containing Papers of a Mathematical and Physical Character*, 88(605):428–438, 1913.
- [BBB⁺18] G. Ban et al. Demonstration of sensitivity increase in mercury free-spin-precession magnetometers due to laser-based readout for neutron electric dipole moment searches. *Nuclear Instruments and Methods in Physics Research Section A: Accelerators, Spectrometers, Detectors and Associated Equipment*, 896:129–138, 2018.
- [BCC⁺14] C.A. Baker et al. Apparatus for measurement of the electric dipole moment of the neutron using a cohabiting atomic-mercury magnetometer. *Nuclear Instruments and Methods in Physics Research Section A: Accelerators, Spectrometers, Detectors and Associated Equipment*, 736:184 – 203, 2014.
- [BDG⁺06] C. A. Baker et al. Improved experimental limit on the electric dipole moment of the neutron. *Phys. Rev. Lett.*, 97:131801, 2006.
- [BDJ⁺95] G. Blaise et al. *High Voltage Vacuum Insulation: Basic Concepts and Technological Practice*. Academic Press, 1995.
- [BGKM88] J. Baumann, R. Gähler, J. Kalus, and W. Mampe. Experimental limit for the charge of the free neutron. *Phys. Rev. D*, 37:3107–3112, 1988.
- [BMDR69] J. K. Baird, P. D. Miller, W. B. Dress, and Norman F. Ramsey. Improved upper limit to the electric dipole moment of the neutron. *Phys. Rev.*, 179:1285–1291, 1969.
- [BOA] BOA: Beamline for Neutron Optics and other Approaches. <https://www.psi.ch/de/sinq/boa>. Accessed: 2021-04-06.
- [BP65] V.G. Baryshevskii and M.I. Podgoretskii. Nuclear precession of neutrons. *Journal of Experimental and Theoretical Physics*, 20(3):704, 1965.
- [BR03] M. Baeva and D. Reiter. Monte carlo simulation of radiation trapping in Hg–Ar fluorescent discharge lamps. *Plasma Chemistry and Plasma Processing*, 23(3):371–387, 2003.
- [BS40] F. Bloch and A. Siegert. Magnetic resonance for nonrotating fields. *Phys. Rev.*, 57:522–527, 1940.
- [CAZ⁺] E. Chanel et al. Characterization of a new fermi chopper design. to be published.
- [CCFT64] J.H. Christenson, J.W. Cronin, V.L. Fitch, and R. Turlay. Evidence for the 2π Decay of the K_2^0 Meson. *Phys. Rev. Lett.*, 13:138–140, 1964.
- [CDS12] Laurent Canetti, Marco Drewes, and Mikhail Shaposhnikov. Matter and antimatter in the universe. *New Journal of Physics*, 14(9):095012, 2012.
- [CDT] The GEM-based CASCADE neutron detector. <https://n-cdt.com/cascade-2d-200/>. Accessed: 2021-05-18.
- [CDVW79] R.J. Crewther, P. Di Vecchia, G. Veneziano, and E. Witten. Chiral estimate of the electric dipole moment of the neutron in quantum chromodynamics. *Physics Letters B*, 88(1):123–127, 1979.

- [CFRMS19] T. E. Chupp, P. Fierlinger, M. J. Ramsey-Musolf, and J. T. Singh. Electric dipole moments of atoms, molecules, nuclei, and particles. *Rev. Mod. Phys.*, 91:015001, 2019.
- [Chu21] T. E. Chupp. The LANL nEDM experiment. Presented at nEDM2021 conference, Les Houches School of Physics, France, 2021.
- [CK84] L-L Chau and W-Y Keung. Comments on the parametrization of the kobayashi-maskawa matrix. *Phys. Rev. Lett.*, 53:1802–1805, 1984.
- [CK97] Andrzej Czarnecki and Bernd Krause. Neutron Electric Dipole Moment in the Standard Model: Complete three-loop calculation of the valence quark contributions. *Phys. Rev. Lett.*, 78:4339–4342, 1997.
- [CL15] John M Carpenter and C-K Loong. *Elements of slow-neutron scattering*. Cambridge University Press, 2015.
- [CMB] An introduction to the cmb. <http://background.uchicago.edu/~whu/intermediate/baryons.html>. Accessed: 2021-07-07.
- [CZ13] Clifford Cheung and Yue Zhang. Electroweak cogenesis. *Journal of High Energy Physics*, 2013(9), 2013.
- [DBC⁺19] Wurm D. et al. The PanEDM neutron electric dipole moment experiment at the ILL. *EPJ Web Conf.*, 219:02006, 2019.
- [DBMR68] W. B. Dress, J. K. Baird, P. D. Miller, and Norman F. Ramsey. Upper limit for the electric dipole moment of the neutron. *Phys. Rev.*, 170:1200–1206, 1968.
- [DGS⁺13] J. Dawidowski, R.G. Granada, J.R. Santisteban, Cantargi F., and Palomino L.A.R. *Appendix - Neutron Scattering Lengths and Cross Sections*, volume 44 of *Experimental Methods in the Physical Sciences*. Academic Press, 2013.
- [DMP⁺77] W. B. Dress, P. D. Miller, J. M. Pendlebury, P. Perrin, and N. F. Ramsey. Search for an electric dipole moment of the neutron. *Phys. Rev. D*, 15:9–21, 1977.
- [DMR73] W. B. Dress, P. D. Miller, and N. F. Ramsey. Improved upper limit for the electric dipole moment of the neutron. *Phys. Rev. D*, 7:3147–3149, 1973.
- [ele] FUG elektronik. Fug hcb datasheet. https://www.fug-elektronik.de/wp-content/uploads/pdf/Datasheets/EN/HCB_data_sheet.pdf. Accessed: 2021-04-06.
- [EZR⁺19] E. Chanel et al. The pulsed neutron beam EDM experiment. *EPJ Web Conf.*, 219:02004, 2019.
- [F⁺36] E. Fermi et al. Motion of neutrons in hydrogenous substances. *Ricerca Scientifica*, 7(2):13–52, 1936.
- [Far] Farnell. 39-01-4050 datasheet. <https://www.farnell.com/datasheets/2695978.pdf>. Accessed: 2021-04-06.

- [Fer13] Martin Christoph Fertl. *A laser based mercury co-magnetometer for the neutron electric dipole moment search*. PhD thesis, ETH ZURICH, 2013.
- [Fil21] H. Filter. panEDM experiment status and overview. Presented at nEDM2021 conference, Les Houches School of Physics, France, 2021.
- [FJK⁺09] V.V. Fedorov et al. Perspectives for nedm search by crystal diffraction. test experiment and results. *Nuclear Physics A*, 827(1):538c–540c, 2009. PANIC08.
- [FM47] E. Fermi and L. Marshall. Interference phenomena of slow neutrons. *Phys. Rev.*, 71:666–677, 1947.
- [FMM47] E. Fermi, J. Marshall, and L. Marshall. A thermal neutron velocity selector and its application to the measurement of the cross section of boron. *Phys. Rev.*, 72:193–196, 1947.
- [FPH14] P. Fileviez Pérez and Patel H. H. The electroweak vacuum angle. *Physics Letters B*, 732:241–243, 2014.
- [GCLH17] B. Graner, Y. Chen, E. G. Lindahl, and B. R. Heckel. Erratum: Reduced limit on the permanent electric dipole moment of ^{199}Hg [phys. rev. lett. 116, 161601 (2016)]. *Phys. Rev. Lett.*, 119:119901, 2017.
- [GD11] K. Garrett and G. Duda. Dark matter: A primer. *Advances in Astronomy*, 2011:22, 2011.
- [GMS20] C-S Guan, T. Ma, and J. Shu. Left-right symmetric composite Higgs model. *Phys. Rev. D*, 101:035032, 2020.
- [GOR97] S.V Grigoriev, A.I Okorokov, and V.V Runov. Peculiarities of the construction and application of a broadband adiabatic flipper of cold neutrons. *Nuclear Instruments and Methods in Physics Research Section A: Accelerators, Spectrometers, Detectors and Associated Equipment*, 384(2):451–456, 1997.
- [Got21] Alexander Gottstein. Passive magnetic shielding characterisation for static fields within the BeamEDM experiment. Master’s thesis, Universität Bern, 2021.
- [Gri95] J. D. Griffiths. *Introduction to Quantum Mechanics*. Pearson Prentice Hall, 1995.
- [GRM⁺79] G. L. Greene et al. Measurement of the neutron magnetic moment. *Phys. Rev. D*, 20:2139–2153, 1979.
- [GRS91] R. Golub, D.J. Richardson, and Lamoreaux S.K. *Ultracold Neutrons*. Taylor & Francis Group, 1991.
- [Gsp21] Andreas Gsponer. Characterization of the magnetic shielding for the Beam EDM experiment. Master’s thesis, Universität Bern, 2021.
- [GZB⁺20] Particle Data Group et al. Review of Particle Physics. *Progress of Theoretical and Experimental Physics*, 2020(8), 2020. 083C01.
- [HBG⁺99] P. G. Harris et al. New experimental limit on the electric dipole moment of the neutron. *Phys. Rev. Lett.*, 82:904–907, 1999.

- [HHX11] Junji Hisano, Wei-Shu Hou, and Fanrong Xu. Updating the neutron electric dipole moment in a fourth generation Standard Model. *Phys. Rev. D*, 84:093005, 2011.
- [HM67] W. Happer and B. S. Mathur. Effective operator formalism in optical pumping. *Phys. Rev.*, 163:12–25, 1967.
- [HvE⁺12] M. Haag, B. van den Brandt, T.R. Eichhorn, P. Hautle, and W.Th. Wenckebach. Spin filtering neutrons with a proton target dynamically polarized using photo-excited triplet states. *Nuclear Instruments and Methods in Physics Research Section A: Accelerators, Spectrometers, Detectors and Associated Equipment*, 678:91–97, 2012.
- [IGC] Stefan Mayer Instruments-GmbH and Co. Magnetic field sensor flc3-70. <https://stefan-mayer.com/en/products/magnetometers-and-sensors/magnetic-field-sensor-flc3-70.html>. Accessed: 2021-04-12.
- [ins] National instruments. Ni 6289 datasheet. <https://www.ni.com/pdf/manuals/375222c.pdf>. Accessed: 2021-04-06.
- [IRMZ14] S. Inoue, M. J. Ramsey-Musolf, and Y. Zhang. cp -violating phenomenology of flavor conserving two Higgs doublet models. *Phys. Rev. D*, 89:115023, 2014.
- [Ite] Item homepage. <https://www.item24.de/en/homepage.html>. Accessed: 2021-06-14.
- [Jar85] C Jarlskog. Commutator of the quark mass matrices in the Standard Electroweak Model and a measure of maximal CP nonconservation. *Phys. Rev. Lett.; (United States)*, 1985.
- [Kas50] Alfred Kastler. Quelques suggestions concernant la production optique et la détection optique d'une inégalité de population des niveaux de quantification spatiale des atomes. application à l'expérience de stern et gerlach et à la résonance magnétique. *J. phys. radium*, 11(6):255–265, 1950.
- [KM73] M. Kobayashi and T. Maskawa. CP-Violation in the Renormalizable Theory of Weak Interaction. *Progress of Theoretical Physics*, 49(2):652–657, 1973.
- [KNPS05] M. Kreuz, V. Nesvizhevsky, A. Petoukhov, and T. Soldner. The crossed geometry of two super mirror polarisers—a new method for neutron beam polarisation and polarisation analysis. *Nuclear Instruments and Methods in Physics Research Section A: Accelerators, Spectrometers, Detectors and Associated Equipment*, 547(2):583–591, 2005.
- [Kom17] Sybille Verena Komposch. *Realization of a high-performance laser-based mercury magnetometer for neutron EDM experiments*. PhD thesis, ETH ZURICH, 2017.
- [KP95] G. Kramer and W. F. Palmer. Electroweak and strong penguin diagrams in $b^{\pm,0} \rightarrow \pi\pi$, πk , and kk^- decays. *Phys. Rev. D*, 52:6411–6421, 1995.
- [KRS91] L. Koester, H. Rauch, and E. Seymann. Neutron scattering lengths: A survey of experimental data and methods. *Atomic Data and Nuclear Data Tables*, 49(1):65–120, 1991.

- [LDD20] F Li, R Dadisman, and Wasilko D.C. Optimization of a superconducting adiabatic radio frequency neutron resonant spin flipper. *Nuclear Instruments and Methods in Physics Research Section A: Accelerators, Spectrometers, Detectors and Associated Equipment*, 955:163300, 2020.
- [LPT15] A. J. Long, H. H. Patel, and M. Trodden. Electroweak vacuum angle at finite temperature and implications for baryogenesis. *Phys. Rev. D*, 92:043513, 2015.
- [LT12] B. Lauss and UCN Project Team. A new facility for fundamental particle physics: The high-intensity ultracold neutron source at the paul scherrer institute. *AIP Conference Proceedings*, 1441(1):576–578, 2012.
- [Mag] Magneticshields. Material technical data. <https://magneticshields.co.uk/technical/material-technical-data>. Accessed: 2021-04-12.
- [Mar13] J. W. Martin. TRIUMF facility for a neutron electric dipole moment experiment. *AIP Conf. Proc.*, 1560(1):134–136, 2013.
- [Mat19] E. Matsinos. A brief history of the pion-nucleon coupling constant. *arXiv*, 2019.
- [MDBR67] P. D. Miller, W. B. Dress, J. K. Baird, and Norman F. Ramsey. Limit to the electric dipole moment of the neutron. *Phys. Rev. Lett.*, 19:381–384, 1967.
- [Mea08] P.J. Mohr and et al. Codata recommended values of the fundamental physical constants: 2006, 2008.
- [Met] Metway. 160bu/163st datasheet. <https://www.metway.co.uk/wp-content/uploads/2014/02/Series-160BU-163ST-3-pole-10A-plugs-and-sockets-with-covers-and-base-plates.pdf>. Accessed: 2021-04-06.
- [MID] Midas. https://midas.triumf.ca/MidasWiki/index.php/Main_Page. Accessed: 2021-04-12.
- [MNS62] Z. Maki, M Nakagawa, and S. Sakata. Remarks on the Unified Model of Elementary Particles. *Progress of Theoretical Physics*, 28(5):870–880, 1962.
- [MPL⁺14] M. Morgano, S. Peetermans, E.H. Lehmann, T. Panzner, and U. Filges. Neutron imaging options at the BOA beamline at Paul Scherrer Institut. *Nuclear Instruments and Methods in Physics Research Section A: Accelerators, Spectrometers, Detectors and Associated Equipment*, 754:46–56, 2014.
- [Mug18] S. F. Mughabghab. *Atlas of Neutron Resonances: Volume 2: Resonance Properties and Thermal Cross Sections Z= 61-102*. Elsevier, 2018.
- [P⁺91] P.C. Peebles et al. The case for the relativistic hot Big Bang cosmology. *Nature*, 352:769–776, 1991.
- [PAA⁺14] Planck Collaboration et al. Planck 2013 results. xvi. cosmological parameters. *A&A*, 571:A16, 2014.
- [PAA⁺15] J. M. Pendlebury et al. Revised experimental upper limit on the electric dipole moment of the neutron. *Phys. Rev. D*, 92:092003, 2015.

[PCI] Ni pcie 8361 datasheet. <https://pdf1.alldatasheet.com/datasheet-pdf/view/395350/NI/NIPCIE-8361.html>. Accessed: 2021-04-06.

[Per09] D. H. Perkins. *Particle astrophysics*. Number 10. Oxford University Press, 2009.

[PF1] Instrument layout of pf1b. <https://www.ill.eu/users/instruments/instruments-list/pf1b/description/instrument-layout>. Accessed: 2021-04-06.

[Pfea] Pfeiffer. Pcr 280 datasheet. <https://www.pfeiffer-vacuum.com/productPdfs/PTR26856.en.pdf>. Accessed: 2021-04-06.

[Pfeb] Pfeiffer. Pkr 361 datasheet. <https://www.pfeiffer-vacuum.com/productPdfs/PTT03140010.en.pdf>. Accessed: 2021-04-06.

[Pfec] Pfeiffer. Tpr 280 datasheet. <https://www.pfeiffer-vacuum.com/productPdfs/PTR26950.en.pdf>. Accessed: 2021-04-06.

[Pie09] Florian Michael Piegza. *Neutron Spin Precession in Samples of Polarised Nuclei and Neutron Spin Phase Imaging*. PhD thesis, Technische Universität München, 2009.

[Pie13] F. M. Piegza. New concept for a neutron electric dipole moment search using a pulsed beam. *Physical Review C*, 88(4), 2013.

[PR50] E. M. Purcell and N. F. Ramsey. On the possibility of electric dipole moments for elementary particles and nuclei. *Phys. Rev.*, 78:807–807, 1950.

[PR05] Maxim Pospelov and Adam Ritz. Electric dipole moments as probes of new physics. *Annals of Physics*, 318(1):119–169, 2005. Special Issue.

[PSG⁺84] J.M. Pendlebury et al. Search for a neutron electric dipole moment. *Physics Letters B*, 136(5):327–330, 1984.

[PSI] Cold neutron source. <https://www.psi.ch/de/bsq/cold-neutron-source>. Accessed: 2021-04-06.

[PW65] A. A. Penzias and R. W. Wilson. A Measurement of Excess Antenna Temperature at 4080 Mc/s. *ApJ*, 142:419–421, 1965.

[PXi] Pxi-4071- pxi digital multimeter. <https://www.ni.com/en-us/support/model.pxi-4071.html>. Accessed: 2021-06-18.

[Ram50] Norman F. Ramsey. A molecular beam resonance method with separated oscillating fields. *Phys. Rev.*, 78:695–699, 1950.

[Raw14] Michał Rawlik. FID signal analysis and new DAQ system in the nEDM experiment. Master’s thesis, Jagiellonian University, 2014.

[Roc09] Stephanie Roccia. *La co-magnétométrie mercure pour la mesure du moment électrique dipolaire du neutron : Optimisation et application au test de l’invariance de Lorentz*. PhD thesis, Laboratoire de Physique Subatomique et de Cosmologie de Grenoble, 2009.

[RTA] Rootana. <https://midas.triumf.ca/MidasWiki/index.php/ROOTANA>. Accessed: 2021-05-18.

- [RZMK38] I. I. Rabi, J. R. Zacharias, S. Millman, and P. Kusch. A new method of measuring nuclear magnetic moment. *Phys. Rev.*, 53:318–318, 1938.
- [Sak67] A. D. Sakharov. Violation of CP invariance, C asymmetry, and baryon asymmetry of the universe. *Journal of Experimental and Theoretical Physics Letters*, 5:24–27, 1967.
- [SCP⁺90] K.F. Smith et al. A search for the electric dipole moment of the neutron. *Physics Letters B*, 234(1):191–196, 1990.
- [Sea86] VF Sears. Neutron scattering, part a. vol. 23, 1986.
- [Sea92] Varley F. Sears. Neutron scattering lengths and cross sections. *Neutron News*, 3(3):26–37, 1992.
- [SEN] SENSYS GmbH. *SENSYS FGM3D Matrix of Technical Parameters*. Version 1.08.
- [Sen15] Chien-Yeah Seng. Reexamination of the Standard Model nucleon electric dipole moment. *Phys. Rev. C*, 91:025502, 2015.
- [Siv11] D.S. Sivia. *Elementary Scattering Theory: For X-ray and Neutron Users*. Oxford University Press., 2011.
- [SKP⁺15] A. P. Serebrov et al. New search for the neutron electric dipole moment with ultracold neutrons at ILL. *Phys. Rev. C*, 92:055501, 2015.
- [SM75] G. Senjanovic and R. N. Mohapatra. Exact left-right symmetry and spontaneous violation of parity. *Phys. Rev. D*, 12:1502–1505, 1975.
- [SN67] C. G. Shull and R. Nathans. Search for a neutron electric dipole moment by a scattering experiment. *Phys. Rev. Lett.*, 19:384–386, 1967.
- [SPR57] J. H. Smith, E. M. Purcell, and N. F. Ramsey. Experimental limit to the electric dipole moment of the neutron. *Phys. Rev.*, 108:120–122, 1957.
- [Sta19] Oliver Stalder. Resonance spin flipper for a pulsed, coldneutron beam. Master’s thesis, Universität Bern, 2019.
- [Ste20] Albert Steyerl. *Ultracold Neutrons*. World Scientific, 2020.
- [SW16] P. Schmidt-Wellenburg. The quest for an electric dipole moment of the neutron. *AIP Conference Proceedings*, 1753(1):060002, 2016.
- [Swi] Swissneutronics. Supermirrors for neutrons. <https://www.swissneutronics.ch/products/neutron-supermirrors/>. Accessed: 2021-05-18.
- [SZ13] Jing Shu and Yue Zhang. Impact of acp-violating Higgs sector: From LHC to baryogenesis. *Physical Review Letters*, 111(9), 2013.
- [TAK⁺19] Soldner T. et al. ANNI - a pulsed cold neutron beam facility for particle physics at the ESS. *EPJ Web Conf.*, 219:10003, 2019.
- [Tak21] Higuchi Takashi. Prospects towards a neutron edm measurement with an advanced ultracold neutron source at triumph. Presented at nEDM2021 conference, Les Houches School of Physics, France, 2021.

[Tar] Spallation target. <https://www.psi.ch/en/bsq/spallation-target>. Accessed: 2021-04-06.

[VL99] B. V L'vov. Kinetics and mechanism of thermal decomposition of mercuric oxide. *Thermochimica Acta*, 333(1):21–26, 1999.

Appendix A

Time evolution operator of the Ramsey apparatus

In this appendix we summarize the derivation in [Pie09] that computes the probability of a spin flip over a Ramsey apparatus with an homogeneous magnetic field, and we complete it with the case of an inhomogeneity of the magnetic field along the apparatus leading to different static magnetic fields in the spin flip regions.

The derivation uses the time-evolution operator of the system and the equation of motion

$$i\hbar \frac{\partial}{\partial t} \hat{U}(t, t_0) = \hat{H}(t) \hat{U}(t, t_0), \quad (\text{A.1})$$

where \hat{U} is the operator that applied to an arbitrary initial state $|\psi(t_0)\rangle$ gives a state $|\psi(t)\rangle$:

$$|\psi(t)\rangle = \hat{U}(t, t_0) |\psi(t_0)\rangle, \quad (\text{A.2})$$

which is solved by

$$\hat{U}(t, t_0) = \exp \left(-\frac{i}{\hbar} \int_{t_0}^t \hat{H}(t') dt' \right). \quad (\text{A.3})$$

In the case of a Ramsey technique or a phase scan, the neutrons interact with a magnetic field $\mathbf{B} = (B_x, B_y, B_z)$ and the Hamiltonian in the general case can be written as

$$\hat{H}(t) = -\frac{\hbar}{2} \gamma_n \boldsymbol{\sigma} \cdot \mathbf{B} = -\frac{\hbar}{2} \gamma_n \begin{pmatrix} B_z & B_x - iB_y \\ B_x + iB_y & -B_z \end{pmatrix} \quad (\text{A.4})$$

where $\boldsymbol{\sigma}$ is the Pauli matrices vector, and γ_n is the gyromagnetic ratio of the neutron [GRM⁺79]. The calculation is then separated in three regions corresponding to the spin flips and the free precession with different static magnetic fields as represented in Fig. A.1.

In the first region, the neutrons see a static field $\mathbf{B} = (0, 0, B_A)$ along the vertical (z axis) and circular oscillating field field of amplitude B_1 rotating in the perpendicular plane at a frequency ω_{RF} . In the second zone, the neutrons see only a static field

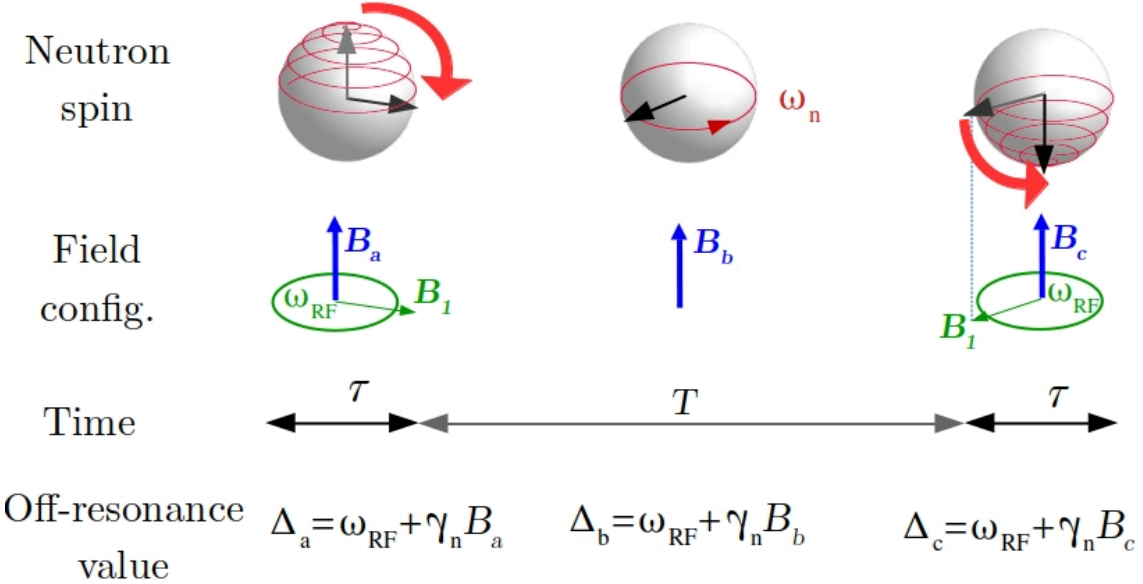


Fig. A.1: Representation of the neutron spin as a function of the fields configuration for the different stages of a Ramsey technique. As additional information, the off-resonance value for each stage is computed.

$\mathbf{B} = (0, 0, B_b)$ and in the third region, a static field $\mathbf{B} = (0, 0, B_c)$ along the vertical (z axis) and circular oscillating field of amplitude B_1 rotating in the perpendicular plane at a frequency ω_{RF} . The time it takes for the neutrons to go through each spin flip region is denoted τ , and T for the time to go through the free precession region.

To simplify the equation, the system is considered in the reference frame rotating with the angular frequency ω_{RF} , which corresponds to the frequency of the oscillating magnetic fields [1]. The fields can be expressed by

$$\begin{aligned}
 \mathbf{B}_A &= \frac{-1}{\gamma_n}(\omega_1, 0, -\Delta_a), \\
 \mathbf{B}_B &= \frac{-1}{\gamma_n}(0, 0, -\Delta_b), \\
 \mathbf{B}_C &= \frac{-1}{\gamma_n}(\omega_1 \cos(\theta_{RF}), \omega_1 \sin(\theta_{RF}), -\Delta_c),
 \end{aligned} \tag{A.5}$$

where $\Delta_k = \omega_{RF} + \gamma_n B_k$ with $k \in \{a, b, c\}$, $\omega_1 = -\gamma_n B_1$, and θ_{RF} is the phase between the two oscillating fields. These equations can be combined with Eqs. (A.3)

and (A.4) and $t_0 = 0$ into

$$\begin{aligned}\hat{U}_A(\tau, 0) &= \begin{pmatrix} \cos\left(\frac{\Omega_a\tau}{2}\right) + \frac{i\Delta_a}{\Omega_a} \sin\left(\frac{\Omega_a\tau}{2}\right) & -\frac{i\omega_1}{\Omega_a} \sin\left(\frac{\Omega_a\tau}{2}\right) \\ -\frac{i\omega_1}{\Omega_a} \sin\left(\frac{\Omega_a\tau}{2}\right) & \cos\left(\frac{\Omega_a\tau}{2}\right) - \frac{i\Delta_a}{\Omega_a} \sin\left(\frac{\Omega_a\tau}{2}\right) \end{pmatrix}, \\ \hat{U}_B(T, 0) &= \begin{pmatrix} \exp\left(\frac{iT\Delta_b}{2}\right) & 0 \\ 0 & \exp\left(-iT\Delta_b\right) \end{pmatrix}, \\ \hat{U}_C(\tau, 0) &= \begin{pmatrix} \cos\left(\frac{\Omega_c\tau}{2}\right) + \frac{i\Delta_c}{\Omega_c} \sin\left(\frac{\Omega_c\tau}{2}\right) & -\frac{i\omega_1}{\Omega_c} \exp(-i\theta_{RF}) \sin\left(\frac{\Omega_c\tau}{2}\right) \\ -\frac{i\omega_1}{\Omega_c} \exp(i\theta_{RF}) \sin\left(\frac{\Omega_c\tau}{2}\right) & \cos\left(\frac{\Omega_c\tau}{2}\right) - \frac{i\Delta_c}{\Omega_c} \sin\left(\frac{\Omega_c\tau}{2}\right) \end{pmatrix}\end{aligned}\quad (\text{A.6})$$

for the three zones, with $\Omega_k = \sqrt{\Delta_k^2 + \omega_1^2}$ and $k \in \{a, b, c\}$. The probability of a spin flip, i.e. a transition from the spin state $|\uparrow\rangle = \begin{pmatrix} 1 \\ 0 \end{pmatrix}$ to $|\downarrow\rangle = \begin{pmatrix} 0 \\ 1 \end{pmatrix}$ can be expressed by

$$\begin{aligned}P &= \left| \langle \downarrow | \hat{U}_c \hat{U}_b \hat{U}_a | \uparrow \rangle \right|^2 \\ &= \left(\frac{\omega_1}{\Omega_a \Omega_c} \right)^2 \left[\Omega_c \cos\left(\frac{\tau\Omega_c}{2}\right) \sin\left(\frac{\tau\Omega_a}{2}\right) + \sin\left(\frac{\tau\Omega_c}{2}\right) F \right] \\ &\quad \times \left[\Omega_c \cos\left(\frac{\tau\Omega_c}{2}\right) \sin\left(\frac{\tau\Omega_a}{2}\right) + \sin\left(\frac{\tau\Omega_c}{2}\right) \bar{F} \right]\end{aligned}\quad (\text{A.7})$$

with

$$F = \exp(-i(T\Delta_b + \theta_{RF})) \Omega_a \cos\left(\frac{\tau\Omega_a}{2}\right) + i [\Delta_c - \Delta_a \exp(-i(T\Delta_b + \theta_{RF}))] \sin\left(\frac{\tau\Omega_a}{2}\right), \quad (\text{A.8})$$

and \bar{F} its complex conjugate. They are the only terms that carry the phase between the phase between the two oscillating magnetic field.

In the case where $B_a = -B_c$, the probability becomes :

$$P = 2 \frac{\omega_1^2}{\Omega_a^4} \cos^2\left(\frac{T\Delta_b + \theta_{RF}}{2}\right) \sin^2\left(\frac{\tau\Omega_a}{2}\right) [2\Delta_a^2 + \omega_1^2 + \omega_1^2 \cos(\tau\Omega_a)] \quad (\text{A.9})$$

In practice, this case corresponds usually to the case where the two spin flippers see a different field and the resonance frequency of the apparatus is in the middle. In that particular configuration, the analysis in [Chapter 4](#) with a cosine is valid.

In the opposite case where $B_a = B_c$, the probability becomes :

$$P = \frac{\omega_1^2}{\Omega_a^4} \left[\Delta_a (1 - \cos(\tau\Omega_a)) \sin\left(\frac{T\Delta_b + \theta_{RF}}{2}\right) + \Omega_a \cos\left(\frac{T\Delta_b + \theta_{RF}}{2}\right) \sin(\tau\Omega_a) \right]^2 \quad (\text{A.10})$$

Here, the analysis in [Chapter 4](#) with a cosine is not valid anymore due to the sinus term in θ_{RF} if $\Delta_a \neq 0$. The result of this effect was simulated with Mathematica using $\omega_1 = 4.6281$, $\Delta_a = -39.8$ Hz, $\Delta_b = -21.4$ Hz, $\Delta_c = 15.2$ Hz, and τ and

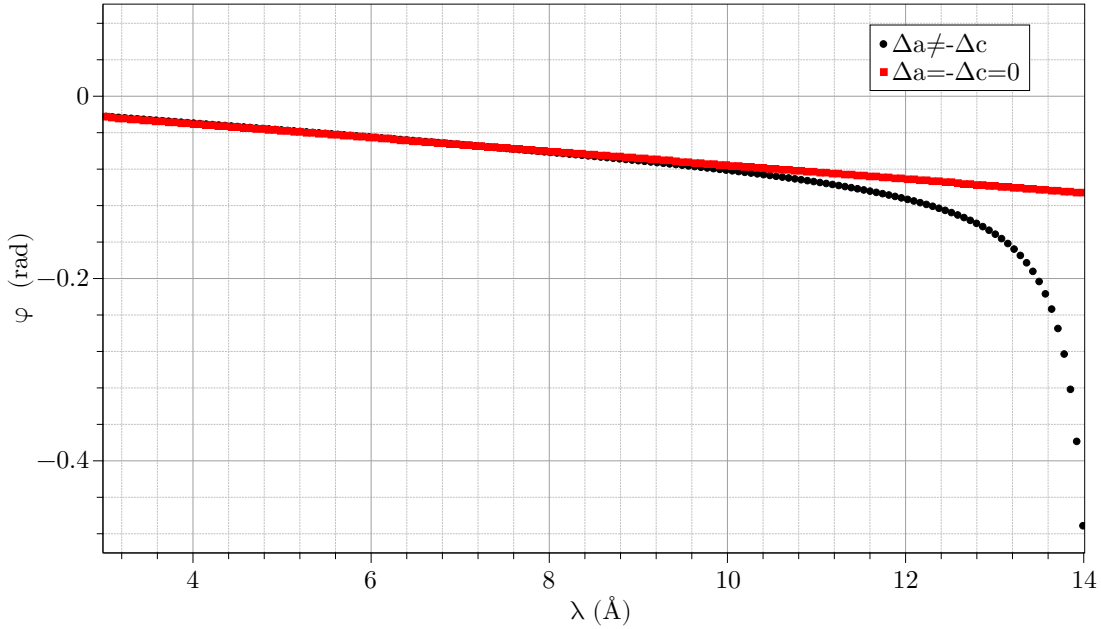


Fig. A.2: Simulation of the neutron phase for Eq. (A.8) with $\omega_1 = 4.6281$, $\Delta_a = -39.8 \text{ Hz}$, $\Delta_b = -21.4 \text{ Hz}$, $\Delta_c = 15.2 \text{ Hz}$, and τ and T corresponding to the apparatus of the beamtime at BOA in 2018 described in Section 5.3, using Mathematica.

T corresponding to the apparatus of the beamtime at BOA in 2018 described in Section 5.3. A phase scan for different time-of-flight is simulated by scanning θ_{RF} and fitting the spin flip probability as a function of θ_{RF} with the cosine defined in Eq. (4.5) for different values of interaction time T . The phase φ of this fit function as a function of the neutron wavelength is shown in Fig. A.2. It deviates from the linear behavior of $\Delta_a = -\Delta_c = 0$.

In the case where $B_a = B_c = 0$, we retrieve:

$$P = \left[\cos \left(\frac{T\Delta_b + \theta_{RF}}{2} \right) \sin(\tau\omega_1) \right]^2 \quad (\text{A.11})$$

where $T\Delta_b$ can be identified with φ of Eq. (4.5) which therefore displays a linear behavior as a function of T .

Appendix B

Documentation of the coils at PF1b, ILL in 2020

Here is the documentation written by Alexander Gottstein in the group wiki. It records the resistance of each coil and the load added to them during the last beamtime at PF1b, ILL in 2020. Y is the vertical axis, ΔY is the gradient coil, and X and Y are the longitudinal traversal axis respectively.

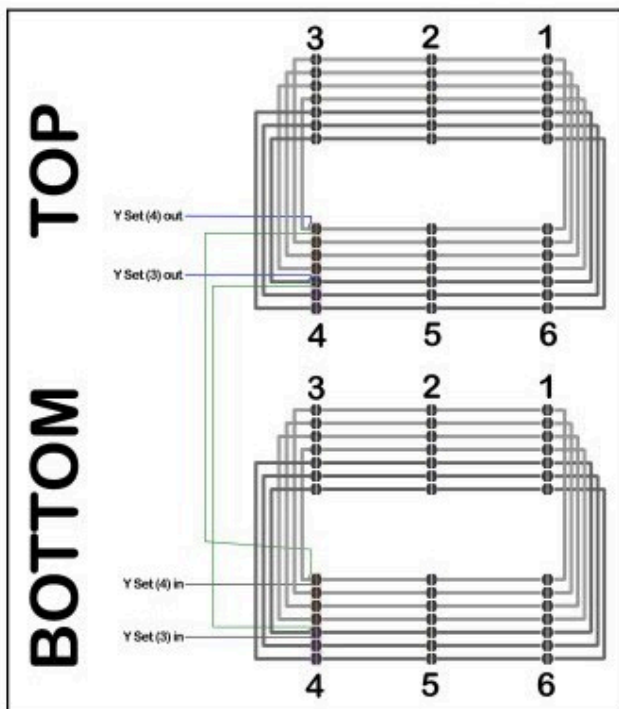
Coil Documentation

Coil Label	Ω Raw*	Additional Resistors	# Bundle windings	# Cable windings	Cable type
Y Set 4 windings	5.824 Ω	Resistorbox 100 Ω	4	20	2
Y Set 3 windings	4.383 Ω	Resistorbox 100 Ω	3	15	2
Y Stab	1.502 Ω	Resistorbox 20 Ω	1	5	2
ΔY Set	1.214 Ω	∞ (left open)	4/5	4	2
ΔY Stab	0.343 Ω	Resistorbox 20 Ω	1/5	1	2
X Set	291.02 Ω	∞ (left open)	8	40	1
X Stab	38.576 Ω	Resistorbox 20 Ω	1	5	1
Z Set	13.537 Ω	∞ (left open)	4/5	4	1
Z Stab	3.693 Ω	Resistorbox 20 Ω	1/5	1	1

*measured with Keysight 34470A 7 1/2 Digit Multimeter Truevolt

Cable type 1 ('old type'): 7mm bundle with 5x 1.8mm Cable
Cable type 2 ('new type'): 10mm bundle with 5x 2.0mm Cable

Resistor Boxes: • 1 Custom 20 Ω resistor box with BNC connections (4 in, 4 out)
• 2 Custom 100 Ω resistor boxes for Y Set Coils, 2.75A max. (air cooled); Nr. 1 24.7.2020 and Nr. 2 24.7.2020



Wiring Scheme Y Set Coil (3 and 4 windings):

Schematic visualisation of the Y Set connectors and wiring, for both, the 3 Winding and 4 Winding Loops.

The Wiring Scheme is similar for the Y Stab Coil (using wires of Connector #7 (5 Cable windings)), the Δ Y Set Coil (Connector #8 (Black, Grey, Yellow & Brown wires)) and the Δ Y Stab Coil (Connector #8 (Blue wire)).

Fig. B.1: *Wiring of the vertical coil, also called Y coil in the above documentation.*

Appendix C

Connection diagram of the leakage current monitor

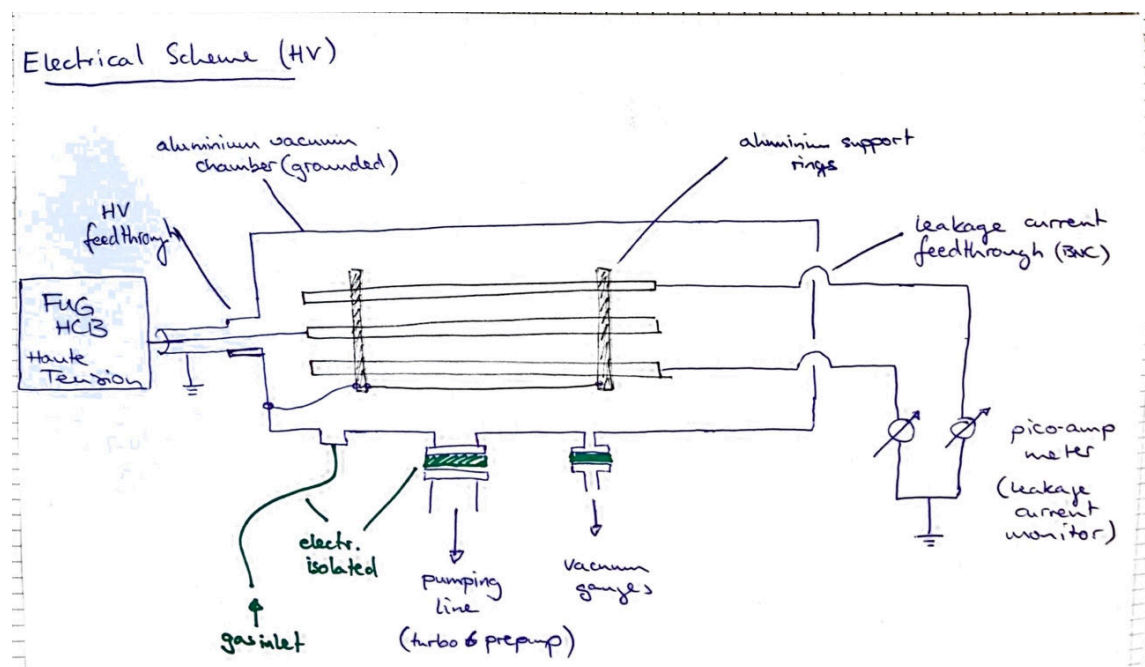


Fig. C.1: Diagram of the wiring of the leakage current monitor made by J. Thorne at PF1b, ILL in 2020.

Appendix D

Documentation on the spin analyzer motors

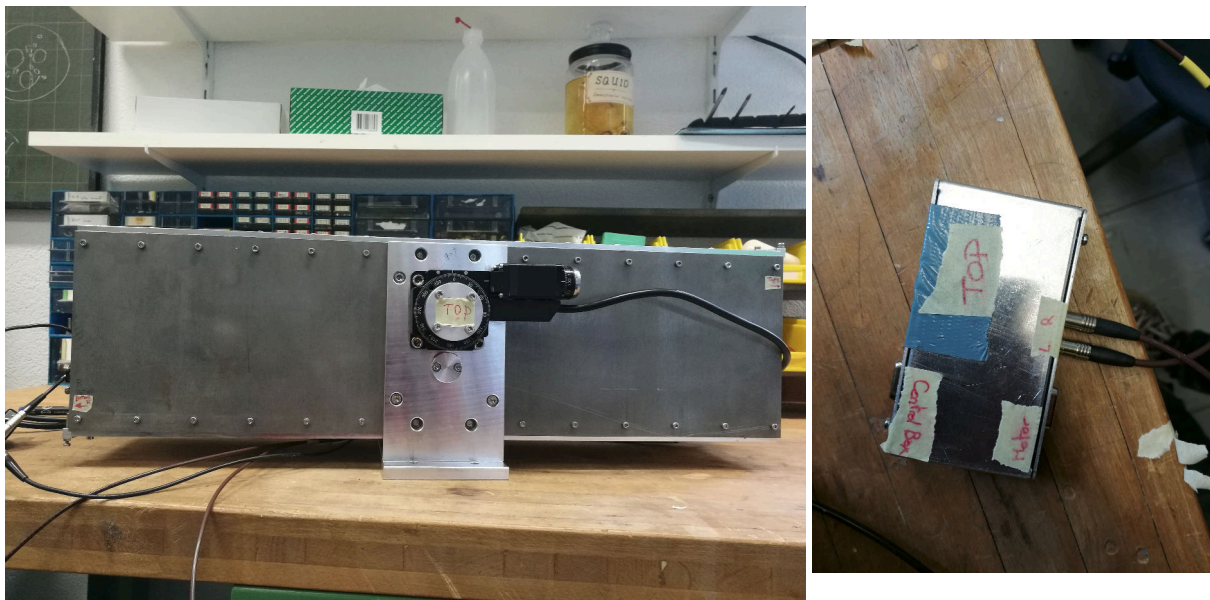


Operating the analyser motor

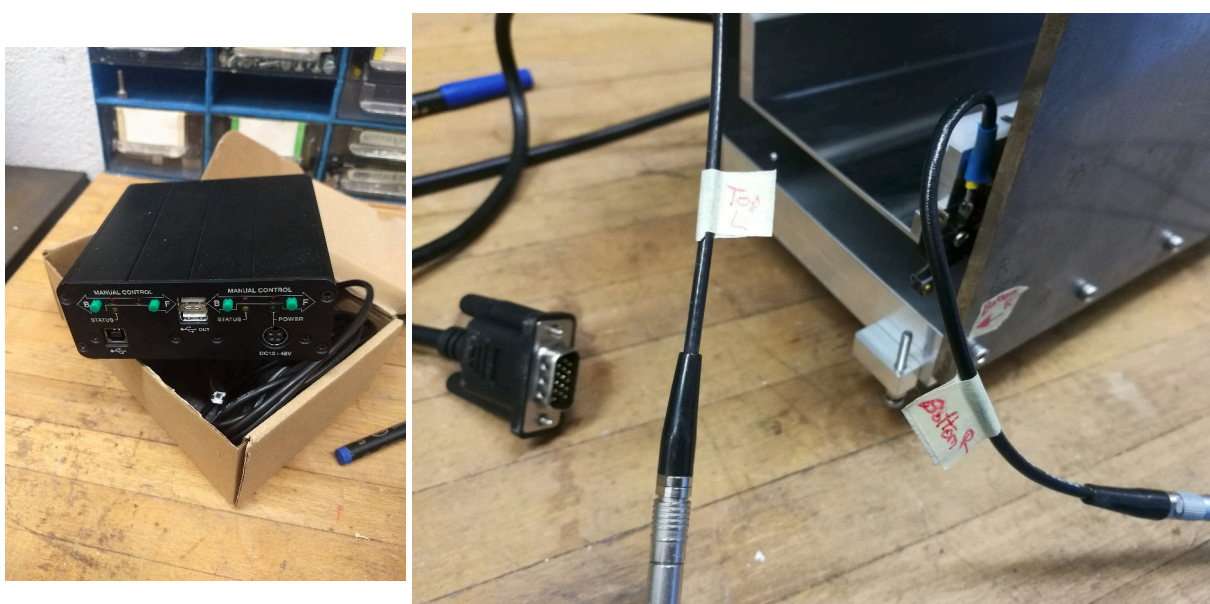
The analyser is composed of 2 sets of super mirror on top and on the bottom which are moved by 2 motors named the same way. To protect the 2 mirrors to collide and therefore be damage, 4 mechanical switch have been install to automatically stop the motor when the switch is closed.

How to plug everything:

The motor with the label BOTTOM (res. TOP) is linked to the box labeled BOTTOM (res. TOP) with their own cable.



The other pseudo VGA plug labeled “CONTROL BOX” is linked to the black control box for the 2 motors via the pseudo VGA cable (axis 1 or 2, it does not matter be remember which one is which).

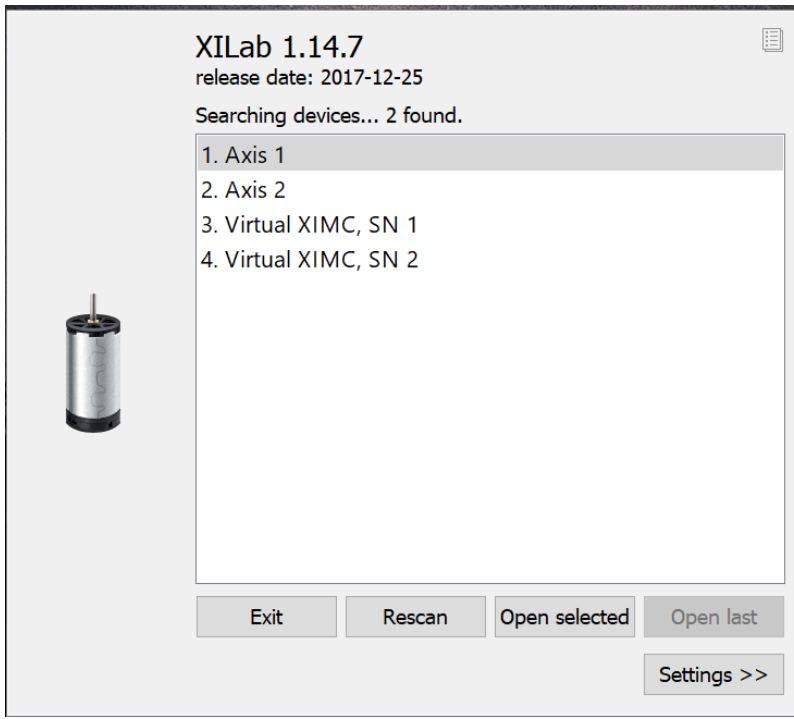


The witch labeled TOP L (res. TOP R, BOT R, BOT L) is connected to the LEMMO plug with the same label. Plug the power cable on the “CONTROL BOX” and the USB cable to the computer with the software.

Important: Make sure that the soldering is still good before using the motor. It can break.

How to use the software:

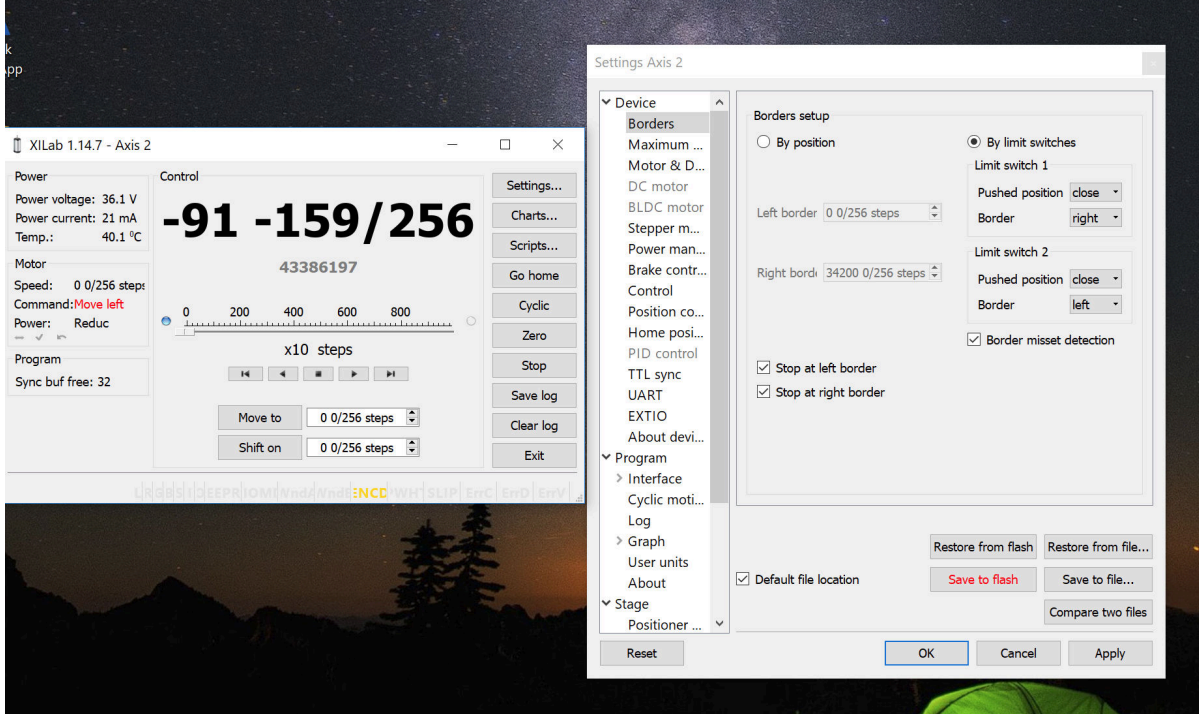
1. Search for Xilab



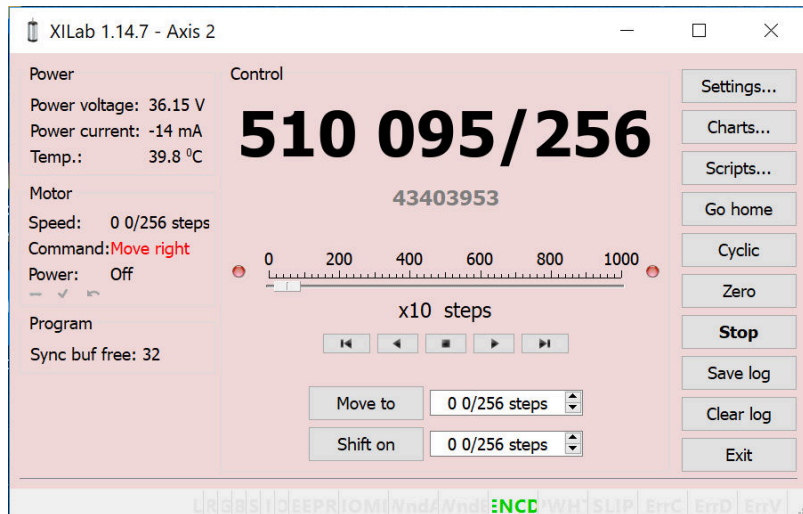
2. choose the motor you want to operate. There is also a simulation mode.

Important: as soon as the control box has power and is link to the computer, one can send command to the motor even if they are not plug which obviously leads to no movement for the motors.

3. Clic on setting -> Device -> Borders and set the borders as in the picture below:



If the switch are plug in inverse, then the main window of the software become red:



analyser_motor.txt · Last modified: 2019/04/15 10:15 by estelle

Appendix E

List of the devices used at ILL in 2020

Here are listed the commercial devices that were brought to ILL in 2020 with their product name and their serial number when found.

E.1 Power supplies for the electric field

- FUG HCB40-200000 15109-01-01
- FUG HCP35-35000 21764-01-01

E.2 Spin flipper system

- generateur de tension 4 channels
- Picoscope 5000 serie 2 channels
- Tektronic TDS2024B 4 channels
- Trueform 33600A serie
- Trueform 33500B serie
- Atomic clock GPS SPCTRA TIME
- Audio amplifier STA-100 IMG stageline C09/001407-2 and 001402-2 and 001414-2

E.3 Vacuum system

- Pfeiffer TPR280 44598761
- Pfeiffer PCR280 44595013
- Pfeiffer PCR280 44595023
- pfeiffer PKR361 44703193
- pfeiffer PKR361 44599462
- Maxigauge D-35614A
- Vacuum pump FIFVACUUM TSH261 18007795
- Vacuum pump FIFAVACUUM HIGH CUBE 80CLASSIC 16201558
- Vacuum pump EDWARDS vacuum NXDS20I 169400561
- Vacuum pump DSXu 10i 1905225341

E.4 Magnetic field

- Fluxgate Sensys FGM3D
- Fluxgate FLC3-70
- National Instument BNC-2090A
- National Instument PCI-GPIB 109F15C
- National Instument PCI-GPIB 109F08A
- Keysight 35500B 2 channels
- FUGNTN1400-200
- Keysight E3634A deux channels
- FUGNTN1400-350

E.5 Detector

- Dectector CDT 2D 16x16
- Powersupply CDT 5V/12A
- Keysight E3634A
- Keysight E3633A
- Powersupply ISEG SHQ226L
- Power supply GwINSREK GPD-43036
- Powersupply HV T2DP66 600490

E.6 Magnetic field USB hall probes

- USB hall probes HU-PT1-164005 123347 1000
- USB hall probes HU-PA1-4805 122571 1000

Appendix F

Fluxgate values during the beamtime at ILL in 2018

During the beamtime at PF1b, ILL in 2018, drifts and jumps of the magnetic field were noticed. To demonstrate this drift the norm of the magnetic for each fluxgate was computed and the value was average over the five fluxgates of the apparatus. In addition, the averaged vertical field was computed over the value of the five fluxgates. It is compared to the value of the vertical field of the middle fluxgate, on which the stabilisation was performed. One can see an offset between the three curves shown in [Fig. F.1A](#). This is due to the inhomogeneity of the magnetic field and the longitudinal and transversal component of the magnetic field. To see the overall drift in the magnetic field, the stabilisation curve was subtracted to the other curves. It was then corrected from the offset too, displayed [Fig. F.1B](#). If the field was drifting in a homogeneous way, the curves in [Fig. F.1B](#) should be constant at zero. This is not the case, which prove a drift of the magnetic field which is not homogeneous and therefore prevented to correct for it by one stabilization system.

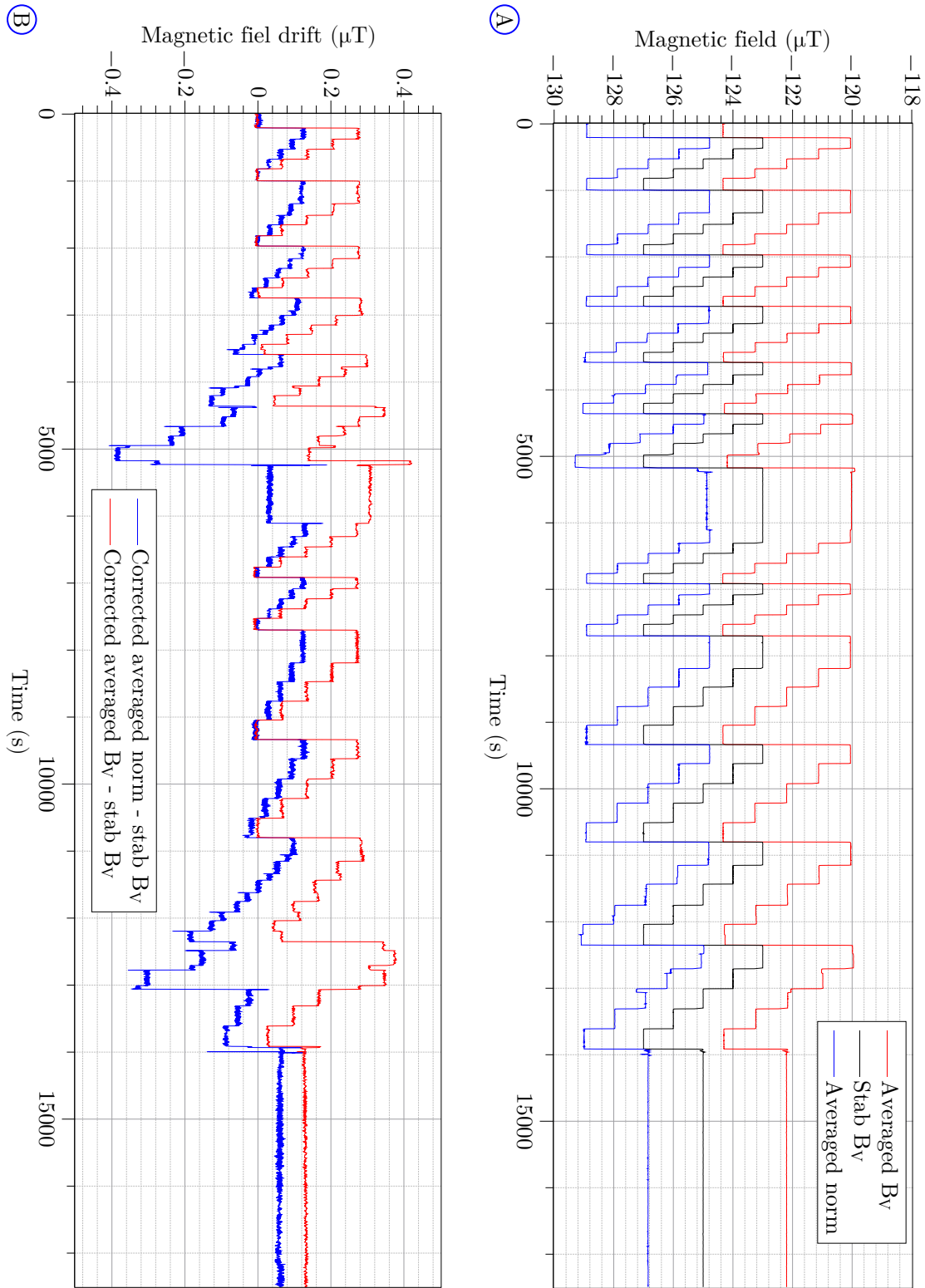


Fig. F.1: A) Vertical magnetic field recorded by the middle fluxgate in black, averaged over all fluxgates in red and the norm average over all fluxgates in blue as a function of the time. B) Estimate of the magnetic field drift computed from the data in A and corrected from the offset at $t=0$. All the data were recorded during the magnetic field characterization at PF1b, ILL in 2018.

Appendix G

Light absorption cross section of mercury

If an atom has two populated states E1 and E2. The population of these two states are ruled by the spontaneous emission from E2 to E1, induced emission from E2 to E1 and induced absorption from E1 to E2. The probability of these interaction are defined by the Einstein coefficient A for the spontaneous emission and B12 (resp B21) for the induced absorption (resp. induced emittion). The probability of induce emission or absorption $d\mathcal{P}_i/dt$ is always proportional to the density of light that shall stimulate it which is expressed as the spectral energy density ρ .

$$\frac{d}{dt}\mathcal{P}_{21}^{ind} = B_{21}\rho \quad (G.1a)$$

$$\frac{d}{dt}\mathcal{P}_{21}^{spont} = A \quad (G.1b)$$

$$\frac{d}{dt}\mathcal{P}_{12}^{ind} = B_{12}\rho \quad (G.1c)$$

In equilibrium, the emission of light is balanced by its absorption.

$$N_2 \frac{d}{dt}\mathcal{P}_{21}^{ind} + N_2 \frac{d}{dt}\mathcal{P}_{21}^{spont} = N_1 \frac{d}{dt}\mathcal{P}_{12}^{ind} \quad (G.2)$$

where N_i is the population density of the state i. In equilibrium it follows a Boltzmann distribution:

$$N_i = N \frac{g_i}{Z} e^{-E_i/kT} \quad (G.3)$$

with N the total population density, g_i the number of degenerate sub-levels and Z a normalization factor.

Using Eq. (G.1) and Eq. (G.3), Eq. (G.2) becomes

$$\rho = \frac{A/B_{21}}{\frac{g_1 B_{12}}{g_2 B_{21}} e^{h\nu/kT} - 1} \quad (G.4)$$

As this must follow Plank's law at all temperature and frequency, the Einstein coefficient have the relations:

$$B_{12} = \frac{g_2^2}{g_1} B_{21} \quad (G.5a)$$

$$A = \frac{8\pi h\nu^3}{c^3} B_{21} \quad (G.5b)$$

The absorption can also be described by it cross section σ_0 with :

$$B_{12} = \frac{c}{\hbar\nu} \sigma_0. \quad (G.6)$$

Reversing this formula and expressing it with A , the cross section becomes:

$$\sigma_0 = \frac{B_{12}\hbar\nu}{c} = \frac{B_{21}\frac{g_2^2}{g_1}\hbar\nu}{c} = \frac{g_2}{g_1} \frac{A}{4} \lambda^2 \quad (G.7)$$

For the Doppler broadened cross section, the cross section has a corrective factor

$$\sigma = \frac{\sigma_0}{\sqrt{2\pi}\Delta} \exp\left(-\frac{(\nu - \nu_{21})^2}{2\Delta^2} 4\pi^2\right) \quad (G.8)$$

As we consider the monochromatic case tuned to the correct frequency $\nu = \nu_{12}$ the exponential term disappear and the cross section is :

$$\sigma = \frac{g_2}{g_1} \frac{A}{4} \frac{\lambda^2}{\sqrt{2\pi}\Delta} \quad (G.9)$$

where

$$\Delta = \sqrt{\frac{kT}{Mc^2}} 2\pi\nu \quad (G.10)$$

In the case of the transition from 6^1S_0 state to the 6^3P_1 one for ^{199}Hg at room temperature, $\Delta = 8.4 \text{ MHz}$ and $g_1 = g_2$ as the can distinguish the hyper-fine structure and only target at the $F = 1/2$ sub-level. Then $\sigma = 2 \times 10^{-17} \text{ m}^2$.

Appendix H

Unpolarized light level $I(t)$ determined from PMT file

The $I(t)$ values have been determined from the PMT files (Fig. 8.4). The error of each datapoint from the PMT file of a same cycle (e.g. each point of Fig. 8.4) is set to the standard deviation evaluated during the first second of the PMT signal. Fig. H.1 show that the PMT has a small drop just before the filling of the chamber and a bump before the emptying. It is assumed that the drop in absorption is due to a realignment of the chamber with the laser and photo-detector when the neutron shutter is closed. This alignment is kept for the duration of the cycle therefore the value of $I(t)$ is evaluated when this alignment is verified.

$I(t_0)$ represents the value of the PMT when the precession chamber is empty. There is no mercury inside the cell to block the light. The analysis algorithm computes the fluctuations between $t = 0$ s and $t = 10$ s. The maximum value on this period is used as threshold for the rising edge of the filling (see Fig. H.1).

```
IF pmt_value > 2*I1_Fluctuation+ initial value
THEN mercury filling = true
```

Then value of $I(t_0)$ is determined by a constant fit for 1.5 s before the filling time which is delimited by the drop. The fit provides the error associate with $I(t_0)$.

$I(t_1)$ represents the amount of mercury in the chamber. It corresponds to the light level of the photo-detector signal if the mercury atoms were unpolarized during the flipping pulse. The value of $I(t_1)$ is determined by a double-cosine function:

$$y = as(t_1)\sqrt{2} \sin(2\pi ft - \varphi_1) \cos(2\pi ft\varphi_2) + I(t_1) \quad (\text{H.1})$$

used to fit the signal for 1.5 s after $t_1 = t_0 + t_w$ where t_w is defined by the time between the filling and the pulse, Table 8.3. Here, the decay of $I(t)$ and $as(t)$ are neglected. The fit also provide the error associate with $I(t_1)$.

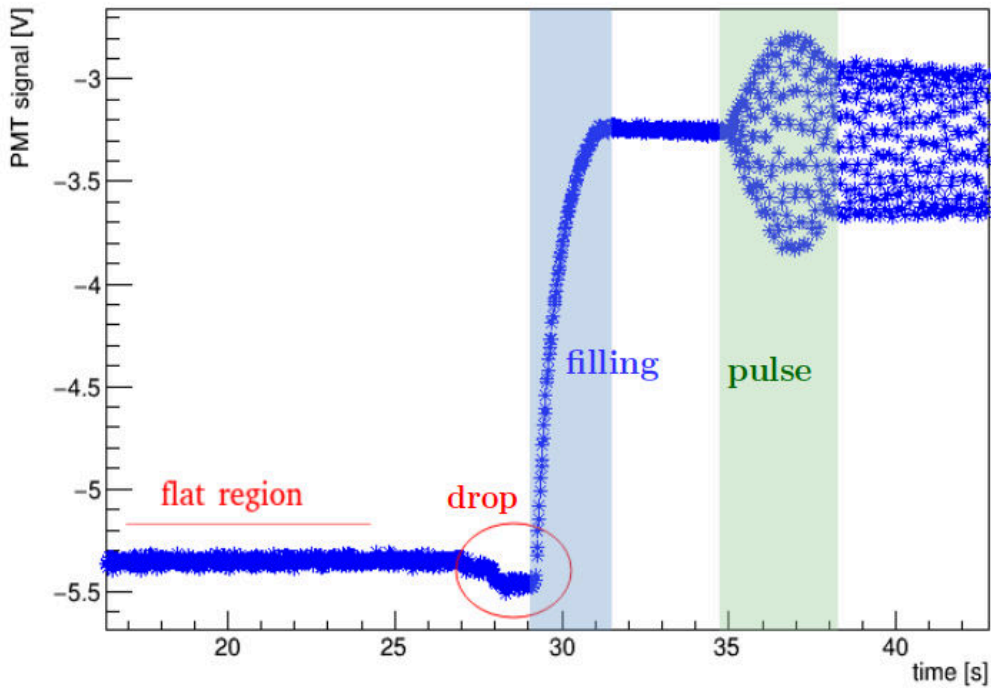


Fig. H.1: PMT signal from run 635 as a function of time zoomed at the beginning of the first cycle.

$I(t_2)$ represents the amount of mercury remaining in the chamber at the end of the measurement. It is determined before the opening of the shutter noticeable by a bump before the emptying. The algorithm estimates a first approximation of the $I(t_2)$ value: the signal at 180 s after the position of the $I(t_0)$ is fitted by a constant for 10 s. This value is used as in threshold condition to determine the position of the emptying of the chamber. This is assuming that the leak time is high (700 s for a maximum amplitude of 0.5 V), therefore, the value of $I(t_2)$ does not change more than 0.2 V over 30 s.

```
IF pmt_value<I3_estimate-0.2V
THEN emptying =true
```

The value of $I(t_2)$ is determined by a sinusoidal fit on a region defined from 3 s to 1.5 s before the start of the emptying, i.e., before the bump. The fit also provide the error associate with $I(t_2)$.

Appendix I

Metafile data for the density-polarization factor

The metafile records several pre-analyzed values as $a_s(t_1), \tau, I(t_0)...$ which can be used to perform a quick analysis of the data. Some of them are extracted from the precession file ($a_s(t_1), \tau$), other are recorded only in the metafile ($I(t_0), I(t_1), I(t_2)$) and some are calculated from the previous values (T_3).

The values of $I(t_0), I(t_1), I(t_2)$ from the metafile are not stable and cannot be used for a precise analysis. These values are computed in the analysis as explained in the section before. T_3 is calculated from $I(t)$ values therefore cannot be trusted either in the metafile.

The values of $a_s(t_1), \tau$ from the metafile are actually extracted from the precession file via a fit.

I.1 Precession file: $a_s(t_1)$ and τ

The precession file is the AC recording of photo-detector signal after a band-pass filter. The data points are recorded in bin with a rate of 100 Hz. The error on the precession signal is determined by the standard deviation of a file without signal send in see [Fig. I.1](#). Its values is ~ 11.7 bin.

Then, the signal is fitted by a cosine modulated with an exponential:

$$PMT = a_s(t_0) \cos(2\pi f_{Hg} t - \varphi) \exp(t/\tau) + C \quad (\text{I.1})$$

with $a_s(t_1)$, τ , C and φ , the variable of the fit and $f_{Hg} \approx 7.87$ Hz.

The parameter $a_s(t_1)$ corresponds to the amplitude in the metafile with a conversion factor of 44325.6 bin/V, see [Fig. I.2](#). This conversion factor was verified by extracting the value of $a_s(t_1)$ in the PMT file from a sinusoidal fit at the end of the flipping pulse $t = t_0 + t_w + 1.5$ s = $t_1 + 1.5$ s, see [Fig. I.2B](#). Then this value

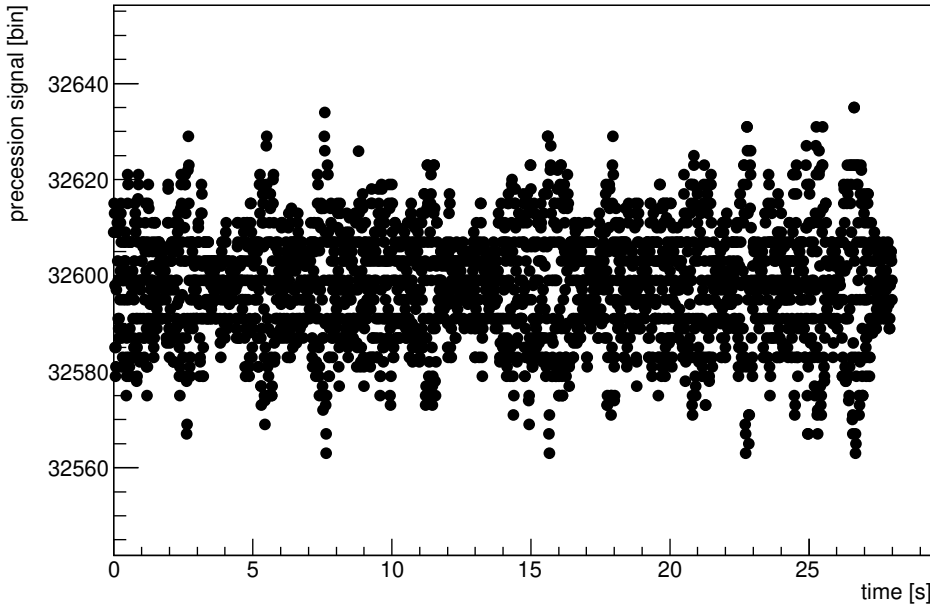


Fig. I.1: Noise PMT value as a function of time from file 012655-2017-08-31. The PMT value is without unit as it is a number of bin.

was compared to the value recorded in the meta file (which is evaluated from the precession file), Fig. I.2C. A linear fit of Fig. I.2C confirms the conversion factor: the slope is 1.0 ± 0.1 and the offset is -0.01 ± 0.05 . As the conversion factor was confirmed, the error associated to the amplitude can be converted in volts.

The values of $as(t_1)$ from the precession file and from the metafile are matching. However, as the metafile does not contain an error associated to this value, the fit from the precession file is used.

A comparison analysis has been performed on the PMT file and gives similar results considering the exponential decay.

τ represents the decay time from the polarization of mercury atoms. The value from the precession file and the metafile are in agreement, therefore, the value from the metafile can be and has been used. The corresponding error is coming from the precession file fit.

I.2 Unpolarized light level values

The precession file records data after a band-pass filter which does not allow to measure the I values. The PMT file data are recorded before the filter, therefore, are not affected by it. The I values from the metafile are ad-hoc measurement directly from the PMT sensor.

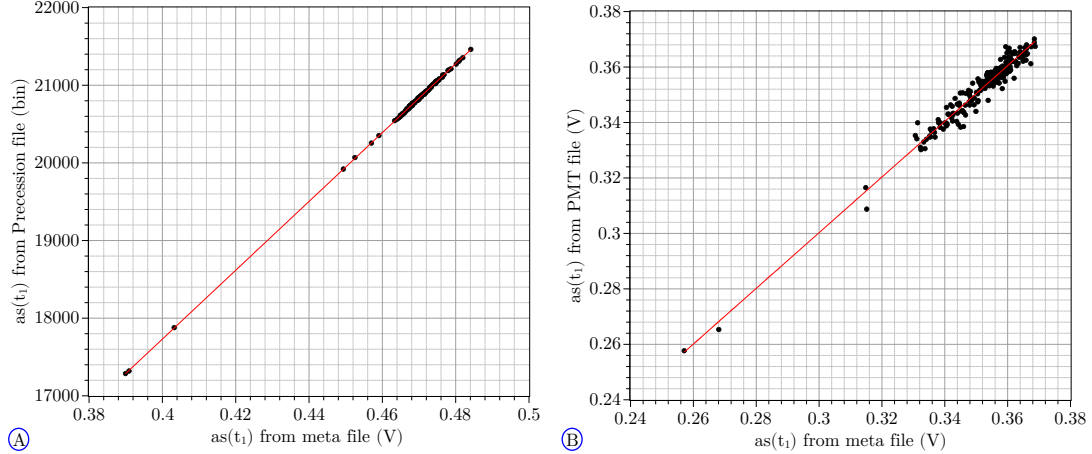


Fig. I.2: A) Comparison of $as(t_1)$ extracted from the precession file and the meta file for all measurement. The red line corresponds to the linear fit which was used to determined the conversion factor. B) Comparison of $as(t_1)$ extracted from the precession file and the meta file for the batch 3. The red line corresponds to the linear fit which was used to confirm the conversion factor.

In the meta file, the value for $I(t_0)$ is measured by the PMT sensor during the opening of the shutter. This raises issues as at that moment the reading is not stable and a scattering appears on the value of $I(t_0)$ over time (Fig. I.3).

In the meta file, the value for $I(t_1)$ is measured by the PMT sensor at the beginning of the mercury flipping pulse. A two state signal, can be observed in the Batch 3.

In the meta file, the value for $I(t_2)$ is measured by the PMT sensor before emptying the chamber out. No problem has been notice for this value but for consistency the value has been extracted from the PMT file .

The calculation for T_3 uses the values of $I(t_0)$ and $I(t_1)$, as the ones from the metafile have a low accuracy, so does T_3 from the metafile.

I.3 Light absorption, density, and polarization

The metafile also contains pre-calculated values like the absorption and the polarization in order to monitor the mercury system during the measurements. Fig. I.4 presents the data before any data selection of the light absorption ratio and the polarization during the presented measurement. For completion the density value has been calculated from the stated polarization and absorption ratio.

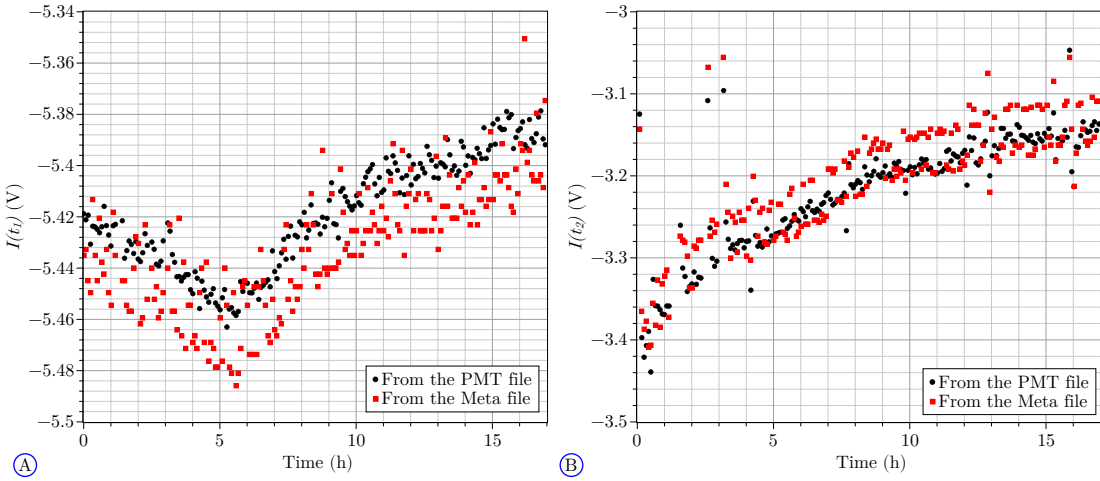


Fig. I.3: A) $I(t_0)$ as a function of time for the PMT file (black circles) and for the metafile (red squares). There is more fluctuation on the short scale for the values extracted from the meta file than from the fit of the PMT file data. B) $I(t_1)$ as a function of time for the PMT file (black circles) and for the metafile (red squares). The data from the meta file shows a two state behavior which does not describe the reality of the measurement. The data are from the batch 3.

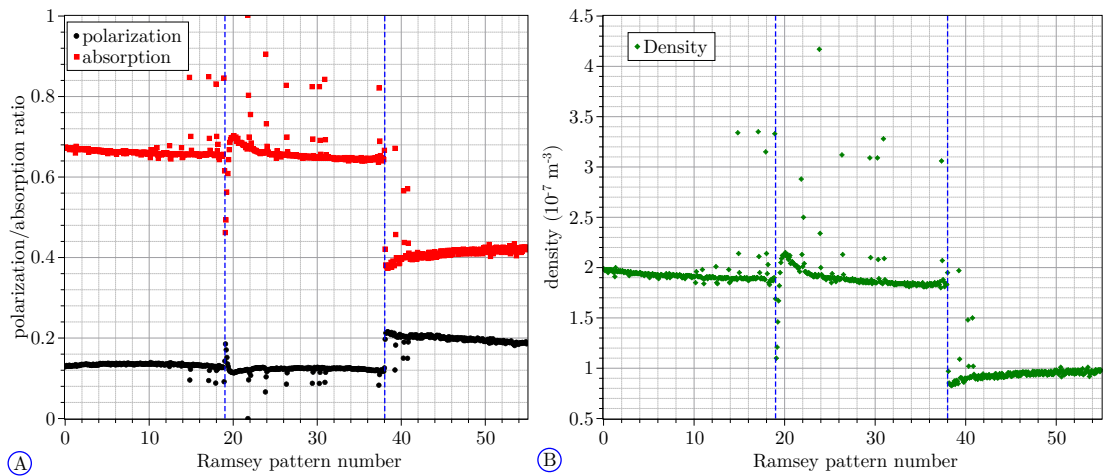


Fig. I.4: A) Value of the polarization and absorption ratios from the meta file. B) Value of the density calculated from the value of the metafile. The dashed blue lines corresponds to the limit of the different batches.

Declaration of consent

on the basis of Article 18 of the PromR Phil.-nat. 19

Name/First Name: Chanel Estelle

Registration Number: 17-127-903

Study program: Physics

Bachelor

Master

Dissertation

Title of the thesis: The Beam EDM experiment and the measurement of the neutron incoherent scattering length of 199 Hg

Supervisor: Prof. Dr. Florian Piegsa

I declare herewith that this thesis is my own work and that I have not used any sources other than those stated. I have indicated the adoption of quotations as well as thoughts taken from other authors as such in the thesis. I am aware that the Senate pursuant to Article 36 paragraph 1 litera r of the University Act of September 5th, 1996 and Article 69 of the University Statute of June 7th, 2011 is authorized to revoke the doctoral degree awarded on the basis of this thesis.

For the purposes of evaluation and verification of compliance with the declaration of originality and the regulations governing plagiarism, I hereby grant the University of Bern the right to process my personal data and to perform the acts of use this requires, in particular, to reproduce the written thesis and to store it permanently in a database, and to use said database, or to make said database available, to enable comparison with theses submitted by others.

Bern, 24/08/2021

Place/Date

Signature



Curriculum Vitae

Contact information

Name: CHANEL Estelle

Work address: University of Bern,
LHEP, Sidlerstrasse 5,
3012 Bern, Switzerland

Work email: estelle.chanel@lhep.unibe.ch

Work mobile number: +41 77 504 71 89

Nationality: French

Private address: Zwyssigstrasse 40,
3007 Bern, Switzerland

Private email: chanel.estelle@hotmail.fr

Private mobile number: +33 (0)7 83 47 92 41

Professional experiences

09/2017 – Present: PhD in the Fundamental Neutron and Precision Physics group
at **University of Bern**, Bern, Switzerland

Thesis : “The BeamEDM experiment and the measurement of neutron incoherent scattering length of 199 Hg ”

- Data analysis BeamEDM and nEDM
- DAQ software development for BeamEDM
- Beamtime experiences for BeamEDM at Institute Laue Langevin and Paul Scherrer Institute
- HV electrodes basic design in COMSOL for n2EDM
- Neutron characterisation of electrodes surface and collimator at Paul Scherrer Institute

03/2017 – 08/2017: M2 internship in nEDM group at **University of Sussex**, Brighton, England

Thesis : “Simulation of systematic effects in the nEDM experiment”

- Improvement of the Monte Carlo software STARucn
- Implementation of spin dependent scattering in STARucn
- Benchmark STARucn on the geometric phase effect

09/2016 – 02/2017: Master laboratory project on the LISE spectrometer at **GANIL**, Caen, France

Thesis : “Study of the distribution in magnetic moment of fragments after Lise's Target at GANIL “

- Simulation software LISE++ and comparison with real data
- Optimisation of the momentum spots selection

05/2016 - 08/2016: M1 internship in UCN group at **Paul Scherrer Institute**, Villigen, Switzerland

Thesis: “Study of dependency parameters of sD₂ crystal on UCN yield in the source”

- MCNPx/6 simulation of the UCN source performances
- Thin film calculations

Education

2017-Present: **PhD in particle physics**, University of Bern, Bern, Switzerland

2016-2017: **Master Nuclei, Atom, Collisions**, Université de Caen Normandie, Caen, France

2014-2017: **Engineering degree in Electronics and Applied Physics**, ENSICAEN, Caen, France
Specialisation in nuclear engineering

Skills

Experimental knowledge

- Neutron EDM: Ramsey and Rabi technique, vxE and geometric phase systematic effects, Measurement and data analysis strategies
- Neutron scattering: Incoherent scattering length with pseudo magnetic field method, Neutron reflectometry for surface characterisation
- UCN conversion: Monte Carlo simulation of UCN source for yield characterisation

Hardware

- High voltage system: Design and operational knowledge
- Vacuum system: Operational knowledge
- Electronics: Design of custom circuits and implementation with veroboard and PCB
- Laboratory work: Assembly of BeamEDM apparatus in the lab. and during beamtimes, Conducting measurements using standard laboratory devices

Programming languages

- High-Level Language: C, C++, ROOT, JAVA, Python
- Low-Level Language: Assembler Language, SCPI (Standard Command for Programmable Instruments)
- DAQ system: Midas (Maximum Integrated Data Acquisition System)

Simulation software

- COMSOL: Finite Element Method software used for static electric field simulations
- MCNPx/6: Monte Carlo Simulation Software for Nuclear reactions
- LISE++: Monte Carlo simulation software applied to nuclear spectrometers

Languages

- French: Native speaker
- English: C1 (Erasmus test 08/2017)
- German: B1
- Italian: A2 (understanding)

List of Publications, Presentations and Posters

Publications with active contribution

- N. Ayres, et al., The design of the n2EDM experiment. *The European Physical Journal C*, 80 (2021) 512.
- Abel, C. et al., Measurement of the Permanent Electric Dipole Moment of the Neutron. *Phys. Rev. Lett.*, 124 (2020) 081803.
- E. Chanel, et al., The pulsed neutron beam EDM experiment. *EPJ Web Conf.*, 219 (2019) 02004.
- Abel, C. et al., The n2EDM experiment at the Paul Scherrer Institute. *EPJ Web Conf.*, 219 (2019) 02002.
- N. Ayres, et al., Monte Carlo Simulations for the Optimization and Data Analysis of Experiments with Ultracold Neutrons. *JPS Conf. Proc.*, 22 (2018) 011032.

Publications with the collaboration

- C. Abel, et al., A search for neutron to mirror-neutron oscillations using the nEDM apparatus at PSI. *Phys. Let. B*, 812 (2021) 135993.
- C. Abel, et al., Optically pumped Cs magnetometers enabling a high-sensitivity search for the neutron electric dipole moment. *Phys. Rev. A*, 101 (2020) 053419.
- N. Ayres, et al., Data blinding for the nEDM experiment at PSI. *The European Physical Journal A*, 57 (2021) 152.
- C. Abel, et al., Magnetic-field uniformity in neutron electric-dipole-moment experiments. *Phys. Rev. A*, 99 (2019) 042112.
- C. Abel, et al., nEDM experiment at PSI: Data-taking strategy and sensitivity of the dataset. *EPJ Web Conf.*, 219 (2019) 02001.

Presentations

- “An EDM Measurement using a Pulsed Cold Neutron Beam”, *Annual Meeting of the Swiss Physical Society Austrian Physical Society* in Zurich, Switzerland, 2019.
- “An EDM Measurement using a Pulsed Cold Neutron Beam”, *Albert Einstein Center Graduate Student Seminar* in Bern, Switzerland, 2019
- Several presentations for *collaboration meetings* on topics including neutron incoherent scattering length, systematic effect calculation, high voltage design of n2EDM, 2017-2021
- Thesis defenses, ENSICAEN and Université de Caen Normandie, Caen, France, 2016-2017

Posters

- “Overview of the BeamEDM project and latest results”, *Physics of fundamental Symmetries and Interactions* in Villigen, Switzerland, 2019
- “Time-of-Flight Ramsey Experiment with a Chopped Neutron Beam”, *International Workshop on Particle Physics at Neutron Sources* in Grenoble, France , 2018
- “Time-of-Flight Ramsey Experiment with a Chopped Neutron Beam”, *Annual Meeting of the Swiss Physical Society* in Lausanne, Switzerland, 2018.